

Weakening of the lithosphere beneath Scotian basin: prelude for initiation of subduction of Atlantic Ocean

by

Ying Zheng

Earth and Planetary Sciences

McGill University

Montréal, Canada

April, 2002

A Thesis submitted to the
Faculty of Graduate Studies and Research
in partial fulfillment of the requirements for the degree of
Doctor of Philosophy

© Ying Zheng, 2002



National Library
of Canada

Bibliothèque nationale
du Canada

Acquisitions and
Bibliographic Services

Acquisitions et
services bibliographiques

395 Wellington Street
Ottawa ON K1A 0N4
Canada

395, rue Wellington
Ottawa ON K1A 0N4
Canada

Your file *Votre référence*

ISBN: 0-612-85759-X

Our file *Notre référence*

ISBN: 0-612-85759-X

The author has granted a non-exclusive licence allowing the National Library of Canada to reproduce, loan, distribute or sell copies of this thesis in microform, paper or electronic formats.

L'auteur a accordé une licence non exclusive permettant à la Bibliothèque nationale du Canada de reproduire, prêter, distribuer ou vendre des copies de cette thèse sous la forme de microfiche/film, de reproduction sur papier ou sur format électronique.

The author retains ownership of the copyright in this thesis. Neither the thesis nor substantial extracts from it may be printed or otherwise reproduced without the author's permission.

L'auteur conserve la propriété du droit d'auteur qui protège cette thèse. Ni la thèse ni des extraits substantiels de celle-ci ne doivent être imprimés ou autrement reproduits sans son autorisation.

Canada

To my parents

Jianzhong Zheng and Zifen Liu

Abstract

While plate tectonic theory has been developed considerably in the last four decades, the of initiation of subduction remains an enigma. In this thesis, I investigate the possible initiation of subduction of North Atlantic oceanic lithosphere at the Scotian basin off east coast of Canada.

On the basis of the relationships between topography, gravity and magnetic anomalies, in both space and Fourier domains, a crustal model is proposed to explain the long- and intermediate-wavelength components of the gravity anomalies of eastern Canada which takes into account the topography, density perturbations in the crust and upper mantle and Moho undulation with certain degree of compensation. No pronounced correlation is observed between the reduced-to-pole magnetic anomalies and topography, as well as between the magnetic anomalies and the vertical gradient of gravity anomalies. The low magnetic susceptibility beneath suture zones indicates thermal demagnetization of the high-magnetic crustal root.

The above topography and gravity analysis method is used to determine the compensation state of the Scotian basin. A 3-D density model that incorporates seawater, sediments, oceanic and continental crust and the lithosphere down to 35 km depth is established, which together with density perturbations inside the crust and mantle of the model, produce the observed gravity anomalies. Regional compensation is required to explain the observations. A 2-D thin elastic plate model is adopted to investigate the flexural response of the lithosphere subjected to the loads due to the sediments and excess density perturbations. The rigidity of the lithosphere beneath the basin is estimated to be about one to two orders of magnitude smaller than elsewhere. The weakening is due to thermal blanketing effects of the thick sediments and the temperature-dependent rheology of lithosphere. The weak lithosphere would have a controlling effect on reactivation of normal faults at the ocean-continent boundary. The possible re-orientation of the spreading ridge of North Atlantic ocean may produce tensional stresses that would decouple the oceanic lithosphere from the continental one at the weak zone, allowing the lithosphere beneath the basin to bend more. Subduction initiation would be facilitated when taking into account further weakening of the lithosphere by extra sediments and subsequent compression.

The rigidity of the lithosphere far from the Scotian basin in the above study is not well constrained because the surface load on this part of the lithosphere is dominated by very long-wavelength components. Flexural response of the lithosphere

subject to loading of the New England seamounts is used to estimate the rigidity of the lithosphere beneath. Fourier domain analysis of the bathymetry and gravity anomalies suggests that density perturbations exist in the crust and/or upper mantle. The rigidity values obtained using a 3-D thin elastic plate model are about $3-7 \times 10^{23}$ Nm for lithospheric ages ranging from 30 to 60 m.y. The base of the elastic part of the lithosphere follows an isotherm in the range of $750^{\circ} - 850^{\circ}C$, suggesting a strong lithosphere of North Atlantic ocean compared to that of the other oceans.

Résumé

Bien que la théorie de la tectonique des plaques ait été considérablement développée durant les quatre dernières décennies, le mécanisme d'initiation de la subduction demeure un mystère. Dans cette thèse, je vais explorer l'initiation possible de la subduction de la lithosphère océanique Atlantique au niveau du bassin Écossais près de la côte est du Canada.

Je vais proposer un modèle de la croûte terrestre qui explique les composantes de moyenne et grande longueur d'onde des anomalies de gravité de l'est du Canada. Ce modèle est basé sur les relations qui existent entre la topographie et les anomalies magnétiques et de gravité, tant dans le domaine de l'espace que dans le domaine de Fourier. Le modèle tient compte de la topographie, des perturbations de densité dans la croûte et la partie supérieure du manteau ainsi que de l'ondulation du Moho avec un certain degré de compensation. Aucune corrélation n'a été observée entre les anomalies magnétiques réduites au pôle et la topographie, de même qu'entre les anomalies magnétiques et le gradient vertical des anomalies de gravité. La basse valeur de susceptibilité magnétique sous les zones de suture indique une démagnétisation thermique des racines de la croûte ultra-magnétique.

La méthode d'analyse topographique et de gravité décrite ci-haut est utilisée pour déterminer l'état de compensation du bassin Écossais. Je vais établir un profil de densité en 3-D jusqu'à une profondeur de 35 km. Ce profil comprendra l'eau de mer, les sédiments, les croûtes océanique et continentale ainsi que la lithosphère. Ce profil permettra, avec l'aide des perturbations de densité de la croûte et du manteau du modèle, de reproduire les anomalies de gravité observées. Il est nécessaire de faire intervenir une compensation régionale pour expliquer les observations. Je vais utiliser un modèle 2-D de plaque élastique mince pour explorer la réponse flexurale de la lithosphère lorsqu'elle est soumise à des chargements dus aux sédiments et à des perturbations de densité excessives. J'ai estimé que la rigidité de la lithosphère sous le bassin doit être environ de une à deux ordres de magnitude moins élevée qu'ailleurs. Cet affaiblissement est dû à l'effet de couverture thermique des sédiments et de la rhéologie de la lithosphère qui dépend grandement de la température. L'affaiblissement de la lithosphère aurait eu un effet contrôlant sur la réactivation des failles normales à la frontière entre l'océan et le continent. La ré-orientation possible de la crête dorsale de l'océan Atlantique Nord produirait des tensions qui découpleraient la lithosphère océanique de la continentale sur la zone faible. Ce découplément permettrait à la

lithosphère sous le bassin de mieux plier. L'initiation de la subduction serait facilitée en tenant compte de l'affaiblissement supplémentaire de la lithosphère par les sédiments ainsi que la subséquente poussée compressive de la crête.

La rigidité de la lithosphère océanique loin du bassin Écossais utilisée dans cette étude est incertaine parce que les chargements de surface sur cette partie de la lithosphère sont dominées par des composantes de grande longueur d'onde. La réponse flexurale de la lithosphère océanique soumise au chargement des monts de mer de la Nouvelle-Angleterre est utilisée pour estimer la rigidité de la lithosphère. Une analyse dans le domaine de Fourier de la bathymétrie et des anomalies de gravité indique que des perturbations de densité existent dans la croûte et/ou dans la partie supérieure du manteau. Les valeurs de rigidité obtenues en utilisant un modèle 3-D de plaque élastique mince sont d'environ $3-7 \times 10^{23}$ Nm pour des ages lithosphériques allant de 30 à 60 millions d'années. La base de la partie élastique de la lithosphère suit un isotherme pouvant aller de 750° à 850° C. Cet isotherme suggère une lithosphère plus forte dans l'océan Atlantique Nord comparée à celle d'autres océans.

Contributions of Authors

This is a manuscript-based thesis. The thesis consists of 6 chapters. Chapters 3 - 5 are written in manuscript format. Chapter 1 is a general introduction. Chapter 2 is a comprehensive literature review, and Chapter 6 presents major conclusions.

The following three papers are included in the thesis as chapters 3 - 5:

Zheng, Y., Arkani-Hamed, J., 1998. Joint inversion of gravity and magnetic anomalies of eastern Canada. *Canadian Journal of Earth Sciences* 35, 832-853.

Zheng, Y., Arkani-Hamed, J., 2002. The elastic properties of the lithosphere beneath Scotian basin. *Tectonophysics* 344, 137-156.

Zheng, Y., Arkani-Hamed, J., 2002. Rigidity of the Atlantic oceanic lithosphere beneath New England seamounts. Submitted to *Tectonophysics*, Feb. 2002.

The candidate, being the first author of the three papers, carried out all of the research work. The co-author, Prof. J. Arkani-Hamed, as the candidate's supervisor, contributed significantly in general ideas and guidance of the research.

The following statement is an excerpt from the "Guidelines for Thesis Preparation" of McGill University.

Manuscript – based Thesis

As an alternative to the traditional thesis format, the dissertation can consist of a collection of papers of which the student is an author or co-author. These papers must have a cohesive, unitary character making them a report of a single program of research. The structure for the manuscript-based thesis must conform to the following:

1. Candidates have the option of including, as part of the thesis, the text of one or more papers submitted, or to be submitted, for publication, or the clearly-duplicated text (not the reprints) of one or more published papers. These texts must conform to the "Guidelines for Thesis Preparation" with respect to font size, line spacing and margin sizes and must be bound together as an integral part of the thesis. (Reprints of published papers can be included in the appendices at the end of the thesis.)

2. The thesis must be more than a collection of manuscripts. All components must be integrated into a cohesive unit with a logical progression from one chapter to

the next. In order to ensure that the thesis has continuity, **connecting texts that provide logical bridges between the different papers are mandatory.**

3. The thesis must conform to all other requirements of the "Guidelines for Thesis Preparation" in addition to the manuscripts.

The thesis must include the following:

(a) a table of contents; (b) an abstract in English and French; (c) an introduction which clearly states the rationale and objectives of the research; (d) a comprehensive review of the literature (in addition to that covered in the introduction to each paper); (e) a final conclusion and summary;

4. As manuscripts for publication are frequently very concise documents, where appropriate, additional material must be provided (e.g., in appendices) in sufficient detail to allow a clear and precise judgement to be made of the importance and originality of the research reported in the thesis.

5. In general, when co-authored papers are included in a thesis the candidate must have made a substantial contribution to all papers included in the thesis. In addition, **the candidate is required to make an explicit statement in the thesis as to who contributed to such work and to what extent.** This statement should appear in a single section entitled "**Contributions of Authors**" as a preface to the thesis. The supervisor must attest to the accuracy of this statement at the doctoral oral defence. Since the task of the examiners is made more difficult in these cases, it is in the candidate's interest to clearly specify the responsibilities of all the authors of the co-authored papers.

Acknowledgements

I would like to express my deepest gratitude to my supervisor, Prof. Jafar Arkani-Hamed for giving me this opportunity to work on this project. I wish to thank him for his guidance and criticism throughout the course of my Ph.D. study. His continuous encouragement gave me confidence and has been a constant source of support to my study and research. His enthusiasm for science, his critical attitude to research, and his diligence will lead me through my future career.

I would like to thank Prof. Olivia Jensen and Prof. Andrew Hynes for being on my thesis advisory committee. Their constructive discussion and valuable suggestion are greatly appreciated. I wish to thank Dr. Walter Roest of Geological Survey of Canada for being on my Ph.D. preliminary oral exam committee, and for his help in providing the geophysical data used in my research.

I appreciate NRC (National Research Council) Research Press for giving me the copyright permission to include my published paper in Canadian Journal of Earth Sciences in the thesis.

I would like to thank my friends and fellow graduate students Dr. Farhad Sobouti and Dr. Abdolreza Ghods for their stimulating discussion on my research and their friendship. Special thanks are given to Phillipe Benoit and Danel Boutin for translating my thesis abstract into French.

Finally, I am greatly indebted to my parents Jianzhong Zheng and Zifen Liu, and my brother Xing Zheng, for their understanding and continuous encouragement during my study at McGill University.

This research is funded by a grant of Natural Science and Engineering Research Council (NSERC) of Canada to Prof. Jafar Arkani-Hamed. It is also supported by fellowships and scholarships from the Department of Earth and Planetary Science, and McGill Major fellowships to the author.

Contents

Abstract	i
Résumé	iii
Contributions of Authors	v
Acknowledgments	vii
List of Figures	ix
1 Introduction	1
2 Previous Work	5
2.1 Topography, Gravity and Magnetic Analysis	5
2.2 Strength of the Lithosphere	7
2.3 Initiation of Subduction	9
3 Joint Inversion of Gravity and Magnetic Anomalies of Eastern Canada	20
3.1 Abstract	21
3.2 Introduction	21
3.3 Topography, Gravity and Magnetic Relationship	22
3.3.1 Topography Map	23
3.3.2 Gravity Map	23
3.3.3 Magnetic Map	26
3.4 Interpretation of Free Air Gravity Anomalies	29
3.4.1 Short-wavelength components:	29
3.4.2 Intermediate-wavelength components:	31
3.4.3 Long-wavelength components:	33
3.5 Modelling Regional Scale Gravity Anomalies	33
3.6 Interpretation of Magnetic Anomalies	35
3.7 Discussion and Conclusions	39
3.8 Acknowledgements	43
3.9 References	44

3.10	Figure Captions	48
4	The Elastic Properties of the Lithosphere Beneath Scotian Basin	63
4.1	Abstract	64
4.2	Introduction	65
4.3	Geological Setting	65
4.4	Modeling the Observed Gravity Anomalies	66
4.5	Support Mechanism	71
4.6	Strength of the Lithosphere	76
4.7	Initiation of Subduction at Scotian Basin	80
4.8	Conclusions	82
4.9	Acknowledgement	82
4.10	References	83
4.11	Figure Captions	87
5	Rigidity of the Atlantic Oceanic Lithosphere Beneath New England	
	Seamounts	101
5.1	Abstract	102
5.2	Introduction	102
5.3	Geological Setting	103
5.4	Gravity and Topography Analysis	104
5.5	Flexure Model	105
5.6	Discussion and Conclusions	109
5.7	Acknowledgement	110
5.8	References	111
5.9	Figure Captions	115
6	Conclusions	120
6.1	Discussion and Conclusions	120
6.2	Shortcomings and Future Research	121
	Appendices	124

List of Figures

3.1	A simplified tectonic map of eastern Canada based on the Tectonic Map of Canada published by Geological Survey of Canada, 1968. The map also shows the locations cited in the text. DPB is the De Pas Batholith, MHC is the Manicouagan-Hart Jaune complex, CSB is the Cap Smith belt.	50
3.2	a) Equivalent rock topography, in km, b) Free air gravity anomalies, in milligals, c) Distribution of gravity stations, and d) space-domain correlation of the topography and gravity anomalies.	51
3.3	a) Power spectra of free air gravity anomalies, the gravity field due to the topography and gravity field of the topography which is compensated at 37 km depth, and b) Spectral-domain degree correlation coefficients between gravity anomalies and topography, reduced-to-pole magnetic anomalies and topography, and reduced-to-pole magnetic anomalies and vertical gradient of gravity anomalies.	52
3.4	a) Magnetic anomalies, b) High altitude magnetic profiles, c) Magsat dawn map, and d)- Low-pass filtered low-altitude magnetic anomalies. Units are in nT.	53
3.5	Comparison of high-altitude magnetic profiles with the upward continued low-altitude magnetic anomalies to 4 km elevation.	54
3.6	a) Reduced-to-pole magnetic anomalies, in nT, b) Space-domain correlation of the reduced-to-pole magnetic anomalies and topography, c) Vertical gradient of gravity anomalies, in 10^{-7} s^{-2} , and d) Space-domain correlation of the reduced-to-pole magnetic anomalies and the gravity gradient.	55
3.7	Short wavelength components of a) the topography, in km and b) the free air gravity anomalies, in milligals. c) Space-domain correlation of the topography and gravity anomalies, and d) Density perturbations within the crust, in kg/m^3	56
3.8	Intermediate wavelength components of a) the topography, in km, b) the free air gravity anomalies, in milligals, c) Density perturbations within the crust, in kg/m^3 , and d) Moho undulation, in km. The anomalies near the boundaries in Labrador Sea and Hudson Bay are artifacts arising from edge effects (see the text).	57

3.9	Intermediate and long wavelength components of a) the topography, in km, b) the free air gravity anomalies, in milligals, c) Moho undulation, in km, and d) Excess Moho undulation compared to the undulation of an isostatically compensated Moho, in km.	58
3.10	Power spectra of the density perturbations in the crust specified by the intermediate and long wavelength components. The numbers on the curves are the α values from -3 to 1 with the increment of 0.5. . .	59
3.11	Histograms of the Moho undulation. The numbers on the curves are the α values from -3 to -.5 with the increment of 0.5.	60
3.12	The intermediate and long wavelength components of a) the vertically averaged density perturbations within the 37 km thick crust, in kg/m ³ , and b) the Moho undulation about the 37 km depth of the selected crustal model, in km.	61
3.13	a) Magnetic susceptibility of a half-space with topography, b) Magnetic susceptibility of the crust bounded by the topography and Moho, c) Short wavelength components of the susceptibility of the crust, and d) Intermediate and long wavelength components of the susceptibility of the crust. Units are in 10 ⁻³ SI.	62
4.1	Location of Scotian Basin and contiguous places based on <i>Figure 1.1</i> from Keen and Piper, 1990. The lines across the Scotian Basin are the locations of the profiles used for gravity analysis and stacking the equivalent rock bathymetry (ERB), depth to basement and density perturbations. The black dot represents Sable island. An equal area projection is used in this figure and other similar figures. The dashed contour lines are contours of the depth to basement with an interval of 2.5 km.	89
4.2	(a) Observed gravity anomalies, free-air on the ocean and Bouguer on lands. (b) The equivalent rock bathymetry (ERB). The ERB of the continental areas is set to zero. (c) The depth to basement (after Oakey and Stark, 1995). The tapered zones near the boundaries, where data were tapered to suppress Gibb's ringing in the Fourier transformation are not shown in these maps, and in other similar maps including <i>Figure 1</i>	90

4.3 Gravity anomaly of different layered models along profile CC' (see Figure 1). Model 1, the nominal model with continental crust density $\rho_c = 2800 \text{ kg/m}^3$; oceanic crust density $\rho_o = 2900 \text{ kg/m}^3$, thinned continental crust density $\rho_t = 2850 \text{ kg/m}^3$ and sediment grain density $\rho_s = 2700 \text{ kg/m}^3$; Model 2, $\rho_c = 2800 \text{ kg/m}^3$, $\rho_o = 2900 \text{ kg/m}^3$, $\rho_t = 2900 \text{ kg/m}^3$ and $\rho_s = 2800 \text{ kg/m}^3$; Model 3, $\rho_c = 2800 \text{ kg/m}^3$, $\rho_o = 2900 \text{ kg/m}^3$, $\rho_t = 2800 \text{ kg/m}^3$ and $\rho_s = 2800 \text{ kg/m}^3$; Model 4, $\rho_c = 2800 \text{ kg/m}^3$, $\rho_o = 2800 \text{ kg/m}^3$, $\rho_t = 2800 \text{ kg/m}^3$ and $\rho_s = 2800 \text{ kg/m}^3$; Model 5, $\rho_c = 2800 \text{ kg/m}^3$, $\rho_o = 2900 \text{ kg/m}^3$, $\rho_t = 2800 \text{ kg/m}^3$, and $\rho_s = 2750 \text{ kg/m}^3$; Model 6, $\rho_c = 2750 \text{ kg/m}^3$, $\rho_o = 2900 \text{ kg/m}^3$, $\rho_t = 2800 \text{ kg/m}^3$, and $\rho_s = 2700 \text{ kg/m}^3$; Model 7, $\rho_c = 2700 \text{ kg/m}^3$, $\rho_o = 2900 \text{ kg/m}^3$, $\rho_t = 2900 \text{ kg/m}^3$, and $\rho_s = 2700 \text{ kg/m}^3$; Model 8, $\rho_c = 2700 \text{ kg/m}^3$, $\rho_o = 2900 \text{ kg/m}^3$, $\rho_t = 2800 \text{ kg/m}^3$, and $\rho_s = 2700 \text{ kg/m}^3$. The densities of sea water and mantle are 1000 kg/m^3 and 3300 kg/m^3 respectively for all models. 91

4.4 Observed gravity anomalies, gravity anomalies of the nominal layered model and the constant sediment density model along four profiles (see Figure 1). The thick solid curves show the observed gravity anomalies. The thin dashed curves show the gravity anomalies of the nominal layered model. The thin solid curves show the gravity anomalies of the constant sediment density model. The thick dashed curves show the bathymetry, depth to basement and depth to Moho along the profiles in 0.1 km for better illustration. 92

4.5 (a) Gravity anomalies of the nominal layered model. (b) Differences between observed gravity anomalies and the gravity anomalies of the nominal layered model (observed minus model). (c) Density perturbations required to be added on to the nominal layered model in order to produce the observed gravity anomalies. (d) Lithostatic pressure at 35 km depth. The features on the continental part are not shown in this figure since we are only concerned with the oceanic part. 93

4.6 (a) Selected profiles of the ERB, the depth to basement and density perturbations (see Figure 1 for the locations of the profiles). The profiles are stacked to the reference point where the deflection is a maximum. 94

4.7	Averaged profile of the depth to basement, and the deflections of various rigidity models. Density perturbations are included in the load. The thick solid curve shows the averaged depth to basement profile. a) deflections of the elastic plates with uniform rigidities, b) deflections of the two-segmented model with weak zone up to 500 km. Rigidity is kept at 10^{23} Nm when x is beyond 500 km and c) deflections of two-segmented models with different weak zone width from 200 km to 500 km. The rigidity of the weak zone is 10^{22} Nm, beyond the weak zone it is 10^{23} Nm. Also included in c is the deflection of a two-segmented model with a weak zone up to 500 km, but with no contribution of the density perturbations to the surface load. Note that the x axis of this figure is shifted by 100 km eastward compared to that of Figure 6 to put the hinge zone at $x = 0$. We also show only the first 1000 km from the hinge zone.	95
4.8	The strength envelopes calculated from the half-space cooling model at 10, 20, 30, 40 and 50 m.y. The vertical thick line shows the elastic thickness of the 10 m.y. old plate, as an example.	96
4.9	The elastic thickness of the simple plate model versus time.	96
4.10	The deflections of the simple plate model at different ages. Numbers on the curves show the ages.	97
4.11	(a) The steady state temperature distribution of the lithosphere using the averaged sedimentary thickness profile. (b) Compressional and (c) Tensional strength envelopes of the lithosphere. The depth is measured from the top of the basaltic crust, i.e., the base of the sediments. (b) and (c) are in absolute values.	98
4.12	Profiles of the strength envelopes at the maximum deflection point and a point far from the basin (142 km and 900 km in Figure 11 respectively). Compression is positive and tension is negative. The profiles at 142 km are multiplied by 100 for better illustration.	99
4.13	The deflections of the elastic plate models with pinned boundary conditions, and the deflections of these models if they are decoupled from the continent. The thin solid curve denotes the two-segmented model with a weak zone rigidity of 10^{22} Nm and a 500 km width under pinned boundary conditions. The thick solid curve denotes the deflection of this model when decoupled from the continent. The long dashed curve denotes the deflection of the elastic plate with a uniform rigidity of 10^{23} Nm. The dashed curve denotes the deflection of the same model when it is decoupled from the continent.	100

5.1	Location of New England seamounts and contiguous area based on Figure 1.1 from Keen and Piper (1990), and Fig. 1 from Duncan (1984). An equal distance projection is used in this figure and Figure 2. The bathymetry is contoured at 0.5 km interval. 1- Nashville, 2- Michael, 3- Allegheny, 4- Gilliss, 5- Vogel, 6- Rehoboth, 7- Manning, 8- Gregg, 9- Gosnold, 10- Atlantis, 11- Kelvin, 12- Balanus.	116
5.2	a) Free-air gravity anomalies. (b) Bathymetry. (c) The band-pass filtered gravity anomalies where the wave numbers greater than 25 are filtered out and those less than 7 are suppressed. (d) The similarly band-pass filtered bathymetry. The mean value is removed, therefore, the seamounts have positive topography relative to average oceanic floor.	117
5.3	(a) Power spectra of the observed gravity anomalies, the gravity anomalies of uncompensated topography, and the gravity anomalies of the Airy compensated topography at 10, 20, 30 and 40 km depth, respectively. (b) Degree correlation of the topography and observed gravity anomalies, and topography and density perturbations for the rigidity value of 10^{23} Nm. (c) Power spectra of density perturbations for rigidity values of 10^{21} , 10^{22} , 10^{23} , and 10^{24} Nm.	118
5.4	Strength envelopes of 30, 40 and 60 m.y. old oceanic lithosphere. . . .	119
5.5	Isotherms for 750 °C and 850 °C from a half-space cooling model. The triangles represent depth to the base of the elastic part of the oceanic lithosphere at 30, 40 and 60 m.y. from our calculation.	119

Chapter 1

Introduction

Subduction plays an important role in plate tectonics. Despite the fact that plate tectonic theory has developed considerably since its foundation in early 1960s, the process of initiation of subduction remains poorly understood. The difficulties come from both observations and theoretical studies. No successful models have been proposed to explain the mechanism and process of initiation of subduction, although much effort has been put in the study, making this topic an outstanding topic in geodynamics. The objective of this thesis is to study the strength of the lithosphere of north Atlantic ocean, and the possibility of initiation of subduction of Atlantic oceanic lithosphere at Scotian basin off east coast of Canada.

The North Atlantic ocean was formed during the Mesozoic rifting of Africa and North America and later seafloor spreading. The North Atlantic ocean, Labrador Sea and Baffin Bay did not develop in one single episode of opening. Rifting and seafloor spreading took place later in the northern part than in the South (Keen and Piper, 1990). The incipient plate motions between Africa and North America in Triassic, at the present Scotian margin and at the Grand Banks, created the rifted margin off Nova Scotia and the transform margin south of the Grand Banks. Plate motion between Greenland and North America and the development of the sedimentary basins began in the Early Cretaceous. Final continental break-up of Greenland and North America, and onset of seafloor spreading formed Labrador Sea, Baffin Bay, and Davis Strait (Keen et al. 1990). Spreading in Labrador Sea and Baffin Bay stopped about 35 m.y. ago. The sedimentary basins on the Atlantic margin were formed during the post-rift phase which is generally a time of passive subsidence and sedimentation in response to cooling and thermal contraction of the lithosphere.

The Scotian basin, located southeast off Nova Scotia, is a mature marginal basin with one of the largest depth to basement and thickest sediment accumulations of the eastern north American margin. The landward side of the Scotian basin is marked by a hinge zone which is a zone of normal faulting, with a thin sedimentary section overlapping the continental lithosphere. However, the normal faults may be too deeply buried to be detected (Keen and Beaumont, 1990). The thickness of sediments

increases rapidly seaward (see Figure 1B, Ericson, 1993).

The thick sedimentary basins on passive margins are preferential places for initiation of subduction due to the flexure induced by the thick sediments in addition to all other driving forces. The major driving forces of initiation of subduction are: 1) the ridge push resulting from the elevation of the spreading ridge relative to the adjacent ocean floor, and 2) the negative buoyancy due to the thickening of the cold lithosphere (McKenzie, 1977). Although cooling of the lithosphere can cause gravitational instability, the lithosphere becomes more rigid with age (Parsons and Sclater, 1977; Watts, 1978). When the total driving forces exceed the strength of the lithosphere the lithospheric failure occurs. Slab pull cannot be taken into account for the initial stage of subduction.

The objective of this thesis is to study the strength of the lithosphere beneath the Scotian basin taking into account the thermal blanketing effect of the thick sediments, and the possibility of initiation of subduction at Scotian basin due to the weakening of the lithosphere beneath. To achieve this objective three steps, presented in three papers, are carried out. I first develop a Fourier domain analysis method to study the relationship between topography/bathymetry, gravity and magnetic anomalies, and to calculate possible density perturbations in the crust and/or upper mantle. I apply this method to eastern Canada which comprises the continental part of eastern Canada and a large portion of the Labrador Sea. It also includes the ocean-continent boundary and the extensive continental shelf created during the continental rifting that produced Labrador Sea. The diverse tectonic processes in this area provide a good opportunity to study the topography/bathymetry, gravity and magnetic anomaly relationship and determine the lateral heterogeneities related to the major tectonic events. Using this established method, I then investigate the compensation state and support mechanism of the lithosphere beneath the Scotian basin. I investigate the possibility of initiation of subduction of the North Atlantic at the Scotian basin due to the fact that the thermal blanketing of the thick sediments weakens the lithosphere beneath the basin and makes it a preferential place for initiation of subduction. The rigidity of the lithosphere far from the basin is not well constrained, because the surface load on this part of the lithosphere is dominated by long wavelength components of the sedimentary load. Therefore, I investigate flexural response of the lithosphere to New England seamount loads, which are located far from the basin, to estimate the rigidity of the lithosphere and confirm our previously obtained rigidity values far from the basin.

Chapter 2 provides a comprehensive review of previous work on 1) the topography, gravity and magnetic analysis of eastern Canada, 2) the strength of the lithosphere, and 3) the initiation of subduction.

In Chapter 3, I use topography, gravity and magnetic data to study the main characteristics of the lateral variations in density and magnetization of the crust in eastern Canada. Comprehensive Fourier domain and space domain methods are developed to study the relationships between these three data sets. I apply these methods to

eastern Canada to extract as much information as possible about their relationships, and obtain useful criteria to distinguish certain physical processes that have created lateral variations within the crust. I use the topography-gravity relationship to constrain the density perturbations in the crust and the thickness of the crust beneath eastern Canada. This provides a means to obtain lateral variations in the crustal magnetization through the inversion of magnetic anomalies that takes into account the effects of the surface topography and Moho undulation. This leads to geophysical interpretations of the tectonic events in this area, as revealed by major characteristics of the gravity and magnetic anomalies. This exercise resulted in a paper that is published in *Canadian Journal of Earth Sciences* (Zheng and Arkani-Hamed, 1998).

In Chapter 4 I use the Fourier domain analysis method developed in Chapter 3 to determine the compensation state of the lithosphere beneath the Scotian basin using more recent gravity, bathymetry and depth to basement data. A 3-D density model is adopted to model the gravity anomalies of the study area and the lateral density perturbations in the lithosphere. Then, I adopt a 2-D thin elastic plate model overlying an inviscid mantle for the oceanic lithosphere to determine the rigidity of the lithosphere both beneath the basin and far from the basin. The thin elastic plate model is subjected to sedimentary load and the load associated with density perturbations in the lithosphere. Finally, I consider the weakening of the lithosphere beneath the basin due to thermal blanketing of the thick sediments and the important role it plays in the initiation of subduction if the continental and oceanic lithosphere decouples at the weak zone, ocean-continent boundary, due to tensional stresses caused by the possible re-orientation of the spreading ridge of North Atlantic ocean. The results presented in this chapter are published in *Tectonophysics* (Zheng and Arkani-Hamed, 2002).

The major objectives of Chapter 5 are: 1) to determine the rigidity of the lithosphere far from the Scotian basin by modeling the flexural response of the lithosphere beneath New England Seamounts, which are located far from the Scotian basin, and 2) to study the age dependence of the strength of the lithosphere. The rigidity of the lithosphere far from the basin determined in Chapter 4 is not well constrained because the sedimentary surface load on this part of the lithosphere is dominated by very long wavelength features. All rigidity values of the order of 10^{23} Nm or lower satisfy the observations of the bathymetry, depth-to-basement and gravity anomalies. Again, the Fourier domain analysis method established in Chapter 3 is used to investigate the compensation state of the lithosphere beneath New England seamounts. The depth to basement data far from the basin are not well resolved. Lateral density perturbations are calculated from modeling of the deformation of lithosphere due to the seamount loads and the load associated with density perturbations in the crust and upper mantle, using a 3-D thin elastic plate model that overlies an inviscid mantle. They are constrained by the observed gravity and bathymetry data. I then determine the rigidity for different ages of the lithosphere from the strength envelope calculations. The strength of the North Atlantic oceanic lithosphere compared with

the strength of the lithosphere in the same age group of other oceans, and its impact on the initiation of subduction of the North Atlantic lithosphere are investigated. This study led to a paper that is submitted for publication in *Tectonophysics* (Zheng and Arkani-Hamed, 2002).

General discussion, major conclusions and shortcomings of my research, as well as possible future work are presented in Chapter 6.

References

- Ericson, S.G., 1993. Sedimentary loading, lithospheric flexure and subduction initiation at passive margins. *Geology* 21, 125-128.
- Keen, C.E., Beaumont, C., 1990. Geodynamics of rifted continental margins. In *Geology of the Continental Margin of Eastern Canada*, chapter 9. Edited by M.J. Keen and G.L. Williams. Geological Survey of Canada, *Geology of Canada*, vol. 2, pp. 391-472.
- Keen, C.E., Loncarevic, B.D., Reid, I., et al., 1990. Tectonic and geophysical overview. In *Geology of the Continental Margin of Eastern Canada*, chapter 2. Edited by M.J. Keen and G.L. Williams. Geological Survey of Canada, *Geology of Canada*, vol. 2, pp. 31-85.
- Keen, M.J., Piper, D.J.W., 1990. Geophysical and historical perspective. In *Geology of the Continental Margin of Eastern Canada*, chapter 1. Edited by M.J. Keen and G.L. Williams. Geological Survey of Canada, *Geology of Canada*, vol. 2, pp. 5-30.
- Mckenzie, D.P., 1977. Initiation of trenches: a finite amplitude instability. In *Island Arcs, Deep Sea Trenches and Back-Arc basins*. Edited by M. Talwani and W. Pitman III. American Geophysical Union, Maurice Ewing Series, vol. 1, 57-62.
- Parsons, B., Sclater, J.G., 1977. An analysis of the variation of ocean floor bathymetry and heat flow with age. *Journal of Geophysical Research* 82, 803-827.
- Watts, A.B. 1978. An analysis of isostasy in the world's oceans, 1, Hawaiian-Emperor seamount chain. *Journal of Geophysical Research* 83, 5989-6004.
- Zheng, Y., Arkani-Hamed, J., 1998. Joint inversion of gravity and magnetic anomalies of eastern Canada. *Canadian Journal of Earth Sciences* 35, 832-853.
- Zheng, Y., Arkani-Hamed, J., 2002. The elastic properties of the lithosphere beneath Scotian basin. *Tectonophysics* 344, 137-156.
- Zheng, Y., Arkani-Hamed, J., 2002. Rigidity of the Atlantic Oceanic lithosphere beneath New England Seamounts. Submitted to *Tectonophysics*, Feb. 2002.

Chapter 2

Previous Work

This chapter reviews the work related to my research in three topics: 1) topography, gravity and magnetic analysis of eastern Canada, 2) strength of the oceanic lithosphere, and 3) initiation of subduction. The focus will be on the initiation of subduction.

2.1 Topography, Gravity and Magnetic Analysis

Gravity anomalies are perturbations in the normal gravity field caused by changes in mass due to topography and density inhomogeneities in the Earth. Gravity measurements are a common geophysical technique used to determine subsurface lateral density variations largely associated with tectonic events. Gravity anomalies that are correlated with topography can be used to study the compensation state and flexure of the elastic lithosphere under surface loading. The concept of isostasy is that the excess mass of the topographic features is compensated by a deficiency of mass below (Banks et al., 1977). The compensating density required by isostasy can be accomplished in several ways. The commonly accepted compensation models include: 1) Pratt model, proposed and developed by J. H. Pratt in 1854 and 1859, assumes horizontal variations in density above a prescribed depth of compensation. The mass of each column of equal cross section above the compensation depth is equal. 2) Airy model, proposed by G. B. Airy in 1855, states that the excess mass associated with the topography of mountains is compensated by a deficiency of mass in an underlying crustal root. Mountains float on a fluid-like higher density mantle, so that the higher the mountain, the deeper it sinks, i.e., the thicker its root. 3) Regional compensation model, in which Vening Meinesz (1939) modified the Airy model and introduced regional instead of local compensation. The topography is considered as a load on an unbroken but yielding elastic crust (Heiskanen and Moritz, 1967). 4) Thermal isostasy model, refers to the thermal subsidence of the oceanic lithosphere after it is created at the mid-ocean ridge by hot mantle rock. The density of the cooling oceanic lithosphere increases, therefore it subsides in order to retain isostasy

at the base of the lithosphere (Turcotte and Schubert, 1982).

Gravity anomalies associated with topographic features contain information about the distribution of compensating mass and subsurface structure, but they do not determine the compensating mass uniquely. Nature is more complicated than simple models. The Canadian Shield is a mosaic of structural provinces, each with characteristic internal structure. Boundaries between provinces represent Precambrian episodes of cratonic convergence. Collision and suturing have been delineated where structural trends are truncated along unconformities or along orogenic fronts (Stockwell, 1961). The Precambrian sutures suggest that plate tectonic processes were active in Precambrian times, and they provide an explanation for the observed regional differences in geologic terranes within present-day continents (Burke et al., 1977; Fountain and Salisbury, 1981; Gibb et al., 1983). Bouguer gravity anomalies across these tectonic boundaries show large negative features with flanking highs (Gibb and Thomas, 1976; Pilkington, 1990; Hynes, 1994). Gibb and Thomas (1976) explain the gravity anomalies across the boundaries between provinces in Canadian Shield as an edge-effect between juxtaposed tectonically older provinces and the more dense and thicker crust of younger provinces. The density discontinuity dips gently towards the younger province to a depth of 14 km, then becomes vertical downwards. The base of the older province dips slowly towards the boundary. Non-isostatic crust is required to fit the gravity anomalies. Their result is supported by Dewey and Burke (1973), who propose a continental collision model that leads to crustal thickening of the younger plate caused by both mechanical thickening due to collision and by basement reactivation. Pilkington (1990) correlates the asymmetrical negative gravity anomaly across suture zones in Canadian Shield with the flexure of older lithosphere as it thrusts under younger, more buoyant plate. Subsurface loads in younger provinces produce the observed positive gravity anomalies. He adopts a fractured elastic plate model rather than continuous one to better fit the gravity observation. Hynes (1994) studies the gravity anomaly associated with the Grenville Front in eastern Quebec and Labrador. An end load is applied to the forward flexural modeling that is constrained by the gravity anomaly. His results show that the elastic thickness of the lower plate is less than 30 km and the deep structure of the eastern Grenville Front is dominated by a major shallow-dipping straight thrust. This is in agreement with seismic studies, which reveal that boundaries between blocks of continental crust in orogenic belts are shallowly dipping (Cook, 1986; Green et al., 1988; Snyder and Flack, 1990; Eaton and Hynes, 2000). The 2-D thermal and gravity modeling of the Canadian lithospheric structure in combination with seismic velocity models show that individual regions have different compensation and different thermal regimes (Cheng et al., 2001). High radioactive heat generation leads to high heat flow and high temperature, which results in a thin elastic lithosphere that in turn is responsible for the observed gravity anomalies. However, topography and gravity analysis of the eastern Canadian shield by Bourlon et al. (2001) reveal that variations in elastic thickness in eastern Canada range between 30 and 100 km, and

no correlation between elastic thickness and heat flow is found. Changes in elastic thickness are more likely due to varying crustal composition.

The non-uniqueness of the inversion of gravity anomalies have to be constrained by other geophysical and geological observations in order to give a reliable interpretation. Seismic data are commonly used to locate the Moho and crustal root of eastern Canada (e.g. Green et al., 1988; Eaton et al., 1995; Martignole and Calvert, 1996; Funck and Loudon, 1998; Eaton and Hynes, 2000; Funck et al., 2000). Pilkington and Grieve (1989) study the magnetization/density ratio in eastern Canada based on the possibility that gravity and magnetic fields from geological sources are correlated in a variety of ways. First, a direct correlation between density and magnetization is predicted from the bulk properties of different rock types. Second, structural features or variations in the thickness of crustal layers provide a relationship between the resulting magnetic and gravity anomalies. The relationship between gravity and magnetic fields due to common sources can be expressed by Poisson's theorem. They find that magnetization/density ratio in eastern Canada is related to changes in regional geological structure and lithology. Arkani-Hamed and Verhoef (1989) present a generalized inversion technique to transform scalar magnetic anomalies into crustal magnetization. Their crustal magnetic susceptibility models show better correlation with geological features off the east coast of Canada than do the observed magnetic anomalies. Pilkington and Percival (2001) invert the satellite magnetic anomaly over the Ungava peninsula, northern Quebec, and show that a direct correlation exists between surface rock properties and satellite magnetic anomalies in this area.

Due to the inter-related nature of topography, gravity and magnetic anomalies, I present in Chapter 3 a joint inversion method of these three data sets over eastern Canada. The density perturbations and Moho undulations obtained from this inversion are constrained by seismic observations.

2.2 Strength of the Lithosphere

The earliest evidence for a strong outer layer of the Earth came from the requirements for stress differences to support the Earth's topography for long periods of time. Seismic evidence shows that the Earth's crust and mantle react as an elastic solid to the passage of seismic disturbance. Studies of lithospheric flexure caused by long-term surface loads such as ice sheets (Walcott, 1970a), seamount chains (Walcott, 1970b; Watts and Cochran, 1974; Watts, 1978; Detrick and Watts, 1979; Calmant and Cazenave, 1986; Calmant, 1987; Maia, 2000), isolated seamounts and oceanic islands (Watts et al., 1975; McNutt and Menard, 1978; Cazenave et al., 1980), and sediments (Walcott, 1972; Cochran, 1973; Cloetingh, 1982; Cloetingh et al. 1982; Ericson, 1993) show that an elastic outer layer can explain the observed topography/bathymetry and gravity anomalies. Investigations of bending of the lithosphere at trenches (McAdoo et al., 1978; Caldwell and Turcotte, 1979; Bodine et al., 1981; McNutt and Menard, 1982; Judge and McNutt, 1991) also show that an elastic layer is needed to explain

the curvatures and widths of the forebulges observed at trenches.

Thin elastic plate models are often employed to calculate flexure of the oceanic plate under loading, in which horizontal dimensions of the plate are much larger than its thickness and vertical deflection is relatively small (Brotchie and Silvester, 1969). The thin elastic surface plates constitute the lithosphere, which floats on a fluid-like mantle. Elastic properties of the plates are deduced by relating the observed flexure of lithosphere to known surface loads. The most useful parameter in flexure studies is the flexural rigidity which is related to the elastic thickness of the plate (Turcotte and Schubert, 1982; see also Chapter 4). Gravity anomalies are often used to estimate the Earth's response to surface loads, and thus determine the strength of the lithosphere.

Depending on the stress distribution, compensation can be classified as local or regional. Regional compensation requires stresses of about an order of magnitude larger than local compensation does (McNutt, 1980). Jeffreys (1976) describes three approaches to determine stress for a given topography: 1) Assume a rheology and mechanism for isostatic compensation. Apply the topographic load, allow the Earth to respond, and calculate the stress. 2) Assume the dynamic processes that form the topography, and find the resulting stress. 3) Calculate all possible stress distributions consistent with the surface load. The distribution that attains the least maximum stress difference provides a lower bound for the strength of the Earth. The estimated rigidity for continental lithosphere is usually in the range of 5×10^{20} up to 2×10^{24} Nm, corresponding to the effective elastic thickness of 2 to 100 km (e.g., Haxby et al., 1976; Banks et al., 1977; McNutt and Parker, 1978; Cochran, 1979; Forsyth, 1985). Forsyth (1985) considers both surface and subsurface loading when calculating the flexure rigidity in the vicinity of Kenya rift valley. Although modeling of an elastic plate in terms of surface loading matches the observed admittance equally well, only those with both surface and subsurface loading are consistent with the observed pattern of coherence between gravity and topography as a function of wavelength, and they yield higher rigidity values. Zuber et al. (1989) investigate the isostatic compensation of Australian lithosphere using 2-D gravity and topography data. The isostatic model assumes regional compensation of an elastic plate that undergoes flexure in response to surface and subsurface loading. The resulting effective elastic thickness of continental Australia is 130 km, which equals to a rigidity of 2×10^{25} Nm. Recent study (Bourlon et al., 2001) of the elastic thickness of the eastern Canadian shield using the coherence between topography and Bouguer gravity anomalies reveals that the elastic thickness in eastern Canada varies from 30 to 100 km.

The fact that oceanic lithosphere is simpler in structure and tectonic history than the continental lithosphere has led many investigators to estimate the strength of the lithosphere from flexure calculations of seamount loading and of the bending of the oceanic plate at trenches. The estimated rigidity values for oceanic lithosphere from these studies are in the range of 7×10^{19} to 1×10^{24} Nm (e.g., Watts and Cochran, 1974; Watts et al. 1975; McKenzie and Bowin, 1976; McNutt and Menard, 1978; McNutt, 1979; Watts et al., 1980; Calmant and Cazenave, 1986; Calmant, 1987;

Judge and McNutt, 1991; Maia, 2001), corresponding to elastic thickness from 2 to 54 km. The elastic plate model requires large bending stress in the range 150 to 700 MPa to explain the observed flexure (Walcott, 1970; Hanks, 1971; Cochran, 1973; Watts and Talwani, 1974).

Experiments on rock deformations indicate that under large stresses associated with the elastic model, rocks would yield by fracture near the Earth's surface and will deform by ductile flow at great depths (Byerlee, 1968; Goetz and Brace, 1972; Kohlstedt and Goetze, 1974; Weertman and Weertman, 1975; Goetz, 1978, Goetz and Evans, 1979; Caristan, 1982). More complex rheology has been used to model lithospheric flexure (Turcotte et al., 1978; McAdoo et al., 1978; Bodine and Watts, 1979; Chapple and Forsyth, 1979). These studies consider an elastic plate model in which the oceanic lithosphere responds elastically to an applied load until some yield stress criteria are met. For bending stresses greater than the yield stress, portions of the plate deform plastically. These models produce flexure curves similar to the elastic models, but the bending stresses they require are smaller than those of the elastic models.

Parsons and Sclater (1977) adopt the cooling plate model to study the topography of the ocean floor with age and reveal the trend that the lithosphere becomes more rigid with age. It is now widely accepted that the thickness of the oceanic lithosphere increases with increasing age at the time of loading due to cooling of the lithosphere (Leeds et al., 1974; Watts, 1978). The depth to the base of the elastic part of the oceanic lithosphere is controlled by the depth to a particular isotherm (Watts et al., 1980; McNutt and Menard, 1982). Most estimates of the best fitting isotherm lie in the 300°–800°C range (Wessel, 1992). A review of elastic thickness modeling (Wessel, 1992) shows that the strength deduced from studies at seamounts is quite different from the strength inferred at trenches and fracture zones. The elastic thickness beneath seamounts follows the 400°C isotherm, whereas that obtained at trenches follows the depth to the 700°–800°C isotherms. Taking into account the thermal stresses in the oceanic lithosphere, the base of the elastic part follows an isotherm in the range of 700°–800 °C (Wessel, 1992). This is in accordance with observations of seismicity in the oceanic lithosphere, which show that very few earthquakes take place beyond the depth of the 700°–800 °C isotherms (Bergman, 1986; Bergman and Solomon, 1984; Wiens and Stein, 1983, 1984).

In chapters 4 and 5, I investigate the strength of the oceanic lithosphere beneath the Scotian basin and New England seamounts by adopting thin elastic plate models. I study the flexural behavior of the lithosphere on the basis of the bathymetry, depth to basement (in Chapter 4) and gravity anomalies of these areas.

2.3 Initiation of Subduction

While extensive studies on the geodynamics of the Earth in the last four decades have made the plate tectonic theory reasonably well understood, little progress is made

on understanding the dynamics of the initiation of subduction. The difficulties come from both observations and theoretical studies. Theoretical studies of subduction initiation require large, sustained in-plane stresses to break the continuous oceanic plate and drive the slab into the mantle before the new subduction process becomes self-sustaining. Various models have been proposed to explain the process of initiation of subduction. The understanding of initiation of subduction can give insights into the geodynamics of plate tectonics and the nature of plate boundaries.

In order to study mechanisms of initiation of subduction, stresses contributing to the process should be understood, and then be applied to preferential sites for incipient subduction, such as passive continental margins, transform faults and fracture zones. The subduction behavior of oceanic lithosphere in relation to its age is studied in detail by Vlaar and Wortel (1976). The penetration depth of subduction increases with increasing lithospheric age. The dominant driving force is the gravitational instability caused by the cooling oceanic lithosphere with age. They conclude that the gravitational instability of the oceanic lithosphere is the major cause of plate tectonics. McKenzie (1977) studies the major driving and resisting forces during trench formation. The driving forces in his calculations are ridge push and the pull of an incipient slab, and the resisting forces are friction force caused by friction on the thrust plane and bending force arising because work must be done against elastic and gravitational forces to form the topography of the trench and island arc. The total driving forces must exceed the total resisting forces in order that a trench be formed. A compressive stress of at least 80 MPa and a rate of approach of at least 1.3 cm/y. are required to form a new trench. Neither condition is easily satisfied. Considerable work must be done by some outside sources to thrust one plate under another and produce a sinking slab about 180 km long before the instability becomes self sustaining.

The mechanics and evolution of passive margins and their possible conversion into active margins have been widely explored because of the tectonic theory in which passive margins would fit into the classic Wilson cycle (e.g., Wilson, 1966; Vlaar and Wortel, 1976; McKenzie, 1977; Oxburgh and Parmentier, 1977; Cloetingh 1982; Cloetingh et al., 1982, 1984, 1989; Muller and Phillips, 1991; Erickson, 1993; Erickson and Arkani-Hamed, 1993; Kemp and Stevenson, 1996; Jull and Kelemen, 2001; Regenauer-Lieb et al. 2001, Sobouti and Arkani-Hamed, 2002). Cloetingh (1982) and co-workers (Cloetingh et al., 1982, 1984, 1989) studied the age dependence properties of passive margins in initiation of subduction. They considered the flexure induced by sediments at passive continental margins, the ridge push, force due to isostasy, together with the negative buoyancy force of the cooling oceanic lithosphere with age. Although the lithosphere becomes gravitationally unstable due to the fact that lithosphere becomes more dense with cooling, the cooling lithosphere becomes more rigid, that makes the lithosphere more difficult to bend. Their model shows that if subduction has not started after a short evolution of the plate (~ 20 m.y.), continued aging of the plate alone does not result in conditions more favourable for

plate rupture and initiation of subduction. Therefore they propose that initiation of subduction may occur more easily at existing weak zones located entirely within oceanic lithosphere than at passive margins.

Three environments as preferential sites for initiation of subduction are proposed by Mueller and Phillips (1991): 1) Passive continental margins, 2) transform faults/fracture zones, and 3) extinct ridges. They consider subduction initiation to be equivalent to overcoming shear resistance on a thrust fault through the lithosphere, and find that none of these sites are expected to convert into subduction zones simply by accumulating of local gravitational stresses. They propose that new trenches may form by in-plane compressional forces associated with the congestion of mature subduction complexes based on models that relate buckling in the Indian Ocean to the India-Asia collision (McAdoo and Sandwell 1985; Cloetingh and Wortel, 1986; Zuber, 1987). This mechanism is also suggested by Okal et al (1986).

However, there are geological observations that passive continental margins have directly been transformed to active margins. Stanistreet et al. (1991) study the Congo and Kalahari Cratons and find that mature passive margin sequences are developed following the rifting that separated the cratons. This is followed by subduction at the passive margins and closure of Khomas Sea. Similarly, the Hikurangi Trough off New Zealand is developed in Early Miocene (Chanier and Derrière, 1991).

Ericson (1993) and Ericson and Arkani-Hamed (1993) investigate the possibility of initiation of subduction at passive margins taking into account fluid pressures exceeding hydrostatic levels and the reheating of a margin by a passing mantle plume. They also emphasize the fact that lithosphere is weaker in tension than in compression (e.g. Brace and Kohlstedt, 1980). Subduction may initiate along a part of a passive margin by extensional or strike-slip deformation rather than shortening. They discuss this with regard to initiation at the continental termination of a transform fault. If it were reactivated, the resulting tension would tend to locally decouple the passive margin from the adjacent continent, resulting in increase in deflection of the oceanic plate and possible initiation of subduction.

Kemp and Stevenson (1996) argue that initiation of subduction at passive margins may not require lithospheric shortening. They consider both flexure and tensional stress caused by already existing mantle drag. Lithospheric failure characterized by a high-angle fault occurs when shear stresses arising from flexure and the applied tension exceed the lithosphere's shear strength. This fault decouples oceanic and continental lithosphere allowing a passive rift to develop. It also allows a hot and less dense mantle column to rise to the height of mid-ocean ridges due to buoyancy flow, which produces additional load on the oceanic lithosphere. Subduction would then be initiated by the sinking oceanic lithosphere and subsequent ridge push.

Due to the mathematical difficulties in numerical modeling which requires more complex and adequate models of geologic features, laboratory experiments of the initiation of subduction are conducted by Shemenda (1992) and Faccenna et al. (1999). The experiments can obviate the mathematical difficulties and give more physical

explanations to the geodynamic processes. Shemenda (1992) uses solid hydrocarbons and powders in oil to model the elasto-visco-plastic lithosphere, and pure water to model the very low viscous asthenosphere. Subduction is simulated on a simple scheme involving the two layers subjected to horizontal compression. His results show that a pre-existing favorably oriented weak zone is required for subduction initiation at passive margins. Faccenna et al. (1999) adopt a silicone putty, representing brittle upper crust and ductile lower crust/upper mantle, which floats on glucose syrup simulating the asthenosphere. Compressional stress is applied to test the possibility of initiation of subduction at a mature passive margin. They investigate the influence of four parameters: 1) the negative buoyancy of oceanic lithosphere, 2) the horizontal body forces between continent and ocean, and 3) the brittle and 4) ductile strength of the passive margin. Their results show that initiation of subduction occurs when the oceanic plate becomes gravitationally unstable and is subjected to low compressional strain over a geological time.

Recent progress on the study of initiation of subduction has been made by co-workers, incorporating more realistic initial conditions and the rheology of the Earth. Passive continental margins are still the most favorable place under investigation. Coakley (2001) suggests that a subduction zone can grow laterally in contrast to breaking the plate in-plane. Adjacent to a pre-existing subduction zone, progressive failure along a passive continental margin would disrupt the oceanic lithosphere to subduct. The subduction becomes self-sustaining as the dense plate sinks into the mantle. The Caribbean plate provides an example of how a micro-plate might nucleate a subduction zone through stress concentration. Lateral compositional buoyancy contrast within the oceanic lithosphere would also create the favored and necessary conditions for initiation of subduction both at passive margins and at intra-plate environments. If one part of the oceanic lithosphere experiences a greater gravitational attraction than its adjacent neighbor prior to or during the initiation of subduction because of lateral density contrast within the lithosphere, an optimal situation for subduction would be created (Niu et al., 2001). Numerical modeling by Regenauer-Lieb et al. (2001) shows that the weak zone required for initiation of subduction at passive margins can be promoted by lubrication due to water. Their model considers a double feedback mechanism (thermo-elastic-rheological). Instability at a passive continental margin can be triggered slowly by sedimentary loading over a time span of 100 m.y. However, water would become volatile with increasing temperature, which is often the case in subduction zones. Jull and Kelemen (2001) propose that initiation of subduction at a passive margin may be aided by convective instability of a thickened igneous crustal section that was emplaced during initial rifting of the margin, such as observed along much of the eastern margins of the North Atlantic. High density basalt-eclogite phase transitions at the base of the thickened basaltic crust result in the gravitational instability, and facilitate the process of initiation of subduction (Sobouti and Arkani-Hamed, 2002).

A passive continental margin is our preferential place for initiation of subduction

based on the theory of plate tectonics and previous studies. The Scotian basin, located on the west boundary of North Atlantic, is a mature marginal basin having the thickest sediment accumulation along east coast of North America. In chapter 4, I study the weakening of the lithosphere beneath the Scotian basin due to the thermal blanketing effect of the thick sediments, and demonstrate the possibility of initiation of subduction in the case that the continental and oceanic lithosphere decouple due to tensional stress caused by a possible future re-orientation of the spreading ridge of North Atlantic ocean.

References

- Banks, R.J., Parker, R.L., Heustis, S.P., 1977. Isostatic compensation on a continental scale: local versus regional mechanisms. *Geophysical Journal of Royal Astronomic Society* 64, 785-799.
- Bergman, E.A., 1986. Intraplate earthquakes and the state of stress in oceanic lithosphere. *Tectonophysics* 132, 1-35.
- Bergman, E.A., Solomon, S.C., 1984. Source mechanisms of earthquakes near mid-ocean ridges from body waveform inversion: Implications for the early evolution of oceanic lithosphere. *Journal of Geophysical Research* 89, 11415-11441.
- Bodine, J.H., Steckler, M.S., Watts, A.B., 1981. Observations of flexure and the rheology of the oceanic lithosphere. *Journal of Geophysical Research* 86, 3695-3707.
- Bodine, J.H., Watts, A.B., 1979. On lithospheric flexure seaward of the Bonin and Mariana trenches. *Earth and Planetary Science Letters* 43, 132-148.
- Bourlon, E., Mareschal, J., Wang, Y., 2001. Effective elastic thickness of the eastern Canadian shield. *Eos Transactions, AGU*, 82(47), Fall Meet. Suppl., Abstract T32B-0885.
- Brace, W.F., Kohlstedt, D.L., 1980. Limits on lithospheric stress imposed by laboratory experiments. *Journal of Geophysical Research* 85, 6248-6252.
- Brotchie, J.F., Silvester, R., 1969. On crustal flexure. *Journal of Geophysical Research* 74, 5240-5252.
- Burke, K., Dewey, J.F., Kidd, W.S.F., 1977. World distribution of sutures - the sites of former oceans. *Tectonophysics* 40, 69-99.
- Byerlee, J.D., 1968. Brittle-ductile transition in rocks. *Journal of geophysical research* 73, 4741-4750.

- Calcagno, P., Cazenave, A., 1994. Subsidence of the sea-floor in the Atlantic and Pacific oceans - regional and large-scale variations. *Earth and Planetary Science Letters* 126, 473-492.
- Caldwell, J.G., Turcotte, D.L., 1979. Dependence of the thickness of the elastic oceanic lithosphere on age. *Journal of Geophysical Research* 84, 7572-7576.
- Calmant, S., 1987. The effective elastic thickness of the lithosphere in the Pacific Ocean. *Earth and Planetary Science Letters* 77, 187-202.
- Calmant, S., Cazenave, A., 1986. The effective elastic lithosphere under the Cook-Austral and Society Islands. *Earth and Planetary Science Letters* 77, 187-202.
- Caristan, Y., 1982. The transition from high temperature creep to fracture in Maryland diabase. *Journal of Geophysical Research* 87, 6781-6790.
- Cazenave, A., Lago, B., Dominti, K., Lambeck, K., 1980. On the response of the ocean lithosphere to seamount loads from Geos 3 satellite radar altimeter observations. *Geophysical Journal of Royal Astronomic Society* 63, 233-252.
- Chanier, F., Ferrière, J., 1991. From a passive to an active margin: tectonic and sedimentary processes linked to the birth of an accretionary prism (Hikurangi margin, New Zealand). *Bull. Soc. of Geol. France* 162, 649-660.
- Chapple, W.M., Forsyth, D.W., 1979. Earthquakes and bending of plates at trenches. *Journal of Geophysical Research* 84, 6729-6749.
- Cheng, L., Ranalli, G., Mareschal, J., et al., 2001. Lithosphere cross section of Canada based on 2D thermal and gravity modeling. *Eos Transactions, AGU* 82(47), Fall Meet. Suppl., Abstract T31E-08.
- Cloetingh, S., 1982. Evolution of passive continental margins and initiation of subduction zones. Ph.D. Thesis. Instituut voor Aardwetenschappen der Rijksuniversiteri te Utrecht, No. 29.
- Cloetingh, S., Wortel, R., 1986. Stress in the Indo-Australian plate. *Tectonophysics* 132, 49-67.
- Cloetingh, S.A.P.L., Wortel, M.J.R., Vlaar, N.J., 1982. Evolution of passive continental margins and initiation of subduction zones. *Nature* 297, 139-141.
- Cloetingh, S.A.P.L., Wortel, M.J.R., Vlaar, N.J., 1984. Passive margin evolution initiation of subduction and the Wilson Cycle. *Tectonophysics* 109, 147-163.
- Cloetingh, S.A.P.L., Wortel, M.J.R., Vlaar, N.J., 1989. On the initiation of subduction zones. *Pure and Applied Geophysics* 129, 7-25.

- Coakley, B., 2001. A model for Wilson cycles. *Eos Transactions, AGU* 82(47), Fall Meet. Suppl., Abstract T42G-10.
- Cochran, J.R., 1973. Gravity and magnetic investigations in the Guiana basin, western equatorial Atlantic. *Geological Society of America Bulliten* 84, 3249-3268.
- Cook, F.A., 1986. Continental evolution by lithospheric shingling. In *Reflection seismology: the continental crust*. Edited by M. Barazangi and I. Brown. American Geophysical Union, Geodynamic Series 14, 13-19.
- Detrick, R.S., Watts, A.B., 1979. an analysis of isostasy in the world's oceans, 3, Aseismic ridges. *Journal of Geophysical Research* 84, 3637-3653.
- Dewey, J.F., Burke, K.C.A., 1973. Tibetan, Variscan and Precambrian basement reactivation: products of continental collision. *Journal of Geology* 81, 683-692.
- Eaton, D.W., Hynes, A., 2000. The 3-D crustal structure in the Manicouagan region: new seismic and gravity constraints. *Canadian Journal of Earth Sciences* 37, 307-324.
- Eaton, D.W., Hynes, A., Indares, A., et al., 1995. Seismic images of eclogites, crustal-scale extension, and Moho relief in the eastern Grenville province, Quebec. *Geology* 23, 855-859.
- Ericson, S.G., 1993. Sedimentary loading, lithospheric flexure and subduction initiation at passive margins. *Geology* 21, 125-128.
- Ericson, S.G., Arkani-Hamed, J., 1993. Subduction initiation at passive margins: the Scotia basin, eastern Canada as a potential example. *Tectonics* 12, 678-687.
- Faccenna, C., Davy, P., Brun, J. et al., 1999. Initiation of subduction at Atlantic-type margins: insights from laboratory experiments. *Journal of Geophysical Research* 104, 2749-2766.
- Forsyth, D.W., 1985. Subsurface loading and estimates of the flexural rigidity of continental lithosphere. *Journal of Geophysical Research* 90, 12623-12632.
- Fountain, D.M., Salisbury, M.H., 1981. exposed cross-sections through the continental crust: implications for crustal structure, petrology and evolution. *Earth and Planetary Science Letters* 56, 263-277.
- Funck, T., Loudon, K.E., 1998. Wide-angle seismic imaging of pristine Archean crust in the Nain Province, Labrador. *Canadian Journal of Earth Sciences* 35, 672-685.
- Funck, T., Loudon, K.E., Wardle, R.J., et al., 2000. Three-dimensional structure of the Torngat Orogen (NE Canada) from active seismic tomography. *Journal of Geophysical Research* 105, 23403-23420.

- Gibb, R.A., Thomas, M.D., 1976. Gravity signature of fossil plate boundaries in the Canadian Shield. *Nature* 262, 199-200.
- Gibb, R.A., Thomas, M.D., Lapointe, P.L. et al., 1983. Geophysics of proposed Proterozoic sutures in Canada. *Precambrian Research* 19, 349-384.
- Goetze, C., 1978. The mechanisms of creep in olivine. *Philos. Trans. Royal Society of London, Ser. A* 288, 99-119.
- Goetze, C., Brace, W.F., 1972. laboratory observations of high-temperature rheology of rocks. *Tectonophysics* 13, 583-600.
- Goetz, C., Evans, B., 1979. Stress and temperature in the bending lithosphere as constrained by experimental rock mechanics. *Geophysical Journal of Royal Astronomic Society* 59, 463-478.
- Green, A.G., Milkereit, B., Davidson, A., et al., 1988. Crustal structure of the Grenville front and adjacent terranes. *Geology* 16, 788-792.
- Haxby, W.F., Turcotte, D.L., Bird, J.M., 1976. Thermal and mechanical evolution of the Michigan basin. *Tectonophysics* 36, 57-75.
- Heiskanen, W.A., Moritz, H., 1967. Physical geodesy, chapter 3. By W.H. Freeman and Company, San Francisco, pp. 126-159.
- Hynes, A., 1994. Gravity, flexure and the deep structure of the Grenville Front, eastern Quebec and Labrador. *Canadian Journal of Earth Sciences* 31, 1002-1011.
- Jeffreys, H., 1976. *The Earth*. Cambridge University Press, New York.
- Judge, A.V., McNutt, M.K., 1991. The relationship between plate curvature and elastic plate thickness: A study of Peru-Chile trench. *Journal of Geophysical Research* 96, 16625-16640.
- Jull, M., Kelemen, P.B., 2001. Can convective instability of a thickened passive margin help initiate subduction? *Eos Transactions, AGU* 82(47), Fall Meet. Suppl., Abstract T42G-08.
- Kemp, D.V., Stevenson, D.J., 1996. A tensile, flexural model for the initiation of subduction. *Geophysical Journal International* 125, 73-94.
- Kohlstedt, D.L., Goetze, C., 1974. Low-stress high-temperature creep in olivine single crystals. *Journal of Geophysical Research* 79, 2045-2051.
- Leeds, A.R., Knopoff, L., Kausel, E.G., 1974. Variations of upper mantle structure under the Pacific ocean. *Science* 186, 141-143.

- Maia, M., Arkani-Hamed, J., 2001. The support mechanism of the young Foundation seamounts inferred from bathymetry and gravity. *Geophysical Journal International*, in press.
- Martignole, J., Calvert, A.J., 1996. Crustal-scale shortening and extension across the Grenville Province of western Québec. *Tectonics* 15, 376-386.
- McAdoo, D.C., Caldwell, J.G., Turcotte, D.L., 1978. On the elastic-perfectly plastic bending of the lithosphere under generalized loading with application to the Kuril trench. *Geophysical Journal of Royal Astronomic Society* 54, 11-26.
- McAdoo, D.C., Sandwell, D.T., 1985. Folding of oceanic lithosphere. *Journal of Geophysical Research* 72, 6261-6273.
- Mckenzie, D.P., 1977. The initiation of trenches: finite amplitude instability. *American Geophysical Union, Maurice Ewing Series* 1, 57-62.
- McKenzie, D.P., Bowin, C., 1976. The relationship between bathymetry and gravity in the Atlantic ocean. *Journal of Geophysical Research* 81, 1903-1915.
- McNutt, M., 1979. Compensation of oceanic topography: An application of the response function technique to the Surveyor area. *Journal of Geophysical Research* 84, 7589-7598.
- McNutt, M., 1980. Implications of regional gravity for state of stress in the earth's crust and upper mantle. *Journal of Geophysical Research* 85, 6377-6396.
- McNutt, M., Menard, H.W., 1978. Lithospheric flexure and uplifted atolls. *Journal of Geophysical Research* 83, 1206-1212.
- McNutt, M.K., Menard, H.W., 1982. Constraints on yield strength in the oceanic lithosphere derived from observations of flexure. *Geophysical Journal of Royal Astronomic Society* 71, 363-394.
- McNutt, M.K., Parker, R.L., 1978. Isostatic compensation in Australia. *Science* 199, 773-775.
- Mueller, S., Phillips, R., 1991. On the initiation of subdcution. *Journal of Geophysical Research* 96, 651-665.
- Niu, Y., O'Hara, M.J., Pearce, J.A., 2001. Initiation of subduction zones: a consequence of lateral compositional buoyancy contrast within the lithosphere. *Eos Transactions, AGU* 82(47), Fall Meet. Suppl., Abstract U22A-0014.
- Okal, E., Woods, D.F., Lay, T., 1986. Intraplate deformation in the Samoa-Gilbert-Ralik area: a prelude to a change of plate boundaries. *Journal of Geological Society of London* 133, 343-355.

- Oxburgh, E.R., Parmentier, E.M., 1977. Compositional and density stratification in oceanic lithosphere: causes and consequences. *Journal of Geological Society of London* 133, 343-355.
- Parsons, B., Sclater, J.G., 1977. An analysis of the variation of ocean floor bathymetry and heat flow with age. *Journal of Geophysical Research* 82, 803-827.
- Pilkington, M., 1990. Lithospheric flexure and gravity anomalies at Proterozoic plate boundaries in the Canadian Shield. *Tectonophysics* 176, 277-290.
- Pilkington, M., Grieve, R.A.F., 1989. Magnetization/density ratio mapping in eastern Canada. In *Statistical applications in the earth sciences*. Edited by F.P. Agterberg and G.F. Bonham-Carter. Geological Survey of Canada, Paper 89-9, pp. 89-98.
- Regenauer-Lieb, K., Yuen, D.A., Branlund, J., 2001. Subduction initiation: criticality by addition of water? *Eos Transactions, AGU* 82(47), Fall Meet. Suppl., Abstract T42G-07.
- Shemenda, A.I., 1992. Horizontal lithosphere compression and subduction: constraints provided by physical modeling. *Journal of Geophysical Research* 97, 11097-11116.
- Sobouti, F., Arkani-Hamed, J., 2002. Thermo-mechanical modeling of subduction of continental lithosphere. *Physics of the Earth and Planetary Interiors*, in press.
- Stanistreet, I.G., Kaula, P.A., Henry, G., 1991. Sedimentary basinal responses to a late Precambrian Wilson cycle: the Damara Orogen and Nama Foreland, Namibia. *Journal of African Sciences* 13, 141-156.
- Stockwell, C.H., 1961. Structural provinces, orogenies and time classification of rocks of the Canadian Precambrian Shield. *Geological Survey of Canada Papers* 61-17, 108-118.
- Synder, D.B., Flack, C.A., 1990. A Caledonian age for reflectors within the mantle lithosphere north and west of Scotland. *Tectonics* 9, 903-922.
- Turcotte, D.L., Schubert, G., 1982. *Geodynamics - Applications of continuum physics to geological problems*, By John Wiley & Sons, New York, chapter 3, pp. 104-133; chapter 5, pp. 198-230.
- Turcotte, D.L., McAdoo, D.C., Caldwell, J.C., 1978. An elastic-perfectly plastic analysis of the bending lithosphere. *Tectonophysics* 47, 193-205.
- Vening Meinesz, F.A., 1939. Tables fondamentales pour la réduction isostatique régionale. *Bulletin Géodésique* 63, 711-776.

- Vlaar, N.J., Wortel, M.J.R., 1976. Lithospheric aging, instability and subduction. *Tectonophysics* 32, 331-351.
- Walcott, R.I., 1970a. Isostatic response to loading of the crust in Canada, *Canadian Journal of Earth Sciences* 7, 716-727.
- Walcott, R.I., 1970b. Flexure of the lithosphere at Hawaii. *Tectonophysics* 9, 435-466.
- Walcott, R.I., 1972. Gravity, flexure and the growth of sedimentary basins at a continental edge. *Geological Society of America Bulliten* 83, 1845.
- Watts, A.B., 1978. An analysis of isostasy in the world's oceans, 1, Hawaiian-Emperor Seamount Chain. *Journal of Geophysical Research* 83, 5989-6004.
- Watts, A.B., Cochran, J.R., 1974. Gravity anomalies and flexure of the lithosphere along the Hawaiian-Emperor Seamount Chain. *Geophysical Journal of Royal Astronomic Society* 38, 119-141.
- Watts, A.B., Cochran, J.R., Selzer, G., 1975. Gravity anomalies and flexure of the lithosphere: A three-dimensional study of the Great Meteor Seamount, northeast Atlantic. *Journal of Geophysical Research* 80, 1391-1398.
- Watts, A.B., Bodine, J.H., Steckler, M.S., 1980. Observations of flexure and state of stress in the oceanic lithosphere. *Journal of Geophysical Research* 85, 6369-6376.
- Weertman, J., Weertman, J.R., 1975. High-temperature creep of rock and mantle viscosity. *Annual Review of Earth and Planetary Sciences* 3, 293-315.
- Wessel, P., 1992. Thermal stresses and bimodal distribution of elastic thickness estimates of the oceanic lithosphere. *Journal of Geophysical Research* 97, 14177-14193.
- Wiens, D.A., Stein, S., 1983. Age dependence of oceanic intraplate seismicity and implications for lithospheric evolution. *Journal of Geophysical Research* 88, 6455-6468.
- Wiens, D.A., Stein, S., 1984. Intraplate seismicity and stresses in young oceanic lithosphere. *Journal of Geophysical Research* 89, 11442-11464.
- Wilson, J.T., 1966. Did the Atlantic close and then re-open?. *Nature* 211, 676-681.
- Zuber, M.T., 1987. Compression of oceanic lithosphere: an analysis of intraplate deformation in the Central Indian Basin. *Journal of Geophysics* 92, 4817-4825.
- Zuber, M.T., Bechtel, T.D., Forsyth, D.W., 1989. Effective elastic thicknesses of the lithosphere and mechanisms of isostatic compensation in Australia. *Journal of Geophysical Research* 94, 9353-9367.

Chapter 3

Joint Inversion of Gravity and Magnetic Anomalies of Eastern Canada

In this chapter, I investigate the relationships between the topography, gravity and magnetic data, and their tectonic characteristics by using joint inversion methods in both Fourier and space domains. I apply these analysis methods to eastern Canada, which includes diverse continental tectonic provinces and a large portion of the Labrador sea, to extract as much tectonic information as possible. The crustal models for eastern Canada are proposed based on the power spectra and degree correlation of the topography and free-air gravity anomalies. This systematic covariance analysis method of topography and gravity anomalies is proven to be a very useful and efficient method to determine the compensation state of the lithosphere, and it provides reliable tectonic interpretations when constrained by seismic and geological observations. This chapter provides a fundamental basis for the studies of the weakening of the lithosphere beneath the Scotian basin, which requires to determine the compensation state of the lithosphere before investigating the support mechanism of the basin. This analysis method will be applied to determine the compensation state of the lithosphere beneath the Scotian basin off east coast of Canada in Chapter 4, and beneath the New England seamounts in Chapter 5.

Joint Inversion of Gravity and Magnetic Anomalies of Eastern Canada

Ying Zheng and Jafar Arkani-Hamed

Earth and Planetary Sciences, McGill University,, Montreal, Quebec, Canada
Published in Canadian Journal of Earth Sciences 35, 832-853, 1998 (Appendix A)

3.1 Abstract

The power spectra and degree correlation of the surface topography and free air gravity anomalies of eastern Canada show that the gravity anomalies are subdivided into three parts. The short wavelength components (30 - 170 km, shorter than 30 km are not well-resolved) largely arise from density perturbations in the crust and to a lesser extent from the surface topography and Moho undulation, whereas the contribution of intracrustal sources to the intermediate wavelength components (170 - 385 km) is comparable with that of the topography. The long wavelength components (385 - 1536 km) are over compensated at the Moho. We present a crustal model for the intermediate and long wavelength components that takes into account the surface topography, density perturbations in the crust, and Moho undulation with a certain degree of isostatic compensation. The general characteristics of this model resemble the crustal structure revealed from seismic measurements. The reduced-to-pole magnetic anomalies of eastern Canada show no pronounced correlation with the topography and with the vertical gradient of the gravity anomalies, suggesting that the source bodies are within the crust and Poisson relationship does not hold over the entire area. Assuming that the magnetic anomalies arise from induced magnetisation, lateral variations of magnetic susceptibility of the crust are determined while taking into account the effects of the surface topography and the Moho undulation of our crustal model. The intermediate and long wavelength components of the susceptibility contrasts delineate major collision zones as low susceptibility regions. We interpret this in terms of thermal demagnetisation of the high-magnetic crustal roots beneath the collision zones.

3.2 Introduction

Several magnetic and gravity anomaly maps have been and are being compiled (e.g., Tanner et al. 1988; Hinze, et al. 1988; Verhoef et al. 1996; Johnson and von Frese 1997) on a continental scale, largely because these maps provide good information about regional tectonic structure of the crust. Difficulty arises partly from the lack of pertinent information about the resolution of the original data used in the compilations, in particular old data, and partly from data processing. It is therefore necessary to examine the compiled maps for internal consistency, and compare them

with other independent observations. Comparison of independently acquired data sets over a given region is by far the most assuring. However, multiple surveying is very costly and time consuming. Alternatively, a compiled map can be compared with maps that reflect other physical properties of the source bodies. For example, studies of the gravity and magnetic anomalies of some well-known structures in a region would yield better understanding of their main characteristics and a better means of interpreting other similar anomalies of the region. In the present paper, we use topography, gravity, and magnetic anomaly maps to study the main characteristics of the lateral variations in density and magnetisation of the crust in the eastern Canada.

The ultimate goal of magnetic and gravity data compilation and analysis is to determine the source distribution. In this paper we conduct a systematic covariance analysis of topography, gravity and magnetic anomalies in order to extract as much information as possible about their relationship, and obtain useful criteria to distinguish certain physical processes that have created lateral variations within the crust. Modelling gravity and magnetic anomalies in terms of common sources is generally carried out by a forward procedure based on the assumption that Poisson relationship holds between these anomalies. This forward modelling is useful on a small scale and usually for a single source body. It is demonstrated in this paper that the assumption is not valid on a large scale, at least over eastern Canada. We use the topography-gravity relationship to constrain the density perturbations in the crust and the thickness of the crust beneath eastern Canada. This in turn is used to obtain lateral variations in the crustal magnetisation through the inversion of magnetic anomalies that takes into account the effects of the surface topography and the Moho undulation. Geophysical implications of the main characteristics of the gravity and magnetic anomalies are discussed in some detail.

3.3 Topography, Gravity and Magnetic Relationship

The area of interest includes the continental part of eastern Canada and a large portion of the Labrador Sea with oceanic crust. The continental area consists of five tectonic provinces; Superior, Churchill, Nain, Makkovik, and Grenville, their collision zones, and numerous local geological features within each province. Figure 1 shows the tectonic provinces and locations cited in this paper. The study area also includes the ocean-continent boundary and extensive continental shelf created during the continental rifting that produced the Labrador Sea. Therefore, diverse tectonic processes in the last 1-2 G.y. have left distinct imprints that provide a good opportunity to study their major characteristics as revealed from lateral heterogeneities they have created in the crust.

The topography, gravity, and magnetic relationships are studied both in Fourier

spectral domain and space domain. For this purpose, a given data set is gridded over 256×256 equal area grid points with a grid interval of 6 km. The Fourier transformations are carried out using a Fast Fourier Transformation technique, in which the underlying implicit assumption is the periodicity of the data. To suppress the Gibb's ringing, that is usually created upon Fourier transformation due to sharp discontinuities at the boundaries, we gradually taper to zero the boundaries of a map by applying a 1-D version of Hanning function (see below) over a narrow strip containing 20 grid points. The mean value of a map is subtracted before tapering, since we are interested in lateral variations.

3.3.1 Topography Map

The equivalent rock topography (called hereafter topography, T , for simplicity) map of the area (Fig. 2a) is derived using the ETOPO5 data base, obtained from Geological Survey of Canada (W. Miles, personal communication). It is identical to the surface topography over continental areas. The offshore water column of density 1000 kg/m^3 is compressed to an equivalent rock density of 2700 kg/m^3 and the resulting thickness is added to the bathymetry to obtain the equivalent rock topography of the Sea.

3.3.2 Gravity Map

For the free air gravity anomaly (called hereafter the gravity anomaly, g^o) map of the area (Fig. 2b), data over the continent are obtained from Geological Survey of Canada (W. Miles, personal communication) and over the Sea from Sandwell and Smith satellite data (Sandwell and Smith, 1997). The gaps between the two data sets are filled using a weighted averaging procedure as follows. The gravity at a grid point with no original data is determined by averaging the gravity at points within a circular window of radius $R = 18 \text{ km}$, weighted by a two-dimensional Hanning function,

$$W(r) = 0.5[1 + \cos(\frac{\pi r}{R})] \quad (3.1)$$

where r is the distance from the grid point.

The power spectrum of the gravity anomalies $P_k^{g^o}$ is determined by

$$P_k^{g^o} = \sum_u \sum_v (|g_{u,v}^o|^2 + |g_{u,-v}^o|^2), \quad (3.2)$$

where indices u, v denote the Fourier transform, and u and v are the wave numbers along the x (west-east) and y (south-north) directions, respectively. k is the two-dimensional wave number defined as

$$k = (u^2 + v^2)^{1/2} \quad (3.3)$$

corresponding to a wavelength $\lambda = L/k$, L is the dimension of the area (1536 km). The power decreases continuously with increasing wavenumber (Fig. 3a), by about 2 orders of magnitude between wavenumbers 1 and 50 (Wavelengths of 1536 and 30 km). Included in Fig. 3a is the power spectrum of the gravity field due to the topography calculated from

$$g_{u,v}^T = 2\pi G \rho_c e^{-kz} T_{u,v} \quad (3.4)$$

where G is the gravitational constant, ρ_c (2700 kg/m³) is the surface rock density and z denotes the altitude which is set to zero. The surface topography is approximated by a surface mass distribution. The observed gravity anomalies arise from the surface topography, lateral variations of density in the crust, undulation of the Moho and possible lateral variations of density in the mantle. The figure presents a very interesting point. The observed gravity anomalies have higher power than those produced by the topography over wave numbers greater than 9 (wavelengths shorter than about 170 km), despite the fact that any possible compensating mass at the Moho would reduce the observed gravity anomaly. This point is illustrated by the power spectrum of the gravity anomaly of the topography which is compensated at the Moho by an Airy compensation mechanism. Included in Fig. 3a is the gravity anomaly of the Airy compensated topography, g' , determined by

$$g'_{u,v} = 2\pi G \rho_c e^{-kz} (1 - e^{-kH_c}) T_{u,v} \quad (3.5)$$

where H_c denotes the average depth to the Moho, assumed 37 km which is an average depth based on seismic measurements (Mereu et al., 1986; Mooney and Braille, 1989). Comparing Equations 4 and 5 shows that g' is always smaller than g^T for finite values of H_c . The effect of the compensating mass at the Moho, however, diminishes exponentially as the wave number increases, and the gravity of the compensated topography approaches that of the topography alone. Note that the power spectrum of the observed gravity anomalies is larger than that of the compensated topography over the entire range of the spectrum. This suggests that a simple Airy compensation model cannot explain the topography/gravity relationship of eastern Canada. Strong density perturbations must exist within the crust.

The topography/gravity relationship is further investigated quantitatively using their degree correlation coefficient η_k (Fig. 3b)

$$\eta_k = \frac{\sum_u \sum_v (T_{u,v} g_{u,v}^o + T_{u,-v} g_{u,-v}^o)}{(P_{u,v}^T P_{u,v}^{g^o})^{1/2}} \quad (3.6)$$

in which the summations are over all values of u and v such that

$$k - 1/2 < (u^2 + v^2)^{1/2} < k + 1/2. \quad (3.7)$$

No significant correlation is found between the topography and gravity anomaly over wave numbers greater than 50 (wavelengths shorter than 30 km). These features of the gravity anomalies are not well-resolved. To resolve a feature with a wavelength of 30 km, it is required to obtain at least 3 samples, and preferably 5, within 30 km. The gravity stations on the continent (Fig. 2c) have quite irregular spacing with distances usually longer than 10 km, confirming our observation that these very short wavelength components are not properly resolved and thus are unreliable. They will not be considered further, and are also filtered out from all of the maps presented in this paper. Over the wave numbers 9-50 (wavelengths between 30 and 170 km, called hereafter the short wavelength components), there is a positive correlation between the topography and gravity anomalies. However, the power of the gravity anomalies is significantly greater than that of the gravity due to the topography. The lateral density perturbations in the crust must be large enough not only to overcome the reducing effect of any possible isostatic compensation of the topography, but also to contribute significantly to the observed anomalies. A positive, but low, correlation exists between the topography and gravity over wave numbers 4-9 (wavelengths between 170 and 385 km, called hereafter the intermediate wavelength components), and the power of the observed gravity anomalies is less than or equal to that of the gravity produced by the topography. The topography is compensated over these wavelengths with different degrees of compensation or at different depths of compensation, depending on the wavelength. And finally, the long wavelength components of the gravity anomalies with wave numbers 1-4 (wavelengths between 385 and 1536 km) show negative correlation with the topography, suggesting that the topography is over compensated.

The above spectral-domain degree correlations provide good information about the correlation over the entire area for features specified by certain wavelengths. They do not, however, show where the features positively correlate and where negatively. To identify the locations, we calculate the space-domain correlation between the topography and gravity anomaly maps. The correlation coefficient, η , at a given grid point is determined by

$$\eta = \frac{\sum_{n=1}^N g_n^o T_n W_n}{[(\sum_{n=1}^N g_n^{o^2} W_n)(\sum_{n=1}^N T_n^2 W_n)]^{1/2}} \quad (3.8)$$

where N is the total number of grid points inside a circle of radius R_o , and W_n is the 2-D Hanning function defined by Equation (1), now centered at the grid point. Several values of R_o are examined. Figure 2d presents the space-domain correlation

calculated using the R_0 value of 30 km, which retains almost the entire reliable signature contained in the topography and gravity anomaly maps. This radius is used in all space-domain correlation maps in this paper. The figure is dominated by the long wavelength components displaying negative correlation over the main parts of the continent and Labrador Sea. This is expected because of the negative correlation of the long wavelength components of the topography and gravity anomalies and their substantially high power (see Fig. 3a). There are positive correlations over some positive gravity anomalies in Grenville and Churchill provinces and in the northwest of Superior province. A well-defined negative correlation delineates the Grenville-superior collision zone, but other collision zones do not seem to be as distinct.

3.3.3 Magnetic Map

The magnetic anomaly map of eastern Canada (Fig. 4a) is derived using the magnetic data base compiled by the Atlantic Geoscience Centre over the north polar region (Macnab et al., 1995). Data over the Labrador Sea are compiled from marine and aeromagnetic surveys using detailed cross-over analysis and stringent selection criteria which resulted in reliable anomalies (Verhoef et al., 1996). The continental part of the data base was extracted directly from an earlier compilation of the North American magnetic anomaly map (Hinze et al., 1988). Comparison of satellite magnetic anomalies of North America with the upward continued version of this compiled map demonstrated that the long wavelengths of the map, longer than about 300 km, are contaminated by compilation processes (Arkani-Hamed and Hinze, 1990). A similar conclusion was drawn by Pilkington and Roest (1996) over the whole of Canada. Further examination of the compiled map over conterminous U.S. showed that wavelengths between 170 and 500 km are more reliable than others (Grauch, 1993). Therefore, we need to assess the magnetic anomalies of the continental part of eastern Canada before further analysis and interpretation. For this purpose, we use the high altitude magnetic profiles over eastern Canada (Fig. 4b) acquired at 4 km elevation by Geological Survey of Canada, a total of 22 profiles (Mark Pilkington, personal communication). Pilkington and Roest (1996) gridded the profiles over the whole of Canada at a 20 km interval, using a 2-D Hanning function of radius 50 km. The large distance between profiles, an average of about 60 km, resulted in a very anisotropic data distribution with a much higher resolution along profiles compared with that across profiles. The resulting magnetic anomaly map probably contained artifacts because the radius of the Hanning function was comparable with the distance between the profiles. The gridding also degraded the high resolution along the profiles. Therefore, no attempt is made in the present paper to grid the high altitude data. Rather, we upward continue the low altitude magnetic anomaly map (Fig. 4a) to 4 km altitude and compare the resulting anomalies with the high-altitude data along the profiles. They are almost identical except for the first 4 profiles in the western part, which are slightly shifted. Figure 5 shows two high-altitude and upward con-

tinued profiles, one with the maximum shift and one with no shift. The other three shifted profiles are shifted by less than 60% of this maximum. The close similarity between the high altitude and the upward continued magnetic anomalies indicates that the short and intermediate wavelength components of the magnetic anomaly map are reliable. To examine the long wavelength components of the magnetic anomaly map, we extract satellite magnetic anomalies over the study area from Magsat dawn data (Fig. 4c), which are least contaminated by non-crustal noise (Ravat et al., 1995), and compare with a low-pass filtered version of the magnetic anomaly map. (We first examined the Fourier-domain upward continuation method, but concluded that it was not suitable over a small area such as eastern Canada, partly because of the high altitude of Magsat, an average of 400 km, and mainly because a large positive satellite magnetic anomaly is centered almost at the western border of the study area. The corresponding anomaly in our magnetic anomaly map is tapered to zero at the border in order to apply the Fast Fourier transformation required for the upward continuation. This tapering strongly reduced the anomaly and shifted its maximum eastward.) Filtering is done in the space domain through weighted averaging over a moving circular window, weighted by the 2-D Hanning function of radius 600 km. The Magsat anomaly map consists of wavelengths longer than about 670 km (Ravat et al., 1995). The resulting low-pass filtered magnetic anomaly map (Fig. 4d) shows good correlation with the satellite map. The correlation is not expected to be much better, as satellite maps do not usually show exact correlation with low altitude magnetic maps (e.g., LaBrecque and Cande, 1984; LaBrecque and Raymond, 1985; Toft and Arkani-Hamed, 1992; Arkani-Hamed et al., 1995). Also Figs. 4c and 4d do not contain exact wavelengths; rather, the space-domain filter is an approximation of the spherical harmonic domain filter used in deriving the Magsat magnetic anomaly map. This good correlation emphasizes that the long wavelength components of the low altitude magnetic anomalies of eastern Canada are not significantly contaminated by the compilation processes. These two examinations provide good confidence in the magnetic anomalies seen in Fig. 4a.

Unlike gravity anomalies that directly correlate with source bodies, magnetic anomalies do not show a direct correlation with magnetic bodies, largely because the core field direction is not vertical, except in polar regions. A body carrying an induced magnetisation produces a strong positive magnetic anomaly directly above itself when it is located at the geomagnetic poles, but a relatively weaker and negative anomaly at the equator. The magnetic anomaly is displaced towards the equator with respect to the body at mid-latitudes. The shift depends on the core field direction, and may change significantly over a large area such as eastern Canada, where the core field direction changes appreciably (see the core field model by IAGA Division V Working Group 8, 1996). To overcome these difficulties, we differentially reduce the magnetic anomalies to the north pole, using the algorithm developed by Arkani-Hamed (1988). Figure 6a shows the resulting reduced-to-pole magnetic anomalies (called hereafter RTP anomalies) that should directly correlate with induced mag-

netic sources. In the continental area, many small scale positive anomalies exist in the northern parts of Superior province and in the eastern parts of Grenville province, and an elongated positive anomaly is associated with De Pas Batholith outlined in the tectonic map of eastern Churchill province (Wardle et al., 1990). The Grenville Front, and the Cape Smith belt are delineated by negative RTP anomalies. Over the Labrador Sea, the continental shelf shows several small scale positive anomalies, and major marine magnetic anomalies are depicted in the oceanic part of the Sea.

No appreciable correlation exists between the topography and RTP anomalies as indicated by their degree correlation coefficients in Fig. 3b, except over a few wavelengths where the correlation is still smaller than 0.5. This lack of consistent correlation is better illustrated in their space-domain correlation map (Fig. 6b). However, there seems an overall negative correlation between the topography and RTP anomalies over the Grenville Front and Cape Smith belt.

It is desirable to investigate whether the gravity and magnetic anomalies are associated with common source bodies. There is no direct relationship between the magnetic properties and densities of rocks. High density mafic rocks are usually more magnetic than low density sedimentary rocks. However, metamorphism may remove remanent magnetisation while producing denser minerals, and serpentinization may precipitate magnetite and enhance magnetisation while reducing the bulk density of rocks (Toft et al., 1990). Hydration in metamorphosed rocks may also reduce magnetisation (Toft et al., 1993). On the other hand, broad features of crustal magnetisation in the continent may correlate directly with the undulation of the Moho, if the Moho is the lower boundary of the magnetic crust as suggested by Wasilewski et al. (1979). Modelling the gravity and magnetic anomalies by a common source body is based on the Poisson relationship between the RTP anomaly, F , and the vertical gradient of the gravity anomaly, V ,

$$F_{u,v} = \left(\frac{\mu_o m}{4\pi G \rho} \right) V_{u,v} \quad (3.9)$$

where μ_o is the magnetic permeability of the air, and m and ρ are the magnetisation intensity and density of the body. The underlying assumption made in deriving this relationship is that the source body has a uniform density and magnetisation. Such modelling is therefore limited to a local area and generally to a single body. The relationship may not hold in an extended area where many bodies of diverse nature contribute to the gravity and magnetic anomalies. To investigate this point we calculate the vertical gradient of the gravity anomalies using

$$V_{u,v} = -k g_{u,v}^o. \quad (3.10)$$

The resulting gravity gradient map (Fig. 6c) is dominated by small scale features because of their substantial enhancement through differentiation. The gravity gradient map better delineates the ocean-continent boundary and Cape Smith belt. Some

small-sized features are scattered over the Superior-Churchill boundary and Grenville Front, which collectively trace these long collision structures. A similar calculation was made by Pilkington and Grieve (1989), who reduced the magnetic anomalies to the pole through a space-domain differential reduction procedure. They divided the continental part of eastern Canada into 7 regions based on their space-domain correlation and Poisson coefficient maps. Although there is a good agreement between our results and theirs over most regions, we do not see clear evidence either in their map or in ours that supports such a division. As a matter of fact, there seems to be no consistent correlation between the gravity gradient and RTP anomalies over the entire area (except for positive correlations over the ocean-continent boundary and Cape Smith belts) as is illustrated by their space-domain correlation map (Fig. 6d) and Fourier-domain degree correlation coefficients (see Fig. 3b). The correlation coefficients are positive, but small, over wavelengths longer than 190 km. This lack of pronounced correlation between the RTP anomalies and gravity gradient indicates that the Poisson relationship is not valid over the entire area, although it is probably useful for some of the small scale local anomalies.

3.4 Interpretation of Free Air Gravity Anomalies

We seek physical processes that are responsible for the diverse characteristics of the topography and gravity spectra discussed above and investigate each part of the spectra accordingly.

3.4.1 Short-wavelength components:

Figures 7a and 7b present the high-pass filtered topography and gravity maps of eastern Canada consisting of the short wavelength components. The filter removed all wavelengths longer than 192 km and kept unchanged those shorter than 154 km. The amplitudes of the remaining wavelengths were suppressed by a 1-D Hanning function in the spectral domain, in order to avoid any sharp cut off that might create ringing in the inverse Fourier transform (Gibb's ringing). The figures are dominated by small scale features, some of which show good correlation with geologic structures, in particular the anomaly associated with the ocean-continent boundary in the Labrador Sea. This is more evident in their space-domain correlation map (Fig. 7c). The correlation is consistently positive and high along the boundary. There are several small-sized positive gravity anomalies in Nain province that correlate with the topography, but no consistent correlation exists elsewhere. The Cape Smith belt is delineated by well-defined gravity anomaly, but does not show a pronounced topography. The other collision zones have no consistent gravity/topography association over these short wavelengths.

The higher power of the short wavelength components of the observed gravity anomalies compared with that of the gravity arising from the topography indicates

that the observed anomalies are strongly dominated by density perturbations within the crust. This is expected for old tectonic zones. For example, during continental collision, adjacent crustal materials intrude from one side to the other due to prevailing strong horizontal forces, mafic and ultramafic intrusions occur because of the reactivation of the bottom of the younger province and related diapiric upwelling, and new minerals are formed through metamorphism (Dewey and Burke, 1973). These processes introduce lasting small-scale density heterogeneities within the crust, whereas small-scale surface topography is easily reduced by subsequent erosion. The wavelengths are short enough for the lateral variations in mantle density and the Moho undulation to have negligible contributions to the observed gravity anomalies. Therefore, the observed gravity anomalies are related to the surface topography and the density perturbations, $\delta\rho$ in the crust with a flat Moho,

$$g_{u,v}^o = 2\pi G e^{-kz} [\rho_c T_{u,v} + \int_{-H_c}^0 e^{kz'} \delta\rho_{u,v} dz'] \quad (3.11)$$

where the topography is regarded as a surface mass distribution and the altitude z is set to zero. The gravity arising from the density perturbations, the second term in the right hand side, depends on the vertically integrated density perturbations weighted by an exponential geometric function. Figure 7d shows the vertically averaged density perturbations, $\langle \delta\rho \rangle$, thus determined using the short wavelength components of the topography and gravity. Compared to the gravity anomalies shown in Fig. 7b, the density perturbations are more localised. This is because the gravity fields of several small scale nearby density perturbations coalesce and give rise to a relatively broader gravity anomaly. The distinct ocean-continent boundary shown in the topography and gravity anomaly maps is strongly suppressed in the density perturbation map, suggesting that the gravity anomaly largely arises from the topography which is probably maintained by stresses in the crust. A significant density perturbation is associated with Cape Smith belt that correlates directly with the gravity anomaly, indicating that the gravity anomaly mainly arises from density perturbations within the crust, because of no significant topography there. No consistent density perturbations are associated with the other collision zones. The Manicouagan-Hart Jaune complex is delineated by a positive topography, positive gravity anomaly, and positive density perturbation. The observed gravity anomaly over this complex is larger than the gravity produced by its surface topography and part of the anomaly is associated with excess mass within the crust. Such is also the case for many small-sized anomalies over the Grenville and Nain provinces. The source bodies of these anomalies are probably at shallow depths and have greater density contrasts compared to the density perturbations displayed in Fig. 7d which are vertically averaged over the 37 km thickness of the crust.

3.4.2 Intermediate-wavelength components:

The intermediate wavelength topography and gravity anomaly maps (Figs. 8a and 8b) are derived through band-pass filtering of the original maps (Figs. 2a and 2b) that removes wavelengths longer than 385 km and those shorter than 170 km, but does not affect the wavelength between 190 and 307 km. The remaining wavelengths are suppressed by a 1-D Hanning function applied over wavelengths between 170 and 190 km, and over those between 307 and 385 km, in order to avoid a sharp cut off. There is no consistent correlation between the topography and gravity anomalies, except for a few places such as Torngat, the northwest-southeast trending positive gravity in the eastern Superior province and the parallel negative anomaly over the superior-east Churchill collision zone, the overall positive gravity anomaly of Grenville province, and the most evident ocean-continent boundary. Therefore, the close proximity between the power spectrum of the observed gravity and the gravity arising from the topography over these wavelengths (see Fig. 3a) cannot be used to argue that the observed gravity arises from the surface topography. The continental topography appears quite smooth, whereas the gravity anomaly map is dynamic showing well-defined positive and negative anomalies, some of which correlate with geologic structures. For example, the Manicouagan-Hart Jaune complex is delineated by a well-defined intermediate wavelength positive gravity anomaly, but has no significant associated topography. The gravity anomaly is largely due to density perturbations within the crust and possible undulation of the Moho. The Grenville Front, the Trans-Hudson orogen in the Cape Smith belt, and the collision zone between east Churchill and Superior provinces are delineated by negative gravity signatures.

In the inversion of the intermediate wavelength gravity anomalies, we take into account the topography, the density perturbations in the crust, and the Moho undulation. The latter is included because it can make a considerable contribution to the observed gravity at these wavelengths. We consider a simple crustal model in order to minimise the number of free parameters and avoid unnecessary mathematical complications. The topography and the base of the crust are assumed to have uniform densities of ρ_c and ρ_t , respectively, whereas the lateral density perturbations, $\delta\rho$, are concentrated within the crust, excluding the topography and the Moho undulation. The constant density of the topography and the Moho undulation avoids coupling of different harmonics and results in a simple relationship. The Moho undulation is determined by assuming that α fraction of the load associated with the topography and the density perturbations in the crust is compensated by the undulation and the rest is supported by the elastic crust. The undulation H^r (assumed positive downward, i.e., when the crust has a root) is determined by

$$H_{u,v}^r = \frac{\alpha}{\rho_m - \rho_t} (\rho_c T_{u,v} + H_c < \delta\rho >_{u,v}), \quad (3.12)$$

where ρ_m (3300 kg/m³) is the mantle density, and $< \delta\rho >$ denotes the vertically

averaged density perturbation in the 37 km thick crust. The compensation depth is the average Moho depth, H_c . The gravity associated with the Moho undulation, g^m , is

$$g_{u,v}^m = 2\pi G(\rho_l - \rho_m)e^{-k(z+H_c)}H_{u,v}^r, \quad (3.13)$$

Equating the gravity produced at the surface by this crustal model with the observed gravity yields the following integral equation to be solved for $\delta\rho_{u,v}$,

$$g_{u,v}^o = 2\pi Ge^{-kz}[\rho_c T_{u,v} + \int_{-H_c}^0 e^{kz'}\delta\rho_{u,v}dz' + (\rho_l - \rho_m)e^{-kH_c}H_{u,v}^r]. \quad (3.14)$$

It is evident from Equation (14) that the solution for the density perturbations is non-unique, adding $\delta\rho_{u,v}^o$ to a given solution does not affect the gravity anomalies if

$$\int_{-H_c}^0 e^{kz'}\delta\rho_{u,v}^odz' = 0 \quad (3.15)$$

In the absence of other independent information about the vertical distribution, we seek a vertically averaged lateral density perturbation $\langle \delta\rho \rangle_{u,v}$, the simplest model, by assuming that $\delta\rho_{u,v}$ does not change vertically. This assumption reduces Equation (14) to

$$\langle \delta\rho \rangle_{u,v} = \frac{ke^{kH_c}}{e^{kH_c} - (1 + k\alpha H_c)} \left[\frac{g_{u,v}^o}{2\pi G} - (1 - \alpha e^{kH_c})\rho_c T_{u,v} \right] \quad (3.16)$$

in which the altitude z is set to zero.

Included in Fig. 8 are the vertically averaged density perturbations in the crust and the Moho undulation, determined by Equations (16) and (12) for the intermediate wavelength components assuming a complete isostatic compensation, $\alpha = 1$. The elongated features near the boundaries in Labrador Sea and Hudson Bay are edge effects and unreliable. They arise because the topography was tapered to zero along the boundaries in the course of applying the Fourier transformation, as mentioned before. The tapering affected a strip of 120 km and artificially increased the intermediate wavelength component of the topography there, as seen in Fig. 8a. We keep these features, rather than masking them out, in order to show the extent to which tapering affects the maps. The good correlation between the gravity anomalies, density perturbations, and the Moho undulation, especially where no significant topography exists, is expected because a gravity anomaly over an almost flat area requires density perturbations in the crust and thus an associated Moho undulation in order to retain isostasy. For example, detailed inspection of the Grenville Front shows

that the minima of the gravity anomalies along the Front occur over topographically low-undulating, almost flat areas. The required negative density perturbations result in a mass deficiency in the crust beneath, which in turn causes mantle uplift to create an excess mass in order to retain isostatic compensation. Such a crustal model, where collisions have resulted in crustal thinning and mantle uplift, is in direct contradiction with the common crustal thickening that occurs through continent-continent collision processes and, therefore, is not realistic.

3.4.3 Long-wavelength components:

The long wavelength components of the topography and gravity anomalies are very interesting. The power spectrum of the observed gravity anomalies is substantially lower than that of the gravity due to the topography (see Fig. 2a), implying a significant degree of compensation of the topography. Airy or Pratt isostasy models, however, cannot explain this compensation, because they result in gravity anomalies which positively correlate with the topography, contrary to the observed negative correlation of the long wavelength components (see Fig. 3b). The negative correlation emphasizes that the topography is over compensated, either by excessive roots at the Moho, or by lateral variations of density in the crust, or both. Although the wavelengths considered are long enough for possible mantle sources to have appreciable contributions to the observed gravity anomalies, we ignore these contributions and seek simple crustal models. One model is a crust with lateral density variations and associated Moho undulation that explains the observed gravity anomalies while retaining isostatic compensation at the Moho. Similar to the model examined above for the intermediate wavelength components, the model requires large density perturbations and correspondingly large Moho undulation. This is because, to over compensate, for example, a positive topography, a large negative density perturbation is required with a total mass deficiency much greater than the excess mass of the topography. The vertically integrated mass would then be negative. It would require an upward displacement of the Moho to create an excess mass in order to retain isostasy there. This upward displacement would give rise to positive gravity anomaly opposing the gravity anomaly associated with the density perturbations. Similar to the results obtained for the intermediate wavelength components, this model leads to mantle uplift beneath positive surface topography, and for the same reason the model is not realistic.

3.5 Modelling Regional Scale Gravity Anomalies

An interesting and yet a simple model is a laterally homogeneous crust with surface topography and undulating Moho but no isostatic compensation at the Moho. This model can be created by collision of two continents of similar density. The newly

formed collision zone is characterised by a thicker crust with a pronounced topography and associated deep crustal root produced in the process of collision. The topography is usually compensated during or shortly after the collision because of frictional heating that weakens the crust and allows rapid mechanical equilibrium. In later times, however, the crust cools and becomes strong, and as the surface topography is reduced through erosion the rebound of the strong crust does not keep in phase with the erosion. The excess buoyancy of the root is supported by crustal strength, for example through flexure of the elastic part of the crust (Pilkington, 1990; Hynes, 1994). According to this simple model, the long wavelength components of the gravity associated with the Moho undulation overwhelm that of the topography and produce the observed gravity anomalies with opposite sign to the topography. Now, if the crust is strong enough to maintain long wavelength components of the Moho undulation, it should also maintain the intermediate wavelength components of the undulation. Therefore, we consider a crustal model with no lateral density perturbations but with topography (Fig. 9a) and gravity anomalies (Fig. 9b) characterised by the intermediate and long wavelength components. The Moho undulation (Fig. 9c) is determined for $\rho_l = 2900 \text{ kg/m}^3$, representing the gabbroic rocks of the lower crust, by equating the gravity anomaly of this crustal model with the observed gravity anomaly,

$$H_{u,v}^r = \frac{e^{kH_c}}{2\pi G(\rho_m - \rho_l)} (2\pi G \rho_c T_{u,v} - g_{u,v}^o). \quad (3.17)$$

All of the collision zones have thicker crust consistently. Figure 9d shows the Moho undulation that is in excess to the undulation required for a simple Airy isostasy model. The model Moho deviates from the isostatic Moho by more than 7 km in the collision zones. The model Moho undulation is also much greater than that observed from seismic measurements (e.g., Gibb and Thomas, 1976; Mereu and Jobidon, 1971; Mereu et al., 1986; Kellett et al., 1994, White et al., 1994). The results are not sensitive to variations of ρ_c , but are more sensitive to the density contrast between the lower crust and the mantle. For example, increasing ρ_c from 2700 kg/m^3 to 2800 kg/m^3 changes the first term in the right hand side by only 4%, whereas using 2800 kg/m^3 for the density of the gabbroic rocks, rather than 2900 kg/m^3 , would decrease the undulation by 20%. The density values we use are reasonable, and the contrast may not be very different from that adopted in these calculations. Still the undulation is too large compared with the observation, suggesting that this crustal model is not realistic either.

A realistic crustal model is probably somewhere in between the two end member models examined above. The major parameter that controls the Moho undulation is the α factor. It is possible in principle to select a α value which yields a Moho undulation that approximates the observed Moho along a particular seismic profile. Such a α value may not, however, result in a Moho undulation that approximates

the Moho along all available seismic profiles. This is partly because of detailed local factors that may control the seismic results, and partly because of different compensation mechanisms at different locations. For example, the Moho undulation shows very diverse characteristics along the Grenville Front (see below) that cannot be explained by a single α factor. Therefore, we seek a crustal model with a Moho undulation that has overall characteristics of the observed Moho. For this purpose, we determine several crustal models with lateral density perturbations and Moho undulation for several α values. Figure 10 shows the power spectra of the density perturbations of the models thus determined. For positive α values, the density perturbations overwhelm the effects of the topography and require crustal thinning beneath the collision zones. The density perturbations in the crust are reduced as α decreases, and the Moho shows crustal thickening beneath the collision zones when α becomes negative. The histograms of the resulting Moho undulation for negative α values (Fig. 11) show that the amplitude of the undulation decreases as α decreases. The α values between -1.5 and -2.5 give rise to amplitudes which are similar to the Moho undulation observed along seismic profiles across Grenville Front (e.g., Mereu and Jobidon, 1971; Mereu et al., 1986). Figure 12 shows the Moho undulation and density perturbations for $\alpha = -2$, which we regard an acceptable crustal density model. The Moho deepens by about 3-4 km beneath the collision zones between the Grenville and Superior, and the Churchill and Superior, provinces. The zones are flanked by the mantle uplift on both sides, which is more pronounced beneath the Grenville and Churchill provinces compared to that beneath the older Superior province. The remaining parts of the provinces have relatively flat Moho.

3.6 Interpretation of Magnetic Anomalies

Magnetic anomalies reflect lateral variations in the magnetisation of the crust and possibly uppermost mantle. The magnetic potential, A , of a magnetic layer is related to its magnetisation, \mathbf{m} , through (Arkani-Hamed and Strangway, 1986)

$$A_{u,v} = -2\pi \frac{e^{-kz}}{k} \mathbf{G} \bullet \mathbf{M}_{u,v} \quad (3.18)$$

where

$$\mathbf{G} = (iu, iv, -k) \quad (3.19)$$

and

$$\mathbf{M}_{u,v} = \int_{s_1}^{s_2} \mathbf{m}_{u,v} e^{kz_0} dz_0 \quad (3.20)$$

s_1 and s_2 in Equation (20) denote the lower and upper surfaces of the layer, both are generally undulating. We assumed $z=300$ m which is the average altitude of the aeromagnetic measurements over the continent. Note that marine magnetic measurements are made at sea level. However, taking z at 300 m elevation will not affect the results significantly. This is because the shortest wavelength considered, 30 km, does not attenuate by more than 6% from sea level to this altitude, and other wavelengths attenuate even less. Equations 18 and 20 show that magnetic potential depends on the vertically integrated magnetisation inside the layer that is weighted by an exponential function. This emphasizes that details of vertical variations of magnetisation cannot be inferred from magnetic anomaly analysis alone. Additional independent data, such as seismic profiles and gravity anomalies, are needed to constrain the vertical dimension of magnetic sources.

The lack of other geophysical information about the vertical distribution of crustal magnetisation over the entire area, and the inability of magnetic anomaly analysis to resolve vertical variations, limit us to determining the vertically averaged magnetisation of the crust, in accord with our general philosophy of seeking simple models, as adopted in the interpretation of the gravity anomalies in the previous section. We also assume that the crustal magnetisation is in the vertical direction. This assumption may not introduce serious errors because the core field direction has already been changed to vertical through the reduction-to-pole procedure. Also, Labrador Sea was formed near the north magnetic pole (Harrison and Lindh, 1982) and the remanent magnetisation of its oceanic crust is almost vertical and has been little affected by the differential reduction to the north pole application. Magnetisation of the continental crust is due to remanent and induced magnetisation. The crust has suffered very many large and small tectonic deformations during the last 1-2 G.y. that most likely rotated different blocks in different directions, resulting in diverse orientations of the previously acquired remanent magnetisation. Furthermore, the strong temperature dependence of viscous magnetisation and the high temperatures of the middle and lower crust suggest that any plausible remanent magnetisation of the deeper parts has been substantially reduced during this long period. And finally, it is demonstrated that different parts of a large body cooling through its magnetic blocking temperature range acquire remanent magnetisation in different directions owing to reversals of the core field and slow cooling rate of the body (Arkani-Hamed and Celeti, 1989). Alternating polarity magnetised zones in a batholith have been observed in the field (Williams and Fuller, 1982). Such a body does not produce an appreciable magnetic anomaly, despite the fact that certain parts of the body carry appreciable remanent magnetisation. This is due to the cancelling effects of the magnetic fields of the oppositely magnetised parts. It is therefore plausible to assume that induced magnetisation is the dominant source of observed magnetic anomalies over the continent. These assumptions greatly simplify the inversion formulas developed by Arkani-Hamed and Verhoef (1989). Their Equations (10)-(13) are now reduced to

$$m_{u,v} = \frac{-1}{e^{ks_2^o} - e^{ks_1^o}} \left(\frac{-e^{kz}}{2\pi} T_{u,v} + \mathbf{G} \bullet \zeta_{u,v} \right) \quad (3.21)$$

and

$$\zeta_{u,v} = \mathbf{m} \left[e^{ks_2^o} \sum_{n=1}^{\infty} \frac{k^{n-1}}{n!} \delta s_2^n - e^{ks_1^o} \sum_{n=1}^{\infty} \frac{k^{n-1}}{n!} \delta s_1^n \right] \quad (3.22)$$

where s_1^o and s_2^o are the mean elevations of the upper and lower surfaces of the magnetic layer, and δs_1^n and δs_2^n denote the undulation of these surfaces. The underlying assumption made in developing the original formulas, and thus in their reduced forms, is that the magnetisation is of induced origin. This assumption is probably reasonable over the continental area as argued above. It overestimates the magnetic susceptibility of the oceanic crust because the remanent magnetisation, which is usually much greater than the induced magnetisation, is regarded as an induced magnetisation in this formulation. This will, however, have no effect on the vertically integrated magnetisation in the oceanic region, as indicated by Equations (18) and (20).

Two models are considered for the magnetic layer; a half-space with the surface topography, and a finite layer with the surface topography and the undulating Moho as its lower surface. The first model provides information about the short wavelength components of the crustal magnetisation. This is because little contribution is made to the RTP anomalies by the magnetic poles at the lower boundary. The lateral variations of susceptibility (Fig. 13a) are very similar to the RTP anomalies (Fig. 6a), but the resolution of the susceptibility map is slightly higher due to enhancement of the short wavelength components through the inversion process. Broad RTP anomalies arise from coalescing of the anomalies associated with nearby small-scale separate magnetic bodies.

The second model illustrates the effect of the finiteness of the magnetic layer thickness. Rock magnetic measurements suggest the Moho as the lower boundary of the magnetic crust beneath continents (Wasilewski et al., 1979). Accordingly, we assume that the lower surface of the magnetic layer coincides with the Moho beneath the continent. The oceanic crust of Labrador Sea is thin and uppermost part of the mantle is at temperatures lower than the Curie temperature of its magnetic minerals. There are ample amounts of evidence that the uppermost oceanic mantle is serpentinized at slow spreading centers such as that of the Labrador Sea (Francis, 1981; Cannat, 1993; Chian and Loudon, 1995) and contains magnetic minerals. The magnetite produced by serpentinization of the uppermost mantle may have significant contributions to the marine magnetic anomalies (Harrison, 1987; Hamano et al., 1990). Also, the anomalous skewness of marine and satellite magnetic anomalies suggests that the uppermost 6 km of the mantle is magnetized (Dyment et al., 1997). Therefore, it is assumed in the second model that the magnetic layer beneath the

Labrador Sea extends from the top of layer 2A to a fixed depth of 15 km from sea level. The short wavelength components of the Moho undulation cannot not have appreciable effects on the observed magnetic anomalies due to strong attenuation of the anomalies with distance. Figure 13b shows the lateral variations in the magnetic susceptibility of the second model determined using the entire spectrum of the RTP anomalies and the topography (all wavelengths longer than 30 km), but the intermediate and long wavelength undulation of the Moho beneath the continent, obtained by adding 37 km (the average crustal thickness) to the Moho undulation in Fig. 12, and a fixed Moho depth of 15 km beneath Labrador Sea. A strip of about 200 km along the ocean-continent boundary is tapered in order to smoothly connect the undulating Moho of the continent to the fixed Moho of the oceanic area. There are pronounced differences between the magnetic susceptibility contrasts seen in Figs 13a and 13b. The long wavelength components are substantially enhanced in the second model, emphasizing the major effect of the finiteness of the layer thickness. This is because the crustal model considered can be envisaged as a collection of vertically magnetised thin vertical prisms, each resembling a long magnetic dipole one pole at the upper and the other at the lower end of the prism. The layer is equivalent to two surfaces, top and bottom, with magnetic monopole distributions of opposite polarity. In the first model, the bottom surface is at infinity and the anomalies are essentially due to the monopole distribution at the surface. In the second model, the bottom monopoles are at an average depth of 37 (or 15) km and the intermediate and long wavelength components of the lower surface monopoles have appreciable contributions to the RTP anomalies. Large cancellations occur between the magnetic fields of the upper and lower surface monopoles owing to their opposite polarity, and the observed magnetic anomalies (thus the RTP anomalies) are residuals of the cancellation. A classic example is a uniformly magnetised horizontal layer of an infinite extent with flat top and bottom surfaces. Such a layer does not produce any magnetic field outside, regardless of the intensity of magnetisation. Therefore, because of a finite layer thickness a high magnetic susceptibility is required for the intermediate and long wavelength components of the second model in order to give rise to the observed magnetic anomalies (see Arkani-Hamed and Verhoef (1989) for a detailed discussion). Note that, similar to the gravity anomalies, the inversion of the magnetic anomalies is not unique. For example, a constant magnetic susceptibility can be added somewhere within the magnetic layer (excluding the surface topography and the Moho undulation) without affecting the observed magnetic anomalies. Figure 13b shows a simple model that reflects the lateral variations in the susceptibility. It indicates that the vertically averaged magnetisation of the crust is laterally more homogeneous than the RTP magnetic anomalies. This is partly because the magnetic anomalies measured at low altitudes are more sensitive to short wavelength near-surface variations of the magnetisation due to cancelling effects of the long wavelength components as mentioned above. Figure 13c shows the short wavelength components of the magnetic susceptibility which are dominated by small-sized features. Except for the Cape

Smith belt, collision zones do not significantly contribute to these features. On the other hand, the collision zones are well-defined as low magnetic susceptibility areas in the magnetic susceptibility map derived from the intermediate and long wavelength components (Fig. 13d). This suggests that the collisions have a considerable effect on the demagnetisation of the lower parts of the crust (see below).

3.7 Discussion and Conclusions

The area of study covers 1536×1536 square km and consists of five geologic provinces with distinct collision zones along their boundaries and numerous local features within each province. The covariance analysis of the equivalent rock surface topography and gravity anomalies shows that the short wavelength gravity anomalies arise predominantly from small-scale and probably near-surface sources and to a lesser extent from the surface topography and the Moho undulation. There is no significant correlation between the intermediate wavelength components of the topography and gravity anomalies. The contribution of density perturbations within the crust to the observed gravity anomalies is comparable to that of the surface topography over these wavelengths. The pronounced negative correlation between the long wavelength components of the topography and gravity anomalies suggests that the topography is over compensated, either by lateral density perturbations within the crust, or by the non-isostatic Moho undulation, or both. It is well beyond the scope of this paper to discuss details of small features. However, the models presented in this paper have sufficient resolution at wavelengths as short as 30 km, and we hope that they will be useful for detailed study of local features. Here we briefly discuss regional characteristics of the continental crust as revealed from the intermediate and long wavelength components of the topography, gravity and magnetic anomalies, focussing mainly on the major collision zones.

Density perturbations in the crust beneath a collision zone may arise from different processes which occurred during and shortly after the collision. Gibb and Thomas (1976) presented 5 free air gravity profiles across the collision zones between Churchill and Slave, east Churchill and Superior along Cape Smith belt, east Churchill and Superior, east Churchill and Grenville, and Grenville and Superior that show very similar features. In each case, the gravity profile decreases gradually from a background level over the older province toward the collision zone, achieving a minimum near the collision boundary, and then sharply increases across the boundary to a relative gravity high over the younger province. The authors interpreted these common characteristics of the gravity profiles in terms of collision of homogeneous but different density provinces. Accordingly, a high density younger and weaker province has overthrust a low density older and rigid province, resulting in an appreciable crustal thickening of the younger province and suppression of the older one, in accordance with the general model suggested by Dewey and Burke (1973). The suture zone dips towards the younger province to a depth of about 14 km, but becomes vertical in

the deeper parts of the crust. Also, the Moho deepens by about 5.5 km beneath the suture, and no isostatic compensation prevails there. Pilkington (1990) modelled the gravity anomalies along 25 profiles across Slave-Churchill, Churchill-Superior, and Grenville-Superior province boundaries in terms of flexure of the crust, using a 1-D thin plate model overlying a fluid interior of higher density. He adopted a fractured elastic layer model together with intracrustal density perturbations in order to interpret the asymmetry of the broad negative gravity anomalies as well as the small positive gravity anomalies of the suture zones. The author later used a 2-D thin plate model and 2-D topography and gravity anomaly maps of the Canadian shield in order to determine lateral variations of the crustal rigidity (Pilkington, 1991). His estimates of the elastic thickness of the continental crust beneath eastern Canada range from 18 to 124 km, mainly around 40-60 km. The Grenville suture is also investigated by Hynes (1994) through stacking several gravity profiles across the collision zone. The resulting type gravity profile is interpreted in terms of collision of a two-layered older and thinner Superior province with a homogeneous and younger Grenville province, which thickens through the collision process. The upper crust in the Superior province is lighter than the lower crust, which has the same density as the Grenville province. The suture zone in his model also dips toward the younger crust, but with a constant dip down to the Moho, and the non-isostatic buoyancy force arising from the Moho undulation is supported by flexure of the elastic core of the crust, with a thickness less than 30 km. This difference in the elastic thickness between the Hynes and Pilkington models is probably due to the fact that Hynes used a continuous plate, whereas Pilkington adopted a fractured plate. Subject to the same loading, a fractured plate requires a higher rigidity (for example, a thicker elastic layer) in order to produce a flexure identical to that of a continuous plate.

The Grenville Front has been studied more extensively than the other collision zones in the study area. Several seismic profiles crossing the suture are available. A seismic profile along Lac Evans (about 51° N and 77° W) and Lac St. Jean (about 47° N and 71° W) line revealed a major structural feature about 50-75 km wide at the Moho just south of the Grenville Front (Mereu and Jobidon, 1971) where the crust is thickened by 5-10 km, probably due to the collision. The Moho is very smooth beneath Superior, slightly dipping toward the collision zone (from 30 km to 34 km depth within about 200 km distance), but there are pronounced undulations as much as 5 km beneath the Grenville province far from the collision zone. Mereu and Jobidon (1971) related the broad negative Bouguer anomaly over the region to this anomalous crustal thickening and lateral density variations in the upper crust, and suggested that the Grenville suture is a major fault which penetrates well into the upper mantle. Three seismic profiles were obtained across the Ottawa-Bonnechere graben and Grenville Front (an area between 44°-48° N and 74°-80° W) as part of the COCRUST program in 1982 (Mereu et al., 1986). The Ottawa-Bonnechere graben is a depressed zone of approximately 60 km wide located immediately south of the Grenville Front. The two subparallel profiles almost normal to the Grenville Front

(see their Fig. 6) show distinctly different Moho structure. One of the profiles (AO) shows a diffuse Moho immediately beneath the Front which becomes sharper and shallower toward the interior part of Grenville province. The other (CD) shows a well defined Moho which is uplifted in the Grenville side, immediately south of the Front. According to this profile, Superior province is thicker than Grenville and mantle is uplifted by about 5 km, contrary to the Lac Evans-Lac St. Jean seismic results. The CD profile also suggests that the Grenville frontal zone is deep-seated and extends to the Moho (Mereu et al., 1986). The seismic profile of Abitibi-Grenville Lithoprobe line 15 (from about 47° 40' N and 79° 40' W to 46° 20' N and 78° 40' W) that crossed the Grenville Front, shows an uplift of about 4 km at the Moho beneath the Grenville suture (Kellett et al, 1994). The Lithoprobe seismic reflection profiles 30-32 in the western Grenville province of southern Ontario (within 44°-46° N and 76°-80° W) show almost constant Moho depth along each profile, but depth to the Moho changes by as much as 3 km from profile to profile (White et al., 1994). The Lithoprobe seismic profile in the eastern Grenville province (from 50°30' N and 68°40' W to 52°20' N and 67°30' W) subparallel to and south of the Grenville Front shows minor deepening of the Moho from south to north (Eaton et al, 1995). And finally, deep seismic reflection survey across the Grenville Province in western Quebec (from 47°40'N and 76°20' W to 46°N and 73°30' W) shows a crust of about 44 km thick beneath the Front which rapidly thins to about 36 km to the southeast (Martignole and Calvert, 1996). These existing seismic profiles across the Grenville Front show quite different crustal structures, indicating that the Grenville Front has a highly variable tectonic character as also concluded by Kellett et al. (1994).

Other collision zones in the study area have not attracted as much attention as the Grenville Front, possibly because the gravity and magnetic signatures of the Grenville Front are remarkably outstanding. However, similar diversity of crustal structure and Moho undulation probably exists elsewhere. For example, the collision zone between Nain and Makkovik provinces is not well delineated in the gravity and magnetic anomaly maps, largely because the entire length of the zone is not long enough to produce the elongated anomalies which are the distinct characteristic of the Grenville suture. However, the seismic refraction data acquired parallel to the shoreline over the continental shelf of the Labrador Sea and across the Nain-Makkovik boundary (from 56°40' N and 60°20' W to 55°20' N and 58°10' W) shows a substantially thinner crust for both Nain and Makkovik and a significant change in the Moho depth by 5 km across the boundary (Reid, 1996). The relatively thinner crust of the continental shelf, about 28 km beneath Nain province and even thinner, 23 km, beneath Makkovik province, is due in part to erosion of the upper crust and crustal extension during rifting of Labrador Sea (Reid, 1996). A sudden change in the Moho depth in Nain province to the north, about 5 km offset within about a 10 km horizontal distance, detected by refraction/wide-angle reflection seismic experiment along Lithoprobe ECSOOT line 4 (from 59°N and 63°W to 58°N and 61°30' W) suggests a normal fault probably related to the Handy Fault, as proposed by Funck

and Loudon (1998). Sharp changes in the Moho depth elsewhere are also related to normal faults (Mereu et al., 1986).

The two-dimensional inversion of the gravity anomalies presented in this paper retains the diverse characteristics of the tectonic features among collision zones as well as along a given orogen. For the interpretation of the intermediate and long wavelength components of the gravity anomalies, we first calculated two extreme models, a crust with lateral density perturbations and isostatic compensation at the Moho, and a homogeneous crust with a non-isostatically undulating Moho which, together with the topography gives rise to the observed gravity. One of the important points revealed in this study is that the Moho structure strongly depends on whether isostatic compensation prevails there or not. The first model results in crustal thinning beneath collision zones, whereas the second model shows crustal thickening but with amplitudes significantly larger than the observed ones. These models are considered unrealistic. Note that the first model requires a zero strength crust, whereas the second indicates a crustal rigidity on the order of $1-10 \times 10^{24}$ N m (Pilkington, 1990, 1991). This emphasizes that surface topography and gravity anomaly data alone cannot provide a good estimate of the strength and the thickness of the elastic part of the crust. Other geophysical (seismic in particular, and heat flow and magnetic anomalies to some extent) and geological (stress patterns in particular, and major structural features) information is needed. The reality may lie somewhere between these two extreme models. This is indicated by the diversity of the Moho structure along the Grenville suture revealed from seismic measurements, which is probably related to the extent of compensation of the surface topography and intracrustal load at the Moho. For example, Gibb and Thomas (1976) and Hynes (1994) included lateral variations of density, by juxtaposing two crusts of different densities, and Pilkington (1990) introduced intracrustal mass load, besides the density differences between the two colliding crusts, in order to account for small scale positive gravity anomalies of the suture zones. None of these authors assumed isostatic compensation at the Moho. To construct a realistic model, we considered both lateral density perturbations in the crust and Moho undulation without imposing isostatic compensation at the Moho. The contribution from the Moho is weighted such that the resulting Moho undulation resembles the observed Moho variations, and the crustal model satisfies the observed gravity anomalies.

The short wavelength components of the lateral contrasts in the magnetic susceptibility of the crust are determined using a half-space crustal model. The northern and central parts of Superior province, the eastern and central parts of east Churchill, and the eastern parts of Grenville are characterised by high susceptibility contrasts. (Note that positive/negative susceptibility in the continent implies high/low magnetic susceptibility of sources, rather than opposite polarity.) Some of the features show good correlation with geology. For example, De Pas Batholith has a very high susceptibility. However, there is no obvious signature of the collision zones over these wavelengths, except for the Cape Smith belt. The lack of a pronounced correlation

between the surface topography and magnetic anomalies implies that the tectonic processes that shaped the eastern part of the Canadian shield have not considerably affected the magnetic properties of the upper parts of the crust. On the other hand, major collision zones are delineated as low magnetic features in the intermediate and long wavelength components of the magnetic susceptibility map, indicating that these components of the magnetic anomalies arise from deep seated magnetic susceptibility contrasts. The satellite magnetic anomalies also suggest a highly magnetic lower crust. The low magnetisation of the continent-continent collision zones has also been observed elsewhere and has been related to the loss of magnetisation in the lower crust through the collision processes (Arkani-Hamed and Strangway, 1986). Several mechanisms operating during or shortly after collision may reduce the magnetisation of the crust, such as frictional heating, hydration, and crustal thickening. Frictional heating is probably important for recent collisions, but it diminishes in time as the crust cools. It is not a significant mechanism to be responsible for the low magnetisation of the old collision zones we are concerned with. The continent-continent collision that occurs after subduction of the pre-existing oceanic lithosphere may introduce water into the crust, resulting in hydration of magnetic minerals and reduction of magnetisation. This mechanism could be appreciable, especially on a local scale (Toft et al., 1993). Finally, crustal thickening produces a high surface topography and a corresponding deep crustal root, created through isostatic compensation during and shortly after the collision when the crust was still warm and weak enough to readily respond to the topographic load as well as the load created by the density perturbations resulting from collision of continents with different densities. The thickening of the less magnetic upper crust also suppresses the highly magnetic lower crust. The topography has subsequently been reduced through erosion, whereas the root has been less affected. The crustal root consists of highly magnetic lower crust which is now suppressed into the hot upper mantle. The average geothermal gradient in the continent suggests that temperature exceeds the Curie temperature of magnetite (680° C) at depths greater than about 35-40 km, and deeper parts of the crustal roots are thermally demagnetized. Therefore, the negative magnetic anomalies of the collision zones are probably related to the depression of the upper boundary of the highly magnetic lower crust and, more importantly, the thermal demagnetisation of parts of the highly magnetic crustal roots.

3.8 Acknowledgements

This research is supported by the Lithoprobe program of Natural Sciences and Engineering Research Council (NSERC) of Canada. We would like to thank Thomas Funck for proving a reprint of his paper, and Andrew Hynes and Keith Loudon for their comments on the preliminary version of this paper.

3.9 References

- Arkani-Hamed, J. 1988. Differential reduction-to-the-pole of regional magnetic anomalies. *Geophysics*, **53**: 1592-1600.
- Arkani-Hamed, J., and Strangway, D.W. 1986. Magnetic susceptibility anomalies of lithosphere beneath eastern Europe and the Middle East. *Geophysics*, **51**: 1711-1724.
- Arkani-Hamed, J., and Verhoef, J. 1989. Generalised inversion of scalar magnetic anomalies: magnetisation of the crust off the east coast of Canada. *Geophysical Monogram, American Geophysical Union*, **51**: 255-270.
- Arkani-Hamed, J., and Celeti, G. 1989. Effects of thermal remanent magnetisation on the magnetic anomalies of intrusives. *Journal of Geophysical Research*, **94**: 7364-7378.
- Arkani-Hamed, J., and Hinze, W.J. 1990. Limitations of the long-wavelength components of the north American magnetic anomaly map. *Geophysics*, **55**: 1577-1588.
- Arkani-Hamed, J., Verhoef, J., Roest, W., and Macnab, R. 1995. The intermediate-wavelength magnetic anomaly maps of the North Atlantic ocean derived from satellite and shipborne data. *Geophysical Journal International*, **123**: 727-743.
- Baer, A.J., Emslie, R.F., Irving, E., and Tanner, J.G. 1974. Grenville geology and plate tectonics. *Geoscience Canada*, **1**: 54-61.
- Cannat, M. 1993. Emplacement of mantle rocks in the seafloor at mid-ocean ridges. *Journal of Geophysical Research*, **98**: 4163-4172.
- Chian, D., and Loudon, K.E. 1995. Crustal structure of the Labrador Sea conjugate margin and implications for the formation of nonvolcanic continental margins. *Journal of Geophysical Research*, **100**: 24239-24253.
- Dewey, J.F., and Burke, K.C.A. 1973. Tibetan, Variscan and Precambrian basement reactivation: products of continental collision. *Journal of Geology*, **81**: 683-692.
- Dyment, J., Arkani-Hamed, J., and Ghods, A. 1997. Contribution of serpentinized ultramafics to marine magnetic anomalies at slow and intermediate spreading centres: insights from the shape of the anomalies. *Geophysical Journal International*, **129**: 691-701.
- Eaton, D.W., Hynes, A., Indares, A., and Rivers, T. 1995. Seismic images of eclogites, crustal-scale extension, and Moho relief in the eastern Grenville province, Quebec. *Geology*, **23**: 855-858.

- Francis, T.J.G. 1981. Serpentinization faults and their role in the tectonics of slow spreading ridges. *Journal of Geophysical Research*, **86**: 11616-11622.
- Funk, T., and Loudon, K. In press. Wide-angle seismic imaging of pristine Archean crust in the Nain province, Labrador. *Canadian Journal of Earth Sciences*.
- Gibb, R.A., and Thomas, M.D. 1976. Gravity signature of fossil plate boundaries in the Canadian Shield. *Nature*, **262**: 199-200.
- Grauch, V.J.S. 1993. Limitations on digital filtering of the DNAG magnetic data set for the conterminous U.S. *Geophysics*, **58**: 1281-1296.
- Hamano, Y., Bina, M.M., and Krammer, K. 1990. paleomagnetism of the serpentinized peridotite from ODP hole 670A. *Proceeding of the ocean drilling Program, Scientific Results*, **106/109**: 257-262.
- Harrison, C.G.A. 1987. Marine magnetic anomalies-the origin of the stripes. *Annual Review of Earth and Planetary Sciences*. **15**: 505-543.
- Harrison, C.G.A., and Lindh, T. 1982. A polar wandering curve for North America during the Mesozoic and Cenozoic. *Journal of Geophysical Research*, **87**: 1903-1920.
- Hinze, W.J., Hood, P.J. and the COMMITTEE FOR THE MAGNETIC ANOMALY MAP OF NORTH AMERICA. 1988. Magnetic anomaly map of north America. *Geophysics: The Leading Edge of Exploration*, **7**: 19-21.
- Hynes, A. 1994. Gravity, flexure, and the deep structure of the Grenville Front, eastern Quebec and Labrador. *Canadian Journal of Earth Sciences*, **31**: 1002-1011.
- IAGA division V Working Group 8. 1996. Revision of the international geomagnetic reference field released. *Eos, Transactions, American Geophysical Union*, **77**: 153.
- Johnson, A.C., von Frese, R.R.B., and the ADMAP Working Group. 1997. Magnetic map will define Antarctica's structure. *Eos, Transactions, American Geophysical Union*, **78**: 185.
- Kellett, R.L., Barnes, A.E., and Rive, M. 1994. The deep structure of the Grenville Front: a new perspective from western Quebec. *Canadian Journal of Earth Sciences*, **31**: 282-292.
- LaBrecque, J.L., and Cande, S.C. 1984. Intermediate-wavelength magnetic anomalies over the central Pacific. *Journal of Geophysical Research*, **89**: 11124-11134.

- LaBrecque, J.L., and Raymond, C.A. 1985. Seafloor spreading anomalies in the Magsat field of the North Atlantic. *Journal of Geophysical Research*, **90**: 2565-2575.
- Langel, R.A. 1990. Global magnetic anomaly maps derived from POGO spacecraft data. *Physics of the Earth and Planetary Interiors*, **62**: 208-230.
- Macnab, R., Verhoef, J., Roest, W., and Arkani-Hamed, J. 1995. New database documents the magnetic character of the Arctic and North Atlantic. *Eos, Transactions, American Geophysical Union*, **76**: 449-458.
- Martignole, J., and Calvert, A.J. 1996. Crustal-scale shortening and extension across the Grenville Province of western Quebec. *Tectonics*, **15**, 376-386.
- Mereu, R.F., and Jobidon G. 1971. A seismic investigation of the Crust and Moho on a line perpendicular to the Grenville Front. *Canadian Journal of Earth Sciences*, **8**: 1553-1583.
- Mereu, R.F., Forsyth, D.A., and Green, A.G. et al. 1986. The 1982 COCRUST seismic experiment across the Ottawa-Bonnechere graben and Grenville Front in Ontario and Quebec. *Geophysical Journal of the Royal Astronomical Society*, **84**: 491-514.
- Mooney, W.D., and Braille, L.W. 1989. The seismic structure of the continental crust and upper mantle of North America. *In* *The Geology of North America - An overview*. Edited by A.W. Bally and A.R. Palmer. Geological Society of America, Boulder, Colo., Vol. A, pp. 39-52.
- Pilkington, M. 1990. Lithospheric flexure and gravity anomalies at Proterozoic plate boundaries in the Canadian Shield. *Tectonophysics*, **176**: 277-290.
- Pilkington, M. 1991. Mapping elastic lithospheric thickness variations in Canada. *Tectonophysics*, **190**: 283-297.
- Pilkington, M., and Grieve, R.A.F. 1989. Magnetization/density ratio mapping in eastern Canada. *In* *Statistical Applications in the Earth Sciences*, ed. F.P. Agterberg and G.F. Bonham-Carter, Geological Survey of Canada, paper 89-9, p. 89-98.
- Pilkington, M., and Roest, W.R. 1996. An assessment of long-wavelength magnetic anomalies over Canada. *Canadian Journal of Earth Sciences*, **33**: 12-23.
- Ravat, D., Langel, R.A., Arkani-Hamed, J., and Alsdorf, D.E. 1995. Global vector and scalar Magsat magnetic anomaly maps. *Journal of Geophysical Research*, **100**: 20111-20136.

- Reid, I. 1996. Crustal structure across the Nain-Makkovik boundary on the continental shelf off Labrador from seismic refraction data. *Canadian Journal of Earth Sciences*, **33**: 460-471.
- Sandwell, D.T., and Smith, W.H.F. 1997. Marine gravity anomaly from Geosat and ERS 1 satellite altimetry. *Journal of Geophysical Research*, **102**: 10039-10054.
- Tanner, J.G. and members of the COMMITTEE FOR THE GRAVITY ANOMALY MAP OF NORTH AMERICA. 1988. Gravity anomaly map of north America. *Geophysics: The Leading Edge of Exploration*, **7**: 15-18.
- Toft, P.B., and Arkani-Hamed, J. 1992. Magnetization of the Pacific ocean lithosphere deduced from Magsat data. *Journal of Geophysical Research*, **97**: 4387-4406.
- Toft, P.B., Arkani-Hamed, J., and Haggerty S.E. 1990. The effects of serpentinization on density and magnetic susceptibility: a petrophysical model. *Physics of the Earth and Planetary Interiors*, **65**: 137-157.
- Toft, P.B., Scowen, P.A.H., Arkani-Hamed, J., and Francis, D. 1993. Demagnetization by hydration in deep-crustal rocks in the Grenville province of Quebec, Canada: implications for magnetic anomalies of continental collision zones. *Geology*, 1993, **21**: 999-1002.
- Verhoef, J., Roest, W.R., Macnab, R., Arkani-Hamed, J., and Members of the Project Team. 1996. Magnetic anomalies of the Arctic and north Atlantic oceans and adjacent land areas. Geological Survey of Canada, Open Files: 3125, 3280, 3281, 3282.
- Wardle, R.J., Ryan, B., and Ermanovics, I. 1990. The eastern Churchill Province, Torngat and New Quebec orogens: An overview. *Geoscience Canada*, **17**: 217-222.
- Wasilewski, P.J., Thomas, H.H., and Mayhew, M.A. 1979. The Moho as a magnetic boundary. *Geophysical Research Letters*, **6**: 541-544.
- White, D.J., Easton, R.M., and Culshaw, N.G. et al. 1994. Seismic images of the Grenville Orogen in Ontario. *Canadian Journal of Earth Sciences*, **31**: 293-307.
- Williams, I., and Fuller, M. 1982. A Miocene polarity transition (R-N) from the Agno Batholith, Luzon. *Journal of Geophysical Research*, **87**: 9408-9418.

3.10 Figure Captions

Figure 3.1 A simplified tectonic map of eastern Canada based on the Tectonic Map of Canada published by Geological Survey of Canada, 1968. The map also shows the locations cited in the text. DPB is the De Pas Batholith, MHC is the Manicouagan-Hart Jaune complex, CSB is the Cap Smith belt.

Figure 3.2 a) Equivalent rock topography, in km, b) Free air gravity anomalies, in milligals, c) Distribution of gravity stations, and d) space-domain correlation of the topography and gravity anomalies.

Figure 3.3 a) Power spectra of free air gravity anomalies, the gravity field due to the topography and gravity field of the topography which is compensated at 37 km depth, and b) Spectral-domain degree correlation coefficients between gravity anomalies and topography, reduced-to-pole magnetic anomalies and topography, and reduced-to-pole magnetic anomalies and vertical gradient of gravity anomalies.

Figure 3.4 a) Magnetic anomalies, b) High altitude magnetic profiles, c) Magsat dawn map, and d) Low-pass filtered low-altitude magnetic anomalies. Units are in nT.

Figure 3.5 Comparison of high-altitude magnetic profiles with the upward continued low-altitude magnetic anomalies to 4 km elevation.

Figure 3.6 a) Reduced-to-pole magnetic anomalies, in nT, b) Space-domain correlation of the reduced-to-pole magnetic anomalies and topography, c) Vertical gradient of gravity anomalies, in 10^{-7} s^{-2} , and d) Space-domain correlation of the reduced-to-pole magnetic anomalies and the gravity gradient.

Figure 3.7 Short wavelength components of a) the topography, in km and b) the free air gravity anomalies, in milligals. c) Space-domain correlation of the topography and gravity anomalies, and d) Density perturbations within the crust, in kg/m^3 .

Figure 3.8 Intermediate wavelength components of a) the topography, in km, b) the free air gravity anomalies, in milligals, c) Density perturbations within the crust, in kg/m^3 , and d) Moho undulation, in km. The anomalies near the boundaries in Labrador Sea and Hudson Bay are artifacts arising from edge effects (see the text).

Figure 3.9 Intermediate and long wavelength components of a) the topography, in km, b) the free air gravity anomalies, in milligals, c) Moho undulation, in km, and d) Excess Moho undulation compared to the undulation of an isostatically compensated Moho, in km.

Figure 3.10 Power spectra of the density perturbations in the crust specified by the intermediate and long wavelength components. The numbers on the curves are the α values from -3 to 1 with the increment of 0.5.

Figure 3.11 Histograms of the Moho undulation. The numbers on the curves are the α values from -3 to -1 with the increment of 0.5.

Figure 3.12 The intermediate and long wavelength components of a) the vertically averaged density perturbations within the 37 km thick crust, in kg/m^3 , and b) the Moho undulation about the 37 km depth of the selected crustal model, in km.

Figure 3.13. a) Magnetic susceptibility of a half-space with topography, b) Magnetic susceptibility of the crust bounded by the topography and Moho, c) Short wavelength components of the susceptibility of the crust, and d) Intermediate and long wavelength components of the susceptibility of the crust. Units are in 10^{-3} SI.

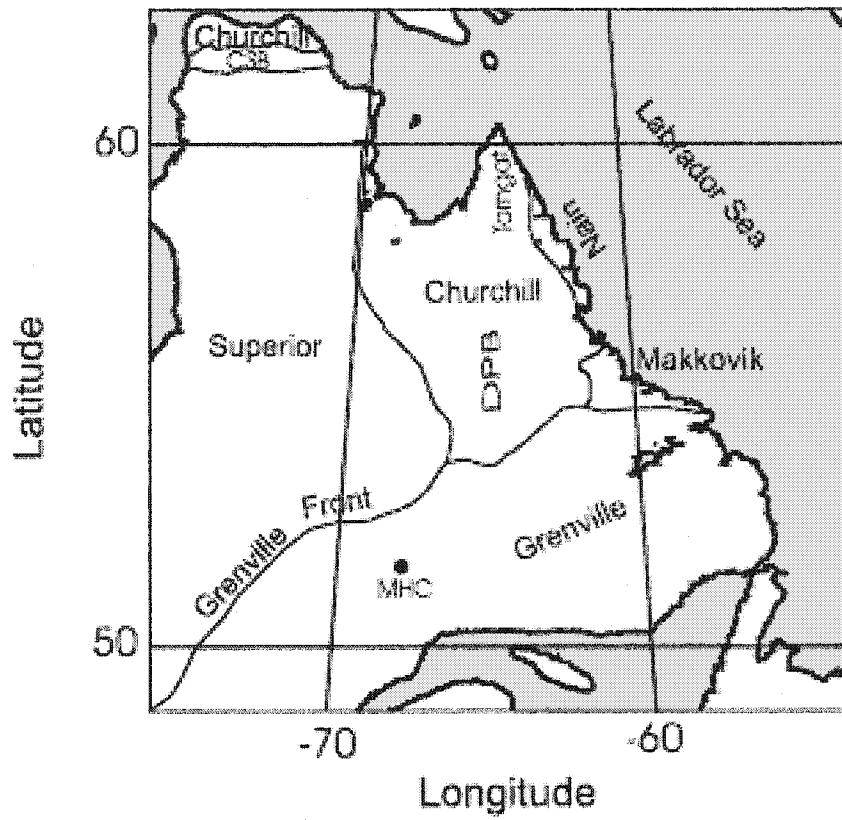


Figure 3.1:

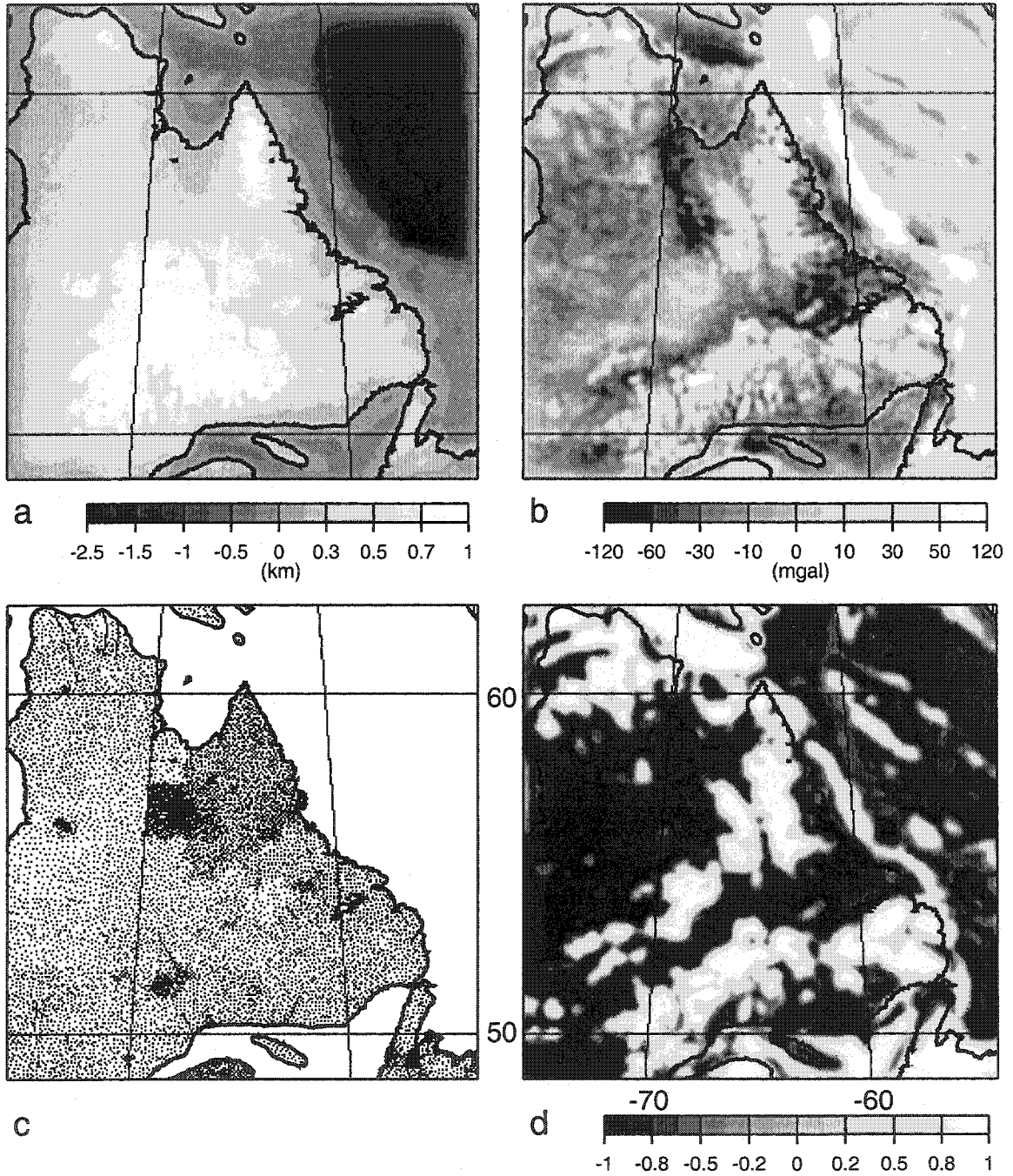


Figure 3.2:

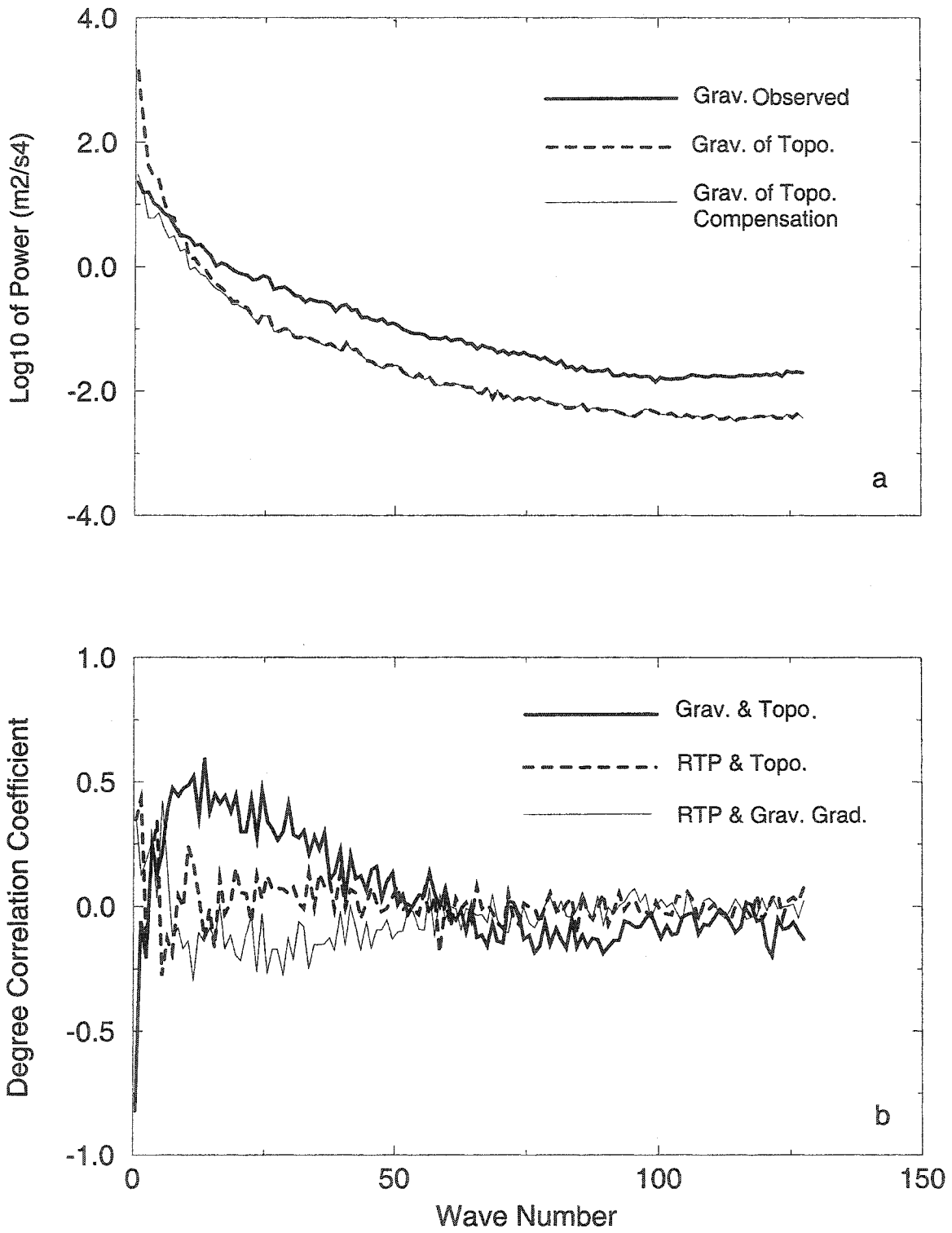


Figure 3.3:

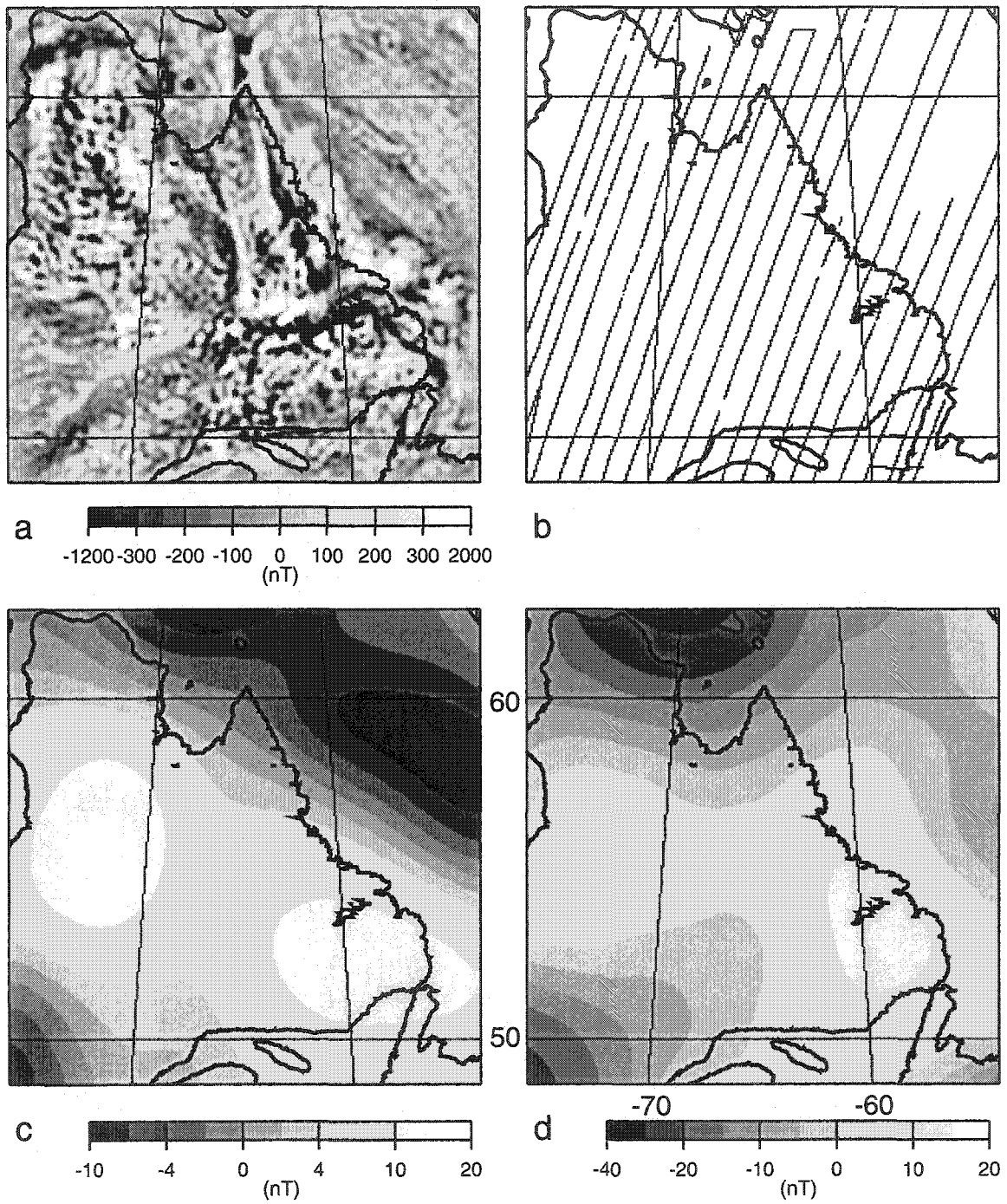


Figure 3.4:

Magnetic Anomaly Profiles

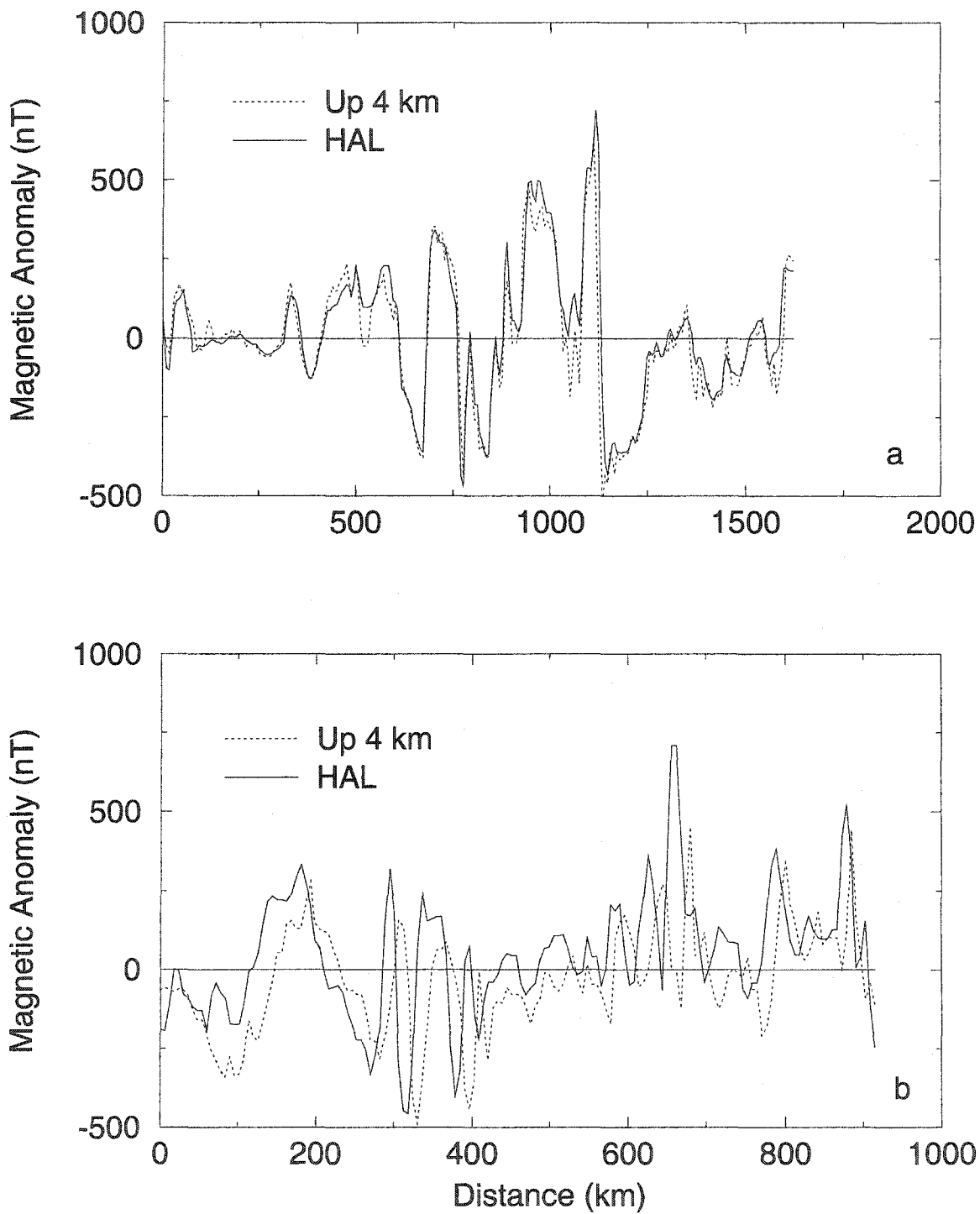


Figure 3.5:

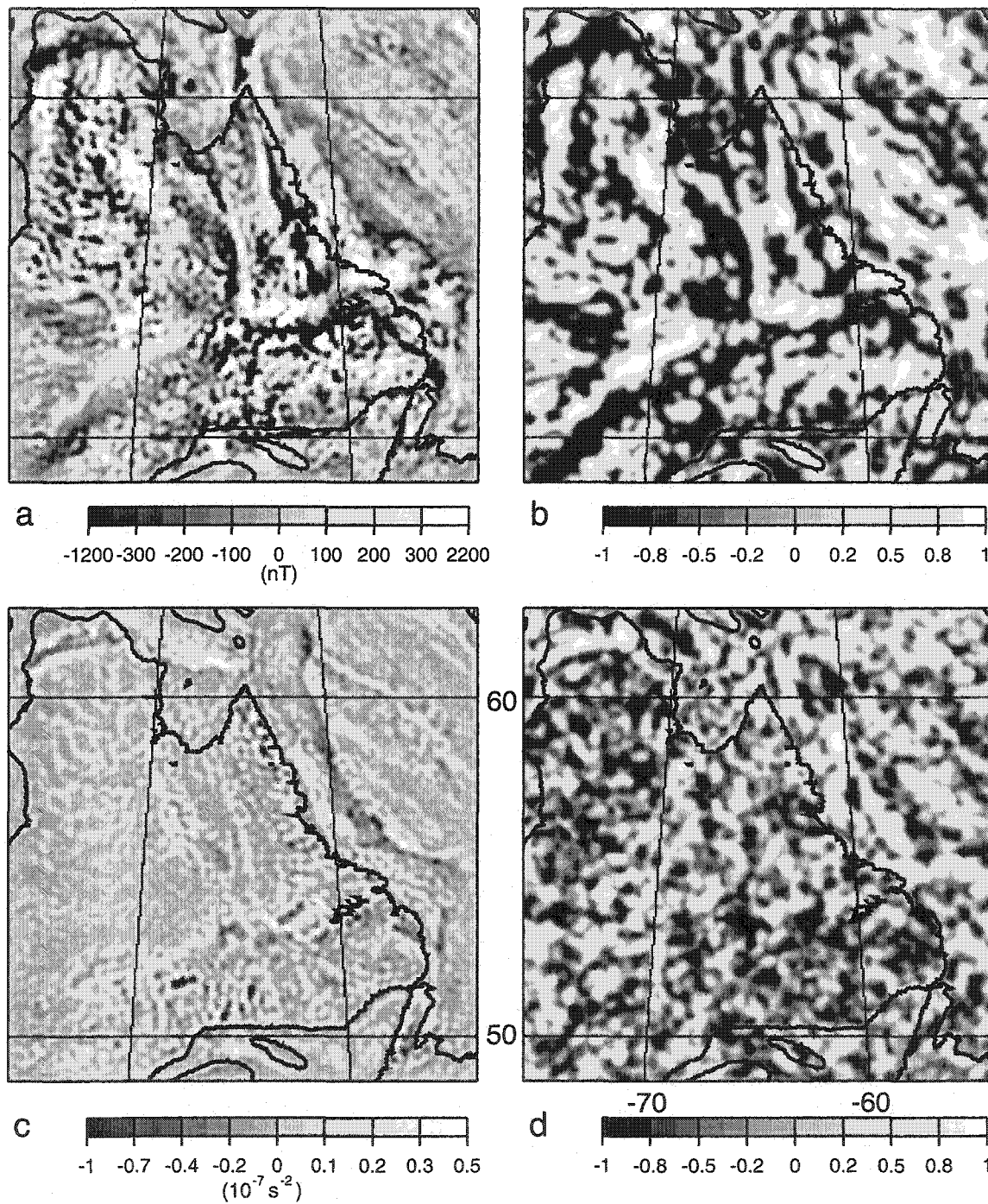


Figure 3.6:

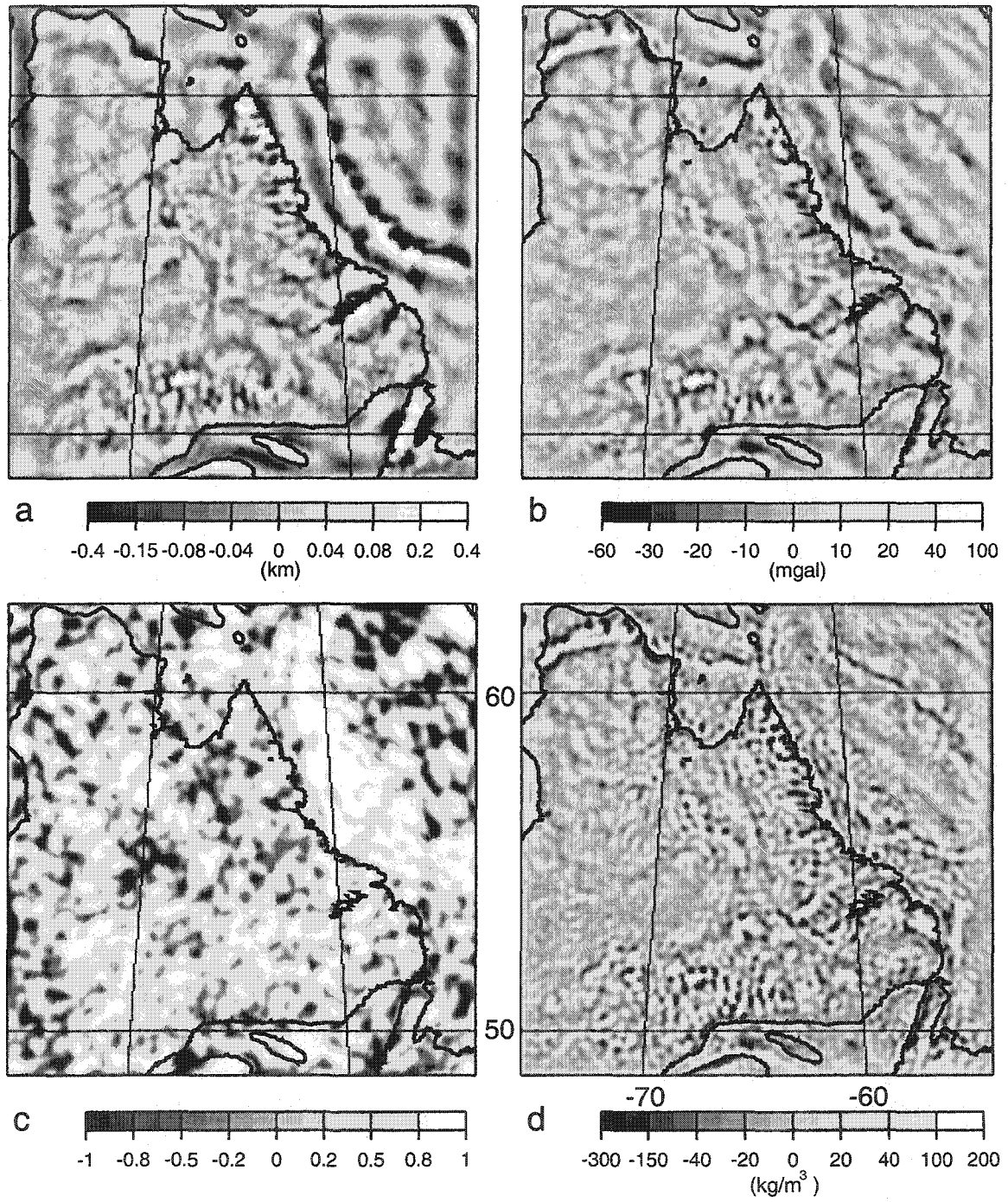


Figure 3.7:

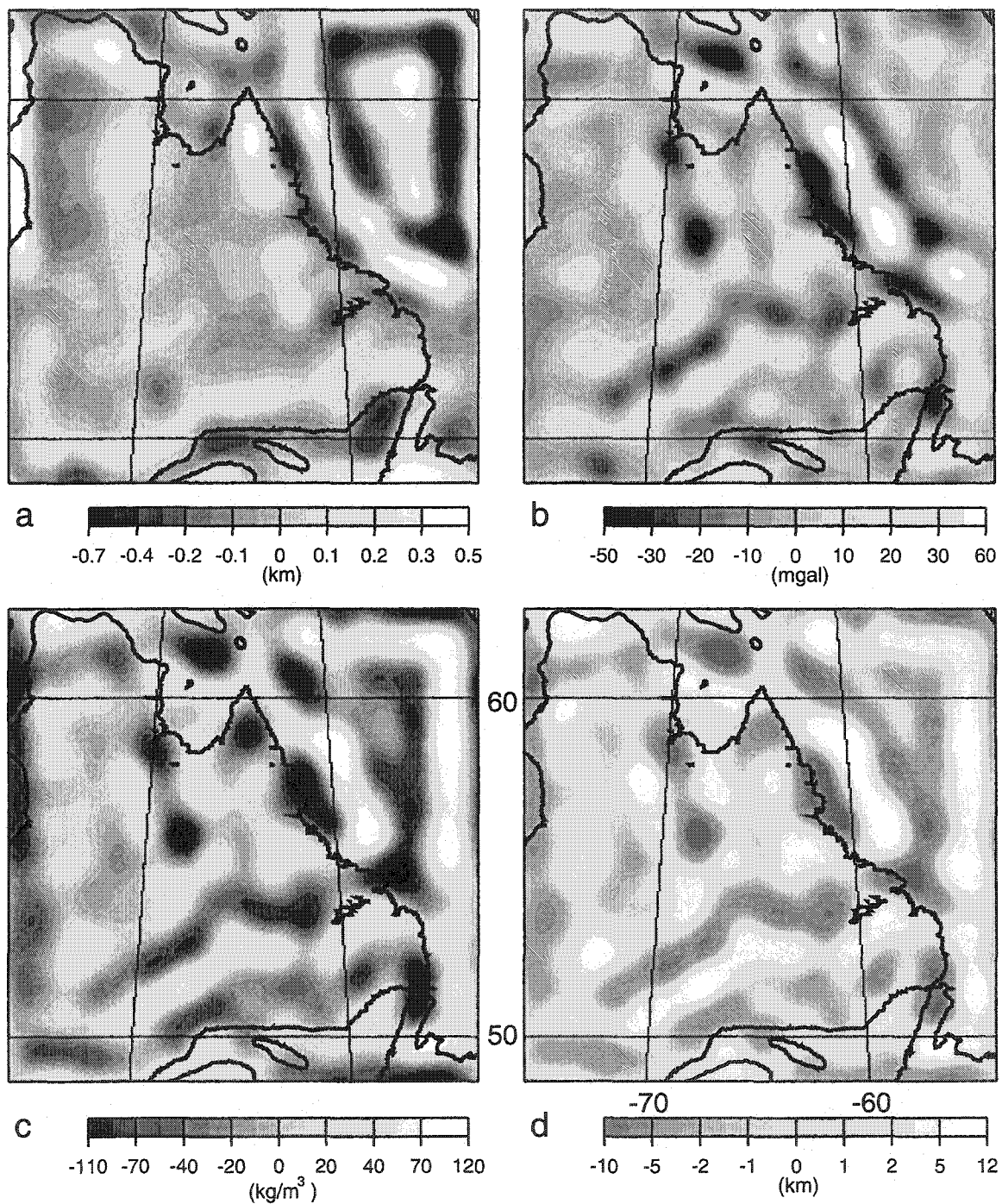


Figure 3.8:

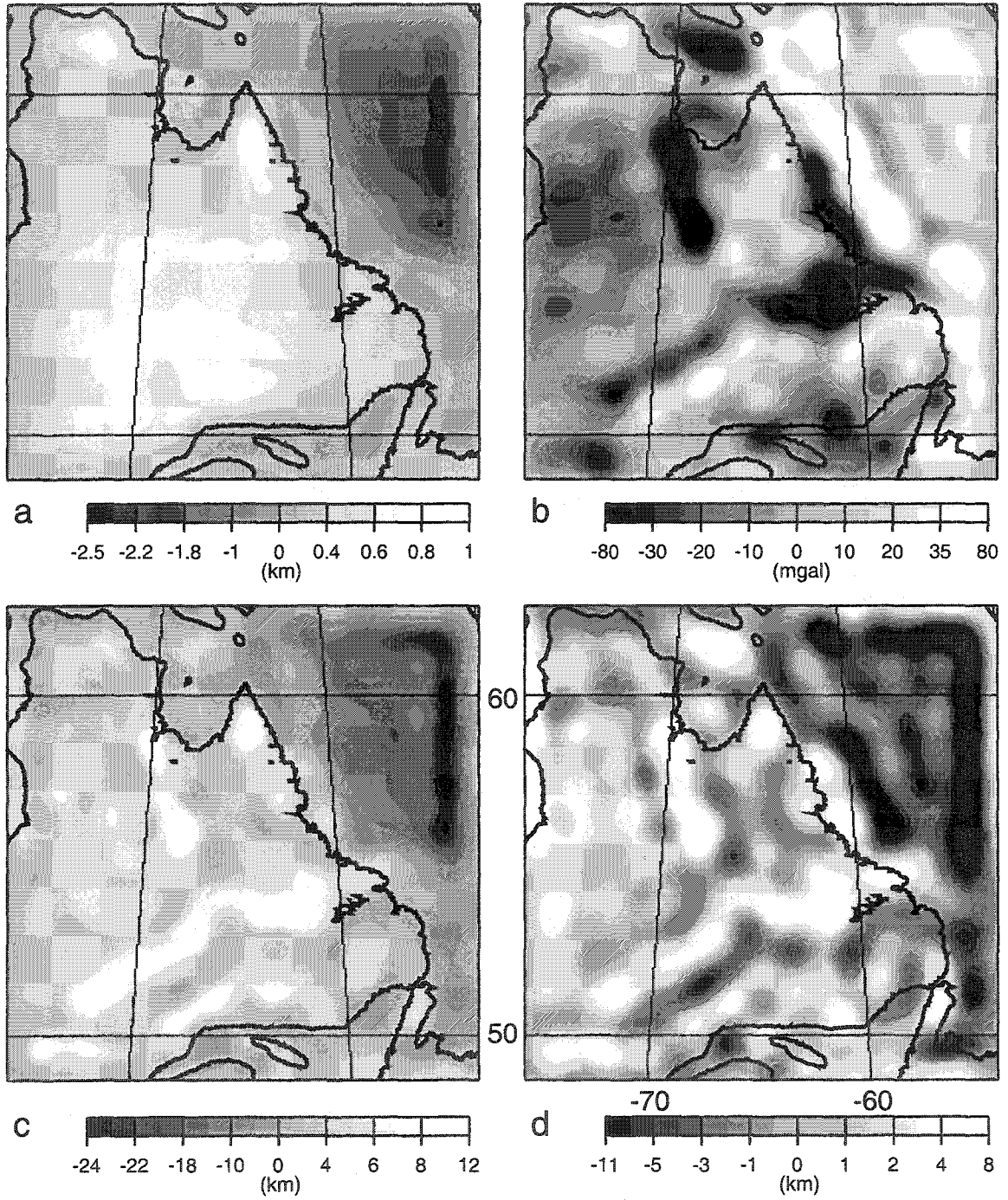


Figure 3.9:

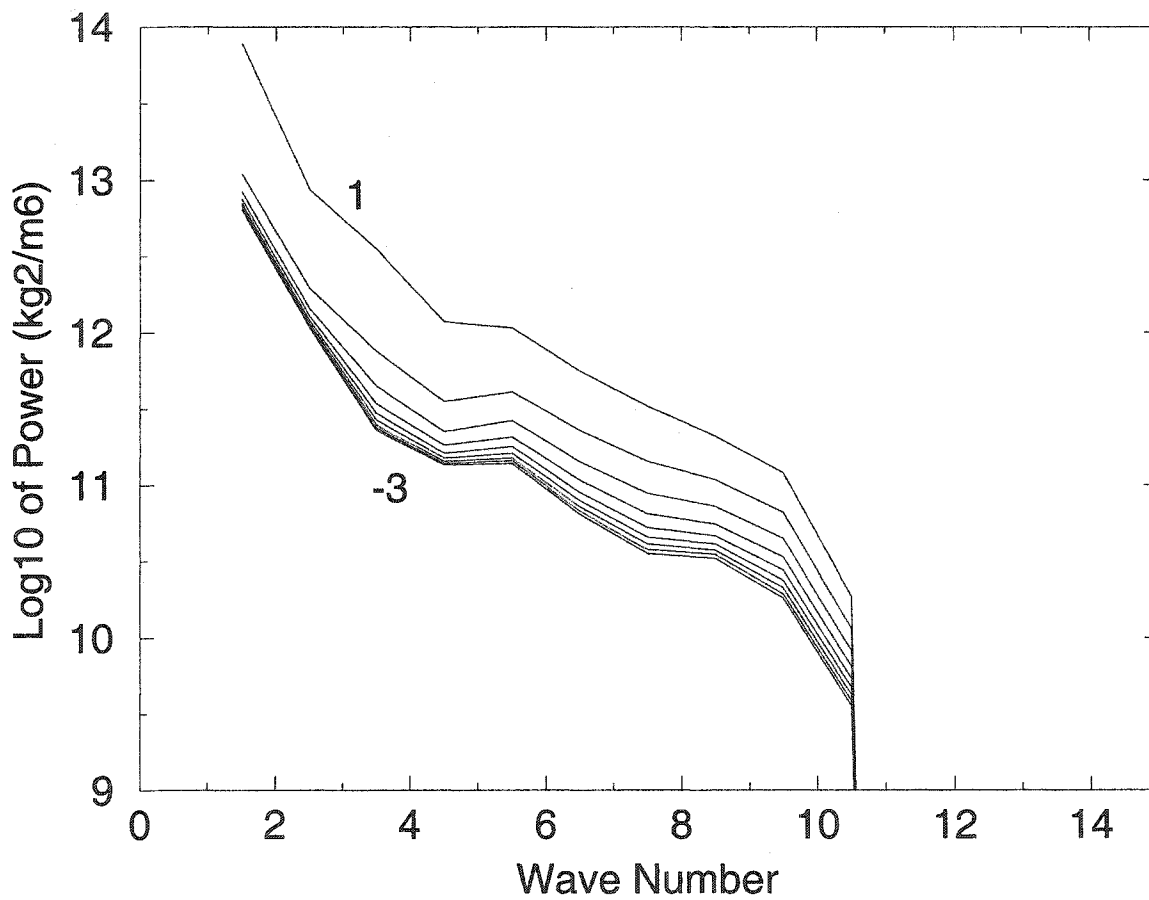


Figure 3.10:

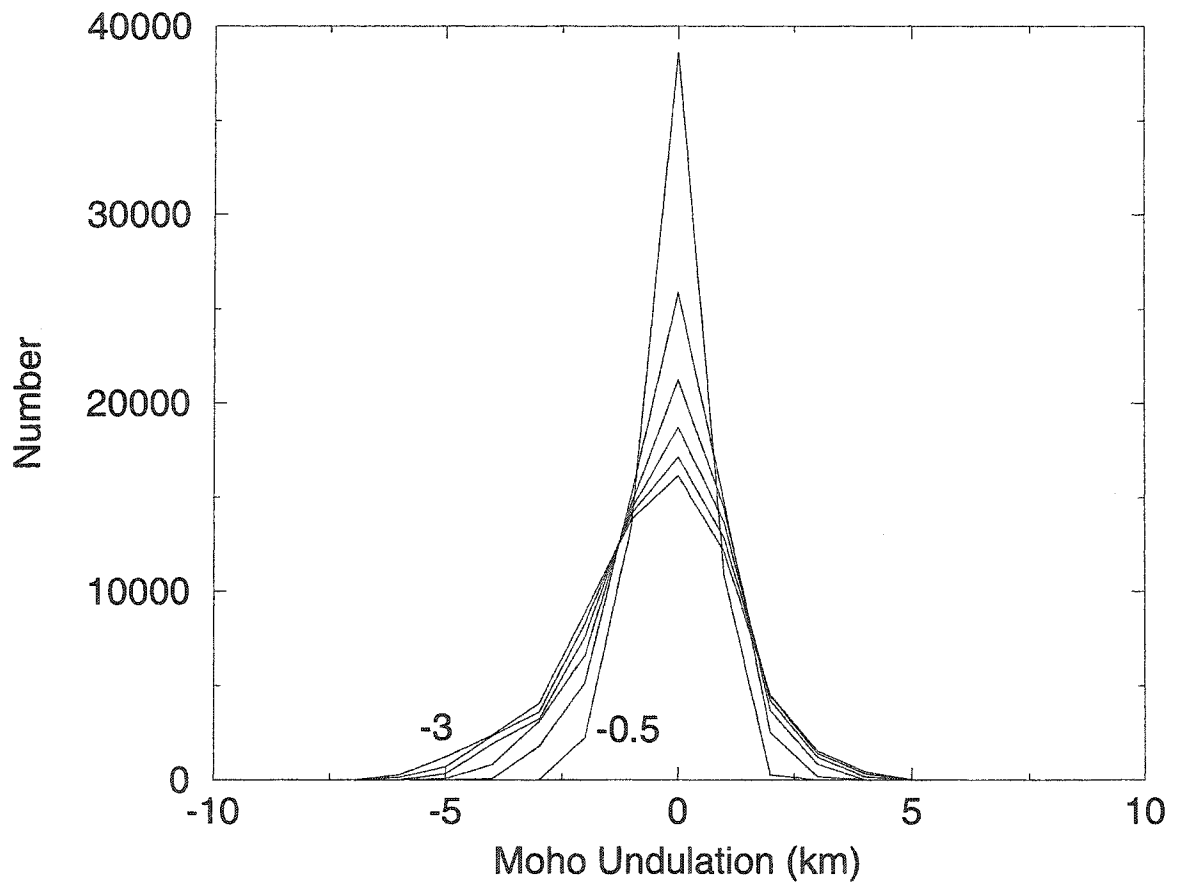


Figure 3.11:

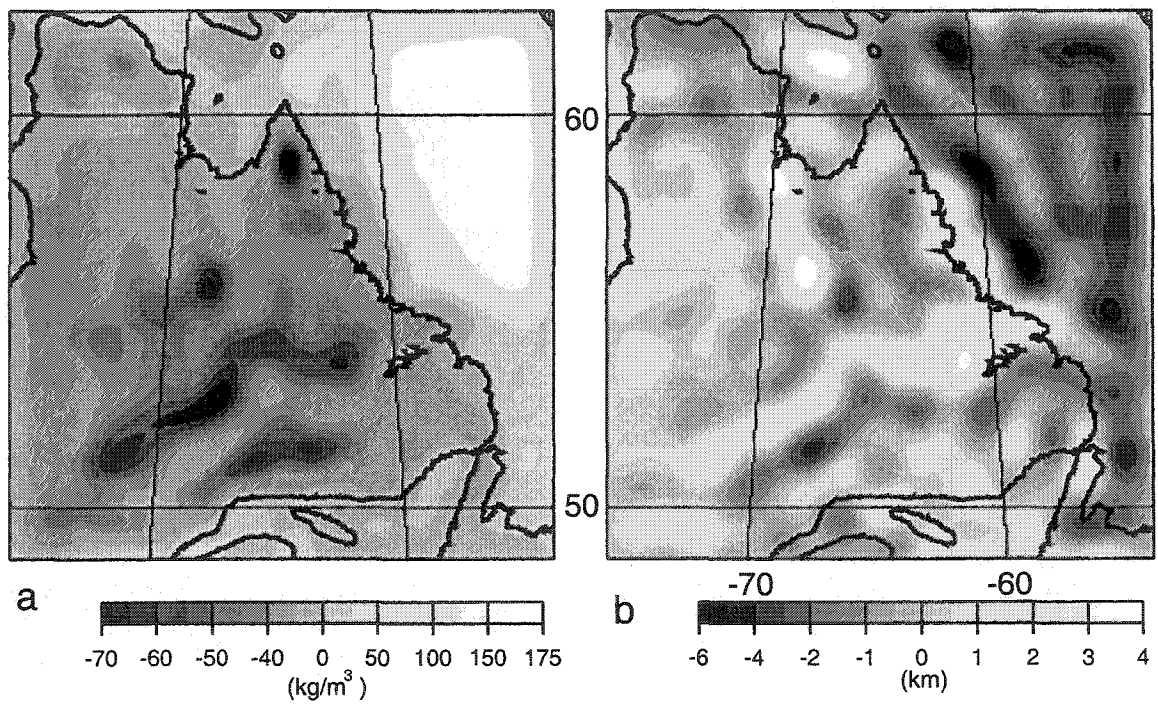


Figure 3.12:

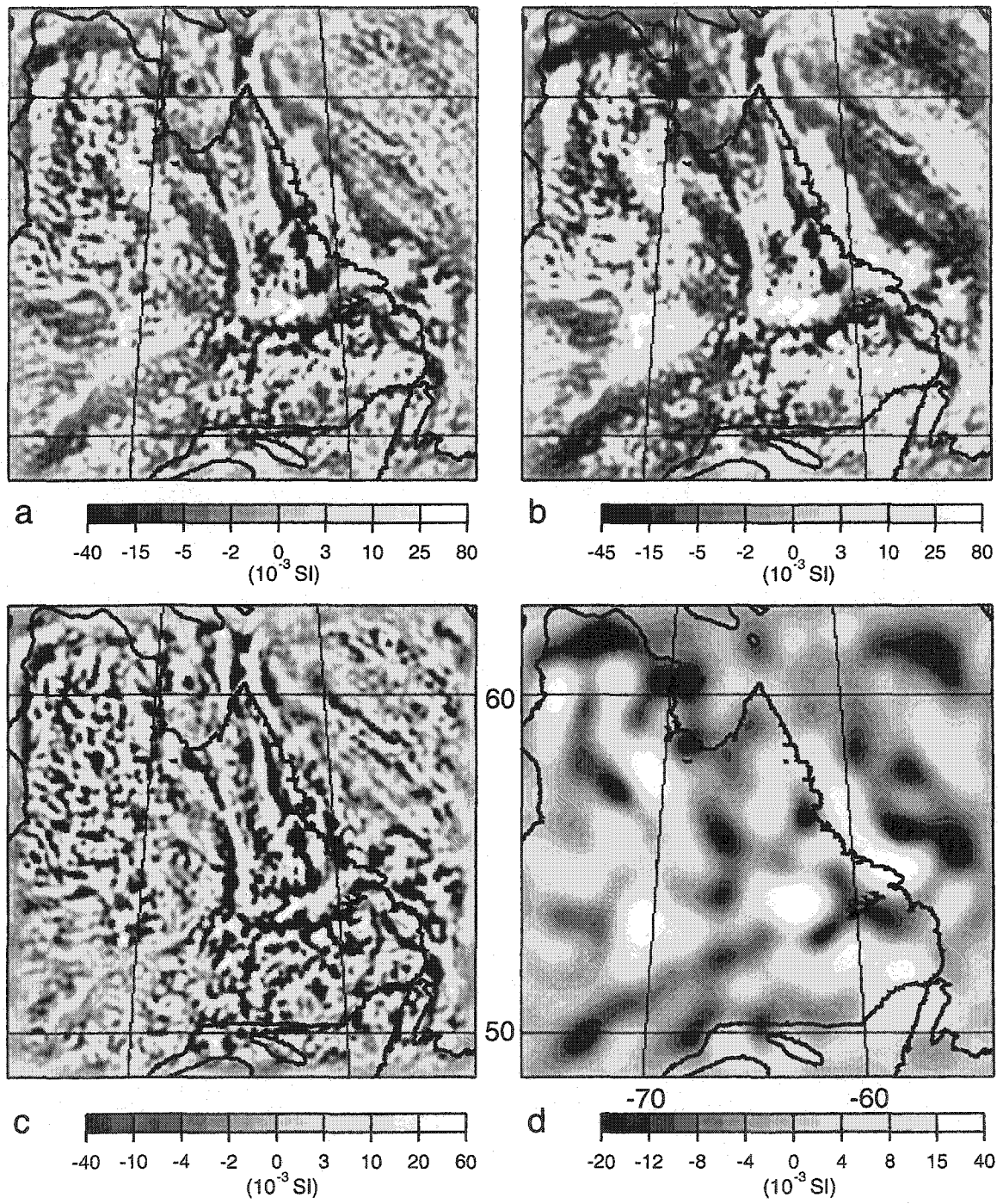


Figure 3.13:

Chapter 4

The Elastic Properties of the Lithosphere Beneath Scotian Basin

In this chapter the systematic topography and gravity analysis method developed in Chapter 3 is used to determine the compensation state of the lithosphere beneath the Scotian Basin. A 3-D density model that incorporates seawater, sediments, oceanic and continental crust and the lithosphere down to 35 km depth is established, which together with density perturbations inside the crust and mantle of the model, produce the observed gravity anomalies. It is demonstrated that the area is not isostatically compensated. Regional, instead of local, compensation is proposed to explain the bathymetry, depth to basement and gravity data. The loads of the sediments and the density perturbations in the crust and/or upper mantle must be elastically supported by the lithosphere beneath. Flexural calculations based on a 2-D thin elastic plate model reveal that the rigidity of the lithosphere beneath the Scotian basin is one to two orders of magnitude lower than that of the lithosphere far from the basin. This weakening arises from the thermal blanketing effect of the thick sediments and temperature-dependent rheology of the lithosphere, and it would facilitate initiation of subduction of the oceanic lithosphere at Scotian basin if the continental and oceanic lithospheres decouple at the hinge of the ocean-continent boundary.

The Elastic Properties of the Lithosphere Beneath Scotian Basin

Ying Zheng and Jafar Arkani-Hamed

Earth and Planetary Sciences, McGill University, Montreal, Quebec, Canada

Published in Tectonophysics 344, 137-156, 2002 (Appendix B)

4.1 Abstract

To assess the possibility that the North Atlantic ocean may subduct at Scotian basin east of Canada, we investigate the present compensation state of this deep basin. A Fourier domain analysis of the bathymetry, depth to basement and observed gravity anomalies over the oceanic area east of Nova Scotia indicates that the basin is not isostatically compensated. Moreover, the analysis emphasizes that in addition to the sediments, density perturbations exist beneath the basin. The load produced by the sediments and these density perturbations must have been supported by the lithosphere. We simulate the flexure of the lithosphere under this load by that of a thin elastic plate overlying an inviscid interior. It is shown that a plate with a uniform rigidity does not adequately represent the lithosphere beneath the basin as well as the oceanic lithosphere far from the basin, rather the rigidity of the lithosphere directly beneath the basin is about one to two orders of magnitude smaller than elsewhere. We relate this weakening to the thermal blanketing effects of the thick sediments and the fact that the lithosphere has a temperature dependent rheology. We suggest that this weak zone would have a controlling effect on the reactivation of normal faults at the hinge zone of the basin, that were formed during the break-up of Africa and North America and were locked in the early stages after the break-up. The weak zone would facilitate reactivation of the faults if tensional stresses were produced by possible reorientation of the spreading direction of the North Atlantic Ocean in the future. The reactivation of the faults would create a free boundary condition at the hinge zone, allowing further bending of the lithosphere beneath the basin and juxtaposition of this lithosphere to the mantle beneath the continent. This may provide a favorable situation for initiation of slow subduction due to subsequent compressional forces.

Keywords: Scotian basin, Initiation of Subduction, Rigidity of lithosphere, gravity anomaly modeling, Thermal weakening of lithosphere.

4.2 Introduction

Sedimentary basins of passive continental margins have been investigated for both tectonic importance and petroleum potential. The origin of the basins is tied to the rifting of the continents and spreading of the oceanic floor. Investigation of the role of the lithosphere, at the earlier stages of extension that resulted in marginal-basin sites and at the later stages when the basins are thickly sedimented, is part of an attempt to understand the initiation of subduction. Gravity and bathymetry relationships have been used to study the compensation state of sedimentary basins (e.g., McNutt, 1980; Zuber et al. 1989; Pilkington, 1990). It is concluded that sedimentary loads are usually compensated on a regional scale, i.e., they are largely supported by the elasticity of the lithosphere. Thin elastic plate models have been employed to investigate the compensation state through the flexure of the lithosphere (Cloetingh, 1982; Cloetingh et al., 1982; Beaumont et al. 1982; Erickson, 1993). Sediments are treated as loads on an elastic plate that overlies a high-density fluid mantle. The extent to which the lithosphere can support the loads is determined by its flexural rigidity, or equivalently its elastic thickness. Most authors have considered constant rigidity plates (Brotchie and Silvester, 1969; Caldwell et al. 1976; Menke, 1981; Cloetingh, 1982; Erickson, 1993). However, weakening of the lithosphere beneath the basins due to thermal blanketing effect of thick sediments must be taken into account for a more realistic modeling of the lithospheric response to sedimentary loads.

The Scotian basin off Eastern Canada is a mature marginal basin with the thickest sediment on the eastern margin of North America. The thermal evolution and subsidence history of the basin have been studied intensively (Beaumont et al. 1982; Keen and Beaumont, 1990; Ghods and Arkani-Hamed, 1998). Beaumont et al. (1982) and Keen and Beaumont (1990) employed thermo-mechanical models, taking into account time-dependent temperature and rigidity. We first investigate the compensation state of the lithosphere in Scotian basin using more recent gravity, bathymetry and depth to basement data. We then model the lithosphere by a thin elastic plate with laterally varying rigidity that is subjected to sedimentary load and the load associated with density perturbations in the lithosphere. The plate overlies a fluid mantle of higher density. We show that the lithosphere must be weaker beneath the basin to explain the observed basement topography. This weakening is related to the blanketing effect of the sediments on the thermal state and thus the rigidity of the lithosphere.

4.3 Geological Setting

The study area includes the rifted margin off Nova Scotia, the transform margin of Grand Banks, the Scotian basin and surroundings (Figure 1). The Scotian basin, located southeast of Nova Scotia, extends from east of Georges Bank to the central Grand Banks, a distance of about 1200 km and has an area of about 300,000 km². It is a part of a system of basins extending from the southeastern United States

to northern Baffin Bay, developed in Mesozoic and Cenozoic time during the initial rifting of Pangaea and seafloor spreading of the Atlantic Ocean (Keen and Piper, 1990; Keen et al. 1990). The continental rifting that created the passive continental margin off Nova Scotia started about 200 m.y. ago (Beaumont et al. 1982; Keen and Piper, 1990; Keen et al. 1990) and final separation between Africa and Nova Scotia occurred in the early Middle Jurassic. During the rifting period of about 20 m.y. and more importantly after the break up of the continent and initiation of sea floor spreading the basin subsided, allowing both syn-rift and post-rift sediments to accumulate (Keen and Beaumont, 1990; Wade and McLean, 1990). The sediment thickness increases rapidly across the hinge zone (which is the zone of normal faulting that separates the basin from the "coastal plain"), delineating the strong thinning of the continental crust beneath the thickest sediments oceanward of the zone.

4.4 Modeling the Observed Gravity Anomalies

Offshore exploration in the study area has been conducted intensively over the last three decades. Geophysical and geological data such as gravity, magnetic, and sediment lithology provide good constraints on the lithospheric models (Keen and Piper, 1990). In this section we model the observed gravity anomalies using bathymetry and depth to basement data. The bathymetry data are extracted from ETOPO5 (NGDC) and the depth to basement data are obtained from Atlantic Geoscience Center (Oakey and Stark, 1995). The observed gravity data consist of Bouguer gravity anomalies determined on the basis of surface gravity measurements on land and the offshore free-air gravity anomalies extracted from Geosat data (National Gravity Data Base, Geomatics, Canada, and Sandwell and Smith, 1997). The original data were in terms of latitude, longitude and the value, and were not uniformly distributed. We therefore gridded the data over 256×256 grid points of 6 km intervals to carry out data analysis in the Fourier domain. We also fill the gaps between the two sets of gravity data by 2-D interpolation. A gravity value in a gap is determined by weighted averaging of the surrounding values using the circular Hanning function for weighting,

$$W(r) = 0.5[1 + \cos(\frac{\pi r}{R})], \quad (4.1)$$

where r is the distance from the grid point and R (=18 km) is the radius of the filter. Although the maps present the most dense gridded data over the entire area, the irregular spacing and many small gaps of the original gravity measurements on land do not allow resolution of wavelengths shorter than 30 km (Zheng and Arkani-Hamed, 1998). These wavelength components are dominated by noise and thus regarded as useless. We filtered out these short wavelength components by Fourier transforming the data and applying a low-pass filter. The mean value of the gravity anomaly map is also removed, since we are concerned with the gravity anomalies. Figure 2 shows

the resulting gravity anomaly, bathymetry, and depth to basement maps, referred to as observed maps hereafter. The depth to basement map delineates the depth to the top of the oceanic basaltic crust. The depth is set to zero on land. Along the rifted Scotian margin and the transform margin of the Grand Banks, positive gravity anomalies exist along the shelf edge. The anomalies vary in amplitude from about 20 mGal southeast of the southern tip of Nova Scotia to over 100 mGal southeast of Sable Island (see Figure 1 for the locations referred to in this paper). Flanking this positive anomaly are gravity lows near the foot of the continental slope and on the inner and middle shelf. The New England seamounts in the southwest part of the study area have strong positive gravity anomalies up to about 150 mGal.

To interpret the observed gravity anomalies it is required to take into account the contributions from water, sediments, crust, mantle, and possible density perturbations within sediments, crust and mantle. Following the first order linear perturbation theory, we first construct a simplistic 3-D density model on the basis of the depth to basement and bathymetry (hereafter called the layered model) and regard this as a first order approximation to a viable density model. We then determine perturbations to this first order model such that the combination of this model and the perturbations produces a viable model that gives rise to the observed gravity anomalies. This is permissible because of the linear relationship between the density distribution and the gravity anomalies that allow superposition of the density of the simplistic model and the density perturbations. This layered model consists of 4 different layers of varying thickness: a water layer of density 1000 kg/m^3 , a sediment layer with a depth dependent density, a crustal layer, and a mantle layer of density 3300 kg/m^3 . The crustal layer consists of a continental crust with a mean density of 2800 kg/m^3 and an oceanic crust with an average density of 2900 kg/m^3 . The mean density of the thinned continental crust beneath the continental shelf is probably somewhat higher than the mean density of the continental crust, since it largely consists of the lower crustal material. This is because, prior to rifting the continent was most likely uplifted and the low-density upper continental material were mainly removed by surface erosion. We use the average of the continental and oceanic crust density for the density of the thinned continent crust. The upper parts of the sediment layer has a lower density due to its appreciable porosity. The sediment density is determined using the porosity data at Scotian basin. The porosity ϕ decreases exponentially with depth,

$$\phi = \phi_0 \cdot e^{-cz} \quad (4.2)$$

where ϕ_0 ($= 60\%$) is the porosity at the top of the sediments, z is depth from the top, and c ($=0.55/\text{km}$) is the inverse of the characteristic length of the porosity decay with depth (Dehler and Keen, 1993). The sediment density ρ_s is calculated by

$$\rho_s = \phi \rho_w + (1 - \phi) \rho_g \quad (4.3)$$

where ρ_w and ρ_g are the densities of water and the sediment grain, respectively (Sclater and Christie, 1980). We adopt two different procedures to estimate : 1) Bearing in mind that sediments are the result of erosion of the upper continental crust and that their grain density must be similar to that of the upper crustal rocks, we assume a ρ_g value of 2700 kg/m^3 which is the mean density of granitic rocks to represent the density of sediment grains, and 2) we test this value based on matching the gravity anomalies of our simplistic model to the observed anomalies (see below). The depth to the Moho for the continent is set to 35 km, which is the average Moho depth obtained from seismic measurements (Keen and Potter, 1995). The depth to the Moho for the ocean is determined by adding 7 km, the average thickness of the oceanic crust, to the depth to basement. The depth to basement map is smoothed before calculating the depth to the Moho, so that small scale features such as the New England seamounts are not reflected in the depth to the Moho. These features are most likely supported by the rigid crust with minor flexure and introduce only minor undulation at the Moho. The ocean-continent transition zone of the Moho is not well defined from seismic velocities and other geophysical data. We calculate the Moho depth beneath the transition zone by a 2-D interpolation between the continental and oceanic Moho depth. The total thickness of the layered model is 35 km and the major characteristics of the model are similar to those of Beaumont et al. (1982).

The gravity anomaly of the layered model is calculated by dividing the model into 1-km-thick horizontal sublayers with laterally varying density. The sublayers are thin enough so that density can be assumed vertically constant within a given sublayer, but it varies laterally to take into account segments of different material (mantle, crust, sediments, and water) within a given sublayer. The boundary between two different materials in a given sublayer usually does not coincide with our grid points. We use linear interpolation of the densities of adjacent materials to determine the density of the grid point. The gravity anomaly of the model is determined by adding the gravity anomaly of each sublayer,

$$\mathbf{g}_{\mathbf{u},\mathbf{v}}(\mathbf{z}) = 2\pi G \frac{e^{-kz}}{k} \sum_{n=1}^N (e^{-kd_n} - e^{-kd_{n-1}}) \quad {}^n\rho_{\mathbf{u},\mathbf{v}}; \quad k = (u^2 + v^2)^{1/2} \quad (4.4)$$

where z is the observation altitude, which is set to zero at the sea level, N ($=35$) is the total number of sublayers, d_n is the depth to the top of the n^{th} sublayer, and ${}^n\rho_{\mathbf{u},\mathbf{v}}$ is the Fourier transform of the density of that sublayer. u and v are wavenumbers in the x and y directions and k is the 2-D wavenumber. Before applying the Fourier transform, the mean density of each sublayer is removed and the density near the boundaries of each sublayer is gradually tapered to zero at the boundaries using the 1-D version of the above Hanning function, to avoid Gibbs ringing. We note that the gravity anomalies of the layered model are consistently lower than the observed ones in the oceanic region, despite the fact that we remove the mean density of each sublayer before calculating its gravity field and also remove the mean of the observed

gravity anomaly map. This systematic difference is most likely due to the fact that we have to use two different gravity data sets. On the continent we use the Bouguer gravity data derived from gravity measurements on land, and on the ocean we use the Geosat data. These two data sets do not have a common zero level. A gravity anomaly map reflects the lateral variations of the gravity field. It does not provide information about the average gravity field, since the observed anomalies do not include the regional mean value. A constant level shift is usually made to the model anomalies in comparing them with the observed ones. The dimension of Scotian basin is small and its gravity field must have little effect on the observed anomalies in the far southeast region as clearly seen in Figure 2a where the anomalies have a negligible mean value. Therefore, we adjust the gravity anomalies of the layered model to have a near zero mean value over the far southeast region in order to compare them with the observed anomalies over the oceanic area, the area of primary concern in this paper.

We calculate gravity anomaly maps of the layered model for 8 different density models in order to determine a density model that minimizes the misfit between the observed and model gravity anomalies. Figure 3 shows the resulting gravity anomalies along profile CC' (see Figure 1 for the location of the profile), as a representative profile. The gravity anomalies are level shifted to near zero values at the right hand side far from the basin. Although no one particular density model explains the observed gravity over the entire length of the profile, many of the model gravity profiles are very close to the observed one over the major part of the basin. The main disagreement between the observed and modeled anomalies occurs over continent and continental shelf. The observed Bouguer anomalies over the continent reflect the lateral density variations in the continental crust. Such variations are not included in our layered model. We select model 1 with sediment grain density of 2700 kg/m^3 and the thinned continental crust density of 2850 kg/m^3 for the density structure of our nominal 3-D layered model, since it seems to explain the observed gravity profile somewhat better than the others.

Figure 4 shows the observed and the nominal layered model gravity anomalies along four profiles seen in Figure 1. The model profiles are vertically shifted to near zero values at the right hand side far from the basin. Also included in the figure are the bathymetry, basement and Moho profiles to illustrate the crustal structure beneath. The profiles span almost the entire extent of the basin and provide a good estimate of the general properties of the basin. The major disagreement between the observed and modeled anomalies occurs over continent and continental shelf, as mentioned above. Over the oceanic area, the observed and model profiles have similar features. They decrease rapidly oceanward from the shelf edge and attain minima in the eastern part of Scotian basin, and gradually increase eastward of the basin. However, the misfit of the model anomalies to the observed ones differ among the profiles, emphasizing that the nominal layered model explains major characteristics of the crust but fails to represent local variations, as expected. Figure 5a shows the

gravity anomaly map of the nominal model, and Figure 5b displays the differences between the observed and model gravity anomalies (observed-model). The model anomalies are lower than the observed ones over Scotian basin. However, they are in good agreement over the featureless regions in the southeast.

We also calculated the gravity anomalies of a model identical to the nominal model except that the sediment is taken to be non-porous having a constant density of 2700 kg/m³. Figure 4 includes the gravity profiles of this model for comparison. Using the constant sediment density has minor effects on the resulting gravity anomalies. This is expected, because the porosity of the upper parts of sediments produces a surface layer parallel to bathymetry where density varies across the depth of the layer but not along the layer. It changes the mean density of the upper sublayers much more than introducing lateral density variations in those sublayers, except near the shelf edge where bathymetry has an appreciable slope. However, the total thickness of the sediments exceeds 10 km in this region and the porosity has minor effects on the total mass of a given sedimentary column there.

We now seek local density perturbations required to add to the nominal model in order to explain the observed gravity anomalies. The difference between the observed and the nominal model gravity anomalies must arise from some density perturbations that were not included in the model. For example, no salt layers, diapiric intrusives that likely occurred during continental rifting, and small scale tectonic features associated with the initial rifting are taken into account in the nominal model. Another plausible source of misfit between the observed and modeled gravity anomalies is the variations of the crustal thickness. We use a mean crustal thickness of 35 km for the continent, by assuming a flat Moho beneath. The depth to the actual Moho more likely varies from place to place by a few km. The thickness of the oceanic crust is taken to be 7 km in the nominal model for the entire oceanic area. Although the oceanic crust does not vary in thickness as much as the continental crust, variations of about 1 km are quite common and are sufficient to explain the misfit over the oceanic area. Here we adopt the simplest model to estimate these density perturbations. Bearing in mind that the gravity anomalies provide information about the lateral variations of the vertically integrated density perturbations, we seek vertically averaged density perturbations within our layered model of thickness H_c ($= 35$ km). The density perturbations $\delta\rho$ are determined using (e.g., Zheng and Arkani-Hamed, 1998),

$$\delta\rho_{u,v} = \frac{ke^{kz}}{2\pi G(1 - e^{-kH_c})} \Delta\mathbf{g}_{u,v} \quad (4.5)$$

where $\Delta\mathbf{g}_{u,v}$ and $\delta\rho_{u,v}$ are the Fourier transforms of the gravity anomaly difference (observed minus the level shifted model) and the density perturbations, respectively. Again z is set to zero at the sea level. The density perturbations thus determined (Figure 5c), together with our simplistic nominal model, give rise to the observed

gravity anomalies. Over the oceanic area, small-scale features of the density perturbations mimic those of the observed gravity anomalies, especially where the layered model's gravity is smooth. At about 100 km towards the ocean, there are positive density perturbations required to add to the nominal model in order to produce the observed gravity anomalies. The density perturbations are on the order of 100 kg/m^3 . The total mass perturbations associated with these density perturbations, i.e. the density perturbations times the thickness of the layered model, are equivalent to an excess oceanic crustal thickness of about 1.2 km.

It is required to assess whether the improved 3-D layered model, the nominal model plus the density perturbations thus obtained, is in local equilibrium or it requires regional support. For this purpose, we calculate the pressure $\mathbf{P}(\mathbf{x}, \mathbf{y})$ at the base of the nominal model by

$$\mathbf{P}(\mathbf{x}, \mathbf{y}) = \int_0^{H_c} g\rho(z)dz \quad (4.6)$$

where $\rho(z)$ is the density at a depth z (density of the nominal model plus the density perturbation) and g is the gravitational acceleration. The results (Figure 5d) show appreciable lateral variations of the pressure, emphasizing that the entire structure is not in equilibrium. The pressure in the central part of the basin is $\sim 50\text{-}60$ MPa more than its surroundings. This is equivalent to the pressure of a sedimentary column of thickness 1.8-2.2 km, about two times the pressure created by the density perturbations alone. This emphasizes that not only the density perturbations, but also a part of the sediments must have been supported by a rigid lithosphere beneath.

4.5 Support Mechanism

Elastic plate models have been used to model the flexure of the lithosphere due to loads associated with surface topography, trenches, seamounts, and passive continental margins (e.g. Caldwell et al., 1976; Lambeck and Nakiboglu, 1980; Lago and Cazenave, 1981; Cloetingh, 1982; Forsyth, 1985; McNutt et al, 1988; Zuber et al., 1989; Erickson, 1993). These studies suggest that the oceanic lithosphere respond to sedimentary loads as a thin elastic plate overlying a fluid-like asthenosphere of higher density. It was demonstrated above that Scotian basin must be supported by a rigid lithosphere. Here we adopt a 2-D thin elastic plate model to estimate the rigidity required for the lithosphere. The undeformed plate is taken on the horizontal x, y plane with an infinite y dimension. It flexes in the z direction under the load consisting of the sediments, the lateral variations of mass associated with the density perturbations, and the overlying water. The water column is added to the bathymetry by calculating the equivalent rock bathymetry. The equivalent rock bathymetry in the ocean is determined by replacing a water column of density 1000 kg/m^3 by an equivalent rock column of density ρ_g while conserving the total mass of

the column, and adding this equivalent rock thickness to the bathymetry. It is set to zero on land to be compatible with the Bouguer gravity anomalies there.

Figure 6 shows the equivalent rock bathymetry, basement topography and density perturbations along the four profiles seen in figure 4. The profiles are stacked to the reference point at which the depth to basement of each profile is a maximum. The differences among the profiles indicate effects of local variations. The profiles present major characteristics of the basin that we are interested in. From west to east the thickness of the equivalent-sediments, i.e. the column between the equivalent rock bathymetry and the basement, increases very rapidly as we enter the thinned continental shelf, achieving a maximum of about 16 km. The thickness then gradually decreases toward the younger parts of the ocean, remaining almost constant at about 3 km at distances farther than about 800 km from the basin. Except very close to the continent, the density perturbations are positive and add to the sediment load. However, the over all amplitude of the perturbations are $\sim 50 \text{ kg/m}^3$, i.e., the mass perturbations $\sim 1.75 \times 10^6 \text{ kg}$ for the entire thickness of 35 km. This is equivalent to an extra $\sim 0.6 \text{ km}$ sediment, which is very small compared to the thickness of the equivalent sediment. We average these profiles to obtain representative profiles of the equivalent rock bathymetry, basement topography and density perturbations, which have been further smoothed to suppress the effects of detailed local features. These averaged profiles will be used in the following calculations.

We assume that the basement profile relative to the reference depth of the oceanic crust far from the basin is the resulting flexure of the plate. This is a first order approximation that does not account for the initial topographic features which were most likely created during the initial rifting, such as rift valleys. These topographic features are usually small scale features compared with the broad depression of the basin that has been resulted from the deflection of the lithosphere under the sedimentary load. The governing equation of the deflection w of a thin elastic plate model under a surface load is (Turcotte and Schubert, 1982)

$$\frac{d^2}{dx^2} \left(D \frac{d^2 w}{dx^2} \right) + P \frac{d^2 w}{dx^2} + \rho_m g w = q(x). \quad (4.7)$$

P is the horizontal force and D is the flexural rigidity of the plate defined by

$$D = \frac{E h^3}{12(1 - \nu^2)} \quad (4.8)$$

where E ($= 8 \times 10^{10} \text{ Pa}$) is Young's modulus, ν ($= 0.25$) is Poisson's ratio, and h is the thickness of the plate. $q(x)$ denotes the surface load. We treat the equivalent-sediments and the excess mass associated with the density perturbations as surface loads on the elastic plate model,

$$q(x) = \left[\int_0^{H_s(x)} \rho_s dz + \delta\rho(x)H_c \right] g, \quad (4.9)$$

where $\rho_s(z)$ is the depth dependent density of the equivalent sediment, $\delta\rho(x)$ denotes the vertically averaged density perturbations and $H_s(x)$ is the thickness of the equivalent-sediment at x .

It is desirable to pose equation (7) as an inverse problem and determine the lateral variations of the rigidity of the plate using the known load function $q(x)$ and the basement topography as the deflection w . However, this is not possible because of the singularities arising at the inflection points where the deflection curve changes from concave to convex, allowing its curvature to become zero. At these points d^2w/dx^2 vanishes and the rigidity term in Equation (7) disappears. Therefore, we solve equation (7) by the forward method, using several rigidity values and comparing the resulting deflection with the basement profile in the ocean to determine the best rigidity estimate. A reasonable value for P that represents the ridge push has minor effects on the deflection, as also concluded by Caldwell et al. (1976). Therefore, P is set to zero. Also we impose pinned boundary conditions at both ends, i.e., $w = 0$ and $dw/dx = 0$. The normal faults, likely produced at the hinge zone during continental rifting, may lock by 10-20 m.y. (Karner and Watts, 1982). In reality, the normal continental lithosphere west of the hinge zone is also deflected by the sedimentary load of the basin because of its coupling to the thinned continental lithosphere directly beneath the basin. However, the depth-to-basement profiles show that the possible deflection is very small (see Figure 6). Erickson (1993) used two different models to investigate the deflection of the lithosphere beneath Scotian basin: an infinite plate of constant rigidity 1.92×10^{23} Nm; and two semi-infinite layers: one for the continent with a rigidity of 1.56×10^{25} Nm, and the other for the ocean with a rigidity of 9.8×10^{22} Nm. The first model showed an unrealistically large deflection of the normal continental lithosphere. The second, his most favored model showed a maximum deflection of about 3.5 km which is still about a factor of 3 more than the observed one (see Figure 2 of Erickson, 1993). This indicates that the normal continental lithosphere has even higher rigidity, and the pinned boundary is appropriate. Moreover, the very small deflection of the continental lithosphere west of the hinge zone only uniformly suppresses the entire lithosphere east of the hinge zone and has little effect on the deflection of the lithosphere directly beneath the basin relative to that of the oceanic lithosphere far from the basin that we are concerned with. Therefore, for the deflection calculations we use pinned boundary condition at the hinge zone and neglect the continental part west of the zone. We also use pinned boundary conditions at the ocean side because of the fact that the depth to the basement does not change appreciably at distances farther than about 800 km from the basin (see Figure 6). Also, the oceanic plate is extended oceanward to have a length of 1500 km, using constant bathymetry and basement topography, to make

sure that the boundary conditions at the ocean end have little effect on the relative deformation of the lithosphere beneath the basin and its immediate surroundings. We also calculate a model using free boundary conditions at the oceanic end. The resulting deflection within ~ 1000 km from the continent is almost identical to that with pinned boundary conditions (see below), ensuring that the boundary conditions have little effect within this distance. The effect of the pinned boundary conditions is appreciable within about 300 km from the boundary, where the deflection gradually goes to zero at the boundary. For the free boundary, the deflection remains almost constant at distances farther than 1000 km from the continent. Therefore, we will show the deflection results up to 1000 km distance from the hinge zone in the following figures.

The vertical load on the plate arises from the sediments depicted in our layered model and the density perturbations determined above. We note that it is possible for the lower parts of the sediments inside the basin to become rigid and thus support part of the load of the overlying sediments. However, the lower parts are confined to the basin and do not produce an extended plate. Therefore, the weight of the lower parts as well as that of the overlying sediments must eventually be supported by the oceanic plate, regardless of the rigidity of the lower parts. We also note that we adopted the simplest model for the density perturbations, by assuming that the perturbations are confined within a flat layer of 35 km thickness and have a vertically uniform distribution. The exact location of the perturbations cannot be constrained on the basis of the gravity anomaly analysis alone. They may be due to density variations in the sediments, in the crust, and/or in the upper parts of the mantle. Therefore, we consider two possibilities by either including or excluding them as a part of the load exerted on the plate. Including them implies that they are located somewhere inside the sediments, the crust, or the upper mantle where they are strongly coupled to the lithosphere. Excluding them implies that they are in the asthenosphere and are not coupled to the lithosphere.

We first examined a suite of elastic plate models with constant rigidity, ranging from 10^{20} to 10^{23} Nm and above mentioned boundary conditions (Figure 7a). We note that the x axis of Figure 7 is shifted eastward by 100 km relative to that of Figure 6 to allow the hinge zone, the pinned boundary, to coincide with $x = 0$. We also note that the continent-ocean topographic dichotomy of Earth, that continents are on the average 5 km above the ocean floors arises because the thick and low-density normal continental crust is essentially in isostatic compensation on a global scale with the thin and denser oceanic crust. This essentially explains the difference between the depth to basement profiles shown in Figure 6 and that shown in Figure 7a. Figure 6 is relative to the surface of the normal continent west of the hinge zone that is set at sea level in the process of calculating the Bouguer anomalies on land, as mentioned before. By matching the observed depth to basement profile to the deflection profiles of the models far from the basin in Figures 7a, we have essentially removed this dichotomy and focused on the deflection of the lithosphere beneath the basin relative

to that far from the basin. For high rigidity values the resulting basin is shallower and has a much smaller slope near the hinge zone compared to the observed one. However, as the rigidity decreases, the model basin approaches the observed one. Note that the deflection of the plate at regions far from the basin remains almost unchanged while the plate rigidity is reduced from 10^{23} to 10^{20} Nm, corresponding to elastic thicknesses of 24.1 to 2.4 km. This is because the load function over this region is dominated by very long wavelength components compared to these elastic thicknesses, and the plate behaves as a non-rigid plate, allowing the load to become isostatically compensated. Therefore, the rigidity of this region cannot be constrained. This point was demonstrated by Turcotte and Schubert (1982) who calculated the deflection of an elastic plate under a sinusoidal surface load. This is also the main reason that the boundary conditions at the oceanic end do not affect the deflection of the lithosphere farther than about 300 km from the boundary. The deflection of the plate with a constant rigidity of lower than about $\sim 10^{22}$ Nm (elastic thickness less than 11.2 km) explains the observed depth to basement over the entire profile. However, due to the unconstrained nature of the rigidity of the region far from the basin, such a constant rigidity plate model may not be adequate for this region. In fact the normal oceanic plate older than about 50 m.y. is much stronger (see Figure 9). The oceanic lithosphere requires a rigidity of about 2.4×10^{23} Nm to support Hawaiian islands, and the oceanic lithosphere near the Mariana trench is estimated to have a rigidity of 1.4×10^{23} Nm (Turcotte and Schubert, 1982). On the other hand, a constant rigidity plate model representative of the oceanic lithosphere far from the basin, with a rigidity of $\sim 10^{23}$ Nm or more, does not represent the lithosphere beneath the basin. Both models of Erickson (1993) resulted in much wider basins than the observed one. The thinned part of the continental lithosphere and the older part of the oceanic lithosphere beneath Scotian basin are overlain by thick sediments. These regions are most likely weakened by the thermal blanketing effects of the sediments (see below), and are most likely weaker than the normal oceanic lithosphere.

To incorporate the thermal blanketing effect, we consider two-segmented plate models with a weaker zone beneath the basin. By varying two parameters, the width of the weak zone and the rigidity of the lithosphere beneath this zone, we investigate the major characteristics of the plate deflection and determine a range of acceptable models. Figure 7b shows the deflection of a plate with a fixed width of 500 km but several rigidity values for the weak zone, and a fixed rigidity of $\sim 10^{23}$ Nm for the oceanic lithosphere farther than 500 km. The weak zone rigidity values of less than 10^{22} Nm are good representatives of the lithospheric rigidity beneath Scotian basin, implying that thermal blanketing might have reduced the rigidity of the lithosphere by at least one order of magnitude. To illustrate the effect of the weak zone size on the plate deflection, we note that the equivalent sediment thickness decreases very rapidly from ~ 16 km beneath the shelf edge to ~ 5 km at about 400 km from the continent, and then decreases slowly from there on (see Figure 6). This suggests that the thermal blanketing effect is more important within 400 km from the continent.

Figure 7c shows the deflection of a plate with the weak zone widths of 500, 400, 300 and 200 km. The plate rigidity is 10^{22} Nm beneath the weak zone and 10^{23} Nm outside the zone. The plate deflection slightly decreases with the decrease of the weak zone width, but the difference is very minor for the weak zone widths of 400 to 500 km. It becomes noticeable for the width of 200 to 300 km. Figures 7b and 7c show that models with a weak zone width of 300-500 km and the lithospheric rigidity of 10^{21} - 10^{22} Nm (elastic thickness of 5-11 km) explain the observed basement profile almost equally. We will use the lithospheric model with a 500 km wide weak zone of 10^{22} Nm rigidity, and 10^{23} Nm rigidity outside the zone in the remaining part of the paper.

We also consider the possibility that the density perturbations reside in the mantle and do not couple to the overlying elastic lithosphere, by removing the contribution of the density perturbations from the surface load function. Included in Figure 7c is the resulting deflection of the plate model with a weak zone of 500 km width and 10^{22} and 10^{23} Nm rigidity beneath the weak zone and elsewhere, respectively. The deflection is slightly less than that of the corresponding model with density perturbations included. This is expected because of small mass associated with the density perturbations compared to the entire mass of an equivalent sediment column, as mentioned earlier.

4.6 Strength of the Lithosphere

During continental rifting the surface topography was most likely supported dynamically. Immediately after continental break-up and the initiation of sea-floor spreading the surface subsided mainly because of thermal contraction as the hot thinned part of the continental lithosphere and the newly formed hot oceanic lithosphere cooled very rapidly. Subsidence was further enhanced by sedimentation which occurred largely on the thinned continental shelf east of Nova Scotia, resulting in a deep basin with a present sedimentary thickness of about 16 km, whereas the thickest sediments on the oceanic crust are only about 7 km (Ghods and Arkani-Hamed, 1998). The thermal evolution of the Scotian basin has been studied intensively by Royden and Keen (1980), Beaumont et al. (1982), Keen and Beaumont (1990), and Ghods and Arkani-Hamed (1998). In particular Keen and Beaumont (1990) examined both thermal and mechanical subsidence of elastic plate models with time-varying rigidity and sedimentary load. In the absence of sediments, the thermal subsidence of the oceanic lithosphere must be more than that of the thinned continental shelf, partly because of higher initial temperature of the oceanic lithosphere, and partly because the oceanic crust and the mantle beneath are denser than the adjacent continental crust.

Here we first assess the early stages of subsidence of the basin due to sedimentary load. Adding subsidence due to thermal contraction will have minor effect on the deflection of the thinned continental shelf relative to that of the oceanic lithosphere. It will only deepen the oceanic part to some extent because of the larger thermal

subsidence of the oceanic lithosphere compared with that of the continental lithosphere. In the early stages of cooling both the thinned continental lithosphere and the newly formed oceanic lithosphere are hot and may not be very different mechanically. Therefore, we model both by a single plate with a constant density of 2900 kg/m³ but with varying rigidity. The plate is overlain by sediments with a constant density of 2700 kg/m³ and varying thickness, and is underlain by an inviscid mantle of density 3300 kg/m³. The model plate extends from the undeformed part of the continent, approximated by the hinge zone, to the oceanic ridge axis that recedes from the continent with time. We assume that the plate has a length that increases by 10 km every m.y., corresponding to a sea floor spreading of 1 cm/year. Also we adopt a sedimentation rate of 1 km per 10 m.y. in the early stages, as observed over this region (Gradstein et al., 1990). The model plate is pinned to the continent but it is free at the oceanic ridge axis. The sedimentary load is assumed to linearly decrease from a maximum at the continent side to zero at the ridge axis. The rigidity of the plate is mainly controlled by the thickness of its elastic core, which itself depends on the thermal state of the plate and the stress differences applied. We study these interconnected relationships through forward modeling. First we calculate the thermal evolution of the plate using the conventional half-space cooling model of the oceanic lithosphere (Turcotte and Schubert, 1982),

$$\frac{T - T_s}{T_m - T_s} = \operatorname{erf}\left(\frac{z}{2\sqrt{\kappa x/u}}\right) \quad (4.10)$$

where T_s ($= 0^\circ\text{C}$) is the surface temperature, T_m ($= 1350^\circ\text{C}$) is the temperature at the ridge axis and beneath the plate. u ($= 10$ km/m.y.) is the spreading rate, and x and z denote the horizontal and vertical coordinates, respectively. x is measured from the ridge axis. κ ($= \frac{K}{\rho c}$) is the thermal diffusivity, where K ($= 3.1$ W/m/K) is the thermal conductivity and c ($= 1250$ J/kg/K) is the specific heat.

We then determine the strength envelope of the model plate. The near surface brittle portion of the plate is governed by Byerlee's law (Byerlee, 1978; Brace and Kohlstedt, 1980), and the deeper ductile portion obeys the creep law. The creep law for differential stresses less than 200 MPa is

$$\dot{\epsilon} = A\sigma^n \exp(-Q/RT) \quad (4.11)$$

where Q is the activation energy, R is the universal gas constant, σ is the differential stress, $\dot{\epsilon}$ is the strain rate, T is the temperature, and A is the pre-exponential constant. For the crust we use Maryland diabase rheology after Caristan (1982), with $A = 6.12 \times 10^{-2}$ MPa^{- n} s⁻¹, $n = 3.05$, and $Q = 276$ kJ/mol. For the mantle, the dry olivine rheology of Goetze (1978) is adopted, with $A = 7 \times 10^4$ MPa^{- n} s⁻¹, $n = 3$, $Q = 510$ kJ/mol. For differential stresses greater than 200 MPa, the creep law is

$$\dot{\epsilon} = A \exp\left[-\frac{Q}{RT}\left(1 - \frac{\sigma}{8500}\right)^2\right] \quad (4.12)$$

Again we adopt the dry olivine rheology for the mantle after Goetze (1978), with $A = 5.7 \times 10^{11} \text{ MPa}^{-n} \text{ s}^{-1}$ and $Q = 535 \text{ kJ/mol}$. The strain rate adopted is 10^{-18} s^{-1} (Cloetingh, 1982). A higher strain rate of 10^{-16} s^{-1} has been used by Watts et al. (1980) and McAdoo and Sandwell (1985). Adopting this higher strain rate will increase the strength by a factor of 4.6. Figure 8 shows the compressional and tensional strength envelopes of the plate under a given point at several times after the breakup. The elastic core is sandwiched between the upper brittle and the lower ductile parts with a thickness determined by the stress differences applied. The elastic thickness is determined from the compressional strength by setting the stress differences equal to the sedimentary load at that point. It rapidly increases in the first 10 m.y. and then increases monotonically but with a decreasing rate (Figure 9). Similar results were obtained by Cloetingh (1982). The elastic rigidity is determined through Equation (8) with the elastic thickness h thus obtained. The rigidity of a given plate substantially decreases towards the ridge axis. For example it decreases by a factor of about 50,000 from the hinge zone to the ridge axis in a 50 m.y. old plate.

In the final step, we determine the deflection of the plate with varying rigidity under the linearly decreasing surface load by solving Equation (7) subject to the above mentioned boundary conditions, i.e., the plate is pinned to the continent but is free at the ridge axis. Figure 10 shows the resulting deflection for several plates of different lengths corresponding to their ages. The similarity of the deflection profiles of these simplistic models to the basement profile of Scotian basin near the hinge zone emphasizes that the oceanic and continental lithospheres beneath the basin have been welded since very early in the history of the basin as also suggested by Karner and Watts (1982), and that major deflection in the basin is more likely associated with the response of the lithosphere to sedimentary loading. The distance between the pinned boundary and the maximum deflection zone of the models increases with the age of the plate. It reaches $\sim 170 \text{ km}$ by 50 m.y., which is $\sim 70\%$ farther than the distance observed in the basin (see figure 7). The major part of the deflection in the Scotian basin has occurred within the first 70 m.y., with a much higher rate in the early stages (Gradstain et al., 1990; Keen and Beaumont, 1990) and the lithosphere has become strong by this time (Cloetingh, 1982). The deflection amplitude of the model plates and the slope of the deflection near the hinge zone increase with the increase of the sediment thickness and length of the plates. However, the maximum deflection for the plate at 50 m.y. age is less than 20% of the maximum observed deflection of Scotian basin. The model plate creates a basin that is much wider and much shallower than Scotian basin. Comparison of Figures 7 and 10 emphasizes that the lithosphere beneath the basin has been weaker than the model plates that cooled monotonically obeying the half-space cooling criterion. The lithosphere beneath Scotian basin has

been further weakened due to the thermal blanketing effects of the sedimentary cover there.

After the break-up of the continent and initiation of sea floor spreading, the continental lithosphere beneath the shelf cools, as does the adjacent oceanic lithosphere. As time passes, the lithosphere becomes stronger and responds less to newly added sedimentary load. Modeling details of the time-varying strengthening process and dynamics of lithosphere requires extensive high-resolution stratigraphic information. Here, we estimate the blanketing effects of the sediments on the strength of the lithosphere beneath the Scotian basin using the steady state temperature condition. The temperature distribution inside an oceanic lithosphere becomes almost steady within the first 70 m.y. during which major sedimentation in the basin has occurred, as mentioned above. The steady state calculation provides a rough estimate of the thermal blanketing effects of the sedimentary cover since 70 m.y.

The steady state temperature distribution T in the model lithosphere is calculated by

$$K \frac{d^2T}{dz^2} = -A \quad (4.13)$$

where K is the thermal conductivity (1.88 W/m/K for sediments and 3.1 W/m/K for the crust and mantle), z is the depth measured from the top of the sediments, and A is the rate of radiogenic heat generation per unit volume, assumed to be constant in time for each layer since the age of the oceanic lithosphere in the study area is much less than the half-lives of the radiogenic elements. Three layers are considered: sediments with a thickness determined from the averaged bathymetry and depth to basement profiles, (note we use bathymetry in this calculation and not the equivalent rock bathymetry), the crust with a thickness of 7 km in the ocean and a varying thickness in the continental shelf, and the mantle down to 100 km depth assumed to be the base of the thermal boundary layer of the mantle convection beneath. We used heat generation rates of 8×10^{-8} W/m³ for the oceanic crust, 10^{-6} W/m³ for continental crust and sediments, and 2×10^{-8} W/m³ for the mantle. The temperature at the base of the lithosphere is kept at 1350°C. It is set to zero at the top of the sediments. The model is one-dimensional and no heat flow is allowed across the vertical boundaries, because the steady state horizontal temperature gradient is much smaller than the vertical temperature gradient. Detailed study of the time varying thermal evolution of Scotian basin by Ghods and Arkani-Hamed (1998) showed that horizontal heat conduction is only significant in the very early stages during continental rifting, and in the later stages only near the oceanic ridge axis. We also note that the thick continental crust with high radiogenic heat sources west of the hinge zone does not directly attach to the oceanic crust with lower radiogenic sources. Rather the continental crust gradually thins within about 180 km-wide transition zone before it is juxtaposed to the oceanic crust. The lateral heat flow from the normal continent to the ocean is substantially suppressed because of this large distance.

Figure 11 shows the temperature distribution in the model lithosphere, where depth is relative to the top of the crust, i.e. the base of the sediment column. The temperature of the lithosphere beneath the basin increases with the increasing thickness of sediments, because of the thermal blanketing due to the sediments. This temperature enhancement has strong effects on the rheology of the crust and mantle beneath. To illustrate this point we calculate the strength envelope of the lithosphere using the equivalent-sedimentary load as pressure at the surface, the temperature distribution shown in Figure 11, and the rheology models of Caristan (1982) and Goetze (1978) described before.

Included in Figure 11 are the compressional and tensional strength envelopes thus obtained. We show the absolute values for better comparison, although the stresses are positive for compression and negative for tension. For a given stress difference, the thickness inside the strength envelope is the elastic core of the lithosphere (see Figure 8). The brittle failure is independent of temperature and rock type, but depends on pressure (Byerlee, 1968). The ductile property, on the other hand, strongly depends on the temperature and rock type (Brace and Kohlstedt, 1980). Diabase ductile rheology assumed for the crust is much weaker than dry olivine rheology used for the mantle. The vertical profiles of the strength envelopes (positive compression and negative tension) one at the maximum deflection point (~ 140 km from the continent) and another at 900 km from the continent are displayed in Figure 12 for better illustration. The profiles at the maximum deflection are multiplied by 100 in order to display them with those at 900 km. The thinned continental crust is weak compared with the upper part of the underlying mantle. The oceanic crust is much thinner, 7 km, and its strength depends on the thickness of the covering sediments. It tends to couple to the mantle and produces a competent layer where sedimentary layer is thin. However, beneath the thick sedimentary cover of Scotian basin, the crust becomes much weaker and decouples from the relatively strong upper part of the mantle. The effective rigidity of the lithosphere is more than two orders of magnitude smaller beneath the Scotian basin compared with that far from the basin, partly because of greater stress differences related to the sedimentary load and partly because of the weakening due to the thermal blanketing by the sediments. This supports our thin plate model with laterally varying rigidity. The weakening of the lithosphere beneath sedimentary basins should be regarded as a significant factor when considering the potential site for initiation of subduction at passive continental margins.

4.7 Initiation of Subduction at Scotian Basin

Despite extensive studies on plate tectonics in the last four decades, the initiation of subduction of an oceanic plate is poorly understood (e.g., Uyeda and Ben Avraham, 1972; McKenzie, 1977; Casey and Dewey, 1984; Okal et al., 1986; Cloetingh et al., 1989; Mueller and Phillips, 1991). The major driving forces, the ridge push and the negative buoyancy of the oceanic lithosphere, are not sufficient to overcome resisting

forces associated with bending of the lithosphere prior to subduction and the frictional force along the thrust fault at the subduction zone. Mueller and Phillips (1991) argued against subduction initiation at passive margins and related the initiation of subduction to congestion at preexisting subduction zones as was suggested earlier by Okal et al. (1986). Erickson and Arkani-Hamed (1993) selected Scotian basin as the most favorable place for initiation of subduction in the North Atlantic and suggested thermal weakening of the continental lithosphere beneath the basin and possible reduction of shear stresses along the subduction zone.

Faulting associated with continental rifting may lock within 10-20 m.y. after rifting (Karner and Watts, 1982). However, reactivation of normal faults in the hinge zone is more likely in an extensional setting. This reactivation almost entirely eliminates the shear forces along the thrust faults and changes the hinge zone from a locked to a decoupled, free boundary. Erickson (1993) considered the possibility that the reorientation of the sea floor spreading may produce tensional forces and break apart the basin at the hinge zone, allowing the plate to further subside at its newly formed free boundary. Kemp and Stevenson (1996) investigated the possibility that the decoupling of the oceanic and continental lithosphere produces a rift through which molten basalt from beneath intrudes and erupts, covering the oceanic plate and creating a heavy load required for the initiation of subduction.

The initiation of subduction at passive margins has also been investigated through laboratory experiments. Shemenda (1992) concluded that a pre-existing favorably oriented weak zone is required for subduction at passive margins. Faccenna et al.'s (1999) experiment showed that a passive margin may transform to an active one when the oceanic plate attains considerable negative buoyancy while it is subjected to low compressional stress over geological times.

The weak part of the lithosphere directly beneath Scotian basin in our model may facilitate reactivation of the old normal faults and thus the break up of the lithosphere if re-orientation of the spreading direction of the North Atlantic Ocean exerts sufficient tensional forces. To investigate this scenario, we let our two-segmented plate model with a 500 km wide weak zone of 10^{22} Nm rigidity break at the hinge zone by imposing a free boundary condition there. The equivalent rock bathymetry is kept unchanged, assuming that breaking of the plate and extra sedimentation occurs synchronously, i.e., sedimentation keeps pace with the fast subsidence. This assumption seems reasonable since the continental wall adjacent to the fast subsiding oceanic lithosphere may readily collapse. It is also possible that, due to the break up, extensive basaltic lava intrudes the crust and floods the sea floor as suggested by Kemp and Stevenson (1996), creating an appreciable load on the plate. The post-break subsidence is so fast that it does not allow enough time for thermal diffusion to change the thermal state of the plate during the subsidence. We therefore assume that the plate retains its rigidity during this rapid subsidence. The resulting deflection (Figure 13) is much more than that of the plate with pinned boundary at the continent side which is also included in the figure for comparison. Also displayed in Figure

13 are the deflection profiles of a plate with a uniform rigidity of 10^{23} Nm but one pinned and the other free at the continent side. The weakening of the lithosphere by thermal blanketing effect of sediments has a much stronger effect on the deflection of the lithosphere when it is pinned to the continent than when it is not.

The broken lithosphere bends and becomes juxtaposed to the mantle beneath the continent. As time passes, the lithosphere becomes weaker, because of slow heating due to thermal blanketing of the extra sediments and the lateral heat flow from the hotter and deeper parts of the adjacent continental mantle to the upper parts of the plate. This scenario leads us to conclude that the possible reactivation of the normal faults that causes rapid deflection of the oceanic plate and subsequent sedimentation may provide a favorable situation for the initiation of subduction as suggested by laboratory experiments. Low amplitude compression, such as ridge push or stresses produced due to possible reorientation of spreading of the North Atlantic Ocean, may then initiate subduction at Scotian basin.

4.8 Conclusions

Our analysis of the observed bathymetry, depth to basement and gravity anomalies over Scotian basin suggests that the basin has been supported by the elastic rigidity of the oceanic and continental lithosphere that became locked shortly after the break-up of Africa and North America and the start of sea floor spreading. Modeling the lithosphere by a thin elastic plate of laterally varying rigidity under the sedimentary load and the load produced by the lateral variations of density shows that the lithosphere is substantially weaker under the basin, by one to two orders of magnitude. We show that this reduction in rigidity may arise from thermal blanketing of the lithosphere by the thick sediments in the basin and the temperature-dependent rheology of the lithosphere. This weaker lithosphere has a tectonic importance. It can facilitate reactivation of normal faults in the hinge zone, leading to the break up of the lithosphere and initiation of subduction of the Atlantic ocean in the Scotian basin.

4.9 Acknowledgement

This research was supported by the Natural Sciences and Engineering Research Council of Canada (NSERC) grant # OGP0041245 to JAH. We would like to thank Walter Roest at Geological Survey of Canada for providing the geophysical data used in this paper, and Andrew Hynes at McGill University for discussions in the early stages of our research. We also like to thank Sonya Dehler, Jean-Claude Mareschal and an anonymous reviewer for their constructive comments.

4.10 References

- Beaumont, C., Keen, C., Boutilier, R., 1982. On the evolution of rifted continental margins: comparison of models and observations for the Nova Scotian margin. *Geophysical Journal of Royal Astronomic Society* 70, 667-715.
- Brace, W.F., Kohlstedt, D.L., 1980. Limits on lithospheric stress imposed by laboratory experiments. *Journal of Geophysical Research* 85, 6248-6252.
- Brotchie, J.F., Silvester, R., 1969. On crustal flexure. *Journal of Geophysical Research* 74, 5240-5252.
- Byerlee, J., 1968. Brittle-ductile transition in rocks. *Journal of Geophysical Research* 73, 4741-4750.
- Byerlee, J., 1978. Friction of Rocks. *Pageoph* 116, 615-626.
- Caldwell, J.G., Haxby, W.F., Karig, D.E., Turcotte, D.L., 1976. On the applicability of a universal elastic trench profile. *Earth and Planetary Science Letters* 31, 239-246.
- Caristan, Y., 1982. The transition from high temperature creep to fracture in Maryland diabase. *Journal of Geophysical Research* 87, 6781-6790.
- Casey, J.F., Dewey, J.F., 1984. Initiation of subduction zones along transforms and accreting plate boundaries, triple junction evolution, and forearc spreading centers: Implications for ophiolitic geology and obduction. In *Ophiolites and oceanic lithosphere*. Edited by I.G. Grass et al. Geological Society of London Special Publication 13, 269-290
- Cloetingh, S., 1982. Evolution of passive continental margins and initiation of subduction zones. Ph.D. Thesis. Instituut voor aardwetenschappen der Rijksuniversiteri te Utrecht, No. 29.
- Cloetingh, S.A.P.L., Wortel, M.J.R., Vlaar, N.J., 1982. Evolution of passive continental margins and initiation of subduction zones. *Nature* 297, 139-141.
- Cloetingh, S.A.P.L., Wortel, M.J.R., Vlaar, N.J., 1989. On the initiation of subduction zones. *Pure and Applied Geophysics* 129, 7-25.
- Dehler, S.A., Keen, C.E., 1993. Effects of rifting and subsidence on thermal evolution of sediments in Canada's east coast basins. *Canadian Journal of Earth Sciences* 30, 1782-1798.
- Erickson, S.G., Arkani-Hamed, J., 1993. Subduction initiation at passive margins: the Scotia basin, eastern Canada as a potential example. *Tectonics* 12, 678-687.

- Erickson, G., 1993. Sedimentary loading, lithospheric flexure, and subduction initiation at passive margins. *Geology* 21, 125-128.
- Faccenna, C., Giardini, D., Davy, P., et al., 1999. Initiation of subduction at Atlantic-type margins: Insights from laboratory experiments. *Journal of Geophysical Research* 104, 2749-2766.
- Forsyth, D., 1985. Subsurface loading and estimates of the flexural rigidity of continental lithosphere. *Journal of Geophysical Research* 90, 12623-12632.
- Goetze, C., 1978. The mechanisms of creep in olivine. *Philos. Trans. Royal Society of London, Ser. A* 288, 99-119.
- Ghods, A., Arkani-Hamed, J., 1998. Interpretation of the satellite magnetic anomaly of the Nova Scotia marginal basin. *Canadian Journal of Earth Sciences* 35, 162-174.
- Gradstein, F.M., Jansa, L.F., Srivastava, S.P., et al., 1990. Aspects of North Atlantic paleo-oceanography. In *Geology of the Continental Margin of Eastern Canada*, chapter 8. Edited by M.J. Keen and G.L. Williams. Geological Survey of Canada, *Geology of Canada*, vol. 2, pp. 351-389.
- Karner, G.D., Watts, A.B., 1982. On isostasy at Atlantic-type margins. *Journal of Geophysical Research* 87, 2923-2984.
- Keen, C.E., Beaumont, C., 1990. Geodynamics of rifted continental margins. In *Geology of the Continental Margin of Eastern Canada*, chapter 9. Edited by M.J. Keen and G.L. Williams. Geological Survey of Canada, *Geology of Canada*, vol. 2, pp. 391-472.
- Keen, C.E., Loncarevic, B.D., Reid, I., et al., 1990. Tectonic and geophysical overview. In *Geology of the Continental Margin of Eastern Canada*, chapter 2. Edited by M.J. Keen and G.L. Williams. Geological Survey of Canada, *Geology of Canada*, vol. 2, pp. 31-85.
- Keen, C.E., Potter, D.P., 1995. Formation and evolution of the Nova Scotian rifted margin: evidence from deep seismic reflection data. *Tectonics* 14, 918-932.
- Keen, M.J., Piper, D.J.W., 1990. Geophysical and historical perspective. In *Geology of the Continental Margin of Eastern Canada*, chapter 1. Edited by M.J. Keen and G.L. Williams. Geological Survey of Canada, *Geology of Canada*, vol. 2, pp. 5-30.
- Kemp, D.V., Stevenson, D.J., 1996. A tensile, flexural model for the initiation of subduction. *Geophysical Journal International* 125, 73-94.

- Lago, B., Cazenave, A., 1981. State of stress in the oceanic lithosphere in response to loading. *Geophysical Journal of Royal Astronomic Society* 64, 785-799.
- Lambeck, K., Nakiboglu, S.M., 1980. Seamount loading and stress in the ocean lithosphere. *Journal of Geophysical Research* 85, 6403-6418.
- McAdoo, D.C., Sandwell, D.T., 1985. Folding of oceanic lithosphere. *Journal of Geophysical Research* 90, 8563-8569.
- Mckenzie, D.P., 1977. Initiation of trenches: a finite amplitude instability. In *Island Arcs, Deep Sea Trenches and Back-Arc basins*. Edited by M. Talwani and W. Pitman III. American Geophysical Union, Maurice Ewing Series, vol. 1, 57-62.
- McNutt, M., 1980. Implications of regional gravity for state of stress in the Earth's crust and upper mantle. *Journal of Geophysical Research* 85, 6377-6396.
- McNutt, M.K., Diament, M., Kogan, M.G., 1988. Variations of elastic plate thickness at continental thrust belts. *Journal of Geophysical Research* 93, 8825-8838.
- Menke, W., 1981. The effect of load shape on the deflection of thin elastic plates. *Geophysical Journal of Royal Astronomic Society* 65, 571-577.
- Muller, S., Phillips, R.J., 1991. On the initiation of subduction. *Journal of Geophysical Research* 96, 651-665.
- Oakey, G.N., Stark, A., 1995. A digital compilation of depth to basement and sediment thickness for the North Atlantic and adjacent coastal land mass, Geological Survey of Canada, open file # 3039, 1995.
- Okal, E.A., Woods, D.F., Lay, T., 1986. Intraplate deformation in the 0-Gilbert-Ralik area: A prelude to a change of plate boundaries in the southwest Pacific? *Tectonophysics* 132, 69-77.
- Pilkington, M., 1990. Lithospheric flexure and gravity anomalies at Proterozoic plate boundaries in Canadian shield. *Tectonophysics* 176, 277-290.
- Royden, L., Keen, C.E., 1980. Rifting process and thermal evolution of the continental margin of eastern Canada determined from subsidence curves. *Earth and Planetary Science Letters* 51, 343-361.
- Sandwell, D.T., Smith, W.H.F., 1997. Marine gravity anomaly from Geosat and ERS 1 satellite altimetry. *Journal of Geophysical Research* 102, 10039-10054.
- Shemenda, A.I., 1992. Horizontal lithosphere compression and subduction: Constraints provided by physical modeling. *Journal of Geophysical Research* 97, 11097-11116.

- Sclater, J.G., Christie, P.A.F., 1980. Continental stretching: an explanation of the post-mid-Cretaceous subsidence of the central North Sea basin. *Journal of Geophysical Research* 85, 3711-3793.
- Turcotte, D.L., Schubert, G., 1982. *Geodynamics - Applications of continuum physics to geological problems*, chapter 3. By John Wiley & Sons, Inc. pp. 104-133.
- Uyeda, S., Ben Avraham, Z., 1972. Origin and development of the Philippine Sea. *Nature* 240, 176-178.
- Wade, J.A., MacLean, B.C., 1990. The geology of the southeastern margin of Canada. In *Geology of the Continental Margin of Eastern Canada*, chapter 5. Edited by M.J. Keen and G.L. Williams. Geological Survey of Canada, *Geology of Canada*, vol. 2, pp. 167-238.
- Watts, A.B., Bodine, J.H., Steckler, M.S., 1980. Observation of Flexure and the State of Stress in the Oceanic Lithosphere. *Journal of Geophysical Research* 85, 6369-6376.
- Zheng, Y., Arkani-Hamed, J., 1998. Joint inversion of gravity and magnetic anomalies of eastern Canada. *Canadian Journal of Earth Sciences* 35, 832-853.
- Zuber, M., Dechtel, T., Forsyth D., 1989. Effective elastic thickness of the lithosphere and mechanisms of isostatic compensation in Australia. *Journal of Geophysical Research* 94, 9353-9367.

4.11 Figure Captions

Figure 4.1 Location of Scotian Basin and contiguous places based on *Figure 1.1* from Keen and Piper, 1990. The lines across the Scotian Basin are the locations of the profiles used for gravity analysis and stacking the equivalent rock bathymetry (ERB), depth to basement and density perturbations. The black dot represents Sable island. An equal area projection is used in this figure and other similar figures. The dashed contour lines are contours of the depth to basement with an interval of 2.5 km.

Figure 4.2 (a) Observed gravity anomalies, free-air on the ocean and Bouguer on lands. (b) The equivalent rock bathymetry (ERB). The ERB of the continental areas is set to zero. (c) The depth to basement (after Oakey and Stark, 1995). The tapered zones near the boundaries, where data were tapered to suppress Gibb's ringing in the Fourier transformation are not shown in these maps, and in other similar maps including Figure 1.

Figure 4.3 Gravity anomaly of different layered models along profile CC' (see Figure 1). Model 1, the nominal model with continental crust density $\rho_c = 2800 \text{ kg/m}^3$, oceanic crust density $\rho_o = 2900 \text{ kg/m}^3$, thinned continental crust density $\rho_t = 2850 \text{ kg/m}^3$ and sediment grain density $\rho_s = 2700 \text{ kg/m}^3$; Model 2, $\rho_c = 2800 \text{ kg/m}^3$, $\rho_o = 2900 \text{ kg/m}^3$, $\rho_t = 2900 \text{ kg/m}^3$ and $\rho_s = 2800 \text{ kg/m}^3$; Model 3, $\rho_c = 2800 \text{ kg/m}^3$, $\rho_o = 2900 \text{ kg/m}^3$, $\rho_t = 2800 \text{ kg/m}^3$ and $\rho_s = 2800 \text{ kg/m}^3$; Model 4, $\rho_c = 2800 \text{ kg/m}^3$, $\rho_o = 2800 \text{ kg/m}^3$, $\rho_t = 2800 \text{ kg/m}^3$ and $\rho_s = 2800 \text{ kg/m}^3$; Model 5, $\rho_c = 2800 \text{ kg/m}^3$, $\rho_o = 2900 \text{ kg/m}^3$, $\rho_t = 2800 \text{ kg/m}^3$, and $\rho_s = 2750 \text{ kg/m}^3$; Model 6, $\rho_c = 2750 \text{ kg/m}^3$, $\rho_o = 2900 \text{ kg/m}^3$, $\rho_t = 2800 \text{ kg/m}^3$, and $\rho_s = 2700 \text{ kg/m}^3$; Model 7, $\rho_c = 2700 \text{ kg/m}^3$, $\rho_o = 2900 \text{ kg/m}^3$, $\rho_t = 2900 \text{ kg/m}^3$, and $\rho_s = 2700 \text{ kg/m}^3$; Model 8, $\rho_c = 2700 \text{ kg/m}^3$, $\rho_o = 2900 \text{ kg/m}^3$, $\rho_t = 2800 \text{ kg/m}^3$, and $\rho_s = 2700 \text{ kg/m}^3$. The densities of sea water and mantle are 1000 kg/m^3 and 3300 kg/m^3 respectively for all models.

Figure 4.4 Observed gravity anomalies, gravity anomalies of the nominal layered model and the constant sediment density model along four profiles (see Figure 1). The thick solid curves show the observed gravity anomalies. The thin dashed curves show the gravity anomalies of the nominal layered model. The thin solid curves show the gravity anomalies of the constant sediment density model. The thick dashed curves show the bathymetry, depth to basement and depth to Moho along the profiles in 0.1 km for better illustration.

Figure 4.5 (a) Gravity anomalies of the nominal layered model. (b) Differences between observed gravity anomalies and the gravity anomalies of the nominal layered model (observed minus model). (c) Density perturbations required to be added on to the nominal layered model in order to produce the observed gravity anomalies.

(d) Lithostatic pressure at 35 km depth. The features on the continental part are not shown in this figure since we are only concerned with the oceanic part.

Figure 4.6 (a) Selected profiles of the ERB, the depth to basement and density perturbations (see Figure 1 for the locations of the profiles). The profiles are stacked to the reference point where the deflection is a maximum.

Figure 4.7 Averaged profile of the depth to basement, and the deflections of various rigidity models. Density perturbations are included in the load. The thick solid curve shows the averaged depth to basement profile. a) deflections of the elastic plates with uniform rigidities, b) deflections of the two-segmented model with weak zone up to 500 km. Rigidity is kept at 10^{23} Nm when x is beyond 500 km and c) deflections of two-segmented models with different weak zone width from 200 km to 500 km. The rigidity of the weak zone is 10^{22} Nm, beyond the weak zone it is 10^{23} Nm. Also included in c is the deflection of a two-segmented model with a weak zone up to 500 km, but with no contribution of the density perturbations to the surface load. Note that the x axis of this figure is shifted by 100 km eastward compared to that of Figure 6 to put the hinge zone at $x = 0$. We also show only the first 1000 km from the hinge zone.

Figure 4.8 The strength envelopes calculated from the half-space cooling model at 10, 20, 30, 40 and 50 m.y. The vertical thick line shows the elastic thickness of the 10 m.y. old plate, as an example.

Figure 4.9 The elastic thickness of the simple plate model versus time.

Figure 4.10 The deflections of the simple plate model at different ages. Numbers on the curves show the ages.

Figure 4.11 (a) The steady state temperature distribution of the lithosphere using the averaged sedimentary thickness profile. (b) Compressional and (c) Tensional strength envelopes of the lithosphere. The depth is measured from the top of the basaltic crust, i.e., the base of the sediments. (b) and (c) are in absolute values.

Figure 4.12 Profiles of the strength envelopes at the maximum deflection point and a point far from the basin (142 km and 900 km in Figure 11 respectively). Compression is positive and tension is negative. The profiles at 142 km are multiplied by 100 for better illustration.

Figure 4.13 The deflections of the elastic plate models with pinned boundary conditions, and the deflections of these models if they are decoupled from the continent. The thin solid curve denotes the two-segmented model with a weak zone rigidity of 10^{22} Nm and a 500 km width under pinned boundary conditions. The thick solid curve denotes the deflection of this model when decoupled from the continent. The long dashed curve denotes the deflection of the elastic plate with a

uniform rigidity of 10^{23} Nm. The dashed curve denotes the deflection of the same model when it is decoupled from the dashed continent.

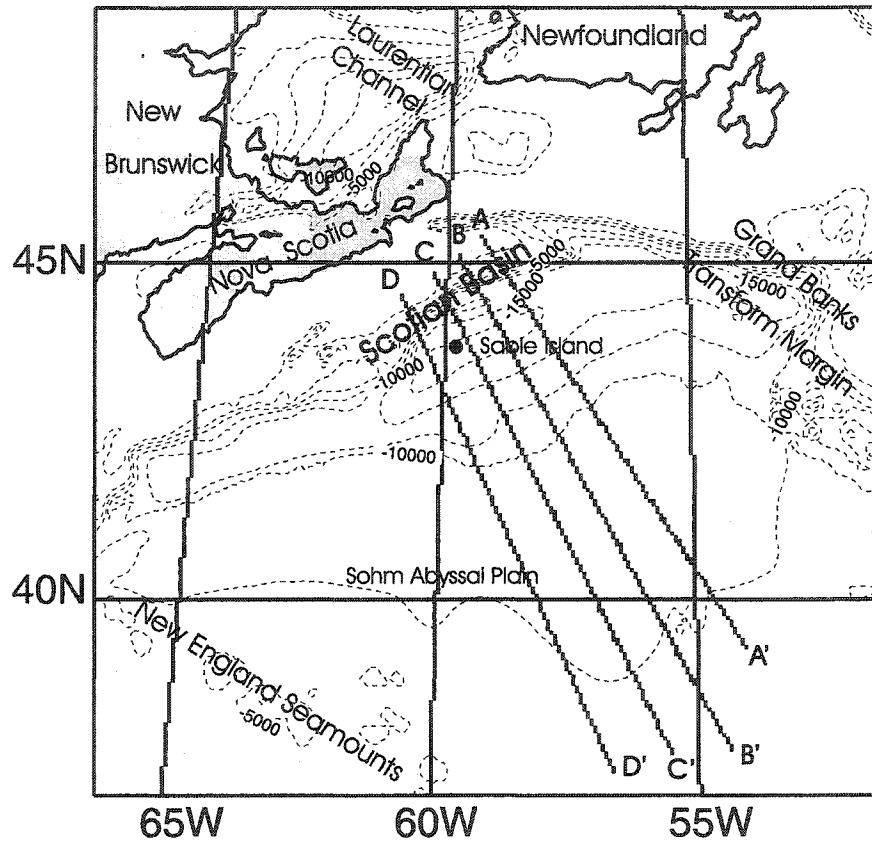


Figure 4.1:

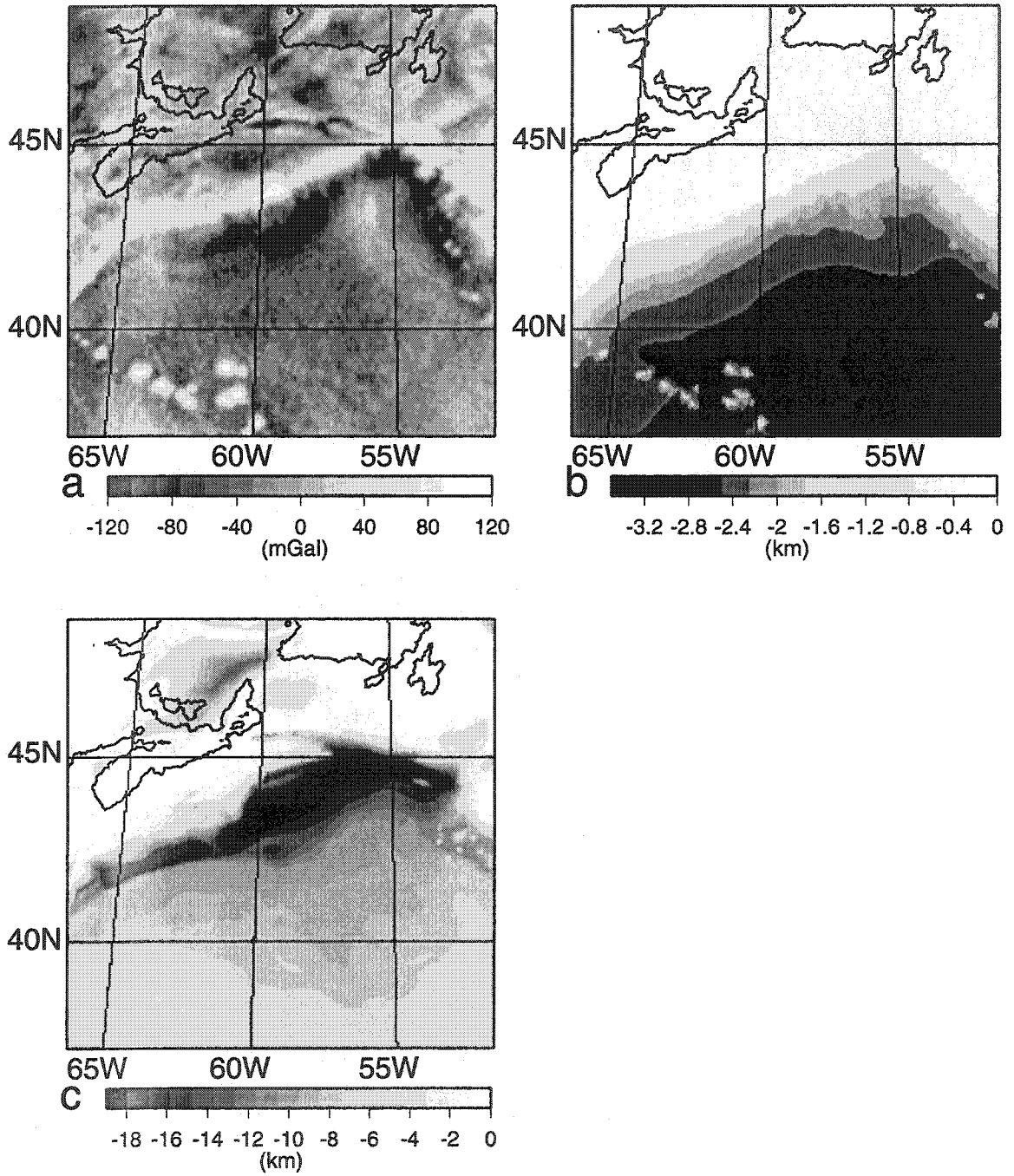


Figure 4.2:

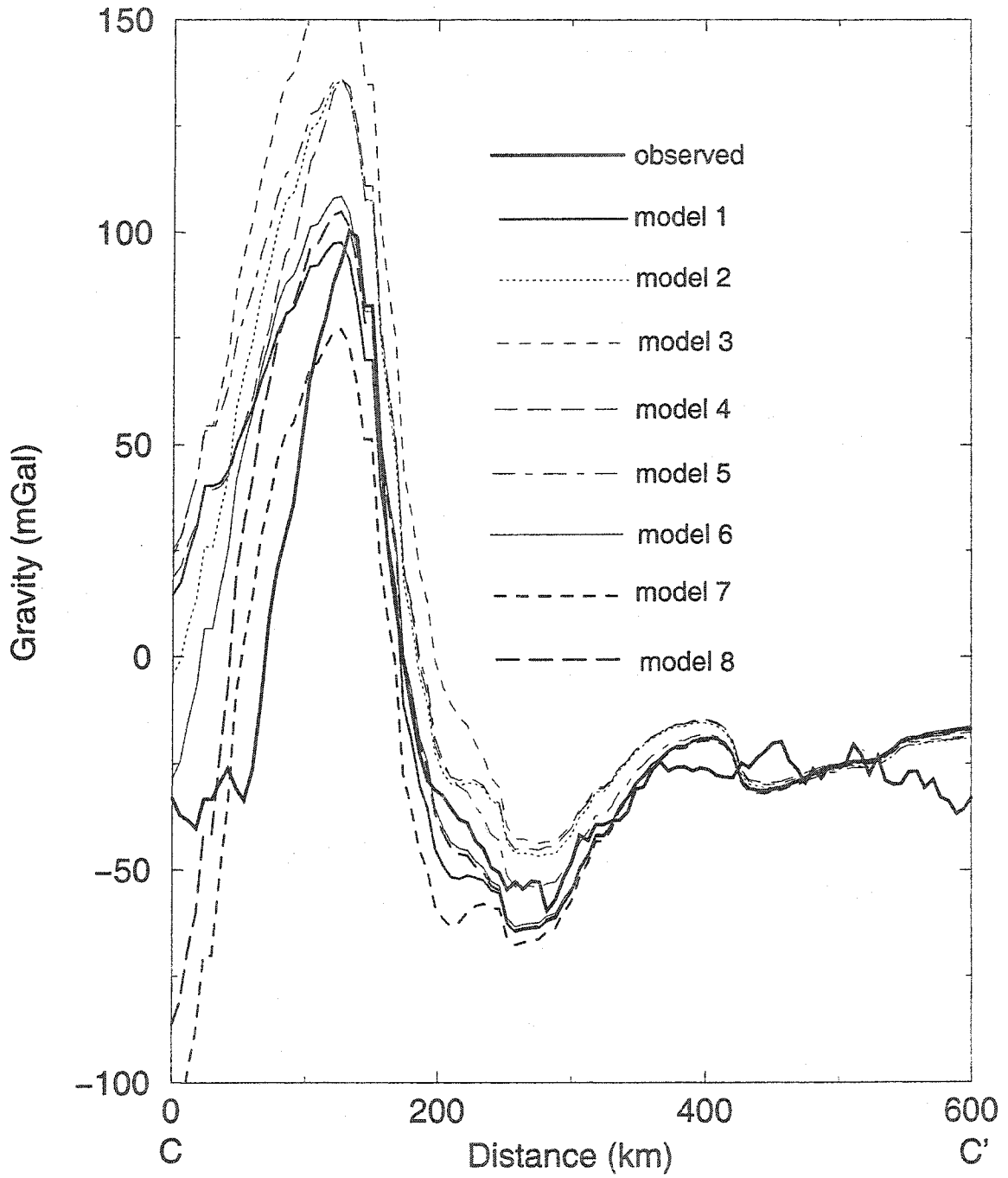


Figure 4.3:

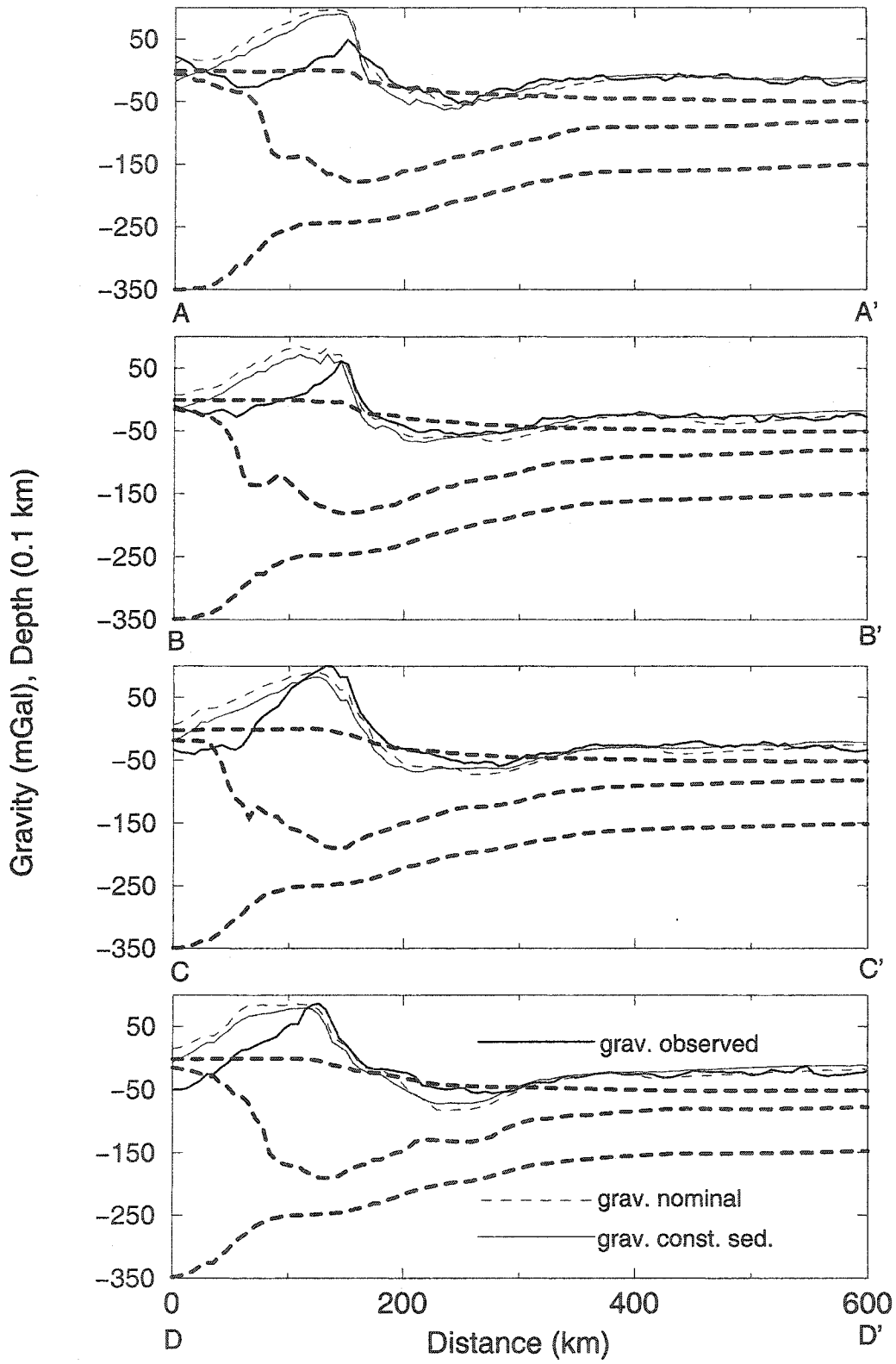


Figure 4.4:

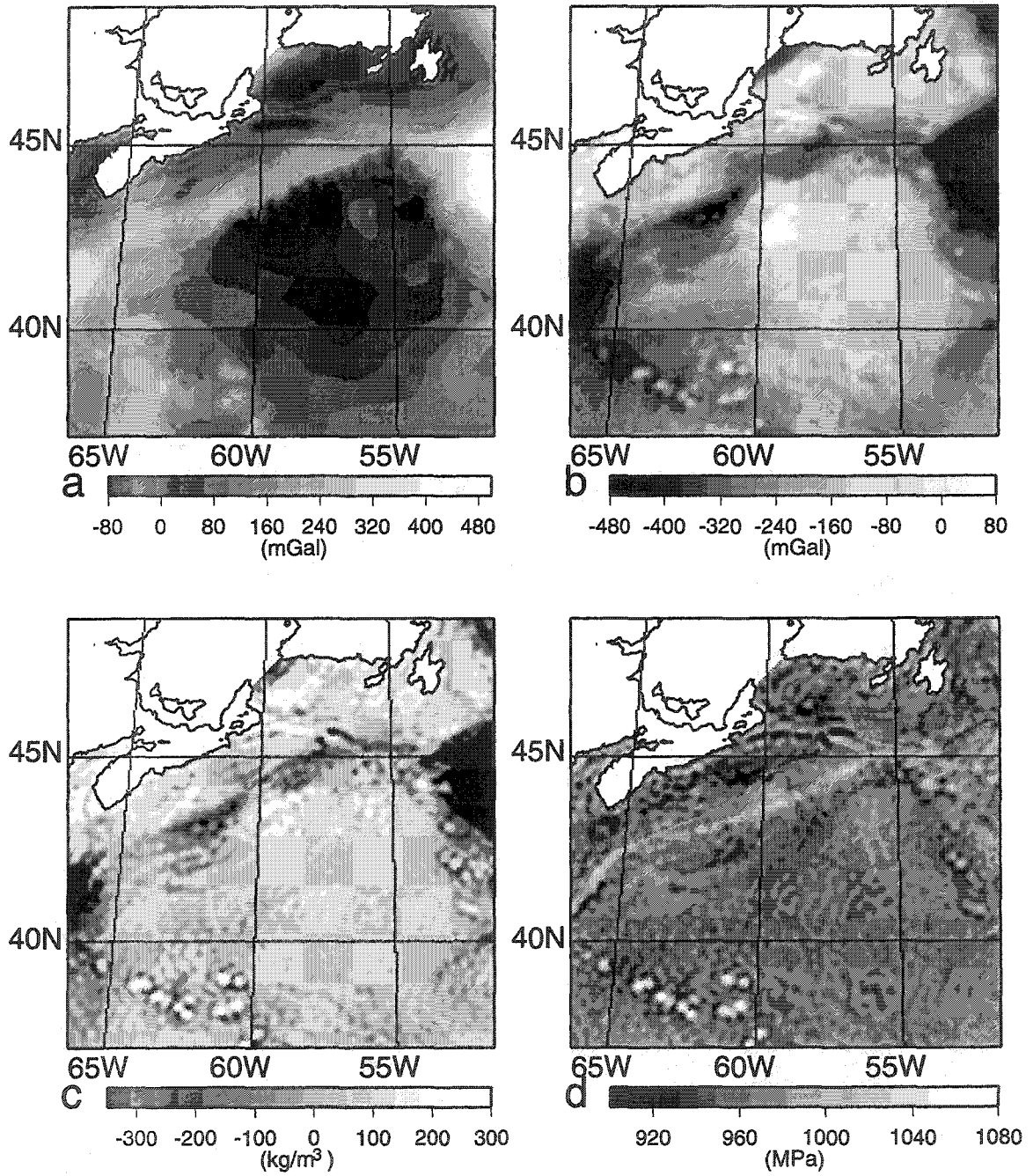


Figure 4.5:

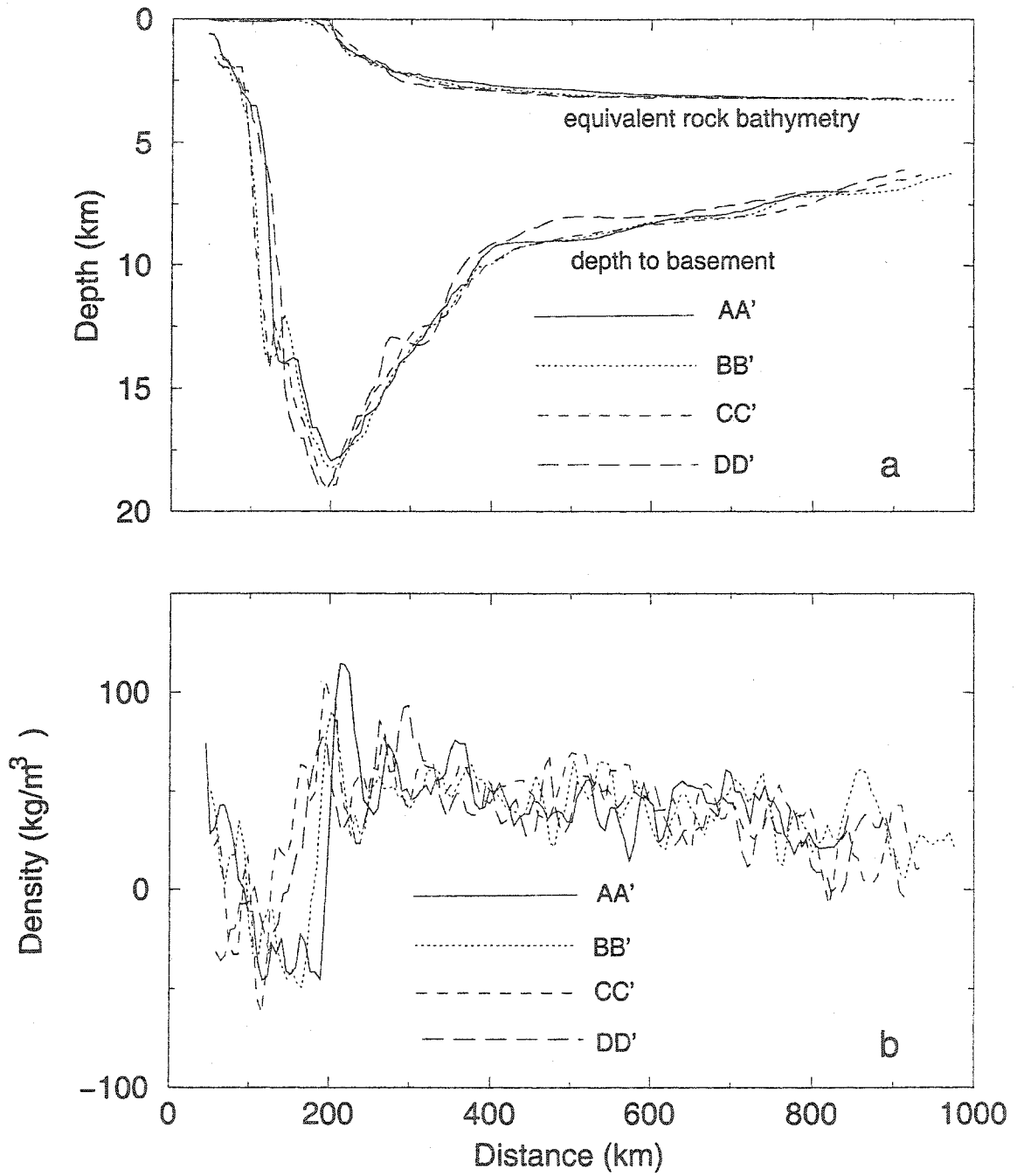


Figure 4.6:

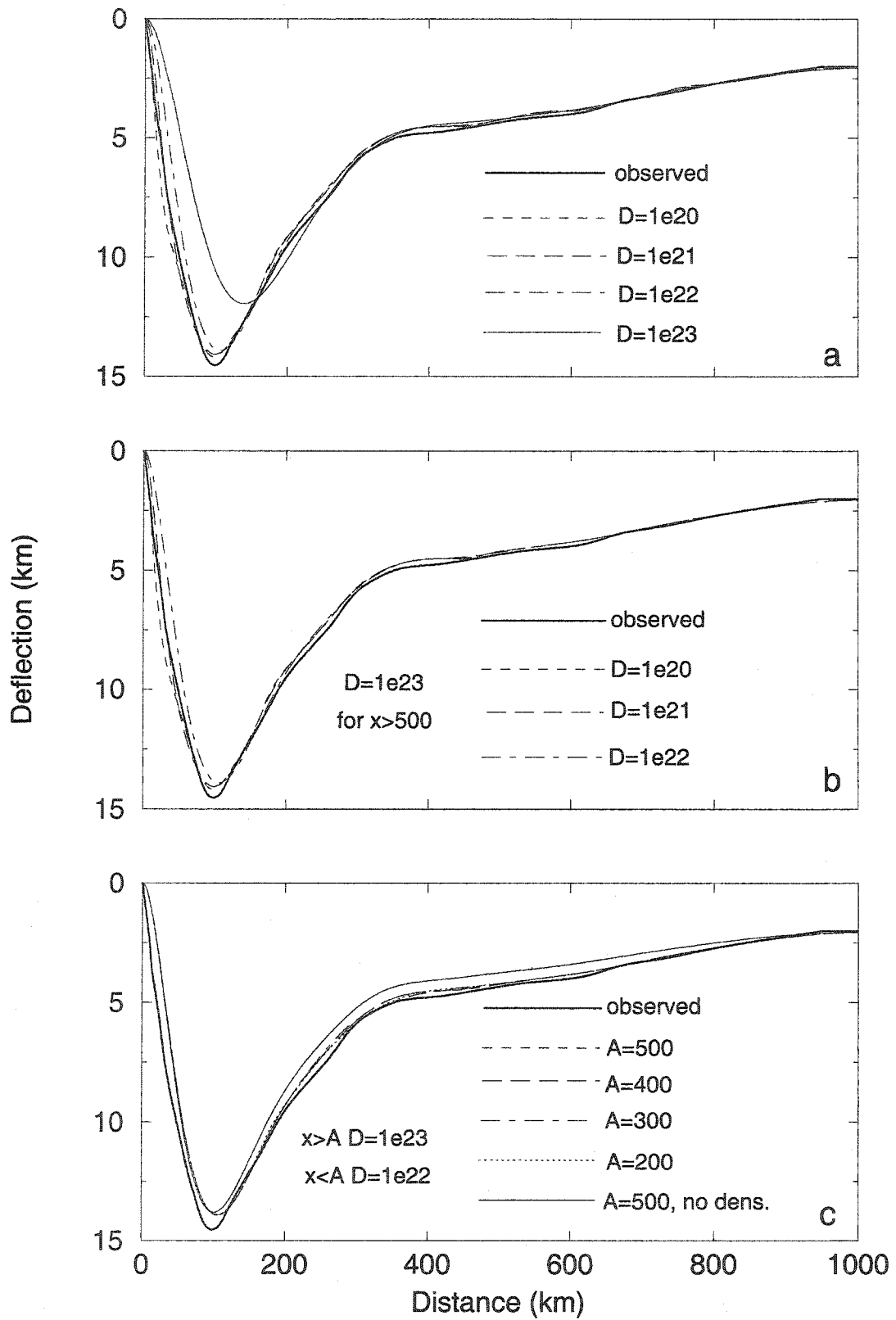


Figure 4.7:

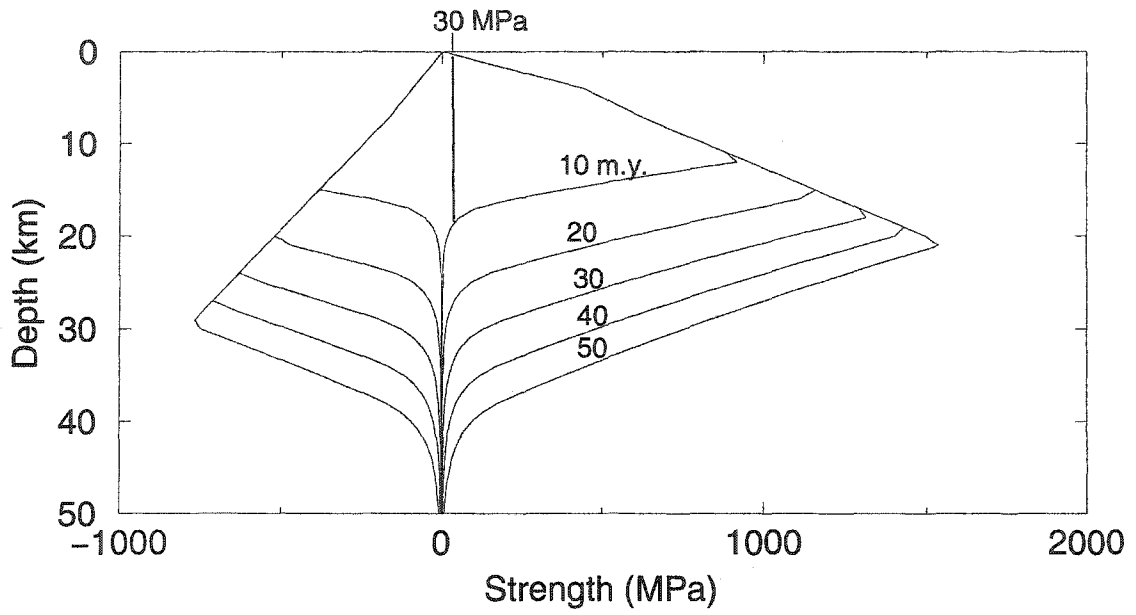


Figure 4.8:

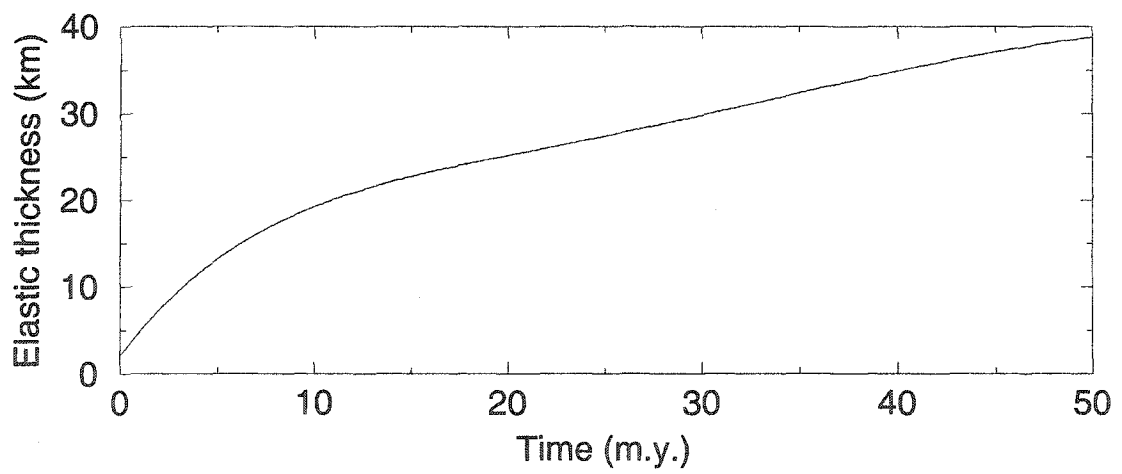


Figure 4.9:

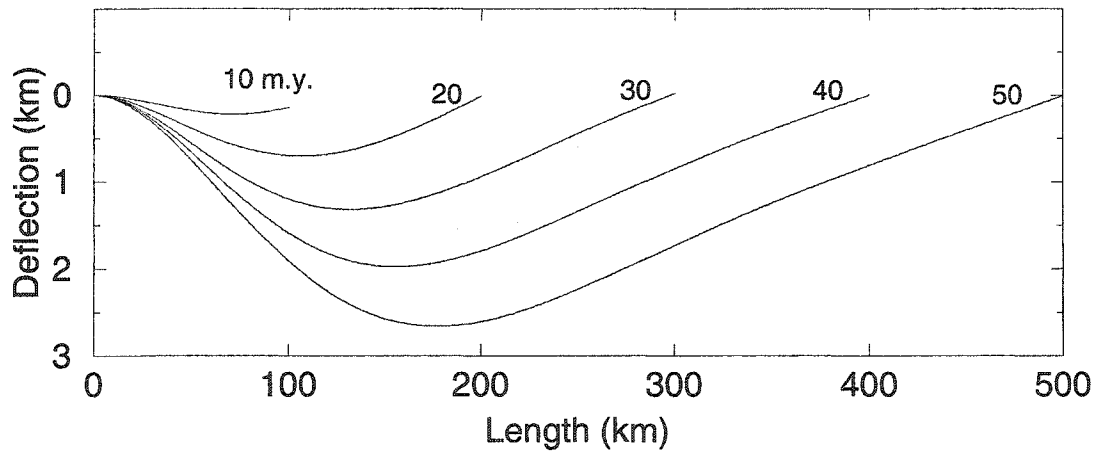


Figure 4.10:

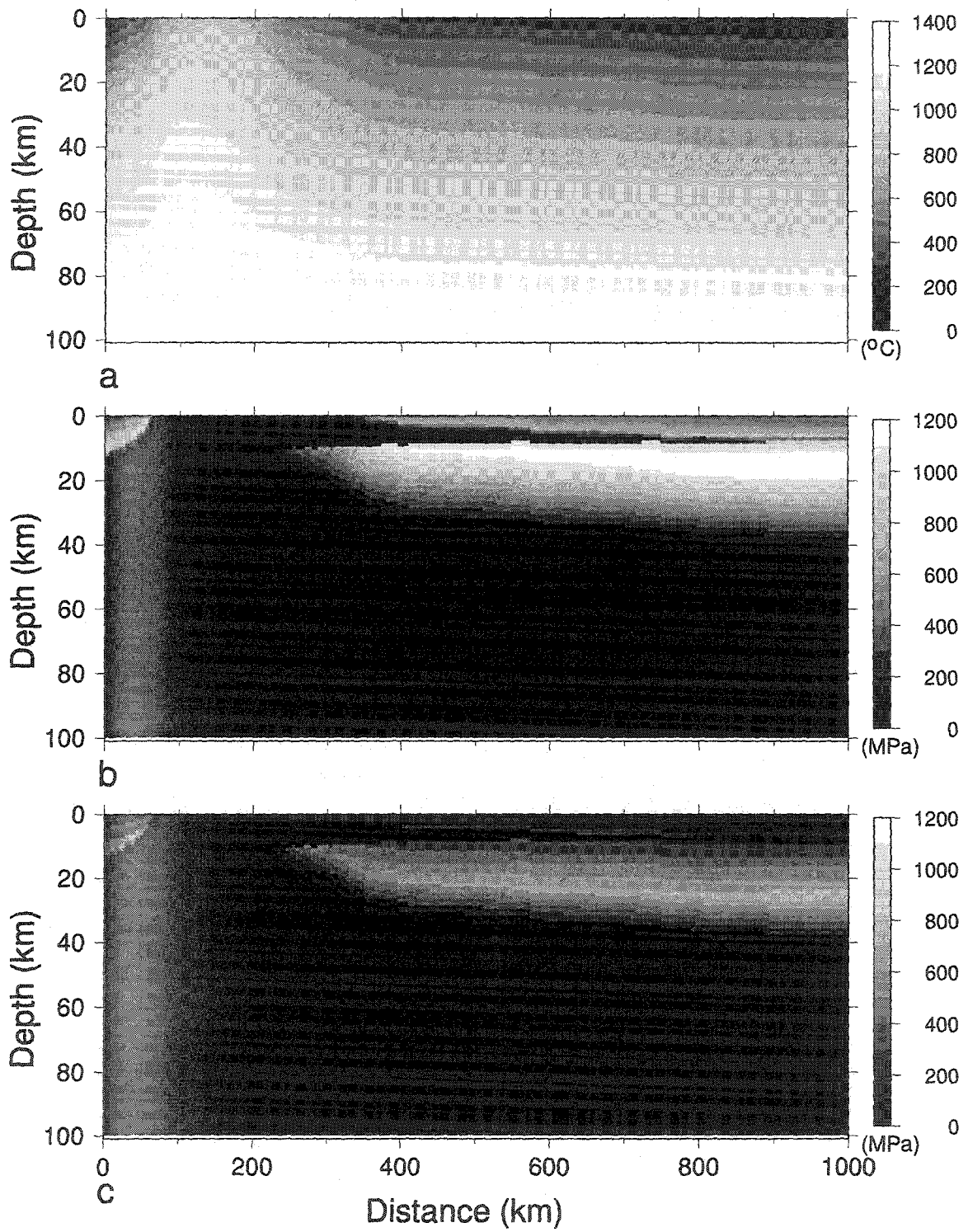


Figure 4.11:

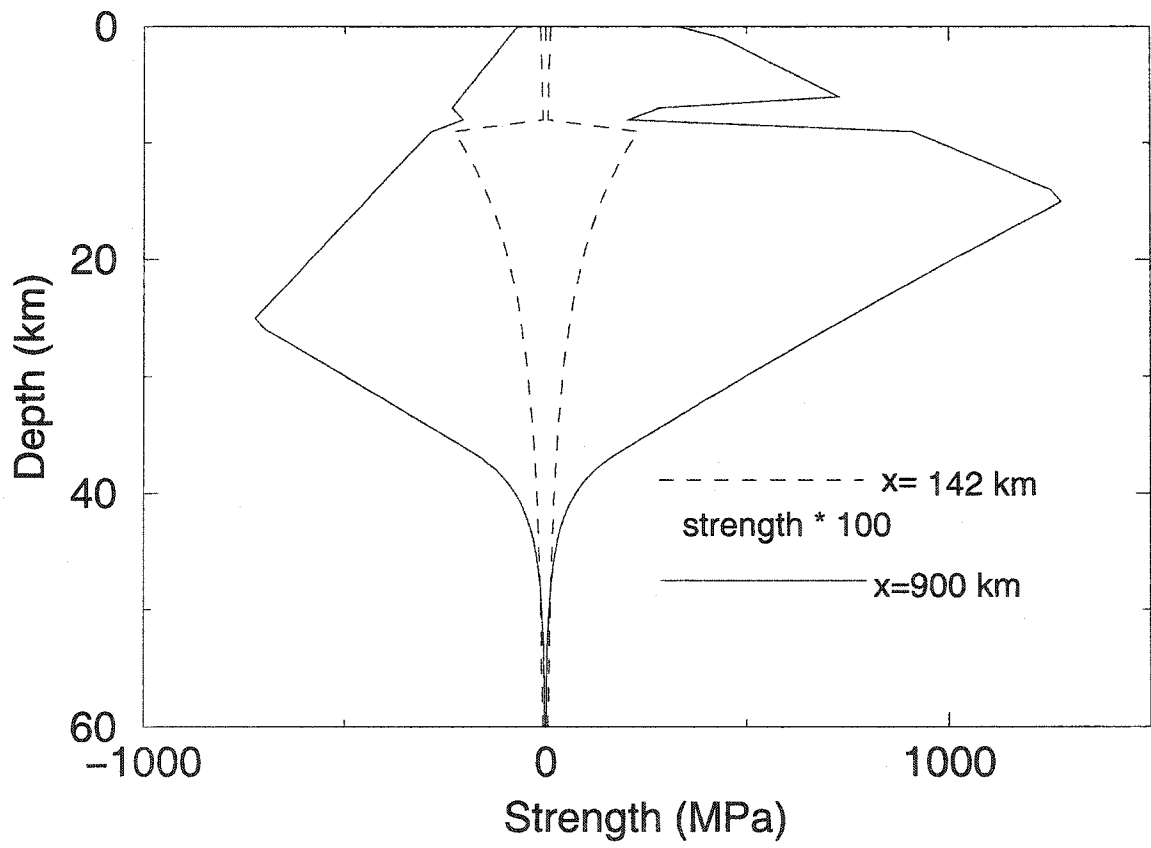


Figure 4.12:

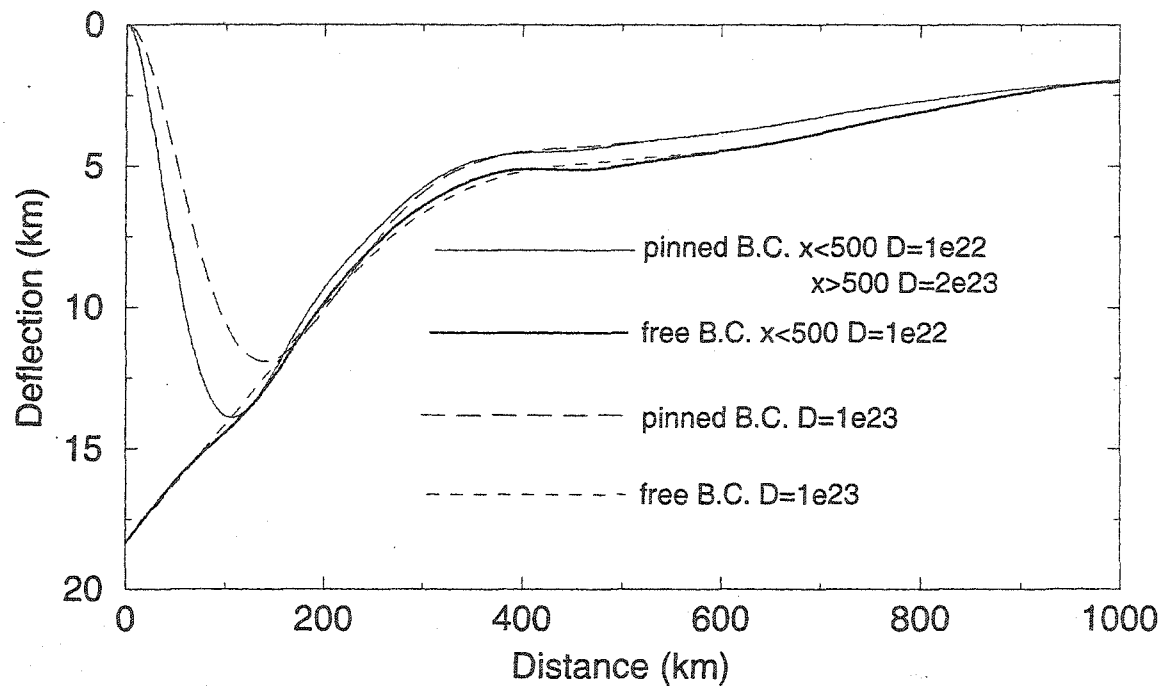


Figure 4.13:

Chapter 5

Rigidity of the Atlantic Oceanic Lithosphere Beneath New England Seamounts

This chapter is a continued study of Chapter 4 in order to determine the rigidity of the lithosphere far from the Scotian basin, which is not well constrained due to the long-wavelength nature of the sedimentary load on this part of the lithosphere. In this chapter, I investigate the elastic properties of the lithosphere beneath the New England seamounts, since these features are short and intermediate wavelength. Again, the topography and gravity analysis method developed in Chapter 3 is employed to investigate the compensation state of the lithosphere beneath the New England seamounts. The result suggests that density perturbations exist in the crust and/or upper mantle that are elastically supported by the lithosphere. Rigidity values obtained from the flexure of a 3-D thin elastic plate model of the lithosphere subjected to loads of the seamounts and density perturbations are in agreement with the rigidity values estimated from the study of Chapter 4. They also suggest that the lithosphere of the North Atlantic ocean is stronger than that of the other oceans.

Rigidity of the Atlantic Oceanic Lithosphere Beneath New England Seamounts

Ying Zheng and Jafar Arkani-Hamed

Earth and Planetary Sciences, McGill University, Montreal, Quebec, Canada

Submitted for publication in Tectonophysics, Feb., 2002 (Appendix C)

5.1 Abstract

Investigation of the flexural response of the oceanic plate subject to loading of New England seamounts provides an insight into the rigidity of the lithosphere. Fourier domain analysis of the bathymetry and gravity anomalies over New England seamounts suggests that internal density perturbations exist in the crust and/or uppermost mantle. The loads due to the topography of the seamounts and density perturbations must have been supported by the lithosphere. We group the seamounts into three representative ages and adopt a 3-D thin elastic plate model over an inviscid mantle to assess the rigidity of the lithosphere under these loads. The rigidity values are about $3 - 7 \times 10^{23}$ Nm for lithospheric ages ranging from 30 to 60 m.y. The base of the elastic part of the lithosphere follows an isotherm in the range of $750^\circ - 850^\circ$ C, suggesting a strong lithosphere that makes the north Atlantic ocean difficult to initiate subduction. However, the thermal blanketing by the thick sediments at Scotian basin reduces the rigidity by one to two orders of magnitude, and may facilitate initiation of subduction of the north Atlantic oceanic lithosphere at Scotian margin.

Keywords: New England Seamounts, north Atlantic ocean, Rigidity, Thin elastic plate, Fourier domain analysis, Initiation of subduction, Scotian basin

5.2 Introduction

The flexural response of the oceanic lithosphere to seamount loads have been proven useful in assessing the elastic properties of the lithosphere. The elastic thickness of the oceanic lithosphere determined by modeling its flexural response to seamount loading (Calmant, 1987; Calmant and Cazenave, 1986, 1987; McNutt, 1984; Walcott, 1970; Watts et al., 1975; Watts and ten Brink, 1989; Wolf and McNutt, 1991) supports the idea that the elastic thickness of the oceanic lithosphere increases as the square root of its age, and the bottom of the elastic part follows the depth to a particular isotherm determined on the basis of a half-space cooling model (Parsons and Sclater, 1977; Watts, 1978).

Study of the flexural deformation of the lithosphere beneath Scotian basin subjected to sedimentary loads reveals that the north Atlantic oceanic lithosphere far from the Scotian basin has a rigidity on the order of 10^{23} Nm, while the rigidity of the lithosphere beneath the basin is reduced by one to two orders of magnitude due to the thermal blanketing effect of the thick sediments and the temperature dependent rheology (Zheng and Arkani-Hamed, 2002). However, the rigidity of the lithosphere far from the basin is not well constrained, because the surface load on this part of the lithosphere is dominated by long wavelength components of the sedimentary load. All rigidity values of the order of 10^{23} Nm or lower satisfy the observations of bathymetry, depth-to-basement and gravity anomalies (Zheng and Arkani-Hamed, 2002). Modeling the flexural response of the lithosphere to New England seamount loads provides a means to constrain the rigidity of the lithosphere far from the basin. The objectives of this paper are: 1) to determine the rigidity of the north Atlantic oceanic lithosphere far from Scotian basin, and 2) to study the age dependence of the strength of the lithosphere. We first analyze the gravity anomalies and topography of the New England seamounts to determine the compensation state of this area. We then adopt uniform thin elastic plate models, but with different rigidity values, to calculate the flexural response of the model plates loaded by the seamounts and possible density perturbations in the crust. We then determine the age dependence of the rigidity of the lithosphere. The final section presents a brief discussion and major conclusions of this study.

5.3 Geological Setting

Located southeast off Scotian basin and extending 1200 km from the Georges Bank off the northeastern United States, New England seamounts are a northwest-southeast trending chain of more than 30 volcanic edifices with an about 2000 km length and a 40-60 km width (Keen et al., 1990) (Figure 1). Most of them are steep sided ($>10^\circ$ slopes) with a thin sedimentary cover (Duncan, 1984). The origin of the New England seamounts is debated. One interpretation relates them to volcanism along a fracture zone (Drake et al., 1968; Uchupi et al., 1970) with the observed ages resulting from southeasterly propagation of the tip of the leaky fracture (Jansa and Pe-Piper, 1988). A widely accepted scenario, however, is that the lineament that extends from the White Mountains of New Hampshire to the New England seamounts was created by the passage of the North American plate over a hot spot (Crough, 1981; Morgan, 1983; Duncan, 1984). Ages of dredged samples dated by the $^{40}\text{Ar}/^{39}\text{Ar}$ total fusion show a systematic progression from 103 m.y. at Bear seamount in the northwest to 82 m.y. at Nashville seamount in the southeast (Duncan, 1984), which supports the hot spot origin (see Figure 1 for the locations cited in this paper).

5.4 Gravity and Topography Analysis

Gravity anomalies of the working area are free-air gravity anomalies at sea level extracted from Geosat data (National Gravity Data Base, Geomatics, Canada, and Sandwell and Smith, 1997). Bathymetry data are extracted from ETOPO5 (NGDC). To better illustrate the data and facilitate further data processing and calculations in Fourier domain, the data are mapped into 128×128 grid points with 6 km intervals using an equal distance projection from their original format of latitude, longitude and the value. The gaps in the gravity data are filled using a 2-D circular weighting function,

$$W(r) = 0.5[1 + \cos(\frac{\pi r}{R})], \quad (5.1)$$

where r is the distance from the grid point to be filled and $R=18$ km is the radius of the circular window. Figure 2a and 2b show the gravity and bathymetry data. The irregular spacing of the original gravity data of the study area does not allow resolution of wavelengths shorter than 30 km (Zheng and Arkani-Hamed, 1998). Therefore the components with wavelengths shorter than 30 km, corresponding to wave numbers greater than 25, are dominated by noise and are filtered out of the gravity and bathymetry data, using a low-pass filter in Fourier domain, before carrying out further analysis. The bathymetry data have long wavelength components that show a gentle slope from northeast to southwest which most likely is not related to the seamounts. Similarly, the very long wavelength components of the gravity data are likely independent of the seamounts. To make the flexure calculations of the oceanic lithosphere subject to the seamount loads, we apply a 2-D Hanning filter to the bathymetry and gravity data. The filter keeps unchanged all the components with wavelengths shorter than 110 km, and gradually suppresses to zero the longer wavelength components corresponding to wave numbers less than 7, using a cosine function. The components with wave numbers less than 4 are suppressed by more than 50%, and have minor effect on our results. We also remove the mean value of the bathymetry (5 km) and express the seamounts as positive topography with respect to the oceanic floor, and thus call the processed bathymetry as the topography hereafter. Included in Figure 2 are the resulting filtered gravity anomalies and topography maps. The gravity exhibits strong positive anomalies ranging from 50 mGal at Nashville seamount to 170 mGal at Gregg seamount.

To understand the compensation state of the topography, the power spectrum of the observed gravity anomalies (see Figure 3a) is calculated by

$$P_k^{g^o} = \sum_u \sum_v (|g_{u,v}^o|^2 + |g_{u,-v}^o|^2) \quad (5.2)$$

where the indices u, v denote the Fourier transform, and u and v are the normalized wave numbers in x (east-west) and y (south-north) directions. In the discrete Fourier

transform, $u = 2\pi n/L$ and $v = 2\pi m/L$, where n and m are the wave numbers in the x and y directions, and L is the dimension of the area (768 km). The 2-D wave number k is defined as $k = (n^2 + m^2)^{1/2}$, which corresponds to wavelength $\lambda = L/k$. The summations are over all values of u and v such that $i - 1/2 < k < i + 1/2$, where i is a specific wave number. Also included in Figure 3a are the power spectra of the gravity anomalies due to uncompensated topography, determined by

$$g_{u,v}^T = 2\pi G\rho e^{-kz}T_{u,v} \quad (5.3)$$

and the Airy compensated topography at 10, 20, 30 and 40 km depths, calculated from

$$g'_{u,v} = 2\pi G\rho e^{-kz}(1 - e^{-kH_c})T_{u,v} \quad (5.4)$$

where $T_{u,v}$ is the Fourier transform of the topography, G is the gravitational constant, ρ (=1800 kg/m³) is the density difference between the seamount and the sea water, z is the observation altitude which is set to 5 km at sea level, and H_c is the depth of compensation. For wave numbers bigger than 4, the power spectrum of the observed gravity anomalies is consistently higher than that of the gravity due to topography, whether compensated or not, indicating possible density perturbations existing inside the crust and/or the uppermost mantle.

To explore the origin of the gravity anomalies, the degree correlation coefficient η_k between observed gravity and topography (Figure 3b) is calculated from

$$\eta_k = \frac{\sum_u \sum_v (T_{u,v}g_{u,v}^o + T_{u,-v}g_{u,-v}^o)}{(P_{u,v}^T P_{u,v}^{g^o})^{1/2}}, \quad (5.5)$$

where $P_{u,v}^T$ is the power spectrum of the topography. The high correlation coefficients indicate that the main part of the observed gravity arises from surface topography of the seamounts.

5.5 Flexure Model

It is demonstrated above that a simple Airy compensation model cannot explain the observed gravity anomalies of the study area. Airy model implies that the crust has no strength, so that the topographic load must give rise to substantial vertical movements of the crust to achieve compensation. However, seamounts are usually localized and small in spatial scale and are supported by the strength of the lithosphere (Banks et al., 1977). Thin elastic plate models have been widely used to investigate the compensation state of surface loads such as topography, sediments,

and seamounts (e.g. Caldwell et al., 1976; Lambeck and Nakiboglu, 1980; Lago and Cazenave, 1981; Cloetingh, 1982; Forsyth, 1985; McNutt et al., 1988; Zuber et al., 1989; Erickson, 1993; Zheng and Arkani-Hamed, 2002). We have demonstrated in our previous study (Zheng and Arkani-Hamed, 2002) that the oceanic lithosphere of the north Atlantic ocean far from the Scotian basin has a rigidity on the order of $\sim 10^{23}$ Nm. In the present paper, we adopt a three dimensional thin elastic plate model over a fluid-like mantle to investigate the elastic properties of the lithosphere beneath the New England seamounts. The thickness of the plate is substantially small compared with its horizontal dimension. We allow the oceanic plate to deflect under the loads of the seamounts and internal density perturbations. It is assumed that the observed gravity anomalies are due to lateral variations of density anomalies arising from the density differences between sea water and the seamounts, the seamounts and the oceanic crust, the oceanic crust and the mantle beneath, and the density perturbations inside the crust and possibly uppermost mantle.

The flexural response of the plate is calculated by solving

$$[D \nabla^4 + g(\rho_m - \rho_l)]W(x, y) = -gT(x, y)(\rho_l - \rho_w) - gh\delta\rho(x, y) \quad (5.6)$$

where

$$D = \frac{ET_e^3}{12(1 - \nu^2)} \quad (5.7)$$

is the flexural rigidity of the plate, with Young's Modulus E ($= 8 \times 10^{10}$ Pa), the elastic thickness T_e , and Poisson's ratio ν ($= 0.25$). W is the deflection of the plate, positive upward, T is the observed topography of the seamounts, ρ_l ($= 2800$ kg/m³) is the density of the seamounts, ρ_w ($= 1000$ kg/m³) is the density of the sea water, ρ_m ($= 3300$ kg/m³) is the density of the underlying mantle, h is the thickness of the oceanic crust, set to 7 km which is the average thickness of the oceanic crust, and $\delta\rho$ is the vertically averaged density perturbation inside the crust. The loads on the plate come from the topography of the seamounts and the internal density perturbations. The depth of the density perturbations can not be uniquely determined (Zheng and Arkani-Hamed, 1998). The vertically integrated density perturbations have the same loading effect on the elastic plate no matter within what thickness the density perturbations are distributed, i.e. it is the mass perturbations that we are concerned with. We assume that the density perturbations are in the crust and consider their vertically averaged values.

Taking 2-D Fourier transform of equation (6) yields

$$W_{u,v} = \frac{-g(\rho_l - \rho_w)T_{u,v} - gh\delta\rho_{u,v}}{Dk^4 + (\rho_m - \rho_l)g} \quad (5.8)$$

where $W_{u,v}$, $T_{u,v}$ and $\delta\rho_{u,v}$ are the Fourier transforms of $W(x, y)$, $T(x, y)$ and $\delta\rho(x, y)$ respectively.

The deflection of the plate results in additional density anomalies at horizontal boundaries where discrete density changes occur. These density anomalies also contribute to the gravity anomalies. The Fourier transform of the gravity anomaly $g_{u,v}^o$ of the flexed structure is determined by

$$g_{u,v}^o = 2\pi G[e^{-k(z-z_1)}(\rho_m - \rho_c)W_{u,v} + e^{-k(z-z_2)}(\rho_c - \rho_l)W_{u,v} + e^{-k(z-z_2)}(\rho_l - \rho_w)T_{u,v} + e^{-k(z-z_2)}h\delta\rho_{u,v}] \quad (5.9)$$

where ρ_c ($=2900 \text{ kg/m}^3$) is the density of the oceanic crust, z_1 is the depth of the Moho discontinuity, and z_2 is the average elevation of the topography. We set the gravity anomalies of the flexed structure to be the observed gravity anomalies, and determine the density perturbations using flexural rigidity D values of 10^{24} , 10^{23} , 10^{22} and 10^{21} Nm respectively.

Figure 3c shows the power spectrum of the density perturbations for different rigidity values. The density perturbations decrease with increasing rigidity. Also as the rigidity increases, the differences between the density perturbations become smaller. The close similarities of the power spectra over wave numbers 10 to 25 for different rigidity values demonstrate that the density perturbations are not very sensitive to the changes of the rigidity, especially when the rigidity value is greater than 10^{23} Nm.

Included in Figure 3b is the degree correlation coefficients between topography and density perturbations obtained for $D = 10^{23}$ Nm, showing no significant correlation and emphasizing that the density perturbations are mainly independent of the topography. The density perturbations cannot be accounted for by simply changing the density ρ_l of the seamount.

According to the widely accepted theory of the origin of the New England seamounts, they are connected with the New England hot spot volcanism with earlier uplift and igneous activity in New England (the White Mountain Igneous Province) and later eruption of the Corner seamounts (Morgan, 1983; Crough, 1981; Foland and Faul, 1977; Duncan, 1984). The ^{40}Ar - ^{39}Ar total fusion and incremental heating ages show an increase in seamount construction ages from southeast to northwest. This also explains the northwest-southeast lineament of the New England seamounts which is consistent with northwest-ward motion of the North American plate over a New England hot spot between 103 m.y. and 82 m.y. ago (Duncan, 1984). The hot spot origin suggests that the volcanic seamounts are much younger than the oceanic lithosphere on which they sit. We determine the ages of the oceanic lithosphere at the time of the New England seamounts formation by subtracting the ages of Nashville, Michael, Allegheny, Gosnold and Atlantis seamounts obtained by Duncan (1984) from the ages of the oceanic lithosphere on which they sit (Dyment and Arkani-Hamed, 1998). Since the oceanic plate has most likely elastically supported the differential stresses created by the seamounts, we assume that the observed topography of the seamounts

and the deformation of the oceanic lithosphere represent the flexural structure at the formation age of the seamounts. Therefore the rigidity of the oceanic lithosphere reflects the strength of the lithosphere at the formation ages of the seamounts.

We group the ages of the oceanic lithosphere at the formation time of the New England seamounts into three representative ages: 30 m.y. for Nashville and Michael seamounts, 40 m.y. for Allegheny seamount, and 60 m.y. for Gosnold and Atlantis seamounts. The thermal states of the oceanic lithosphere at these three ages are determined using a half-space cooling model (Turcotte and Schubert, 1982),

$$\frac{\theta - \theta_s}{\theta_m - \theta_s} = \operatorname{erf}\left(\frac{z}{2\sqrt{\kappa x/V}}\right) \quad (5.10)$$

where θ is the depth dependent temperature, θ_s ($=0$ °C) is the surface temperature, and θ_m ($=1350$ °C) is the temperature at the ridge axis and beneath the plate. V ($=10$ km/m.y.) is the spreading rate, and x and z denote the horizontal and vertical coordinates respectively. κ ($=K/\rho_c c$) is the thermal diffusivity, where K ($=3.1$ W/m/K) is the thermal conductivity and c ($=1250$ J/kg/K) is the specific heat. Figure 4 shows the strength envelopes of the model we obtained using the Byerlee's law (Byerlee, 1978; Brace and Kohlstedt, 1980) for the near surface brittle portion, and the creep law of dry olivine (Goetze 1978) for the deeper ductile portion (see Zheng and Arkani-Hamed, [2002] for the details of the parameters used in the strength envelope calculation). The elastic core is sandwiched between the upper brittle and the lower ductile parts with a thickness determined by the applied differential stress. The elastic thickness of the oceanic lithosphere at a specific age is obtained from the compressional strength envelope by setting the differential stress equal to the load due to the maximum topography of the similar age seamounts plus the load of density perturbations beneath that maximum topography. The density perturbations are those we obtained before for $D = 10^{23}$ Nm. We then determine the rigidity D from equation (7) using elastic thickness T_e thus obtained. The resulting rigidities for the oceanic lithosphere of 30, 40 and 60 m.y. are about 3×10^{23} , 5×10^{23} and 7×10^{23} Nm respectively. We note that these are the minimum rigidities under maximum differential stress exerted. The sedimentary cover on New England seamounts is very thin (Duncan, 1984), and has minor contribution to the surface load specified by wave numbers of 4-25 considered in this study.

We note that the density perturbations used in determining the differential stress are calculated with a prescribed rigidity value $D = 10^{23}$ Nm, which differs from the resulting values. To further adjust the rigidity values, we use the resulting rigidity values to re-calculate the density perturbations. Using the newly obtained density perturbations and repeating the above procedure, we determine new rigidity values that are almost identical to the previous ones. The final rigidity values of 3×10^{23} , 5×10^{23} and 7×10^{23} Nm for the three age groups show that the lithosphere becomes more rigid with age. Estimates of the rigidity of the north Atlantic oceanic lithosphere from

modeling of the flexure of the oceanic plate under the sedimentary loads at Scotian basin yield the same order of magnitude, i.e. 10^{23} Nm (Zheng and Arkani-Hamed, 2002).

Comparing the effective elastic thicknesses of our three age groups with the isotherms obtained from the half-space cooling model, we find that the bottom of the elastic plate matches the depth to the isotherms between 750°C and 850°C (Figure 5). The elastic thickness of the normal oceanic lithosphere increases with the square root of its age (Parsons and Sclater, 1977) and follows the depth to the isotherms in the range of 300° - 600°C (Watts, 1978). Elastic thickness estimated from loading of the seamounts fall between the depth to the isotherms of 200°C and 400°C (Calmant and Cazenave, 1987; McNutt and Fischer, 1987; McNutt and Judge, 1990). Elastic thickness estimates from trenches are consistently higher than those determined from seamount studies for the lithosphere of the same age and are described by isotherms in the 600° - 800°C range (McAdoo et al., 1985; McNutt, 1984; Judge and McNutt, 1991). Taking into account the thermal stresses in the oceanic lithosphere, the base of the elastic part follows an isotherm in the range of 700° - 800°C (Wessel, 1992). Observations of seismicity in the oceanic lithosphere show that very few earthquakes take place beyond the depth of the 700° - 800°C isotherms (Bergman, 1986; Bergman and Solomon, 1984; Wiens and Stein, 1983, 1984). The hotter isotherms revealed from our elastic thickness estimates suggest that the north Atlantic oceanic lithosphere beneath New England seamounts is stronger than the normal oceanic lithosphere.

5.6 Discussion and Conclusions

We estimated the rigidities of the north Atlantic oceanic lithosphere from its flexural response to the surface loads by New England seamounts using the gravity anomalies and bathymetry of the seamounts and adopting a 3-D thin elastic plate model over an inviscid fluid mantle. The estimated rigidity values of $3 - 7 \times 10^{23}$ Nm are consistent with the rigidity of $\sim 10^{23}$ Nm obtained from modeling of the flexure of the Atlantic oceanic lithosphere by sedimentary loads (Zheng and Arkani-Hamed, 2002). The base of the elastic part of the lithosphere versus age follows the depth to the isotherms in the range of 750° - 850°C , suggesting a strong lithosphere of the north Atlantic ocean.

The oceanic lithosphere at the margin of north Atlantic ocean is 200 m.y. old. It is the oldest passive margin on Earth. The oceanic and continental lithosphere became locked after 10-20 m.y. of the break-up of North America and Africa (Karner and Watts, 1982). The strong oceanic lithosphere suggested in our study makes the initiation of subduction of the Atlantic ocean even more difficult. However, the thermal blanketing effect of the thick sediments over the lithosphere beneath Scotian basin reduces the rigidity of the lithosphere by one to two orders of magnitude (Zheng and Arkani-Hamed, 2002), and may facilitate reactivation of the normal faults at the

hinge zone when a considerable amount of tension is created by the possible re-orientation of the spreading ridge of the north Atlantic ocean in the future (Ericson and Arkani-Hamed, 1993). Changing the hinge zone from a coupled to a decoupled one allows additional flexing of the oceanic lithosphere. This enhances the thermal blanketing effect by allowing more sediments, and further weakens the lithosphere (Zheng and Arkani-Hamed, 2002). The break-up of the lithosphere at the hinge zone facilitates initiation of subduction of the Atlantic ocean lithosphere at Scotian margin.

5.7 Acknowledgement

This research is supported by the Natural Sciences and Engineering Research Council of Canada (NSERC) to JAH. We would like to thank Walter Roest and Gordon Oakey of Geological Survey of Canada for providing us the bathymetry and gravity data used in this study, Jerome Dymant of University of Brest, France, for the oceanic age data, and Sonya Dehler of Atlantic Geoscience Centre for suggesting good references.

5.8 References

- Banks, R.J., Parker, R.L., Heustis, S.P., 1977. Isostatic compensation on a continental scale: local versus regional mechanisms. *Geophysical Journal of Royal Astronomic Society* 64, 785-799.
- Bergman, E.A., 1986. Intraplate earthquakes and the state of stress in oceanic lithosphere. *Tectonophysics* 132, 1-35.
- Bergman, E.A., Solomon, S.C., 1984. Source mechanisms of earthquakes near mid-ocean ridges from body waveform inversion: Implications for the early evolution of oceanic lithosphere. *Journal of Geophysical Research* 89, 11415-11441.
- Brace, W.F., Kohlstedt, D.L., 1980. Limits on lithospheric stress imposed by laboratory experiments. *Journal of Geophysical Research* 85, 6248-6252.
- Byerlee, J., 1978. Friction of Rocks. *Pageoph* 116, 615-626.
- Caldwell, J.G., Haxby, W.F., Karig, D.E., Turcotte, D.L., 1976. On the applicability of a universal elastic trench profile. *Earth and Planetary Science Letters* 31, 239 - 246.
- Calmant, S., 1987. The elastic thickness of the lithosphere in the Pacific ocean. *Earth and Planetary Science Letters* 85, 277-288.
- Calmant, S., Cazenave, A., 1986. The effective elastic lithosphere under the Cook-Austral and Society islands. *Earth and Planetary Science Letters* 77, 187-202.
- Calmant, S., Cazenave, A., 1987. Anomalous elastic thickness of the oceanic lithosphere in the south-central Pacific. *Nature* 328, 236-238.
- Cloetingh, S., 1982. Evolution of passive continental margins and initiation of subduction zones. Ph.D. Thesis. Instituut voor aardwetenschappen der Rijksuniversiteri te Utrecht, No. 29.
- Crough, S.T., 1981. Mesozoic hot spot epeirogeny in eastern North America. *Geology* 9, 2-6.
- Drake, C.L., Ewing, J.I., Stockard, H., 1968. The continental margin of the eastern United States. *Canadian Journal of Earth Sciences* 5, 993-1010.
- Duncan, R.A., 1984. Age progressive volcanism in the New England seamounts and the opening of the central Atlantic ocean. *Journal of Geophysical Research* 89, 9980-9990.

- Dyment, J., Arkani-Hamed, J., 1998. Contribution of lithospheric remanent magnetization to satellite magnetic anomalies over the world's oceans. *Journal of Geophysical Research* 103, 15423-15441.
- Erickson, G., 1993. Sedimentary loading, lithospheric flexure, and subduction initiation at passive margins. *Geology* 21, 125-128.
- Erickson, S.G., Arkani-Hamed, J., 1993. Subduction initiation at passive margins: the Scotia basin, eastern Canada as a potential example. *Tectonics* 12, 678-687.
- Foland, K.A., Faul, H., 1977. Ages of the White Mountain intrusives—New Hampshire, Vermont, and Maine, U.S.A. *American Journal of Science* 277, 888-904.
- Forsyth, D., 1985. Subsurface loading and estimates of the flexural rigidity of continental lithosphere. *Journal of Geophysical Research* 90, 12623-12632.
- Goetze, C., 1978. The mechanisms of creep in olivine. *Philosophical Transactions of Royal Society of London, Series A* 288, 99-119.
- Jansa, L.F., Pe-Piper, G., 1988. Middle Jurassic to early Cretaceous igneous rocks along eastern North American continental shelf. *Bulletin of the American Association of Petroleum Geologists* 72, 347-366.
- Judge, A.V., McNutt, M.K., 1991. The relationship between plate curvature and elastic plate thickness: A study of the Peru-Chile trench. *Journal of Geophysical Research* 96, 16625-16640.
- Karner, G.D., Watts, A.B., 1982. On isostasy at Atlantic-type margins. *Journal of Geophysical Research* 87, 2923-2984.
- Keen, C.E., Loncarevic, B.D., Reid, I., et al., 1990. Tectonic and geophysical overview. Chapter 2 in *Geology of the Continental Margin of Eastern Canada*. Keen, M.J., Williams, G.L. (ed.). Geological Survey of Canada, *Geology of Canada*, vol. 2, 31-85.
- Keen, M.J., Piper D.J.W., 1990. Geological and historical perspective. Chapter 1 in *Geology of the Continental Margin of Eastern Canada*. Keen, M.J., Williams, G.L. (ed.). Geological Survey of Canada, *Geology of Canada*, vol. 2, 5-30.
- Lago, B., Cazenave, A., 1981. State of stress in the oceanic lithosphere in response to loading. *Geophysical Journal of Royal Astronomic Society* 64, 785 - 799.
- Lambeck, K., Nakiboglu, S.M., 1980. Seamount loading and stress in the ocean lithosphere. *Journal of Geophysical Research* 85, 6403-6418.
- McAdoo, D.C., Martin, C.F., Poulouse, S., 1985. Seasat observations of flexure: Evidence for a strong lithosphere. *Tectonophysics* 116, 209-222.

- McNutt, M.K., 1984. Lithosphere flexure and thermal anomalies. *Journal of Geophysical Research* 89, 11180-11194.
- McNutt, M.K., Diament, M., Kogan, M.G., 1988. Variations of elastic plate thickness at continental thrust belts. *Journal of Geophysical Research* 93, 8825-8838.
- McNutt, M.K., Fischer, K.M., 1987. The south Pacific superswell, in *Seamounts, Islands and Atolls*. Geophysical Monograph Series 43, edited by Keating, B.H., Fryer, P., Batiza, R., and Boehlert, G.W., AGU, Washington, D.C., 25-34.
- McNutt, M.K., Judge, A.V., 1990. The superswell and mantle dynamics beneath the south Pacific. *Science* 248, 969-975.
- Morgan, W.J., 1983. Hotspot tracks and the early rifting of the Atlantic. *Tectonophysics* 94, 123-139.
- Parsons, B., Sclater, J.G., 1977. An analysis of the variation of ocean floor bathymetry and heat flow with age. *Journal of Geophysical Research* 82, 803-827.
- Sandwell, D.T., Smith, W.H.F., 1997. Marine gravity anomaly from Geosat and ERS 1 satellite altimetry. *Journal of Geophysical Research* 102, 10039-10054.
- Turcotte, D.L., Schubert, G., 1982. *Geodynamics - applications of continuum physics to geological problems*, chapter 3. John Wiley & Sons, New York, 104 - 133.
- Uchupi, E., Phillips, J.D., Prada, K.E., 1970. Origin and structure of the New England seamount chain. *Deep Sea Research* 17, 483-494.
- Walcott, R.I., 1970. Flexure of the lithosphere at Hawaii. *Tectonophysics* 9, 435-446.
- Watts, A.B. 1978. An analysis of isostasy in the world's oceans, 1, Hawaiian-Emperor seamount chain. *Journal of Geophysical Research* 83, 5989-6004.
- Watts, A.B., ten Brink U.S., 1989. Crustal structure, flexure, and subsidence history of the Hawaiian islands. *Journal of Geophysical Research* 80, 1391-1398.
- Watts, A.B., Cochran, J.R., Selzer, G., 1975. Gravity anomalies and flexure of the lithosphere: A three-dimensional study of the Great Meteor seamount, northeast Atlantic. *Journal of Geophysical Research* 80, 1391-1398.
- Wessel, P., 1992. Thermal stress and bimodal distribution of elastic thickness estimates of the oceanic lithosphere. *Journal of Geophysical Research* 97, 14177-14193.
- Wiens, D.A., Stein, S., 1983. Age dependence of oceanic intraplate seismicity and implications for lithospheric evolution. *Journal of Geophysical Research* 88, 6455-6468.

- Wiens, D.A., Stein, S., 1984. Intraplate seismicity and stresses in young oceanic lithosphere. *Journal of Geophysical Research* 89, 11442-11464.
- Wolf, C.J., McNutt, M.K., 1991. Compensation of Cretaceous seamounts of the Darwin Rise, northwest Pacific ocean. *Journal of Geophysical Research* 96, 2363-2374.
- Zheng, Y., Arkani-Hamed, J., 1998. Joint inversion of gravity and magnetic anomalies of eastern Canada. *Canadian Journal of Earth Sciences* 35, 832-853.
- Zheng, Y., Arkani-Hamed, J., 2002. The elastic properties of the lithosphere beneath Scotian basin. *Tectonophysics*, in press.
- Zuber, M., Dechtel, T., Forsyth D., 1989. Effective elastic thickness of the lithosphere and mechanisms of isostatic compensation in Australia. *Journal of Geophysical Research* 94, 9353-9367.

5.9 Figure Captions

Figure 5.1 Location of New England seamounts and contiguous area based on Figure 1.1 from Keen and Piper (1990), and Fig. 1 from Duncan (1984). An equal distance projection is used in this figure and Figure 2. The bathymetry is contoured at 0.5 km interval. 1- Nashville, 2- Michael, 3- Allegheny, 4- Gilliss, 5- Vogel, 6- Rehoboth, 7- Manning, 8- Gregg, 9- Gosnold, 10- Atlantis, 11- Kelvin, 12- Balanus.

Figure 5.2 (a) Free-air gravity anomalies. (b) Bathymetry. (c) The band-pass filtered gravity anomalies where the wave numbers greater than 25 are filtered out and those less than 7 are suppressed. (d) The similarly band-pass filtered bathymetry. The mean value is removed, therefore, the seamounts have positive topography relative to average oceanic floor.

Figure 5.3 (a) Power spectra of the observed gravity anomalies, the gravity anomalies of uncompensated topography, and the gravity anomalies of the Airy compensated topography at 10, 20, 30 and 40 km depth, respectively. (b) Degree correlation of the topography and observed gravity anomalies, and topography and density perturbations for the rigidity value of 10^{23} Nm. (c) Power spectra of density perturbations for rigidity values of 10^{21} , 10^{22} , 10^{23} , and 10^{24} Nm.

Figure 5.4 Strength envelopes of 30, 40 and 60 m.y. old oceanic lithosphere.

Figure 5.5 Isotherms for 750 °C and 850 °C from a half-space cooling model. The triangles represent depth to the base of the elastic part of the oceanic lithosphere at 30, 40 and 60 m.y. from our calculation.

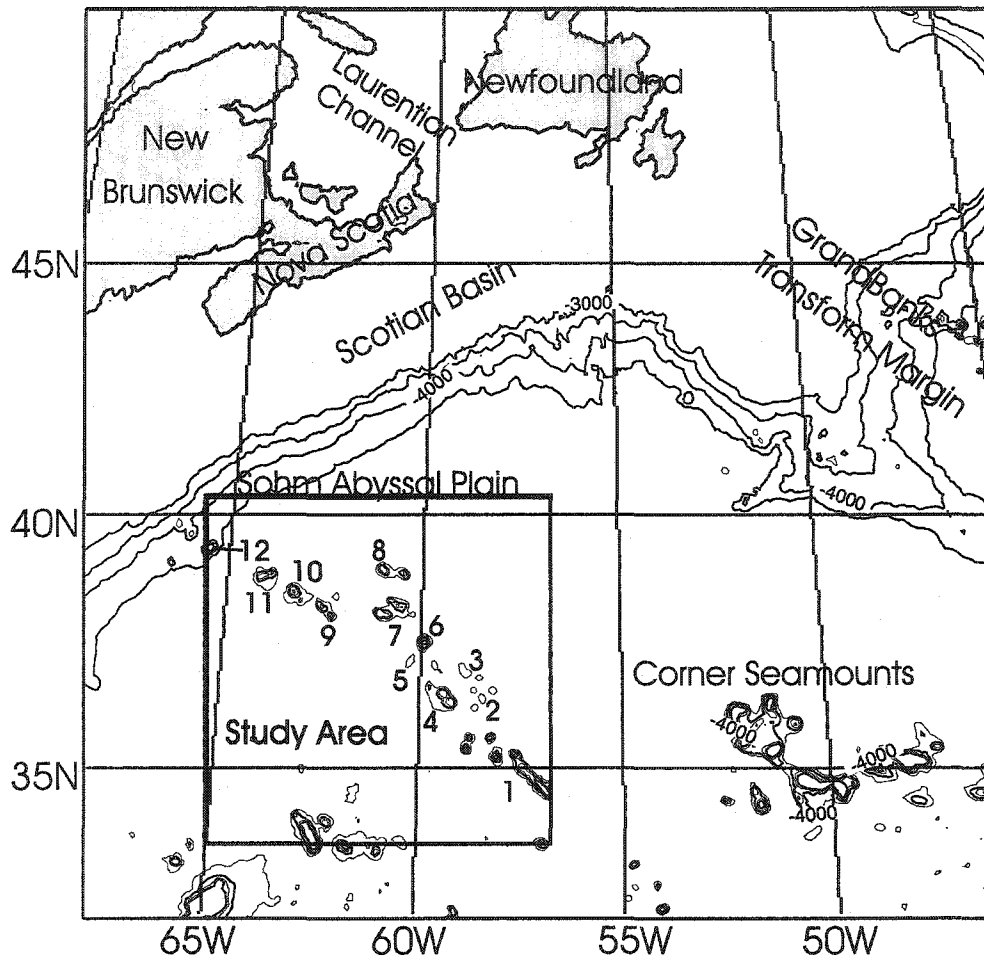


Figure 5.1:

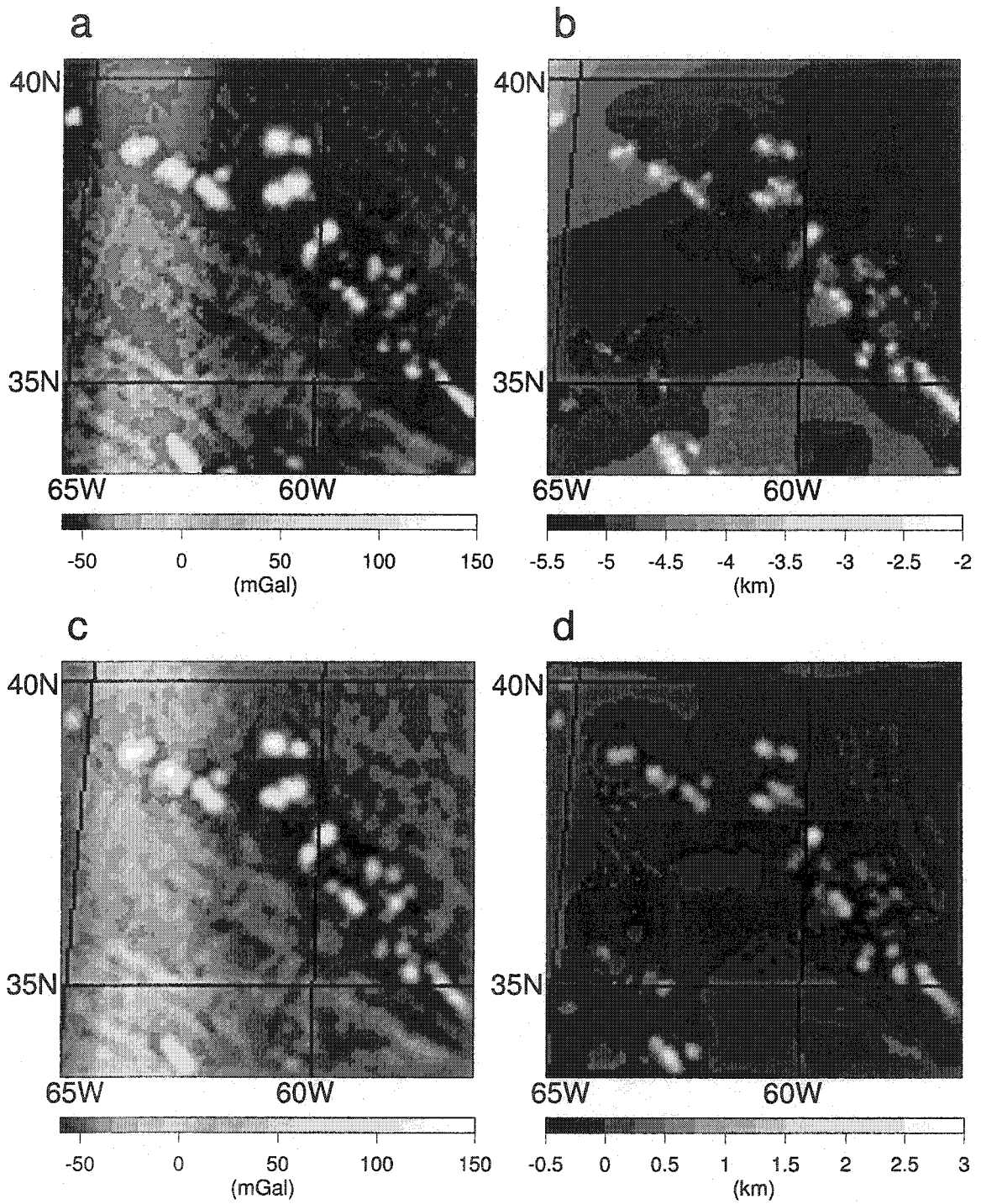


Figure 5.2:

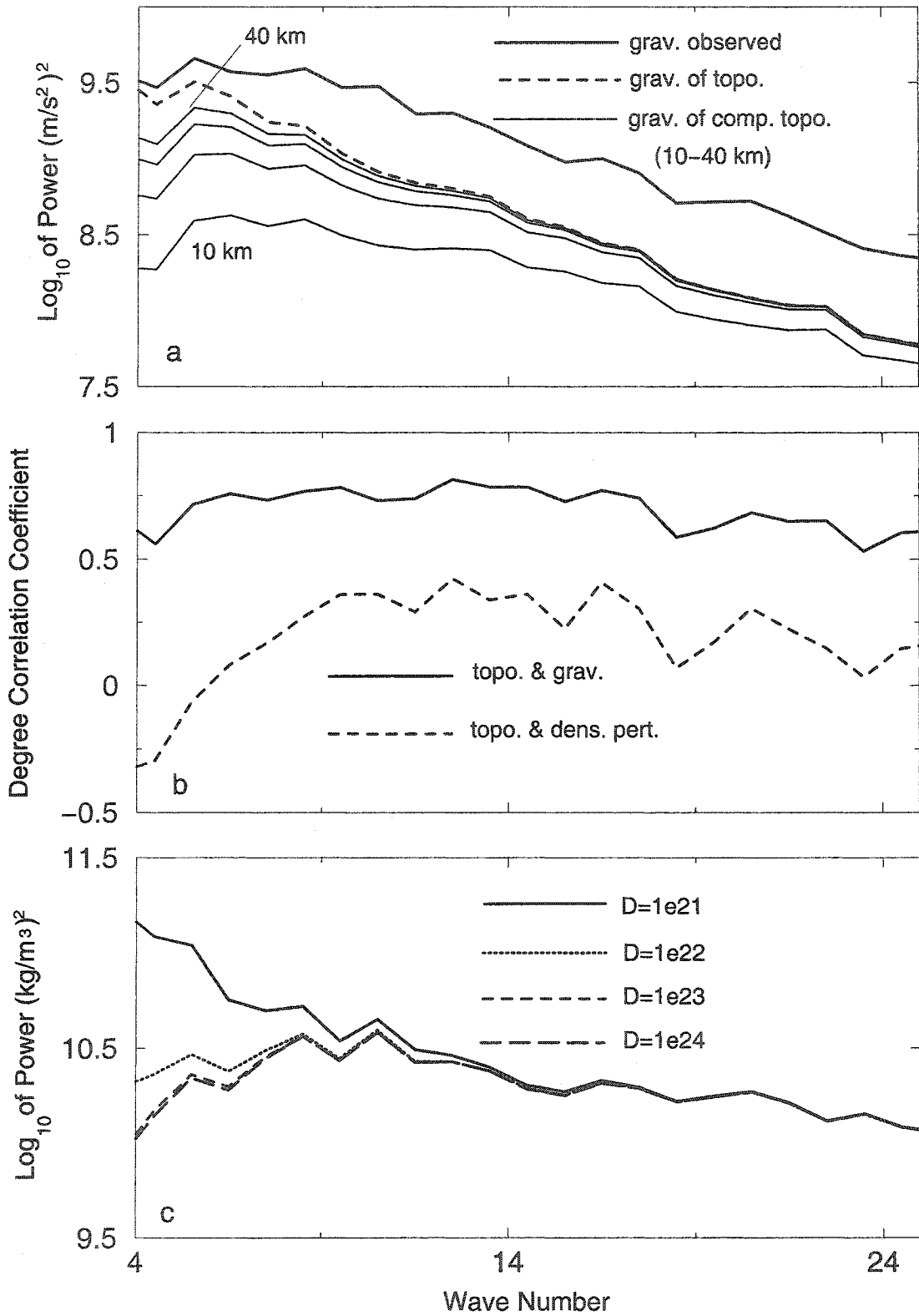


Figure 5.3:

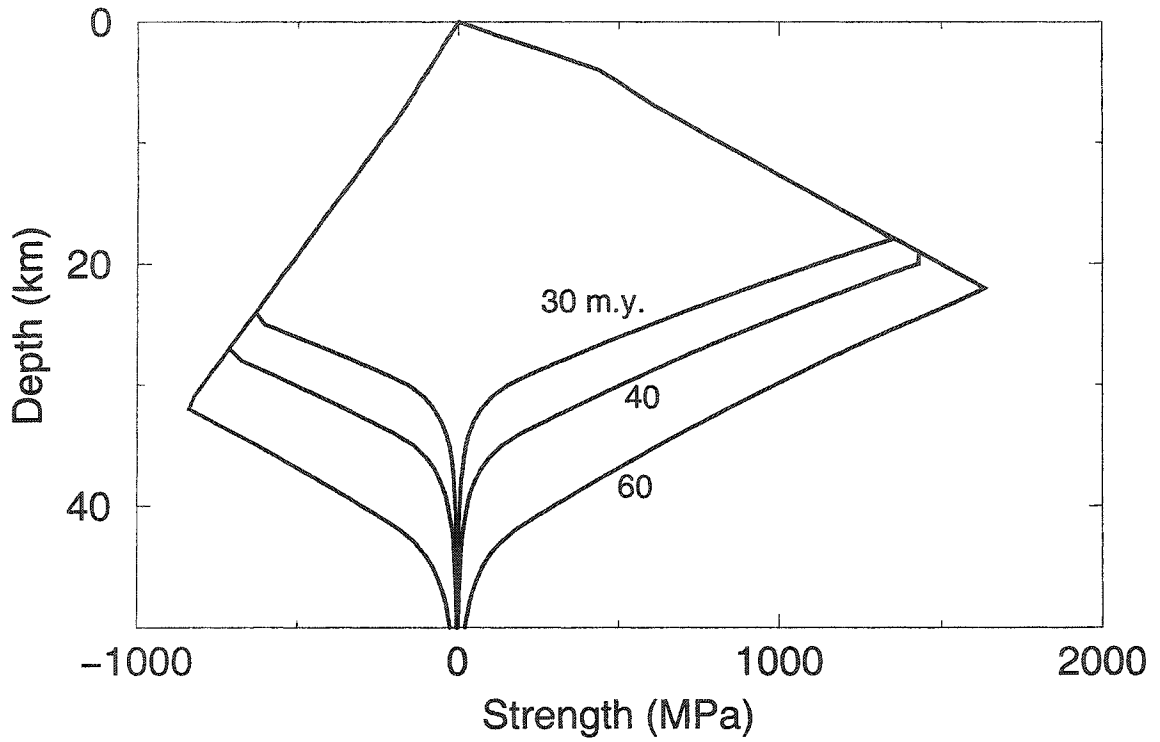


Figure 5.4:

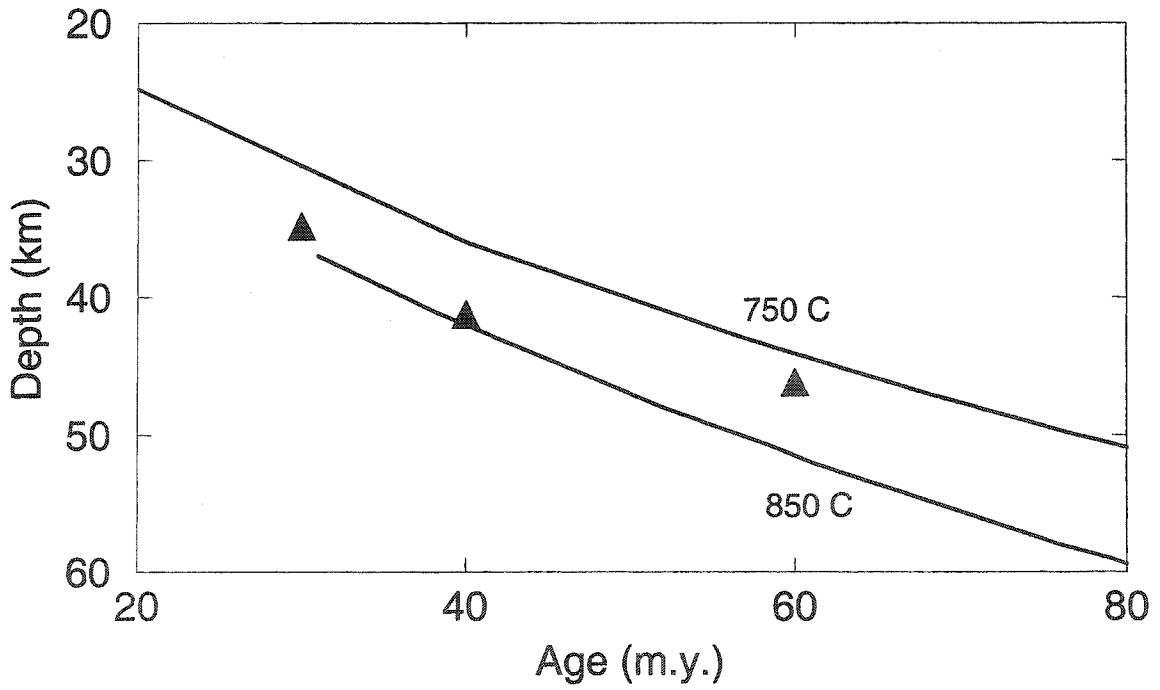


Figure 5.5:

Chapter 6

Conclusions

This chapter presents the major conclusions of the thesis. A proposal for possible future work is also provided.

6.1 Discussion and Conclusions

In this thesis I have developed Fourier and space domain methods for topography/bathymetry, gravity and magnetic data analysis. The methods are applied to eastern Canada, the Scotian basin and the New England seamounts to investigate the compensation state and strength of the lithosphere of the studied area. They have been proven very useful in analyzing the compensation state of lithosphere, density perturbations in the crust and/or upper-mantle, and their tectonic implications. Different compensation models are proposed for the three study areas. The interpretation of the long- and intermediate- wavelength components of gravity anomalies of eastern Canada involves both lateral density perturbations in the crust and Moho undulation without imposing isostatic compensation at the Moho. The resulting Moho undulation of this model resembles the observed Moho variations from seismic studies, and the crustal model satisfies the observed gravity anomalies. The lithosphere beneath the Scotian basin is not isostatically compensated, and density perturbations exist inside the lithosphere that contribute to the observed gravity anomalies. The same is true for the lithosphere beneath the New England seamounts. The sediments in the Scotian basin and the New England seamounts are elastically supported.

While extensive computation is made for the compensation state of the lithosphere of the three studied areas, the focus of this thesis is on the strength of the North Atlantic oceanic lithosphere beneath the Scotian basin, and its impact on the possibility of initiation of subduction of the lithosphere at the basin. The thin elastic plate modeling of the flexure of the lithosphere beneath the Scotian basin and the New England seamounts reveals that the lithosphere beneath the basin is one to two orders of magnitude weaker (with rigidity values $\sim 10^{21} - 10^{22}$ Nm) than the lithosphere beneath New England seamounts far from the basin (with rigidity values

$\sim 10^{23}$ Nm). I propose that this weakening arises from the thermal blanketing effect of the thick sediments at the basin, and the temperature-dependent rheology of the lithosphere. The weakening of the lithosphere would have a controlling effect on decoupling the continental and oceanic lithosphere at the hinge zone if tensional stress is exerted on the passive continental margin off eastern Canada.

Although passive continental margins are conventionally assumed to be under compression due to the ridge push, ridge push oblique to a margin could produce local tensional or strike-slip reactivation of marginal faults (Ericson, 1993; Ericson and Arkani-Hamed, 1993). The eastern Canadian continental margin is an example of a passive margin oriented oblique to ridge push. A change in spreading direction in the Atlantic 80 m.y. ago has caused the orientation of the ridge push, as indicated by the orientations of recent fracture zones (Klitgord and Schouten, 1986) and measured maximum compressional horizontal stress (Keen and Piper, 1990), to be oblique to both the passive margin of the Scotian basin and the adjacent Grand Banks transform margin. Along the passive margin, an oblique ridge push could produce tensional instead of compressional stress, that would reactivate the pre-existing normal faults created during continental rifting of Africa and North America. The transform margin might also decouple the oceanic and continental lithosphere as a result of the favorable orientation of the transform faults at the margin with respect to ridge push. The weakening of the lithosphere beneath Scotian basin would enhance the possibility of the decoupling. Decoupling of the locked passive margin at the hinge zone by fault reactivation would produce a free boundary flexural condition of the oceanic plate. This would allow the lithosphere beneath the basin to bend more, and juxtapose the oceanic lithosphere to the mantle beneath the continent. The extra sedimentation would further weaken the lithosphere. If subsequent future re-orientation of the spreading ridge produces compressional stress on the margin (Feccenna et al., 1999), subduction of the North Atlantic oceanic lithosphere would initiate along Scotian margin. If a subduction zone can grow laterally, then the whole margins of Atlantic ocean would transform from a passive to an active one (Coakley, 2001).

6.2 Shortcomings and Future Research

The 2-D thin elastic plate modeling of the flexural behaviors of Scotian basin shows that a weak zone exists in the lithosphere beneath the basin that could facilitate initiation of subduction of the North Atlantic lithosphere. The 2-D thin elastic plate model adopted in the thesis is a typical model obtained by averaging several profiles across the basin. It does not, however, reflect the effects of the shape and boundaries of the basin on the flexural response of the lithosphere to the applied loads. A 3-D thin elastic plate model would provide a better understanding of elastic properties of the lithosphere beneath the basin. The Scotian basin has a complex geometry. The change in orientation of the basin from north-northeast off Scotian margin to northeast around Grand Banks transform margin might be reflected in the flexural

properties of the lithosphere beneath. The 3-D thin elastic plate model will incorporate the geometry of the basin as well as variable rigidity values for the oceanic lithosphere beneath the basin and far from the basin. The 3-D flexure equation will be solved using finite difference method in space domain by imposing pinned boundary conditions. The deflection of the oceanic lithosphere when decoupled from the continental lithosphere will be assessed by substantially reducing the rigidity at the ocean-continent boundary to simulate free boundary conditions. The weakening of the lithosphere beneath the basin and its relation with the shape of the basin will be better investigated.

I show in the thesis the possibility of initiation of subduction at the Scotian basin. However, this proposition does not actually demonstrate the dynamic process of initiation of subduction. The final goal of this research will lead to dynamic modeling of the process of the initiation of subduction at the Scotian basin. In the dynamic model, more realistic rheology of the lithosphere and the lower mantle will be used while taking into account the weak zone beneath the basin. Decoupling of the continental and oceanic lithospheres caused by reactivation of the pre-existing faults at the hinge zone will be considered as well as the extra sediments due to the increased deflection of the decoupled oceanic lithosphere. In Kemp and Stevenson's (1996) model, decoupling of the ocean-continent lithosphere leads to up-welling of the underlying mantle to cover the oceanic plate and create a heavy load required for initiation of subduction. I will study the effect of the up-welling of the mantle on initiation of subduction by changing the load due to the extra sediments to the load of more dense basalt. This will further enhance the possibility of initiation of subduction at passive continental margins. Other factors that facilitate initiation of subduction such as the high density phase transition from gabbro to eclogite that increases the gravitational instability of the oceanic lithosphere, the drag induced by the underlying convecting mantle, and the ridge push will be incorporated in the model. A control volume based finite difference method will be used to solve the convection equations. The dynamic modeling will give a deep understanding of the mechanism of initiation of subduction, and show the effects of various driving forces and rheology of the lithosphere and lower mantle on initiation of subduction, therefore, verify my proposition whether subduction could actually initiate at passive continental margin of the Scotian basin.

The 2-D and 3-D thin elastic plate models adopted to investigate the strength of the lithosphere beneath the Scotian basin, and the dynamic modeling of initiation of subduction at the basin can also be applied to study other sedimentary basins on passive continental margins and the possibility of initiation of subduction of the oceanic lithosphere at those basins. The sedimentary basins on the passive margins of the South Atlantic ocean are potential places for future studies. Subduction started at the passive margins along Brazil, but stopped after a short period. The strength of the lithosphere and the applied driving and resisting forces must have played an important role in this process. The 2-D and 3-D thin elastic plate models, and the

dynamic models that are established for studying the Scotian basin can provide a deep understanding of the initial process of subduction along the South Atlantic passive margins.

References

- Coakley, B., 2001. A model for Wilson cycles. *Eos Transactions, AGU* 82(47), Fall Meet. Suppl., Abstract T42G-10.
- Ericson, S.G., 1993. Sedimentary loading, lithospheric flexure and subduction initiation at passive margins. *Geology* 21, 125-128.
- Ericson, S.G., Arkani-Hamed, J., 1993. Subduction initiation at passive margins: the Scotia basin, eastern Canada as a potential example. *Tectonics* 12, 678-687.
- Faccenna, C., Davy, P., Brun, J. et al., 1999. Initiation of subduction at Atlantic-type margins: insights from laboratory experiments. *Journal of Geophysical Research* 104, 2749-2766.
- Keen, M.J., Piper, D.J.W., 1990. Geophysical and historical perspective. In *Geology of the Continental Margin of Eastern Canada*, chapter 1. Edited by M.J. Keen and G.L. Williams. Geological Survey of Canada, *Geology of Canada*, vol. 2, pp. 5-30.
- Kemp, D.V., Stevenson, D.J., 1996. A tensile, flexural model for the initiation of subduction. *Geophysical Journal International* 125, 73-94.
- Klitgord, K.D., Schouten, H., 1986. Plate kinematics of the central Atlantic. In Vogt, P.R. and Tucholke, B.E., eds., *The western North Atlantic region*: Boulder, Colorado, Geological Society of America, *geology of North America*, v. M, pp. 351-378.

Appendix A



National Research
Council Canada

Conseil national
de recherches Canada

NRC · CNRC

Reprinted from
**Canadian
Journal of
Earth
Sciences**

Réimpression de la
**Revue
canadienne
des sciences
de la Terre**

**Joint inversion of gravity and magnetic
anomalies of eastern Canada**

Ying Zheng and Jafar Arkani-Hamed

Volume 35 • Number 7 • 1998

Pages 832–853

Joint inversion of gravity and magnetic anomalies of eastern Canada

Ying Zheng and Jafar Arkani-Hamed

Abstract: The power spectra and degree correlation of the surface topography and free-air gravity anomalies of eastern Canada show that the gravity anomalies are subdivided into three parts. The short-wavelength components (30–170 km, shorter than 30 km are not well resolved) largely arise from density perturbations in the crust and to a lesser extent from the surface topography and Moho undulation, whereas the contribution of intracrustal sources to the intermediate-wavelength components (170–385 km) is comparable with that of the topography. The long-wavelength components (385–1536 km) are overcompensated at the Moho. We present a crustal model for the intermediate- and long-wavelength components which takes into account the surface topography, density perturbations in the crust, and Moho undulation with a certain degree of isostatic compensation. The general characteristics of this model resemble the crustal structure revealed from seismic measurements. The reduced-to-pole magnetic anomalies of eastern Canada show no pronounced correlation with the topography and with the vertical gradient of the gravity anomalies, suggesting that the source bodies are within the crust and Poisson's relationship does not hold over the entire area. Assuming that the magnetic anomalies arise from induced magnetization, lateral variations of magnetic susceptibility of the crust are determined while taking into account the effects of the surface topography and the Moho undulation of our crustal model. The intermediate- and long-wavelength components of the susceptibility contrasts delineate major collision zones as low-susceptibility regions. We interpret this in terms of thermal demagnetization of the high-magnetic crustal roots beneath the collision zones.

Résumé : La courbe de puissance et le degré de corrélation de la topographie de surface avec les anomalies du champ de pesanteur après correction à l'air libre, dans l'Est du Canada, montrent que les anomalies gravimétriques sont subdivisées en trois parties. Les composantes des longueurs d'ondes courtes (30–170 km, celles plus courtes que 30 km ne sont pas bien résolues) sont reliées principalement aux perturbations de densité dans la croûte et elles sont influencées, à un moindre degré, par la topographie de surface et l'ondulation du Moho, tandis que la contribution de sources intracrustales aux composantes de longueur d'ondes intermédiaires (170–385 km) est comparable à celle de la topographie. Les composantes des longueurs d'ondes longues (385–1536 km) sont surcompensées au niveau du Moho. Nous présentons un modèle crustal des composantes de longueur d'ondes intermédiaire et longue, qui tient compte de la topographie de surface, des perturbations de la densité au sein de la croûte, et de l'ondulation du Moho avec une certaine compensation isostatique. L'essentiel exprimé dans ce modèle ressemble à la structure crustale déduite des images sismiques. Les anomalies magnétiques, réduites à des pôles, de l'Est du Canada, ne montrent pas de corrélation évidente avec la topographie et ni avec le gradient vertical des anomalies gravimétriques, ce qui suggère que les corps responsables des anomalies sont localisés à l'intérieur de la croûte, et qu'il serait imprudent d'appliquer la relation de Poisson d'un bout à l'autre de la région. Si on admet que les anomalies magnétiques sont causées par une aimantation induite, il est donc possible de déterminer les variations latérales de la susceptibilité magnétique de la croûte en tenant compte des effets de la topographie de surface et de l'ondulation du Moho décrits dans notre modèle crustal. Les composantes des longueurs d'ondes intermédiaire et longue des contrastes de susceptibilité identifient les zones de collision majeure comme étant des régions de faible susceptibilité. Ces données sont interprétées en termes de désaimantation thermique des racines crustales de haut-magnétique sous-jacentes aux zones de collision.

[Traduit par la Rédaction]

Introduction

Magnetic and gravity anomaly maps have been being compiled (e.g., Tanner et al. 1988; Hinze et al. 1996; Johnson et al. 1997) on a continental scale, largely because these maps provide good infor-

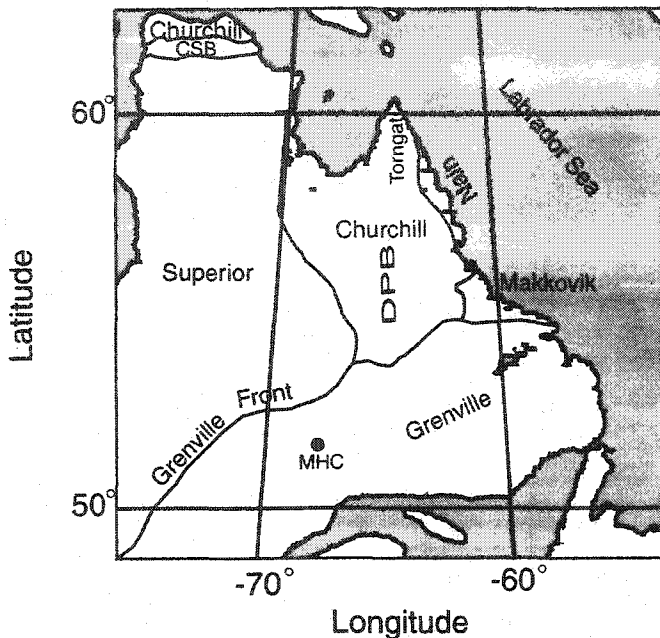
mation about regional tectonic structure of the crust. Difficulty arises partly from the lack of pertinent information about the resolution of the original data used in the compilations, in particular old data, and partly from data processing. It is therefore necessary to examine the compiled maps for internal consistency and compare them with other independent observations. Comparison of independently acquired data sets over a given region is by far the most assuring. However, multiple surveying is very costly and time consuming. Alternatively, a compiled map can be compared with maps that reflect other physical properties of the source bodies. For example, studies of the gravity and magnetic anomalies of some well-known structures in a region would

Received October 8, 1997. Accepted April 3, 1998.

Ying Zheng and J. Arkani-Hamed.¹ Earth and Planetary Sciences, McGill University, 3450 University Street, Montreal, QC H3A 2A7, Canada.

Corresponding author (e-mail: jafar@planet.eps.mcgill.ca).

Fig. 1. A simplified tectonic map of eastern Canada based on the *Tectonic map of Canada* (Geological Survey of Canada 1968). The map also shows the locations cited in the text. CSB, Cape Smith belt; DPB, De Pas Batholith; MHC, Manicouagan - Hart Jaune complex.



yield better understanding of their main characteristics and a better means of interpreting other similar anomalies of the region. In the present paper, we use topography and gravity and magnetic anomaly maps to study the main characteristics of the lateral variations in density and magnetization of the crust in the eastern Canada.

The ultimate goal of magnetic and gravity data compilation and analysis is to determine the source distribution. In this paper we conduct a systematic covariance analysis of topography, gravity, and magnetic anomalies to extract as much information as possible about their relationship and obtain useful criteria to distinguish certain physical processes that have created lateral variations within the crust. Modelling gravity and magnetic anomalies in terms of common sources is generally carried out by a forward procedure based on the assumption that Poisson's relationship holds between these anomalies. This forward modelling is useful on a small scale and usually for a single source body. It is demonstrated in this paper that the assumption is not valid a large scale, at least over eastern Canada. We use the topography-gravity relationship to constrain the density perturbations in the crust and the thickness of the crust beneath eastern Canada. This in turn is used to obtain lateral variations in the crustal magnetization through the inversion of magnetic anomalies that takes into account the effects of the surface topography and the Moho undulation. Geophysical implications of the main characteristics of the gravity and magnetic anomalies are discussed in some detail.

Topography, gravity, and magnetic relationship

The area of interest includes the continental part of eastern Canada and a large portion of the Labrador Sea with

oceanic crust. The continental area consists of five tectonic provinces, Superior, Churchill, Nain, Makkovik, and Grenville, their collision zones, and numerous local geological features within each province. Figure 1 shows the tectonic provinces and locations cited in this paper. The study area also includes the ocean-continent boundary and extensive continental shelf created during the continental rifting that produced the Labrador Sea. Therefore, diverse tectonic processes in the last 1-2 Ga have left distinct imprints that provide a good opportunity to study their major characteristics as revealed from lateral heterogeneities they have created in the crust.

The topography, gravity, and magnetic relationships are studied both in Fourier spectral domain and space domain. For this purpose, a given data set is gridded over 256×256 equal-area grid points with a grid interval of 6 km. The Fourier transformations are carried out using a Fast Fourier Transformation technique, in which the underlying implicit assumption is the periodicity of the data. To suppress the Gibb's ringing, which is usually created upon Fourier transformation due to sharp discontinuities at the boundaries, we gradually taper to zero the boundaries of a map by applying a one-dimensional (1D) version of the Hanning function (see below) over a narrow strip containing 20 grid points. The mean value of a map is subtracted before tapering, since we are interested in lateral variations.

Topography map

The equivalent rock topography (called hereafter topography, T , for simplicity) map of the area (Fig. 2a) is derived using the ETOPO5 data base, obtained from the Geological Survey of Canada (W. Miles, personal communication, 1997). It is identical to the surface topography over continental areas. The offshore water column of density 1000 kg/m^3 is compressed to an equivalent rock density of 2700 kg/m^3 , and the resulting thickness is added to the bathymetry to obtain the equivalent rock topography of the sea.

Gravity map

For the free-air gravity anomaly (called hereafter the gravity anomaly, g^0) map of the area (Fig. 2b), data over the continent are obtained from the Geological Survey of Canada (W. Miles, personal communication, 1997) and over the sea from satellite data from Sandwell and Smith (1997). The gaps between the two data sets are filled using a weighted averaging procedure as follows. The gravity at a grid point with no original data is determined by averaging the gravity at points within a circular window of radius $R = 18 \text{ km}$, weighted by a two-dimensional Hanning function:

$$[1] \quad W(r) = 0.5 \left[1 + \cos\left(\frac{\pi r}{R}\right) \right]$$

where r is the distance from the grid point.

The power spectrum of the gravity anomalies $P_k^{g^0}$ is determined by

$$[2] \quad P_k^{g^0} = \sum_u \sum_v (|g_{u,v}^0|^2 + |g_{u,-v}^0|^2)$$

where indices u, v denote the Fourier transform, and u and v are the wave numbers along the x (west-east) and y (south-

Fig. 2. (a) Equivalent rock topography. (b) Free-air gravity anomalies. (c) Distribution of gravity stations. (d) Space-domain correlation of the topography and gravity anomalies.

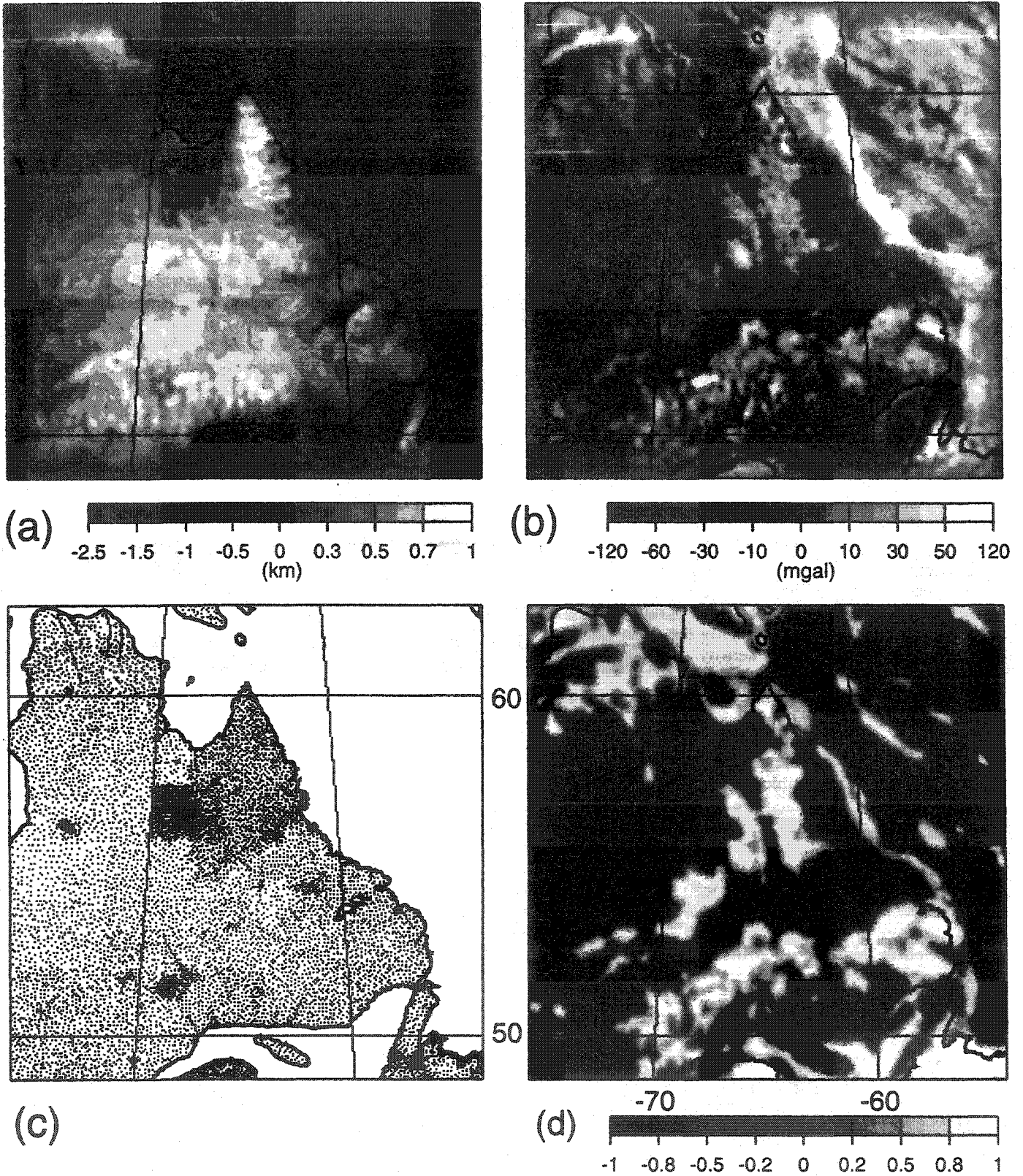
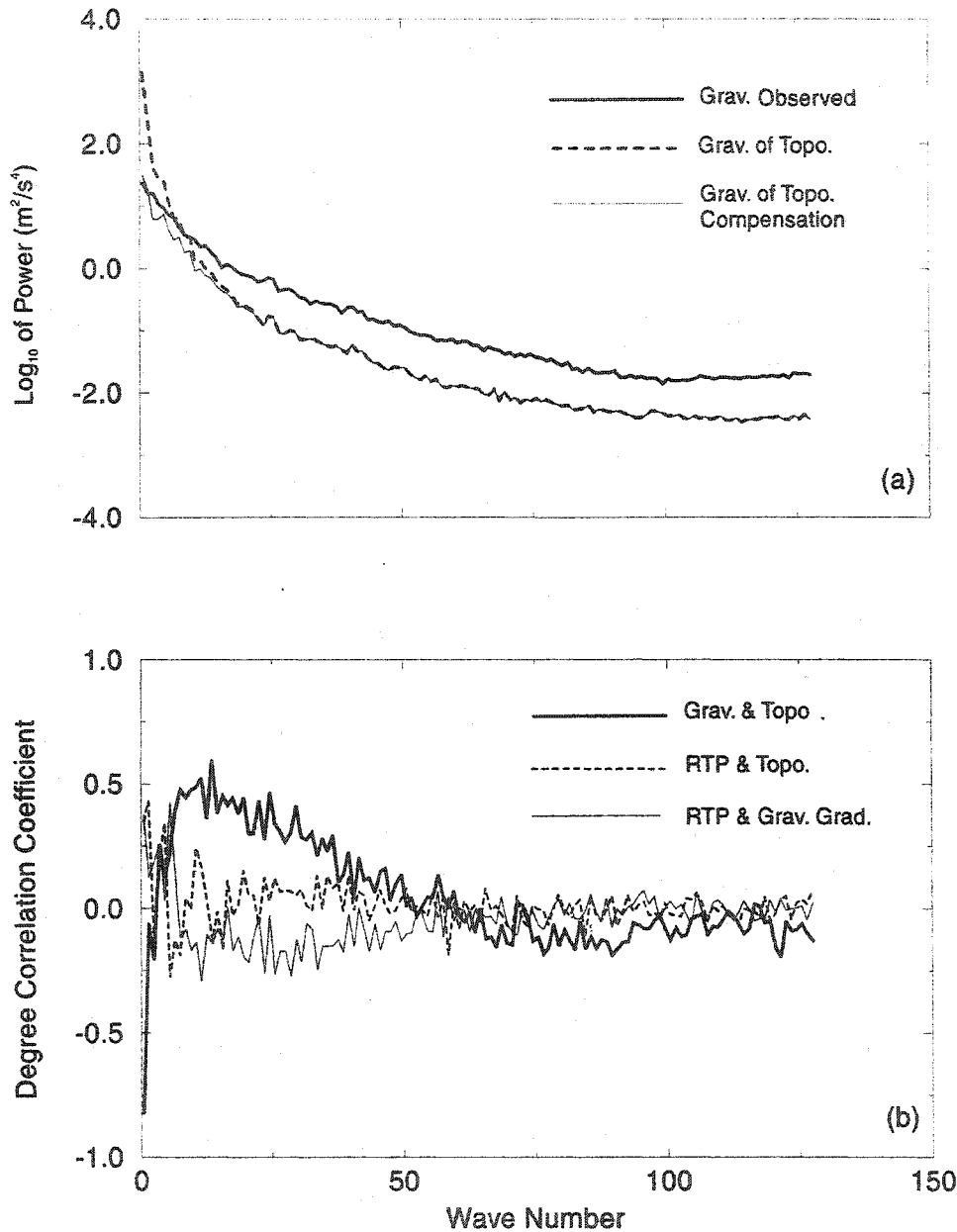


Fig. 3. (a) Power spectra of free-air gravity anomalies, the gravity field due to the topography, and the gravity field of the topography which is compensated at 37 km depth. (b) Spectral-domain degree correlation coefficients between gravity anomalies and topography, reduced-to-pole (RTP) magnetic anomalies and topography, and reduced-to-pole magnetic anomalies and vertical gradient of gravity anomalies.



north) directions, respectively; and k is the two-dimensional wave number defined as

$$k = (u^2 + v^2)^{1/2}$$

responding to a wavelength $\lambda = L/k$, where L is the dimension of the area (1536 km). The power decreases continuously with increasing wave number (Fig. 3a), by about two orders of magnitude between wave numbers 1 and 50 (wavelengths of 1536 and 30 km). Included in Fig. 3a is the power spectrum of the gravity field due to the topography calculated from

$$g_{u,v}^T = 2\pi G \rho_c e^{-kz} T_{u,v}$$

where G is the gravitational constant, ρ_c (2700 kg/m³) is the surface rock density, and z denotes the altitude, which is set to zero. The surface topography is approximated by a surface mass distribution. The observed gravity anomalies arise from the surface topography, lateral variations of density in the crust, undulation of the Moho, and possible lateral variations of density in the mantle. The figure presents a very interesting point. The observed gravity anomalies have higher power than those produced by the topography over wave numbers greater than nine (wavelengths shorter than about 170 km), despite the fact that any possible compensating mass at the Moho would reduce the observed gravity anomaly. This point is illustrated by the power spectrum of the gravity anomaly of the topography which is compensated at

the Moho by an Airy compensation mechanism. Included in Fig. 3a is the gravity anomaly of the Airy-compensated topography, g' , determined by

$$[5] \quad g'_{u,v} = 2\pi G\rho_c e^{-kz} (1 - e^{-kH_c}) T_{u,v}$$

where H_c denotes the average depth to the Moho, assumed to be 37 km, which is an average depth based on seismic measurements (Mereu et al. 1986; Mooney and Braille 1989). Comparing eqs. [4] and [5] shows that g' is always smaller than g^T for finite values of H_c . The effect of the compensating mass at the Moho, however, diminishes exponentially as the wave number increases, and the gravity of the compensated topography approaches that of the topography alone. Note that the power spectrum of the observed gravity anomalies is larger than that of the compensated topography over the entire range of the spectrum. This suggests that a simple Airy compensation model cannot explain the topography-gravity relationship of eastern Canada. Strong density perturbations must exist within the crust.

The topography-gravity relationship is further investigated quantitatively using the degree correlation coefficient η_k between gravity anomalies and topography (Fig. 3b):

$$[6] \quad \eta_k = \frac{\sum_u \sum_v (T_{u,v} g'_{u,v} + T_{u,-v} g'_{u,-v})}{(P_{u,v}^T P_{u,v}^{g'})^{1/2}}$$

in which the summations are over all values of u and v such that

$$[7] \quad k - \frac{1}{2} < (u^2 + v^2)^{1/2} < k + \frac{1}{2}$$

No significant correlation is found between the topography and gravity anomaly over wave numbers greater than 50 (wavelengths shorter than 30 km). These features of the gravity anomalies are not well resolved. To resolve a feature with a wavelength of 30 km, at least three samples, and preferably five, must be obtained within 30 km. The gravity stations on the continent (Fig. 2c) have quite irregular spacing, with distances usually greater than 10 km, confirming our observation that these very short wavelength components are not properly resolved and thus are unreliable. They will not be considered further and are also filtered out from all of the maps presented in this paper. Over wave numbers 9–50 (wavelengths between 30 and 170 km, called hereafter the short-wavelength components), there is a positive correlation between the topography and gravity anomalies. However, the power of the gravity anomalies is significantly greater than that of the gravity due to the topography. The lateral density perturbations in the crust must be large enough not only to overcome the reducing effect of any possible isostatic compensation of the topography, but also to contribute significantly to the observed anomalies. A positive, but low, correlation exists between the topography and gravity over wave numbers 4–9 (wavelengths between 170 and 385 km, called hereafter the intermediate-wavelength components), and the power of the observed gravity anomalies is less than or equal to that of the gravity produced by the topography. The topography is compensated over these wavelengths with different degrees of compensation or at different depths of compensation, depending on the wave-

length. Finally, the long-wavelength components of the gravity anomalies with wave numbers 1–4 (wavelengths between 385 and 1536 km) show negative correlation with the topography, suggesting that the topography is overcompensated.

The above spectral-domain degree correlations provide good information about the correlation over the entire area for features specified by certain wavelengths. They do not, however, show where the features correlate positively and where negatively. To identify the locations, we calculate the space-domain correlation between the topography and gravity anomaly maps. The correlation coefficient, η , at a given grid point is determined by

$$[8] \quad \eta = \frac{\sum_{n=1}^N g_n^o T_n W_n}{\left[\left(\sum_{n=1}^N (g_n^o)^2 W_n \right) \left(\sum_{n=1}^N T_n^2 W_n \right) \right]^{1/2}}$$

where N is the total number of grid points inside a circle of radius R_o , and W_n is the 2D Hanning function defined by eq. [1], now centred at the grid point. Several values of R_o are examined. Figure 2d presents the space-domain correlation calculated using the R_o value of 30 km, which retains almost the entire reliable signature contained in the topography and gravity anomaly maps. This radius is used in all space-domain correlation maps in this paper. Figure 2d is dominated by the long-wavelength components displaying negative correlation over the main parts of the continent and Labrador Sea. This is expected because of the negative correlation of the long-wavelength components of the topography and gravity anomalies and their substantially high power (see Fig. 3a). There are positive correlations over some positive gravity anomalies in Grenville and Churchill provinces and in the northwest of Superior Province. A well-defined negative correlation delineates the Grenville-Superior collision zone, but other collision zones do not seem to be as distinct.

Magnetic map

The magnetic anomaly map of eastern Canada (Fig. 4a) is derived using the magnetic data base compiled by the Atlantic Geoscience Centre over the north polar region (Macnab et al. 1995). Data over the Labrador Sea are compiled from marine and aeromagnetic surveys using detailed cross-over analysis and stringent selection criteria which resulted in reliable anomalies (Verhoef et al. 1996). The continental part of the data base was extracted directly from an earlier compilation of the North American magnetic anomaly map (Hinze et al. 1988). Comparison of satellite magnetic anomalies of North America with the upward continued version of this compiled map demonstrated that the long wavelengths of the map, longer than about 300 km, are contaminated by compilation processes (Arkani-Hamed and Hinze 1990). A similar conclusion was drawn by Pilkington and Roest (1996) over the whole of Canada. Further examination of the compiled map over conterminous United States showed that wavelengths between 170 and 500 km are more reliable than

Fig. 4. (a) Magnetic anomalies. (b) High-altitude magnetic profiles. (c) Magsat dawn map. (d) Low-pass filtered low-altitude magnetic anomalies.

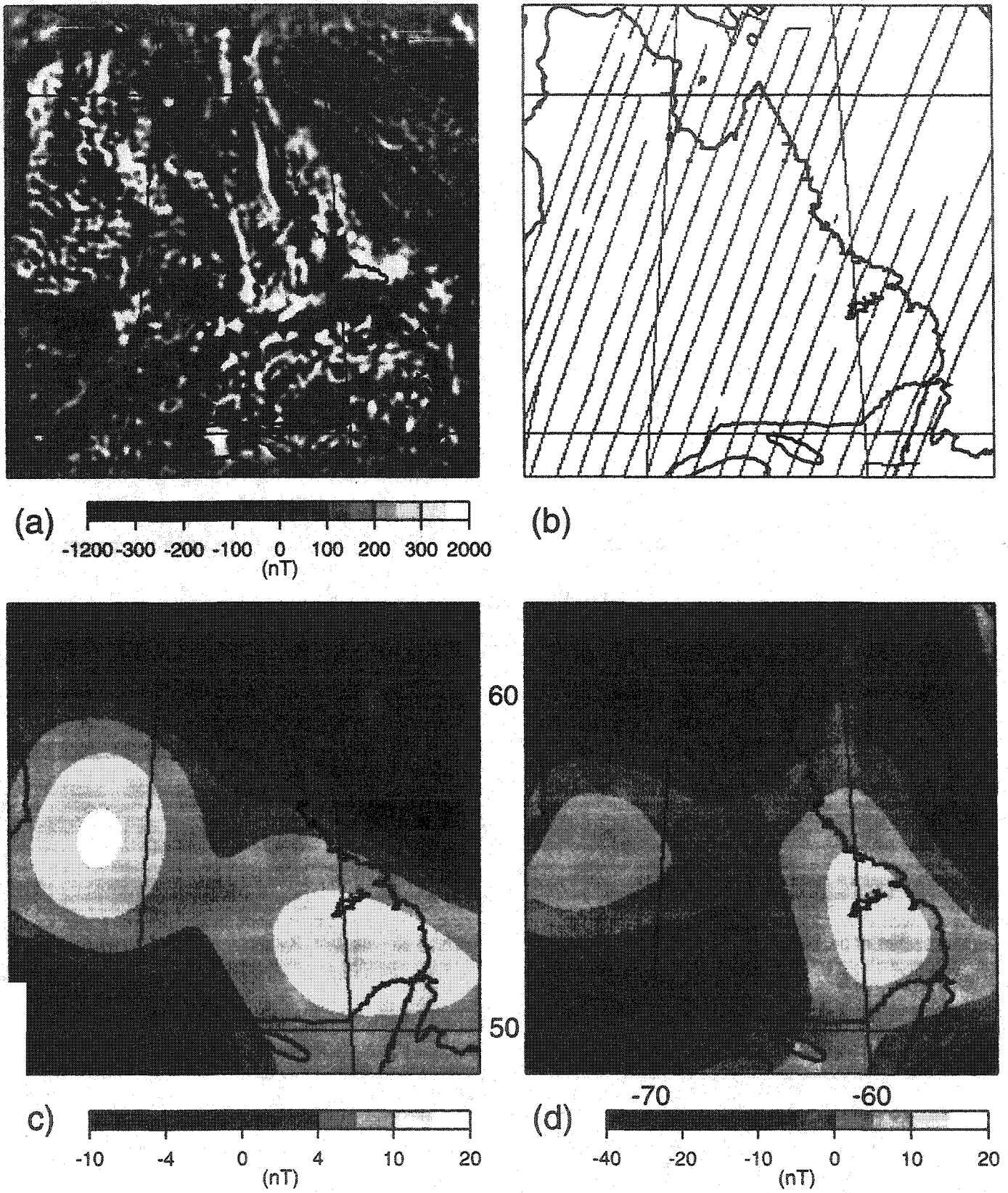
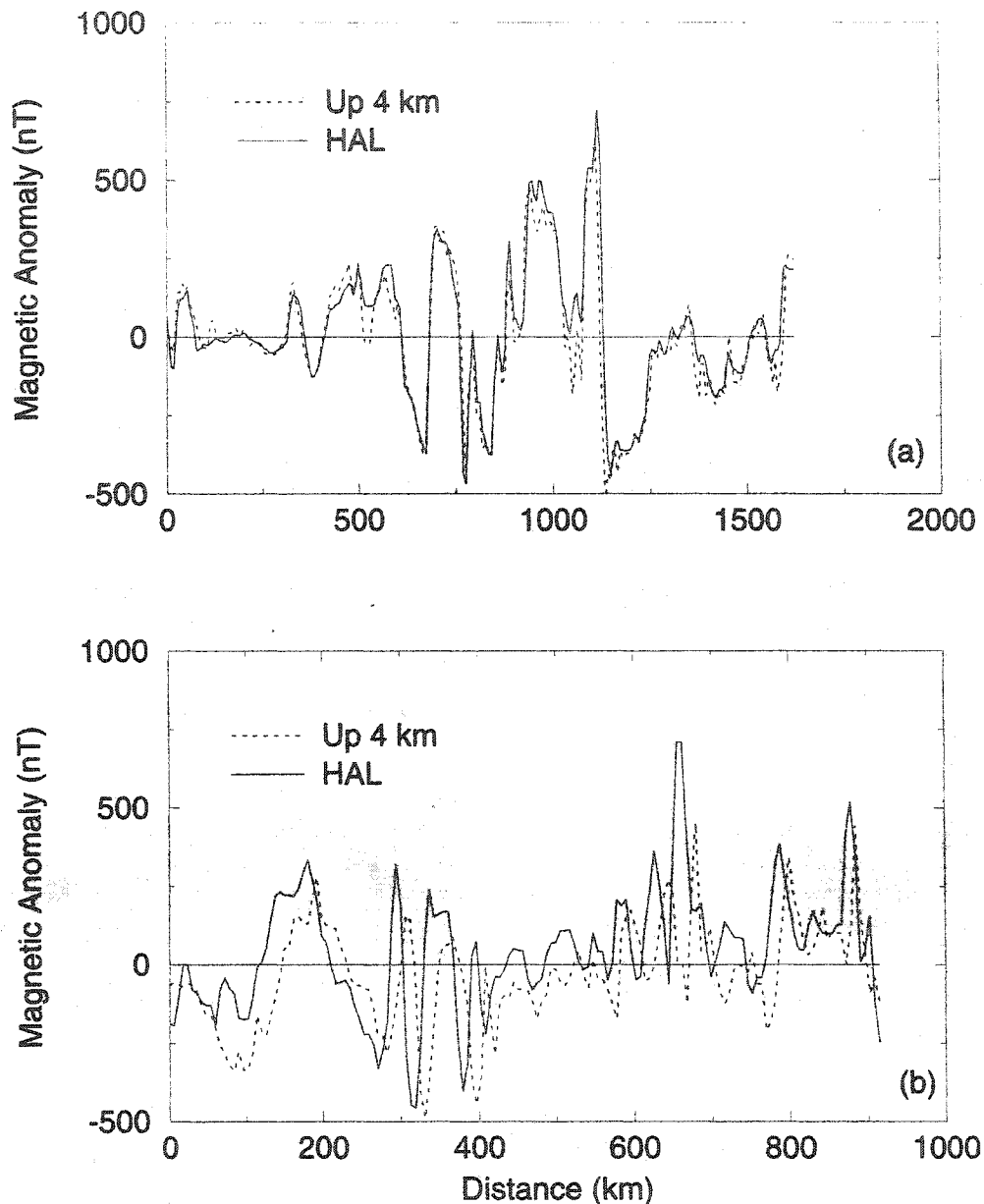


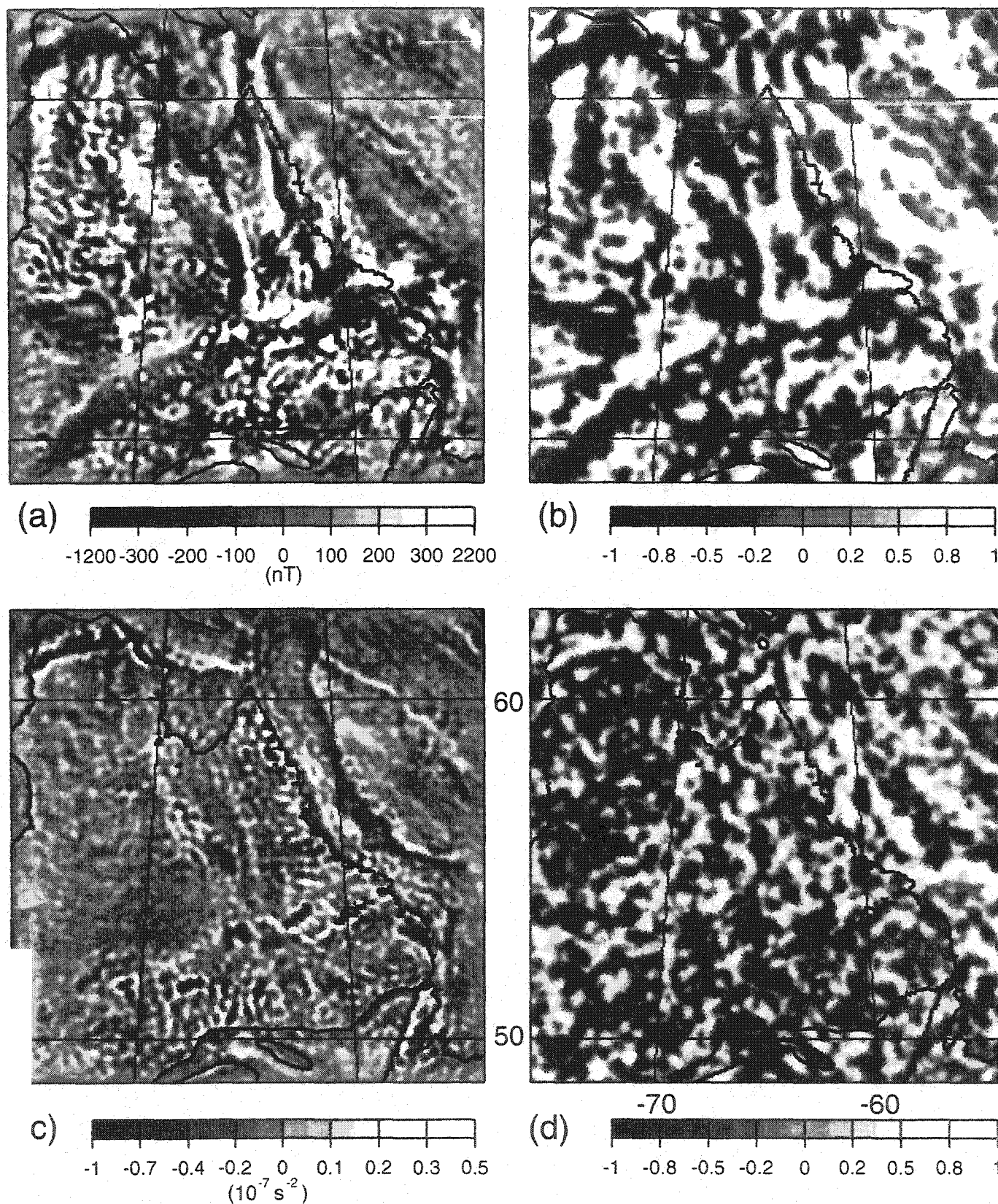
Fig. 5. Comparison of high-altitude magnetic anomaly profiles (HAL) with the upward-continued, low-altitude magnetic anomalies to 4 km elevation.



others (Grauch 1993). Therefore, we need to assess the magnetic anomalies of the continental part of eastern Canada before further analysis and interpretation. For this purpose, we use the high-altitude magnetic profiles over eastern Canada (Fig. 4b) acquired at 4 km elevation by the Geological Survey of Canada, a total of 22 profiles (M. Pilkington, personal communication, 1997). Pilkington and Roest (1996) gridded the profiles over the whole of Canada at a 20 km interval, using a 2D Hanning function of radius 50 km. The large distance between profiles, an average of about 60 km, resulted in a very anisotropic data distribution with a much higher resolution along profiles compared with that across profiles. The resulting magnetic anomaly map probably contained artifacts because the radius of the Hanning function was comparable with the distance between the profiles. The gridding also degraded the high resolution along the profiles.

Therefore, no attempt is made in the present paper to grid the high-altitude data. Rather, we upward continue the low-altitude magnetic anomaly map (Fig. 4a) to 4 km altitude and compare the resulting anomalies with the high-altitude data along the profiles. They are almost identical except for the first four profiles in the western part, which are slightly shifted. Figure 5 shows two high-altitude and upward-continued profiles, one with the maximum shift and one with no shift. The other three shifted profiles are shifted by less than 60% of this maximum. The close similarity between the high-altitude and the upward-continued magnetic anomalies indicates that the short- and intermediate-wavelength components of the magnetic anomaly map are reliable. To examine the long-wavelength components of the magnetic anomaly map, we extract satellite magnetic anomalies over the study area from Magsat dawn data (Fig. 4c),

Fig. 6. (a) Reduced-to-pole magnetic anomalies. (b) Space-domain correlation of the reduced-to-pole magnetic anomalies and topography. (c) Vertical gradient of gravity anomalies. (d) Space-domain correlation of the reduced-to-pole magnetic anomalies and the gravity gradient.



which are least contaminated by noncrustal noise (Ravat et al. 1995), and compare with a low pass filtered version of the magnetic anomaly map. (We first examined the Fourier-domain upward-continuation method, but concluded that it was not suitable over a small area such as eastern Canada, partly because of the high altitude of Magsat, an average of 400 km, and mainly because a large positive satellite magnetic anomaly is centred almost at the western border of the study area. The corresponding anomaly in our magnetic anomaly map is tapered to zero at the border to apply the Fast Fourier transformation required for the upward continuation. This tapering strongly reduced the anomaly and shifted its maximum eastward.) Filtering is done in the space domain through weighted averaging over a moving circular window, weighted by the 2D Hanning function of radius 600 km. The Magsat anomaly map consists of wavelengths longer than about 670 km (Ravat et al. 1995). The resulting low pass filtered magnetic anomaly map (Fig. 4d) shows good correlation with the satellite map. The correlation is not expected to be much better, as satellite maps do not usually show exact correlation with low-altitude magnetic maps (e.g., LaBrecque and Cande 1984; LaBrecque and Raymond 1985; Toft and Arkani-Hamed 1992; Arkani-Hamed et al. 1995). Also, Figs. 4c and 4d do not contain exact wavelengths; rather, the space-domain filter is an approximation of the spherical harmonic domain filter used in deriving the Magsat magnetic anomaly map. This good correlation emphasizes that the long-wavelength components of the low-altitude magnetic anomalies of eastern Canada are not significantly contaminated by the compilation processes. These two examinations provide good confidence in the magnetic anomalies seen in Fig. 4a.

Unlike gravity anomalies that directly correlate with source bodies, magnetic anomalies do not show a direct correlation with magnetic bodies, largely because the core field direction is not vertical, except in polar regions. A body carrying an induced magnetization produces a strong positive magnetic anomaly directly above itself when it is located at the geomagnetic poles, but a relatively weaker and negative anomaly at the equator. The magnetic anomaly is displaced towards the equator with respect to the body at mid-latitudes. The shift depends on the core field direction, and may change significantly over a large area such as eastern Canada, where the core field direction changes appreciably (see the core field model by IAGA Division V Working Group 8 1996). To overcome these difficulties, we differentially reduce the magnetic anomalies to the north pole using the algorithm developed by Arkani-Hamed (1988). Figure 6a shows the resulting reduced-to-pole magnetic anomalies (called hereafter RTP anomalies) that should directly correlate with induced magnetic sources. In the continental area, many small-scale positive anomalies exist in the northern parts of Superior Province and in the eastern parts of Grenville Province, and an elongated positive anomaly is associated with De Pas Batholith outlined in the tectonic map of eastern Churchill Province (Wardle et al. 1990). The Grenville Front and the Cape Smith belt are delineated by negative RTP anomalies. Over the Labrador Sea, the continental shelf shows several small-scale positive anomalies, and major marine magnetic anomalies are depicted in the oceanic part of the sea.

No appreciable correlation exists between the topography and RTP anomalies as indicated by their degree correlation coefficients in Fig. 3b, except over a few wavelengths where the correlation is still less than 0.5. This lack of consistent correlation is better illustrated in their space-domain correlation map (Fig. 6b). However, there seems an overall negative correlation between the topography and RTP anomalies over the Grenville Front and Cape Smith belt.

It is desirable to investigate whether the gravity and magnetic anomalies are associated with common source bodies. There is no direct relationship between the magnetic properties and densities of rocks. High-density mafic rocks are usually more magnetic than low-density sedimentary rocks. However, metamorphism may remove remanent magnetization while producing denser minerals, and serpentinization may precipitate magnetite and enhance magnetization while reducing the bulk density of rocks (Toft et al. 1990). Hydration in metamorphosed rocks may also reduce magnetization (Toft et al. 1993). On the other hand, broad features of crustal magnetization in the continent may correlate directly with the undulation of the Moho, if the Moho is the lower boundary of the magnetic crust as suggested by Wasilewski et al. (1979). Modelling the gravity and magnetic anomalies by a common source body is based on the Poisson relationship between the RTP anomaly, F , and the vertical gradient of the gravity anomaly, V :

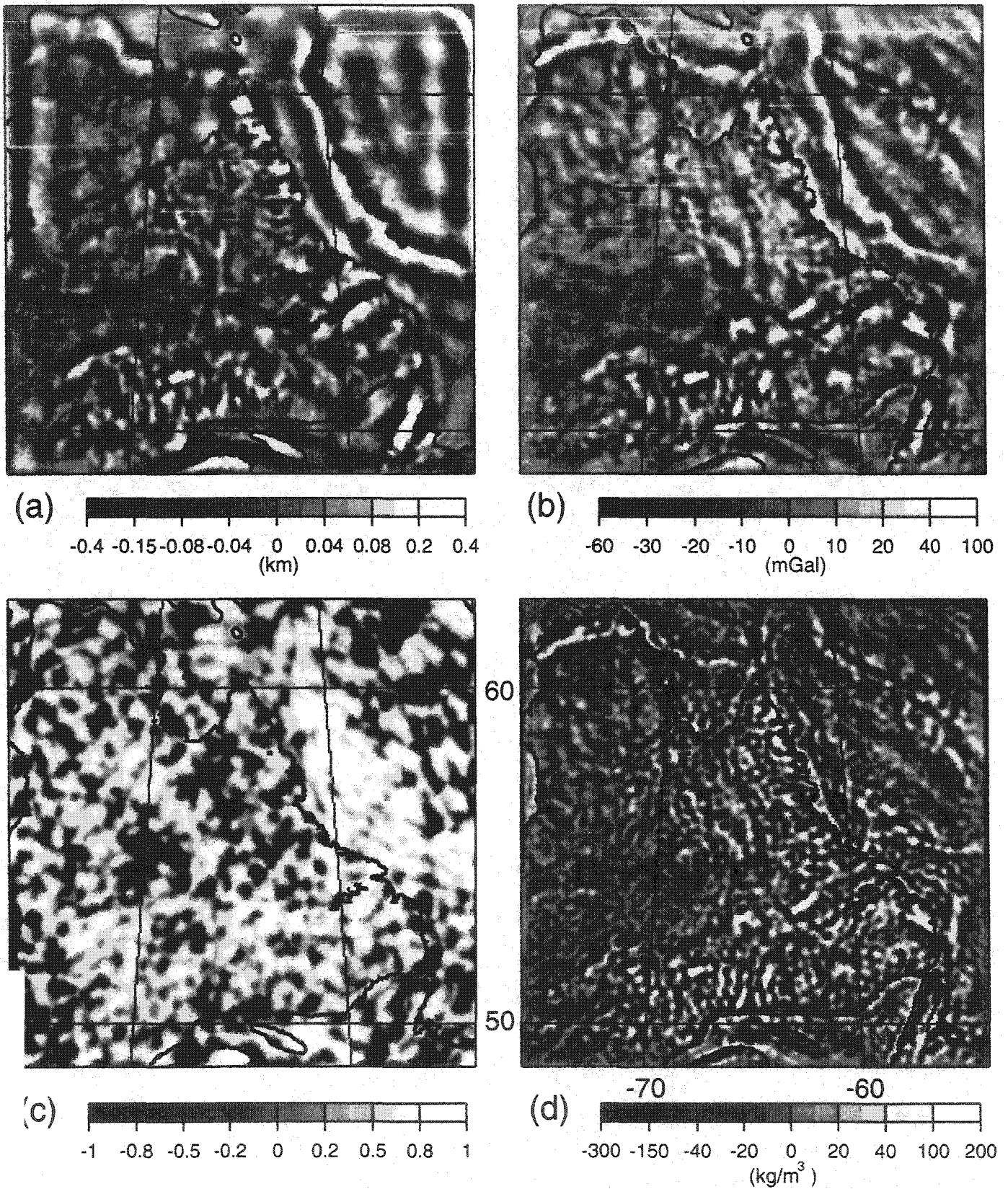
$$[9] \quad F_{u,v} = \left(\frac{\mu_0 m}{4\pi G\rho} \right) V_{u,v}$$

where μ_0 is the magnetic permeability of the air; and m and ρ are the magnetization intensity and density of the body, respectively. The underlying assumption made in deriving this relationship is that the source body has a uniform density and magnetization. Such modelling is therefore limited to a local area and generally to a single body. The relationship may not hold in an extended area where many bodies of diverse nature contribute to the gravity and magnetic anomalies. To investigate this point we calculate the vertical gradient of the gravity anomalies using

$$[10] \quad V_{u,v} = -kg_{u,v}^0$$

The resulting gravity gradient map (Fig. 6c) is dominated by small-scale features because of their substantial enhancement through differentiation. The gravity gradient map better delineates the ocean-continent boundary and Cape Smith belt. Some small-sized features are scattered over the Superior-Churchill boundary and Grenville Front, which collectively trace these long collision structures. A similar calculation was made by Pilkington and Grieve (1989), who reduced the magnetic anomalies to the pole through a space-domain differential reduction procedure. They divided the continental part of eastern Canada into seven regions based on their space-domain correlation and Poisson's coefficient maps. Although there is good agreement between our results and theirs over most regions, we do not see clear evidence either in their map or in our map that supports such a division. As a matter of fact, there seems to be no consistent correlation between the gravity gradient and RTP anomalies over the entire area (except for positive correlations over the ocean-continent boundary and Cape Smith belt), as illus-

Fig. 7. (a) Short-wavelength components of the topography. (b) Short-wavelength components of the free-air gravity anomalies. (c) Space-domain correlation of the topography and gravity anomalies. (d) Density perturbations within the crust.



trated by their space-domain correlation map (Fig. 6d) and Fourier-domain degree correlation coefficients (see Fig. 3b). The correlation coefficients are positive, but small, over wavelengths longer than 190 km. This lack of pronounced correlation between the RTP anomalies and gravity gradient indicates that the Poisson relationship is not valid over the entire area, although it is probably useful for some of the small-scale local anomalies.

Interpretation of free-air gravity anomalies

We seek physical processes that are responsible for the diverse characteristics of the topography and gravity spectra discussed above and investigate each part of the spectra accordingly.

Short-wavelength components

Figures 7a and 7b present the high-pass filtered topography and gravity maps of eastern Canada consisting of the short-wavelength components. The filter removed all wavelengths longer than 192 km and kept unchanged those shorter than 154 km. The amplitudes of the remaining wavelengths were suppressed by a 1D Hanning function in the spectral domain to avoid any sharp cutoff that might create ringing in the inverse Fourier transform (Gibb's ringing). The figures are dominated by small-scale features, some of which show good correlation with geologic structures, in particular the anomaly associated with the ocean-continent boundary in the Labrador Sea. This is more evident in their space-domain correlation map (Fig. 7c). The correlation is consistently positive and high along the boundary. There are several small-sized positive gravity anomalies in Nain Province that correlate with the topography, but no consistent correlation exists elsewhere. The Cape Smith belt is delineated by a well-defined gravity anomaly, but does not show a pronounced topography. The other collision zones have no consistent gravity-topography association over these short wavelengths.

The higher power of the short-wavelength components of the observed gravity anomalies compared with that of the gravity arising from the topography indicates that the observed anomalies are strongly dominated by density perturbations within the crust. This is expected for old tectonic zones. For example, during continental collision, adjacent crustal materials intrude from one side to the other due to prevailing strong horizontal forces, mafic and ultramafic intrusions occur because of the reactivation of the bottom of the younger province and related diapiric upwelling, and new minerals are formed through metamorphism (Dewey and Burke 1973). These processes introduce lasting small-scale density heterogeneities within the crust, whereas small-scale surface topography is easily reduced by subsequent erosion. The wavelengths are short enough for the lateral variations in mantle density and the Moho undulation to have negligible contributions to the observed gravity anomalies. Therefore, the observed gravity anomalies are related to the surface topography and the density perturbations $\delta\rho$ in the crust with a flat Moho:

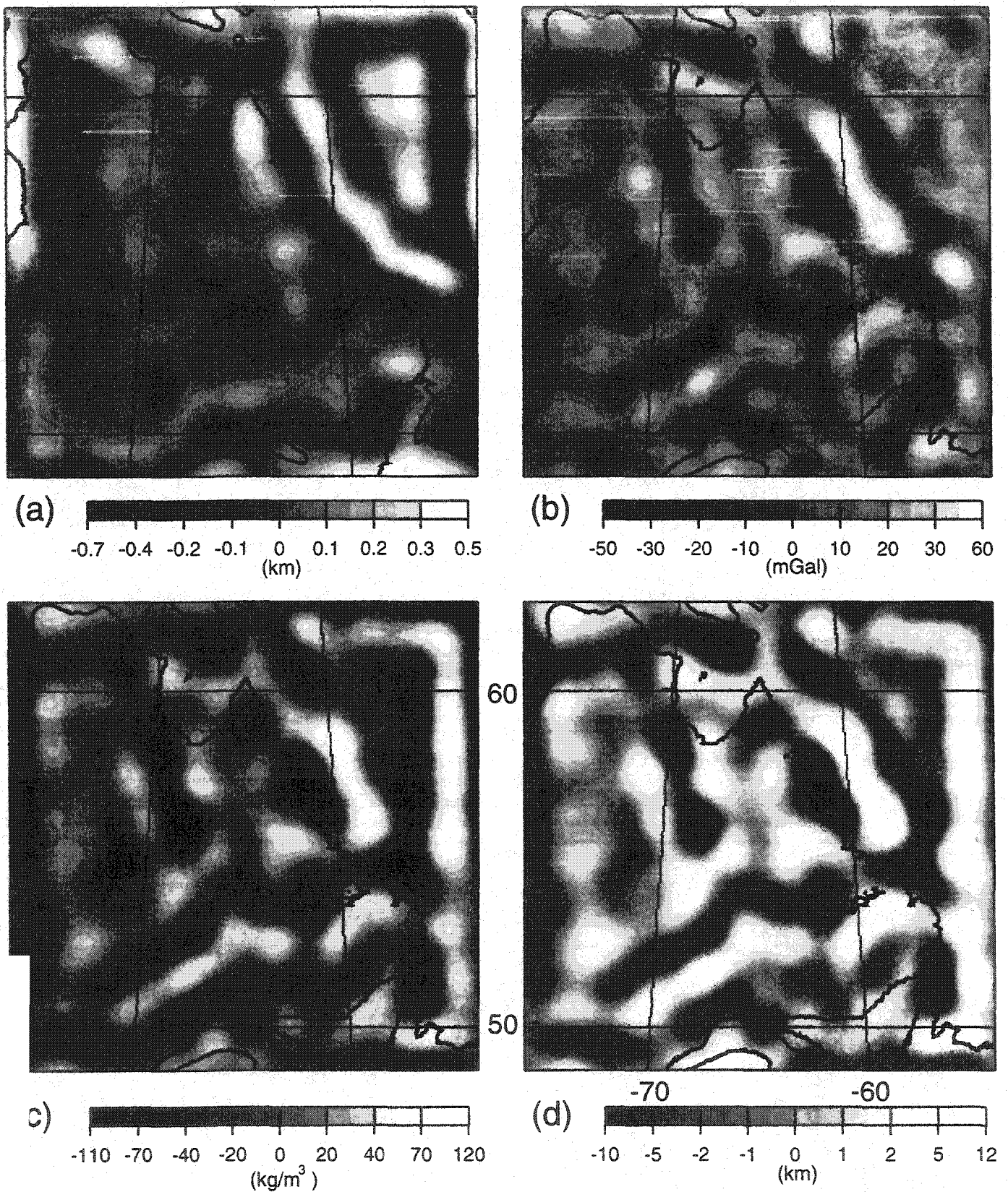
$$[11] \quad g_{u,v}^0 = 2\pi G e^{-kz} \left[\rho_c T_{u,v} + \int_{-H}^0 e^{kz'} \delta\rho_{u,v} dz' \right]$$

where the topography is regarded as a surface mass distribution and the altitude z is set to zero. The gravity arising from the density perturbations, the second term in the right-hand side, depends on the vertically integrated density perturbations weighted by an exponential geometric function. Figure 7d shows the vertically averaged density perturbations, $\langle \delta\rho \rangle$, thus determined using the short-wavelength components of the topography and gravity. Compared to the gravity anomalies shown in Fig. 7b, the density perturbations are more localized. This is because the gravity fields of several small-scale nearby density perturbations coalesce and give rise to a relatively broader gravity anomaly. The distinct ocean-continent boundary shown in the topography and gravity anomaly maps is strongly suppressed in the density perturbation map, suggesting that the gravity anomaly largely arises from the topography which is probably maintained by stresses in the crust. A significant density perturbation is associated with the Cape Smith belt which correlates directly with the gravity anomaly, indicating that the gravity anomaly mainly arises from density perturbations within the crust, because of no significant topography there. No consistent density perturbations are associated with the other collision zones. The Manicouagan - Hart Jaune complex is delineated by a positive topography, positive gravity anomaly, and positive density perturbation. The observed gravity anomaly over this complex is larger than the gravity produced by its surface topography, and part of the anomaly is associated with excess mass within the crust. Such is also the case for many small-sized anomalies over the Grenville and Nain provinces. The source bodies of these anomalies are probably at shallow depths and have greater density contrasts compared with the density perturbations displayed in Fig. 7d which are vertically averaged over the 37 km thickness of the crust.

Intermediate-wavelength components

The intermediate-wavelength topography and gravity anomaly maps (Figs. 8a, 8b) are derived through band-pass filtering of the original maps (Figs. 2a, 2b) which removes wavelengths longer than 385 km and shorter than 170 km, but does not affect wavelengths between 190 and 307 km. The remaining wavelengths are suppressed by a 1D Hanning function applied over wavelengths between 170 and 190 km, and over those between 307 and 385 km, in order to avoid a sharp cutoff. There is no consistent correlation between the topography and gravity anomalies, except for a few places such as Torngat, the northwest-southeast-trending positive gravity in the eastern Superior Province and the parallel negative anomaly over the Superior - east Churchill collision zone, the overall positive gravity anomaly of Grenville Province, and the most evident ocean-continent boundary. Therefore, the close proximity between the power spectrum of the observed gravity and the gravity arising from the topography over these wavelengths (see Fig. 3a) cannot be used to argue that the observed gravity arises from the surface topography. The continental topography appears quite smooth, whereas the gravity anomaly map is dynamic, showing well-defined positive and negative anomalies, some of which correlate

Fig. 8. (a) Intermediate-wavelength components of the topography. (b) Intermediate-wavelength components of the free-air gravity anomalies. (c) Density perturbations within the crust. (d) Moho undulation. The anomalies near the boundaries in the Labrador Sea and Hudson Bay are artifacts arising from edge effects (see the text).



with geologic structures. For example, the Manicouagan – Hart Jaune complex is delineated by a well-defined, intermediate-wavelength positive gravity anomaly, but has no significant associated topography. The gravity anomaly is largely due to density perturbations within the crust and possible undulation of the Moho. The Grenville Front, the Trans-Hudson Orogen in the Cape Smith belt, and the collision zone between east Churchill and Superior provinces are delineated by negative gravity signatures.

In the inversion of the intermediate-wavelength gravity anomalies, we take into account the topography, the density perturbations in the crust, and the Moho undulation. The latter is included because it can make a considerable contribution to the observed gravity at these wavelengths. We consider a simple crustal model to minimize the number of free parameters and avoid unnecessary mathematical complications. The topography and the base of the crust are assumed to have uniform densities of ρ_c and ρ_1 , respectively, whereas the lateral density perturbations, $\delta\rho$, are concentrated within the crust, excluding the topography and the Moho undulation. The constant density of the topography and the Moho undulation avoids coupling of different harmonics and results in a simple relationship. The Moho undulation is determined by assuming that α fraction of the load associated with the topography and the density perturbations in the crust is compensated by the undulation and the rest is supported by the elastic crust. The undulation H^T (assumed positive downward, i.e., when the crust has a root) is determined by

$$[12] \quad H_{u,v}^T = \frac{\alpha}{\rho_m - \rho_1} (\rho_c T_{u,v} + H_c <\delta\rho>_{u,v})$$

where ρ_m (3300 kg/m³) is the mantle density, and $<\delta\rho>$ denotes the vertically averaged density perturbation in the 37 km thick crust. The compensation depth is the average Moho depth, H_c . The gravity associated with the Moho undulation, g^m , is

$$[13] \quad g_{u,v}^m = 2\pi G(\rho_1 - \rho_m)e^{-k(z+H_c)}H_{u,v}^T$$

Equating the gravity produced at the surface by this crustal model with the observed gravity yields the following integral equation to be solved for $\delta\rho_{u,v}$:

$$[14] \quad g_{u,v}^o = 2\pi Ge^{-kz} \left[\rho_c T_{u,v} + \int_{-H_c}^0 e^{kz'} \delta\rho_{u,v} dz' + (\rho_1 - \rho_m)e^{-kH_c} H_{u,v}^T \right]$$

It is evident from eq. [14] that the solution for the density perturbations is non-unique; adding $\delta\rho_{u,v}^o$ to a given solution does not affect the gravity anomalies if

$$[15] \quad \int_{-H_c}^0 e^{kz'} \delta\rho_{u,v}^o dz' = 0$$

In the absence of other independent information about the vertical distribution, we seek a vertically averaged lateral density perturbation $<\delta\rho>_{u,v}$, the simplest model, by assuming that $\delta\rho_{u,v}$ does not change vertically. This assumption reduces eq. [14] to

$$[16] \quad <\delta\rho>_{u,v} = \frac{ke^{kH_c}}{e^{kH_c} - (1 + k\alpha H_c)} \times \left[\frac{g_{u,v}^o}{2\pi G} - (1 - \alpha e^{kH_c}) \rho_c T_{u,v} \right]$$

in which the altitude z is set to zero.

Included in Fig. 8 are the vertically averaged density perturbations in the crust and the Moho undulation, determined by eqs. [16] and [12] for the intermediate-wavelength components assuming a complete isostatic compensation ($\alpha = 1$). The elongated features near the boundaries in Labrador Sea and Hudson Bay are edge effects and unreliable. They arise because the topography was tapered to zero along the boundaries in the course of applying the Fourier transformation, as mentioned before. The tapering affected a strip of 120 km and artificially increased the intermediate-wavelength component of the topography there, as seen in Fig. 8a. We keep these features, rather than masking them out, to show the extent to which tapering affects the maps. The good correlation between the gravity anomalies, density perturbations, and the Moho undulation, especially where no significant topography exists, is expected because a gravity anomaly over an almost flat area requires density perturbations in the crust and thus an associated Moho undulation to retain isostasy. For example, detailed inspection of the Grenville Front shows that the minima of the gravity anomalies along the front occur over topographically low undulating, almost flat areas. The required negative density perturbations result in a mass deficiency in the crust beneath, which in turn causes mantle uplift to create an excess mass in order to retain isostatic compensation. Such a crustal model, where collisions have resulted in crustal thinning and mantle uplift, is in direct contradiction with the common crustal thickening that occurs through continent–continent collision processes and, therefore, is not realistic.

Long-wavelength components

The long-wavelength components of the topography and gravity anomalies are very interesting. The power spectrum of the observed gravity anomalies is substantially lower than that of the gravity due to the topography (see Fig. 2a), implying a significant degree of compensation of the topography. Airy or Pratt isostasy models, however, cannot explain this compensation because they result in gravity anomalies which positively correlate with the topography, contrary to the observed negative correlation of the long-wavelength components (see Fig. 3b). The negative correlation emphasizes that the topography is overcompensated, either by excessive roots at the Moho, or by lateral variations of density in the crust, or both. Although the wavelengths considered are long enough for possible mantle sources to have appreciable contributions to the observed gravity anomalies, we ignore these contributions and seek simple crustal models. One model is a crust with lateral density variations and associated Moho undulation that explains the observed gravity anomalies while retaining isostatic compensation at the Moho. Similar to the model examined above for the intermediate-wavelength components, the model requires large density perturbations and correspondingly large Moho

Fig. 9. (a) Intermediate- and long-wavelength components of the topography. (b) Intermediate- and long-wavelength components of the free-air gravity anomalies. (c) Moho undulation. (d) Excess Moho undulation compared with the undulation of an isostatically compensated Moho.

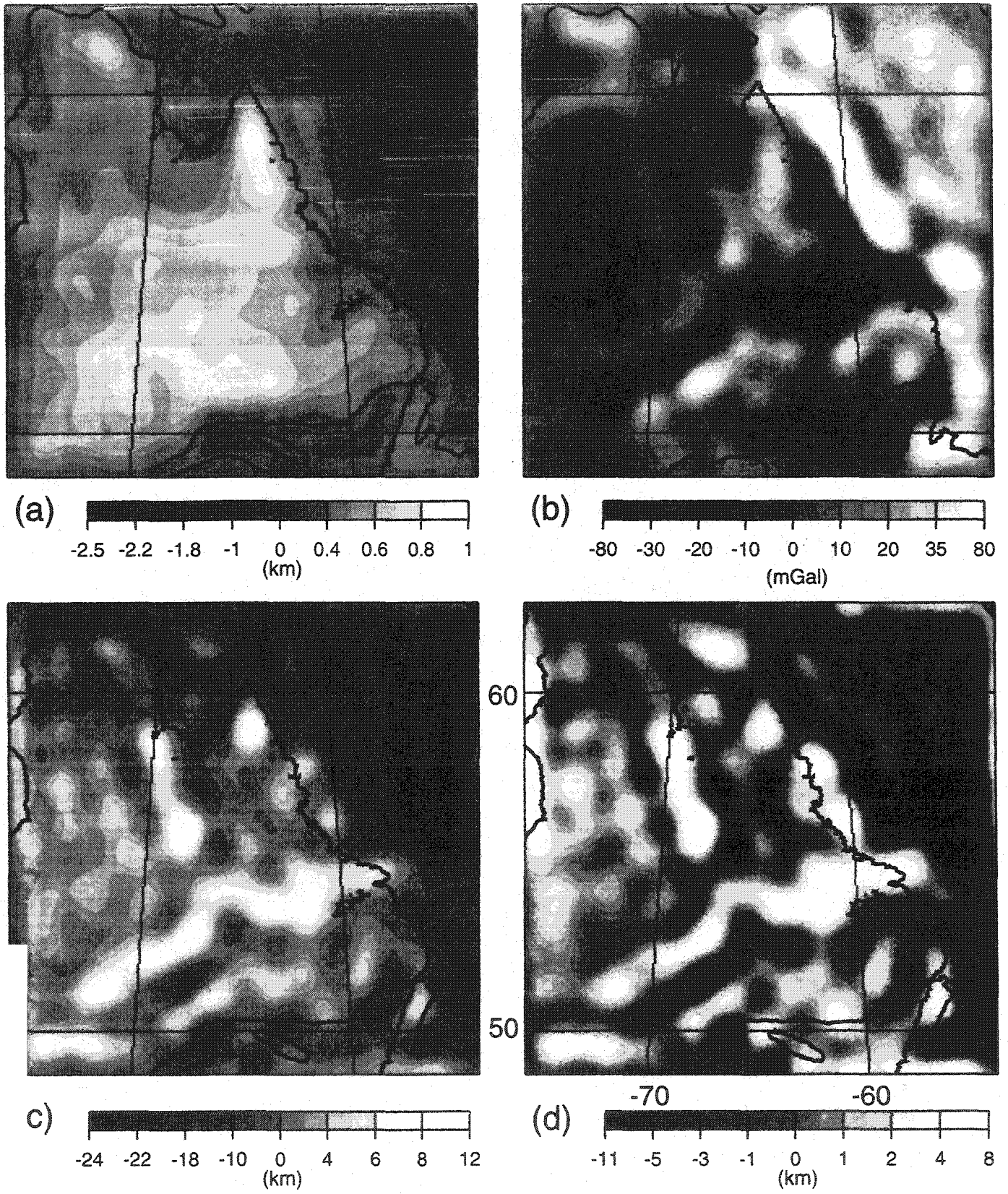
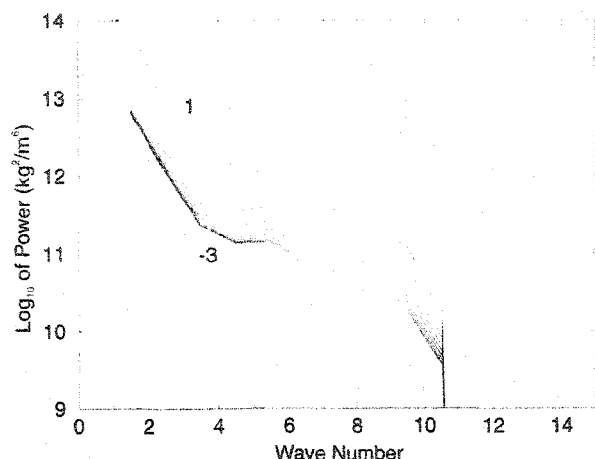


Fig. 10. Power spectra of the density perturbations in the crust specified by the intermediate- and long-wavelength components. The numbers on the curves are the α values from -3 to 4 with an increment of 0.5 .

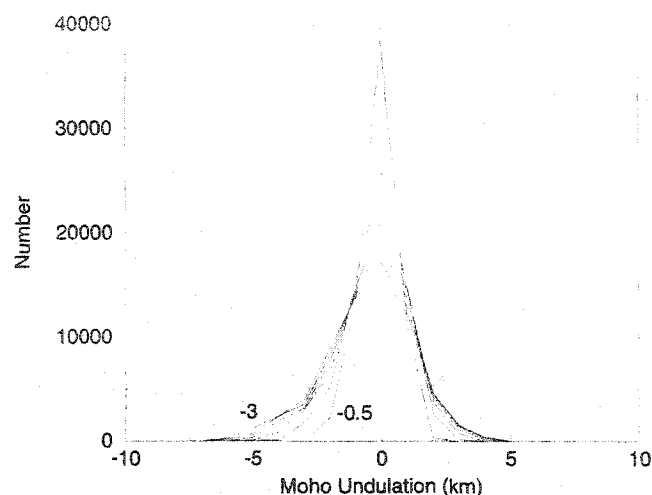


undulation. This is because, to overcompensate, for example, a positive topography, a large negative density perturbation is required with a total mass deficiency much greater than the excess mass of the topography. The vertically integrated mass would then be negative. It would require an upward displacement of the Moho to create an excess mass to retain isostasy there. This upward displacement would give rise to a positive gravity anomaly opposing the gravity anomaly associated with the density perturbations. Similar to the results obtained for the intermediate-wavelength components, this model leads to mantle uplift beneath positive surface topography, and for the same reason the model is not realistic.

Modelling regional-scale gravity anomalies

An interesting and yet simple model is a laterally homogeneous crust with surface topography and undulating Moho but no isostatic compensation at the Moho. This model can be created by collision of two continents of similar density. The newly formed collision zone is characterized by a thicker crust with a pronounced topography and associated deep crustal root produced in the process of collision. The topography is usually compensated during or shortly after the collision because of frictional heating that weakens the crust and allows rapid mechanical equilibrium. In later times, however, the crust cools and becomes strong, and as the surface topography is reduced through erosion the rebound of the strong crust does not keep in phase with the erosion. The excess buoyancy of the root is supported by crustal strength, for example, through flexure of the elastic part of the crust (Pilkington 1990; Hynes 1994). According to this simple model, the long-wavelength components of the gravity associated with the Moho undulation overwhelm that of the topography and produce the observed gravity anomalies with opposite sign to the topography. Now, if the crust is strong enough to maintain long-wavelength components of the Moho undulation, it should also maintain the intermediate-wavelength components of the undulation.

Fig. 11. Histograms of the Moho undulation. The numbers on the curves are the α values from -3 to -0.5 with an increment of 0.5 .



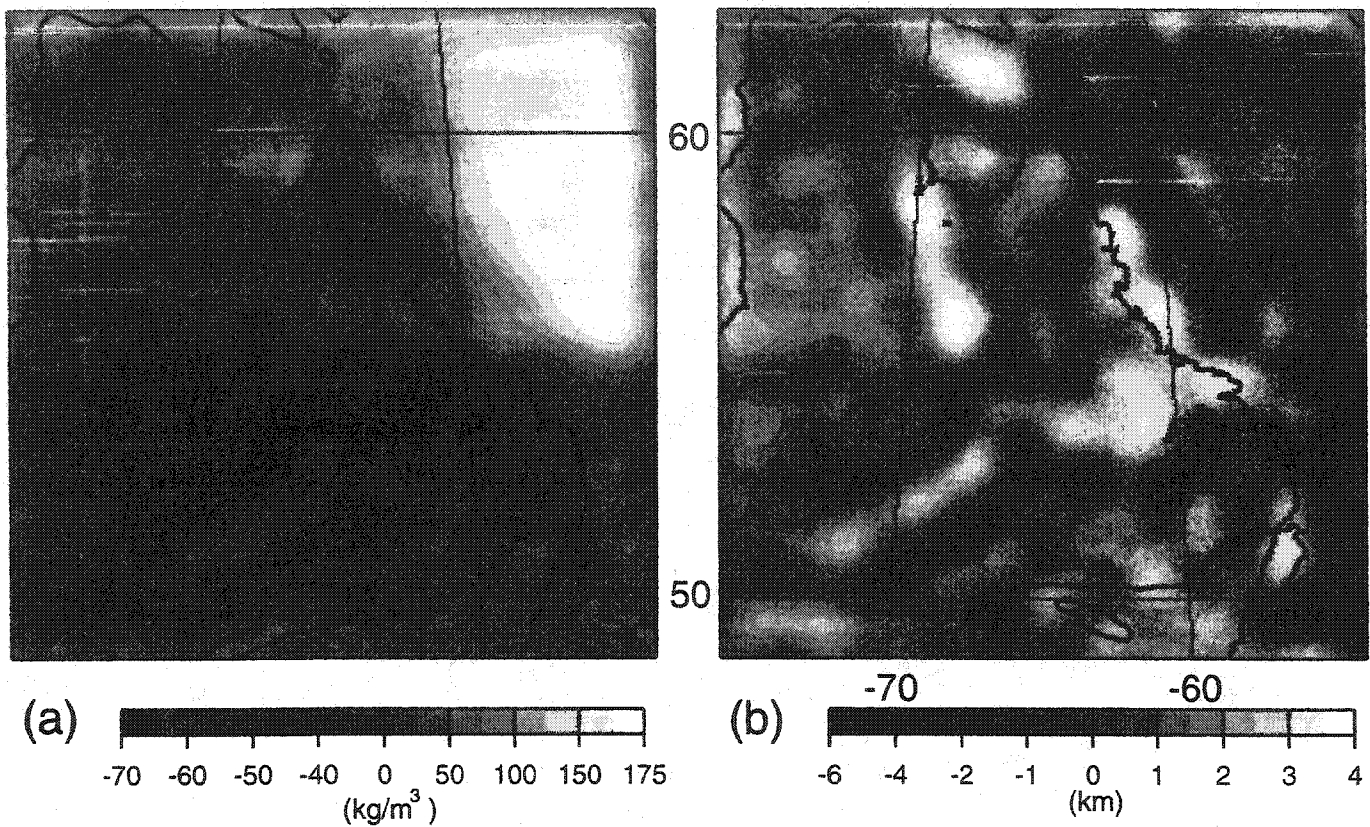
Therefore, we consider a crustal model with no lateral density perturbations but with topography (Fig. 9a) and gravity anomalies (Fig. 9b) characterized by the intermediate- and long-wavelength components. The Moho undulation (Fig. 9c) is determined for $\rho_l = 2900 \text{ kg/m}^3$, representing the gabbroic rocks of the lower crust, by equating the gravity anomaly of this crustal model with the observed gravity anomaly:

$$[17] \quad H_{u,v}^I = \frac{e^{kH_c}}{2\pi G(\rho_m - \rho_l)} (2\pi G \rho_c T_{u,v} - g_{u,v}^o)$$

All of the collision zones have thicker crust consistently. Figure 9d shows the Moho undulation that is in excess of the undulation required for a simple Airy isostasy model. The model Moho deviates from the isostatic Moho by more than 7 km in the collision zones. The model Moho undulation is also much greater than that observed from seismic measurements (e.g., Gibb and Thomas 1976; Mereu and Jobidon 1971; Mereu et al. 1986; Kellett et al. 1994; White et al. 1994). The results are not sensitive to variations of ρ_c , but are more sensitive to the density contrast between the lower crust and the mantle. For example, increasing ρ_c from 2700 to 2800 kg/m^3 changes the first term in the right-hand side by only 4%, whereas using 2800 kg/m^3 for the density of the gabbroic rocks, rather than 2900 kg/m^3 , would decrease the undulation by 20%. The density values we use are reasonable, and the contrast may not be very different from that adopted in these calculations. However, the undulation is too large compared with that observed, suggesting that this crustal model is not realistic either.

A realistic crustal model is probably somewhere in between the two end-member models examined above. The major parameter that controls the Moho undulation is the α factor. It is possible in principle to select an α value which yields a Moho undulation that approximates the observed Moho along a particular seismic profile. Such an α value may not, however, result in a Moho undulation that approximates the Moho along all available seismic profiles. This is partly because of detailed local factors that may control the

Fig. 12. The intermediate- and long-wavelength components of (a) the vertically averaged density perturbations within the 37 km thick crust, and (b) the Moho undulation about the 37 km depth of the selected crustal model.



seismic results, and partly because of different compensation mechanisms at different locations. For example, the Moho undulation shows very diverse characteristics along the Grenville Front (see below) which cannot be explained by a single α factor. Therefore, we seek a crustal model with a Moho undulation that has overall characteristics of the observed Moho. For this purpose, we determine several crustal models with lateral density perturbations and Moho undulation for several values of α . Figure 10 shows the power spectra of the density perturbations of the models thus determined. For positive α values, the density perturbations overwhelm the effects of the topography and require crustal thinning beneath the collision zones. The density perturbations in the crust are reduced as α decreases, and the Moho shows crustal thickening beneath the collision zones when α becomes negative. The histograms of the resulting Moho undulation for negative α values (Fig. 11) show that the amplitude of the undulation decreases as α decreases. The α values between -1.5 and -2.5 give rise to amplitudes which are similar to the Moho undulation observed along seismic files across the Grenville Front (e.g., Mereu and Jobidon '1; Mereu et al. 1986). Figure 12 shows the Moho undulation and density perturbations for $\alpha = -2$, which we regard as an acceptable crustal density model. The Moho deepens about 3–4 km beneath the collision zones between the Grenville and Superior provinces and between the Churchill and Superior provinces. The zones are flanked by the mantle uplift on both sides, which is more pronounced beneath the Grenville and Churchill provinces than beneath the older Su-

prior Province. The remaining parts of the provinces have relatively flat Moho.

Interpretation of magnetic anomalies

Magnetic anomalies reflect lateral variations in the magnetization of the crust and possibly uppermost mantle. The magnetic potential, A , of a magnetic layer is related to its magnetization, \mathbf{m} , through (Arkani-Hamed and Strangway 1986)

$$[18] \quad A_{u,v} = -2\pi \frac{e^{-kz}}{k} \mathbf{G} \cdot \mathbf{M}_{u,v}$$

where

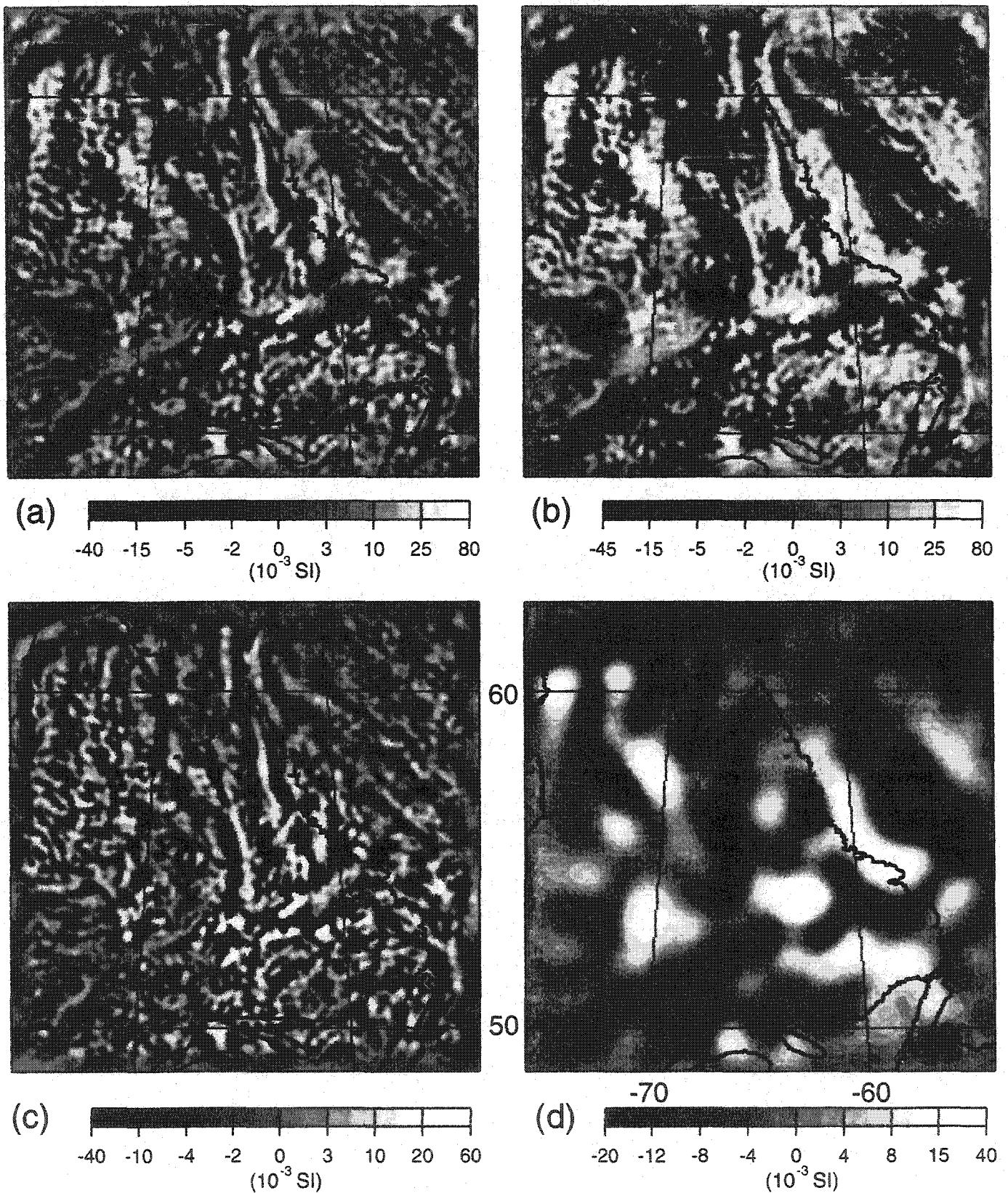
$$[19] \quad \mathbf{G} = (iu, iv, -k)$$

and

$$[20] \quad \mathbf{M}_{u,v} = \int_{s_1}^{s_2} \mathbf{m}_{u,v} e^{kz_0} dz_0$$

where s_1 and s_2 denote the lower and upper surfaces of the layer, respectively, and both are generally undulating. We assumed $z = 300$ m, which is the average altitude of the aeromagnetic measurements over the continent. Note that marine magnetic measurements are made at sea level. However, taking z at 300 m elevation will not affect the results significantly because the shortest wavelength considered, 30 km, does not attenuate by more than 6% from sea level to this al-

Fig. 13. (a) Magnetic susceptibility of a half space with topography. (b) Magnetic susceptibility of the crust bounded by the topography and Moho. (c) Short-wavelength components of the susceptibility of the crust. (d) Intermediate- and long-wavelength components of the susceptibility of the crust.



titude, and other wavelengths attenuate even less. Equations [18] and [20] show that magnetic potential depends on the vertically integrated magnetization inside the layer which is weighted by an exponential function. This emphasizes that details of vertical variations of magnetization cannot be inferred from magnetic anomaly analysis alone. Additional independent data, such as seismic profiles and gravity anomalies, are needed to constrain the vertical dimension of magnetic sources.

The lack of other geophysical information about the vertical distribution of crustal magnetization over the entire area and the inability of magnetic anomaly analysis to resolve vertical variations limit us to determining the vertically averaged magnetization of the crust, in accord with our general philosophy of seeking simple models, as adopted in the interpretation of the gravity anomalies in the previous section. We also assume that the crustal magnetization is in the vertical direction. This assumption may not introduce serious errors because the core field direction has already been changed to vertical through the reduction-to-pole procedure. Also, Labrador Sea was formed near the north magnetic pole (Harrison and Lindh 1982) and the remanent magnetization of its oceanic crust is almost vertical and has been little affected by the differential reduction to the north pole application. Magnetization of the continental crust is due to remanent and induced magnetization. The crust has suffered very many large and small tectonic deformations during the last 1–2 Ga which most likely rotated different blocks in different directions, resulting in diverse orientations of the previously acquired remanent magnetization. Furthermore, the strong temperature dependence of viscous magnetization and the high temperatures of the middle and lower crust suggest that any plausible remanent magnetization of the deeper parts has been substantially reduced during this long period. And finally, it is demonstrated that different parts of a large body cooling through its magnetic blocking temperature range acquire remanent magnetization in different directions owing to reversals of the core field and slow cooling rate of the body (Arkani-Hamed and Celeti 1989). Alternating polarity magnetized zones in a batholith have been observed in the field (Williams and Fuller 1982). Such a body does not produce an appreciable magnetic anomaly, despite the fact that certain parts of the body carry appreciable remanent magnetization. This is due to the cancelling effects of the magnetic fields of the oppositely magnetized parts. It is therefore plausible to assume that induced magnetization is the dominant source of observed magnetic anomalies over the continent. These assumptions greatly simplify the inversion formulas developed by Arkani-Hamed and Verhoef (1989). Their eqs. [10]–[13] are now reduced to

$$m_{u,v} = \frac{-1}{e^{ks_2^0} - e^{ks_1^0}} \left(\frac{-e^{kz}}{2\pi} T_{u,v} + G \cdot \zeta_{u,v} \right)$$

$$\zeta_{u,v} = m \left[e^{ks_2^0} \sum_{n=1}^{\infty} \frac{k^{n-1}}{n!} \delta s_2^n - e^{ks_1^0} \sum_{n=1}^{\infty} \frac{k^{n-1}}{n!} \delta s_1^n \right]$$

where s_1^0 and s_2^0 are the mean elevations of the upper and lower surfaces of the magnetic layer, respectively; and δs_1^0 and δs_2^0 denote the undulation of these surfaces. The underlying assumption made in developing the original formulas, and thus in their reduced forms, is that the magnetization is of induced origin. This assumption is probably reasonable over the continental area as argued above. It overestimates the magnetic susceptibility of the oceanic crust because the remanent magnetization, which is usually much greater than the induced magnetization, is regarded as an induced magnetization in this formulation. This will, however, have no effect on the vertically integrated magnetization in the oceanic region, as indicated by eqs. [18] and [20].

Two models are considered for the magnetic layer, a half space with the surface topography, and a finite layer with the surface topography and the undulating Moho as its lower surface. The first model provides information about the short-wavelength components of the crustal magnetization. This is because little contribution is made to the RTP anomalies by the magnetic poles at the lower boundary. The lateral variations of susceptibility (Fig. 13a) are very similar to the RTP anomalies (Fig. 6a), but the resolution of the susceptibility map is slightly higher due to enhancement of the short-wavelength components through the inversion process. Broad RTP anomalies arise from coalescing of the anomalies associated with nearby small-scale separate magnetic bodies.

The second model illustrates the effect of the finiteness of the magnetic layer thickness. Rock magnetic measurements suggest the Moho as the lower boundary of the magnetic crust beneath continents (Wasilewski et al. 1979). Accordingly, we assume that the lower surface of the magnetic layer coincides with the Moho beneath the continent. The oceanic crust of Labrador Sea is thin and the uppermost part of the mantle is at temperatures lower than the Curie temperature of its magnetic minerals. There is ample evidence that the uppermost oceanic mantle is serpentinized at slow spreading centres, such as that of the Labrador Sea (Francis 1981; Cannat 1993; Chian and Loudon 1995), and contains magnetic minerals. The magnetite produced by serpentinization of the uppermost mantle may have significant contributions to the marine magnetic anomalies (Harrison 1987; Hamano et al. 1990). Also, the anomalous skewness of marine and satellite magnetic anomalies suggests that the uppermost 6 km of the mantle is magnetized (Dyment et al. 1997). Therefore, it is assumed in the second model that the magnetic layer beneath the Labrador Sea extends from the top of layer 2A to a fixed depth of 15 km from sea level. The short-wavelength components of the Moho undulation cannot have appreciable effects on the observed magnetic anomalies due to strong attenuation of the anomalies with distance. Figure 13b shows the lateral variations in the magnetic susceptibility of the second model determined using the entire spectra of the RTP anomalies and the topography (all wavelengths longer than 30 km), and the intermediate- and long-wavelength undulation of the Moho beneath the continent, obtained by adding 37 km (the average crustal thickness) to the Moho undulation in Fig. 12, and a fixed Moho depth of 15 km beneath the Labrador Sea. A strip of about 200 km along the ocean–continent boundary is tapered to smoothly connect the undulating Moho of the continent to the fixed Moho of the oceanic area. There are

pronounced differences between the magnetic susceptibility contrasts seen in Figs. 13a and 13b. The long-wavelength components are substantially enhanced in the second model, emphasizing the major effect of the finiteness of the layer thickness. This is because the crustal model considered can be envisaged as a collection of vertically magnetized thin vertical prisms, each resembling a long magnetic dipole one pole at the upper and the other at the lower end of the prism. The layer is equivalent to two surfaces, top and bottom, with magnetic monopole distributions of opposite polarity. In the first model, the bottom surface is at infinity and the anomalies are essentially due to the monopole distribution at the surface. In the second model, the bottom monopoles are at an average depth of 37 (or 15) km and the intermediate- and long-wavelength components of the lower surface monopoles have appreciable contributions to the RTP anomalies. Large cancellations occur between the magnetic fields of the upper and lower surface monopoles owing to their opposite polarity, and the observed magnetic anomalies (thus the RTP anomalies) are residuals of the cancellation. A classic example is a uniformly magnetized horizontal layer of an infinite extent with flat top and bottom surfaces. Such a layer does not produce any magnetic field outside, regardless of the intensity of magnetization. Therefore, because of a finite layer thickness a high magnetic susceptibility is required for the intermediate- and long-wavelength components of the second model to give rise to the observed magnetic anomalies (see Arkani-Hamed and Verhoef 1989 for a detailed discussion). Note that, similar to the gravity anomalies, the inversion of the magnetic anomalies is not unique. For example, a constant magnetic susceptibility can be added somewhere within the magnetic layer (excluding the surface topography and the Moho undulation) without affecting the observed magnetic anomalies. Figure 13b shows a simple model that reflects the lateral variations in the susceptibility. It indicates that the vertically averaged magnetization of the crust is laterally more homogeneous than the RTP magnetic anomalies. This is partly because the magnetic anomalies measured at low altitudes are more sensitive to short-wavelength, near-surface variations of the magnetization due to cancelling effects of the long-wavelength components as mentioned above. Figure 13c shows the short-wavelength components of the magnetic susceptibility which are dominated by small-sized features. Except for the Cape Smith belt, collision zones do not significantly contribute to these features. On the other hand, the collision zones are well defined as low magnetic susceptibility areas in the magnetic susceptibility map derived from the intermediate- and long-wavelength components (Fig. 13d). This suggests that the collisions have a considerable effect on the demagnetization of the lower parts of the crust (see below).

Discussion and conclusions

The area of study covers $1536 \times 1536 \text{ km}^2$ and consists of five geologic provinces with distinct collision zones along their boundaries and numerous local features within each province. The covariance analysis of the equivalent rock surface topography and gravity anomalies shows that the short-wavelength gravity anomalies arise predominantly from small-scale and probably near-surface sources and to a lesser

extent from the surface topography and the Moho undulation. There is no significant correlation between the intermediate-wavelength components of the topography and gravity anomalies. The contribution of density perturbations within the crust to the observed gravity anomalies is comparable to that of the surface topography over these wavelengths. The pronounced negative correlation between the long-wavelength components of the topography and gravity anomalies suggests that the topography is overcompensated, either by lateral density perturbations within the crust, or by the nonisostatic Moho undulation, or both. It is well beyond the scope of this paper to discuss details of small features. However, the models presented in this paper have sufficient resolution at wavelengths as short as 30 km, and we hope that they will be useful for detailed study of local features. Here we briefly discuss regional characteristics of the continental crust as revealed from the intermediate- and long-wavelength components of the topography and gravity and magnetic anomalies, focussing mainly on the major collision zones.

Density perturbations in the crust beneath a collision zone may arise from different processes which occurred during and shortly after the collision. Gibb and Thomas (1976) presented five free-air gravity profiles across the collision zones between Churchill and Slave, east Churchill and Superior along Cape Smith belt, east Churchill and Superior, east Churchill and Grenville, and Grenville and Superior which show very similar features. In each case, the gravity profile decreases gradually from a background level over the older province toward the collision zone, achieving a minimum near the collision boundary, and then sharply increases across the boundary to a relative gravity high over the younger province. The authors interpreted these common characteristics of the gravity profiles in terms of collision of homogeneous but different density provinces. Accordingly, a high-density younger and weaker province has overthrust a low-density older and rigid province, resulting in an appreciable crustal thickening of the younger province and suppression of the older one, in accordance with the general model suggested by Dewey and Burke (1973). The suture zone dips towards the younger province to a depth of about 14 km, but becomes vertical in the deeper parts of the crust. Also, the Moho deepens by about 5.5 km beneath the suture, and no isostatic compensation prevails there. Pilkington (1990) modelled the gravity anomalies along 25 profiles across Slave-Churchill, Churchill-Superior, and Grenville-Superior province boundaries in terms of flexure of the crust using a 1D thin plate model overlying a fluid interior of higher density. He adopted a fractured elastic layer model together with intracrustal density perturbations to interpret the asymmetry of the broad negative gravity anomalies as well as the small positive gravity anomalies of the suture zones. The author later used a 2D thin plate model and 2D topography and gravity anomaly maps of the Canadian Shield to determine lateral variations of the crustal rigidity (Pilkington 1991). His estimates of the elastic thickness of the continental crust beneath eastern Canada range from 18 to 124 km, mainly around 40–60 km. The Grenville suture is also investigated by Hynes (1994) through stacking several gravity profiles across the collision zone. The resulting type gravity profile is interpreted in terms of collision of a two-

layered older and thinner Superior Province with a homogeneous and younger Grenville Province, which thickens through the collision process. The upper crust in the Superior Province is lighter than the lower crust, which has the same density as the Grenville Province. The suture zone in his model also dips toward the younger crust, but with a constant dip down to the Moho, and the nonisostatic buoyancy force arising from the Moho undulation is supported by flexure of the elastic core of the crust, with a thickness of less than 30 km. This difference in the elastic thickness between the Hynes and Pilkington models is probably due to the fact that Hynes used a continuous plate, whereas Pilkington adopted a fractured plate. Subject to the same loading, a fractured plate requires a higher rigidity (for example, a thicker elastic layer) to produce a flexure identical to that of a continuous plate.

The Grenville Front has been studied more extensively than the other collision zones in the study area. Several seismic profiles crossing the suture are available. A seismic profile along the Lac Evans (about 51°N and 77°W) and Lac St. Jean (about 47°N and 71°W) line revealed a major structural feature about 50–75 km wide at the Moho just south of the Grenville Front (Mereu and Jobidon 1971) where the crust is thickened by 5–10 km, probably due to the collision. The Moho is very smooth beneath Superior, slightly dipping toward the collision zone (from 30 to 34 km depth within about 200 km distance), but there are pronounced undulations as much as 5 km beneath the Grenville Province far from the collision zone. Mereu and Jobidon (1971) related the broad negative Bouguer anomaly over the region to this anomalous crustal thickening and lateral density variations in the upper crust, and suggested that the Grenville suture is a major fault which penetrates well into the upper mantle. Three seismic profiles were obtained across the Ottawa–Bonnechere graben and Grenville Front (an area between 44 and 48°N and 74 and 80°W) as part of the COCRUST program in 1982 (Mereu et al. 1986). The Ottawa–Bonnechere graben is a depressed zone of approximately 60 km wide located immediately south of the Grenville Front. The two subparallel profiles almost normal to the Grenville Front (see Fig. 6 in Mereu et al. 1986) show distinctly different Moho structure. One of the profiles (AO) shows a diffuse Moho immediately beneath the front which becomes sharper and shallower toward the interior part of Grenville Province. The other (profile CD) shows a well-defined Moho which is uplifted in the Grenville side, immediately south of the front. According to this profile, Superior Province is thicker in Grenville Province and mantle is uplifted by about 4 km, contrary to the Lac Evans – Lac St. Jean seismic results. Profile CD also suggests that the Grenville frontal ne is deep-seated and extends to the Moho (Mereu et al. 1986). The seismic profile of Abitibi–Grenville Lithoprobe line 15 (from about 47°40'N and 79°40'W to 46°20'N and 73°40'W) that crossed the Grenville Front shows an uplift of about 4 km at the Moho beneath the Grenville suture (Kellett et al. 1994). The Lithoprobe seismic reflection profiles 30–32 in the western Grenville Province of southern Ontario (within 44–46°N and 76–80°W) show almost constant Moho depth along each profile, but depth to the Moho changes by as much as 3 km from profile to profile (White et al. 1994). The Lithoprobe seismic profile in the eastern

Grenville Province (from 50°30'N and 68°40'W to 52°20'N and 67°30'W) subparallel to and south of the Grenville Front shows minor deepening of the Moho from south to north (Eaton et al. 1995). And finally, deep seismic reflection survey across the Grenville Province in western Quebec (from 47°40'N and 76°20'W to 46°N and 73°30'W) shows a crust of about 44 km thick beneath the Grenville Front which rapidly thins to about 36 km to the southeast (Martignole and Calvert 1996). These existing seismic profiles across the Grenville Front show quite different crustal structures, indicating that the Grenville Front has a highly variable tectonic character, as also concluded by Kellett et al. (1994).

Other collision zones in the study area have not attracted as much attention as the Grenville Front, possibly because the gravity and magnetic signatures of the Grenville Front are remarkably outstanding. However, similar diversity of crustal structure and Moho undulation probably exists elsewhere. For example, the collision zone between Nain and Makkovik provinces is not well delineated in the gravity and magnetic anomaly maps, largely because the zone is not long enough to produce the elongated anomalies which are the distinct characteristic of the Grenville suture. However, the seismic refraction data acquired parallel to the shoreline over the continental shelf of the Labrador Sea and across the Nain–Makkovik boundary (from 56°40'N and 60°20'W to 55°20'N and 58°10'W) shows a substantially thinner crust for both Nain and Makkovik and a significant change in the Moho depth by 5 km across the boundary (Reid 1996). The relatively thinner crust of the continental shelf, about 28 km beneath Nain Province and even thinner, 23 km, beneath Makkovik Province, is due in part to erosion of the upper crust and crustal extension during rifting of the Labrador Sea (Reid 1996). A sudden change in the Moho depth in Nain Province to the north, about 5 km offset within about a 10 km horizontal distance, detected by refraction – wide-angle reflection seismic experiments along Lithoprobe ECSOOT line 4 (from 59°N and 63°W to 58°N and 61°30'W), suggests a normal fault probably related to the Handy Fault, as proposed by Funck and Loudon (1998). Sharp changes in the Moho depth elsewhere are also related to normal faults (Mereu et al. 1986).

The two-dimensional inversion of the gravity anomalies presented in this paper retains the diverse characteristics of the tectonic features among collision zones as well as along a given orogen. For the interpretation of the intermediate- and long-wavelength components of the gravity anomalies, we first calculated two extreme models, a crust with lateral density perturbations and isostatic compensation at the Moho and a homogeneous crust with a nonisostatically undulating Moho which, together with the topography, give rise to the observed gravity. One of the important points revealed in this study is that the Moho structure strongly depends on whether isostatic compensation prevails there or not. The first model results in crustal thinning beneath collision zones, whereas the second model shows crustal thickening but with amplitudes significantly larger than the observed ones. These models are considered unrealistic. Note that the first model requires a zero strength crust, whereas the second indicates a crustal rigidity on the order of 1×10^{24} to 10×10^{24} N-m (Pilkington 1990, 1991). This emphasizes that surface topography and gravity anomaly

data alone cannot provide a good estimate of the strength and thickness of the elastic part of the crust. Other geophysical (seismic in particular, and heat flow and magnetic anomalies to some extent) and geological (stress patterns in particular, and major structural features) information is needed. The reality may lie somewhere between these two extreme models. This is indicated by the diversity of the Moho structure along the Grenville suture revealed from seismic measurements, which is probably related to the extent of compensation of the surface topography and intracrustal load at the Moho. For example, Gibb and Thomas (1976) and Hynes (1994) included lateral variations of density by juxtaposing two crusts of different densities, and Pilkington (1990) introduced intracrustal mass load, besides the density differences between the two colliding crusts, to account for small-scale positive gravity anomalies of the suture zones. None of these authors assumed isostatic compensation at the Moho. To construct a realistic model, we considered both lateral density perturbations in the crust and Moho undulation without imposing isostatic compensation at the Moho. The contribution from the Moho is weighted such that the resulting Moho undulation resembles the observed Moho variations, and the crustal model satisfies the observed gravity anomalies.

The short-wavelength components of the lateral contrasts in the magnetic susceptibility of the crust are determined using a half-space crustal model. The northern and central parts of Superior Province, the eastern and central parts of east Churchill Province, and the eastern parts of Grenville Province are characterized by high susceptibility contrasts. (Note that positive-negative susceptibility in the continent implies high-low magnetic susceptibility of sources, rather than opposite polarity.) Some of the features show good correlation with geology. For example, De Pas Batholith has a very high susceptibility. However, there is no obvious signature of the collision zones over these wavelengths, except for the Cape Smith belt. The lack of a pronounced correlation between the surface topography and magnetic anomalies implies that the tectonic processes that shaped the eastern part of the Canadian Shield have not considerably affected the magnetic properties of the upper parts of the crust. On the other hand, major collision zones are delineated as low magnetic features in the intermediate- and long-wavelength components of the magnetic susceptibility map, indicating that these components of the magnetic anomalies arise from deep-seated magnetic susceptibility contrasts. The satellite magnetic anomalies also suggest a highly magnetic lower crust. The low magnetization of the continent-continent collision zones has also been observed elsewhere and has been related to the loss of magnetization in the lower crust through the collision processes (Arkani-Hamed and Strangway 1986). Several mechanisms operating during or shortly after collision may reduce the magnetization of the crust, such as frictional heating, hydration, and crustal thickening. Frictional heating is probably important for recent collisions, but it diminishes in time as the crust cools. It is not a significant mechanism to be responsible for the low magnetization of the old collision zones we are concerned with. The continent-continent collision that occurs after subduction of the preexisting oceanic lithosphere may introduce water into the crust, resulting in hydration of magnetic

minerals and reduction of magnetization. This mechanism could be appreciable, especially on a local scale (Toft et al. 1993). Finally, crustal thickening produces a high surface topography and a corresponding deep crustal root, created through isostatic compensation during and shortly after the collision when the crust was still warm and weak enough to readily respond to the topographic load as well as the load created by the density perturbations resulting from collision of continents with different densities. The thickening of the less magnetic upper crust also suppresses the highly magnetic lower crust. The topography has subsequently been reduced through erosion, whereas the root has been less affected. The crustal root consists of highly magnetic lower crust which is now suppressed into the hot upper mantle. The average geothermal gradient in the continent suggests that temperature exceeds the Curie temperature of magnetite (680°C) at depths greater than about 35–40 km, and deeper parts of the crustal roots are thermally demagnetized. Therefore, the negative magnetic anomalies of the collision zones are probably related to the depression of the upper boundary of the highly magnetic lower crust and, more importantly, the thermal demagnetization of parts of the highly magnetic crustal roots.

Acknowledgments

This research is supported by the Lithoprobe program of the Natural Sciences and Engineering Research Council of Canada (NSERC). We would like to thank Thomas Funck for providing a reprint of his paper, and Andrew Hynes and Keith Loudon for their comments on the preliminary version of this paper.

References

- Arkani-Hamed, J. 1988. Differential reduction-to-the-pole of regional magnetic anomalies. *Geophysics*, **53**: 1592–1600.
- Arkani-Hamed, J., and Celeti, G. 1989. Effects of thermal remanent magnetization on the magnetic anomalies of intrusives. *Journal of Geophysical Research*, **94**: 7364–7378.
- Arkani-Hamed, J., and Hinze, W.J. 1990. Limitations of the long-wavelength components of the North American magnetic anomaly map. *Geophysics*, **55**: 1577–1588.
- Arkani-Hamed, J., and Strangway, D.W. 1986. Magnetic susceptibility anomalies of lithosphere beneath eastern Europe and the Middle East. *Geophysics*, **51**: 1711–1724.
- Arkani-Hamed, J., and Verhoef, J. 1989. Generalised inversion of scalar magnetic anomalies: magnetisation of the crust off the east coast of Canada. *Geophysical Monogram, American Geophysical Union*, **51**: 255–270.
- Arkani-Hamed, J., Verhoef, J., Roest, W., and Macnab, R. 1995. The intermediate-wavelength magnetic anomaly maps of the North Atlantic Ocean derived from satellite and shipborne data. *Geophysical Journal International*, **123**: 727–743.
- Cannat, M. 1993. Emplacement of mantle rocks in the seafloor at mid-ocean ridges. *Journal of Geophysical Research*, **98**: 4163–4172.
- Chian, D., and Loudon, K.E. 1995. Crustal structure of the Labrador Sea conjugate margin and implications for the formation of nonvolcanic continental margins. *Journal of Geophysical Research*, **100**: 24 239 – 24 253.
- Dewey, J.F., and Burke, K.C.A. 1973. Tibetan, Variscan and Precambrian basement reactivation: products of continental collision. *Journal of Geology*, **81**: 683–692.

- Dyment, J., Arkani-Hamed, J., and Ghods, A. 1997. Contribution of serpentinized ultramafics to marine magnetic anomalies at slow and intermediate spreading centres: insights from the shape of the anomalies. *Geophysical Journal International*, **129**: 691–701.
- Eaton, D.W., Hynes, A., Indares, A., and Rivers, T. 1995. Seismic images of eclogites, crustal-scale extension, and Moho relief in the eastern Grenville province, Quebec. *Geology*, **23**: 855–858.
- Francis, T.J.G. 1981. Serpentinization faults and their role in the tectonics of slow spreading ridges. *Journal of Geophysical Research*, **86**: 11 616 – 11 622.
- Funck, T., and Loudon, K.E. 1998. Wide-angle seismic imaging of pristine Archean crust in the Nain Province, Labrador. *Canadian Journal of Earth Sciences*, **35**: 672–685.
- Geological Survey of Canada. 1968. Tectonic map of Canada. Geological Survey of Canada, Map 1251A, scale 1 : 5 000 000.
- Gibb, R.A., and Thomas, M.D. 1976. Gravity signature of fossil plate boundaries in the Canadian Shield. *Nature (London)*, **262**: 199–200.
- Grauch, V.J.S. 1993. Limitations on digital filtering of the DNAG magnetic data set for the conterminous U.S. *Geophysics*, **58**: 1281–1296.
- Hamano, Y., Bina, M.M., and Krammer, K. 1990. Paleomagnetism of the serpentinized peridotite from ODP hole 670A. *Proceeding of the Ocean Drilling Program, Scientific Results*, **106/109**: 257–262.
- Harrison, C.G.A. 1987. Marine magnetic anomalies—the origin of the stripes. *Annual Review of Earth and Planetary Sciences*, **15**: 505–543.
- Harrison, C.G.A., and Lindh, T. 1982. A polar wandering curve for North America during the Mesozoic and Cenozoic. *Journal of Geophysical Research*, **87**: 1903–1920.
- Hinze, W.J., Hood, P.J., and the Committee for the Magnetic Anomaly Map of North America. 1988. Magnetic anomaly map of North America. *Geophysics: The Leading Edge of Exploration*, **7**: 19–21.
- Hynes, A. 1994. Gravity, flexure, and the deep structure of the Grenville Front, eastern Quebec and Labrador. *Canadian Journal of Earth Sciences*, **31**: 1002–1011.
- IAGA Division V Working Group 8. 1996. Revision of the international geomagnetic reference field released. *Eos*, **77**: 153.
- Johnson, A.C., von Frese, R.R.B., and the ADMAP Working Group. 1997. Magnetic map will define Antarctica's structure. *Eos*, **78**: 185.
- Kellett, R.L., Barnes, A.E., and Rive, M. 1994. The deep structure of the Grenville Front: a new perspective from western Quebec. *Canadian Journal of Earth Sciences*, **31**: 282–292.
- LaBrecque, J.L., and Cande, S.C. 1984. Intermediate-wavelength magnetic anomalies over the central Pacific. *Journal of Geophysical Research*, **89**: 11 124 – 11 134.
- LaBrecque, J.L., and Raymond, C.A. 1985. Seafloor spreading anomalies in the Magsat field of the North Atlantic. *Journal of Geophysical Research*, **90**: 2565–2575.
- Macnab, R., Verhoef, J., Roest, W., and Arkani-Hamed, J. 1995. New database documents the magnetic character of the Arctic and North Atlantic. *Eos*, **76**: 449–458.
- Martin, J., and Calvert, A.J. 1996. Crustal-scale shortening and extension across the Grenville Province of western Quebec. *Tectonics*, **15**: 376–386.
- Martin, R.F., and Jobidon, G. 1971. A seismic investigation of the crust and Moho on a line perpendicular to the Grenville Front. *Canadian Journal of Earth Sciences*, **8**: 1553–1583.
- Martin, R.F., Forsyth, D.A., Green, A.G., et al. 1986. The 1982 COCRUST seismic experiment across the Ottawa–Bonaventure graben and Grenville Front in Ontario and Quebec. *Geophysical Journal of the Royal Astronomical Society*, **84**: 491–514.
- Mooney, W.D., and Braille, L.W. 1989. The seismic structure of the continental crust and upper mantle of North America. *In The geology of North America—An overview. Edited by A.W. Bally and A.R. Palmer. Geological Society of America, The Geology of North America. Vol. A. pp. 39–52.*
- Pilkington, M. 1990. Lithospheric flexure and gravity anomalies at Proterozoic plate boundaries in the Canadian Shield. *Tectonophysics*, **176**: 277–290.
- Pilkington, M. 1991. Mapping elastic lithospheric thickness variations in Canada. *Tectonophysics*, **190**: 283–297.
- Pilkington, M., and Grieve, R.A.F. 1989. Magnetization/density ratio mapping in eastern Canada. *In Statistical applications in the earth sciences. Edited by F.P. Agterberg and G.F. Bonham-Carter. Geological Survey of Canada, Paper 89-9, pp. 89–98.*
- Pilkington, M., and Roest, W.R. 1996. An assessment of long-wavelength magnetic anomalies over Canada. *Canadian Journal of Earth Sciences*, **33**: 12–23.
- Ravat, D., Langel, R.A., Arkani-Hamed, J., and Alsdorf, D.E. 1995. Global vector and scalar Magsat magnetic anomaly maps. *Journal of Geophysical Research*, **100**: 20 111 – 20 136.
- Reid, I. 1996. Crustal structure across the Nain–Makkovik boundary on the continental shelf off Labrador from seismic refraction data. *Canadian Journal of Earth Sciences*, **33**: 460–471.
- Sandwell, D.T., and Smith, W.H.F. 1997. Marine gravity anomaly from Geosat and ERS 1 satellite altimetry. *Journal of Geophysical Research*, **102**: 10 039 – 10 054.
- Tanner, J.G., and Members of the Committee for the Gravity Anomaly Map of North America. 1988. Gravity anomaly map of North America. *Geophysics: The Leading Edge of Exploration*, **7**: 15–18.
- Toft, P.B., and Arkani-Hamed, J. 1992. Magnetization of the Pacific Ocean lithosphere deduced from Magsat data. *Journal of Geophysical Research*, **97**: 4387–4406.
- Toft, P.B., Arkani-Hamed, J., and Haggerty, S.E. 1990. The effects of serpentinization on density and magnetic susceptibility: a petrophysical model. *Physics of the Earth and Planetary Interiors*, **65**: 137–157.
- Toft, P.B., Scowen, P.A.H., Arkani-Hamed, J., and Francis, D. 1993. Demagnetisation by hydration in deep-crustal rocks in the Grenville province of Quebec, Canada: implications for magnetic anomalies of continental collision zones. *Geology*, **21**: 999–1002.
- Verhoef, J., Roest, W.R., Macnab, R., Arkani-Hamed, J., and Members of the Project Team. 1996. Magnetic anomalies of the Arctic and north Atlantic oceans and adjacent land areas. Geological Survey of Canada, Open Files 3125, 3280, 3281, and 3282.
- Wardle, R.J., Ryan, B., and Ermanovics, I. 1990. The eastern Churchill Province, Torngat and New Quebec orogens: an overview. *Geoscience Canada*, **17**: 217–222.
- Wasilewski, P.J., Thomas, H.H., and Mayhew, M.A. 1979. The Moho as a magnetic boundary. *Geophysical Research Letters*, **6**: 541–544.
- White, D.J., Easton, R.M., Culshaw, N.G., et al. 1994. Seismic images of the Grenville Orogen in Ontario. *Canadian Journal of Earth Sciences*, **31**: 293–307.
- Williams, I., and Fuller, M. 1982. A Miocene polarity transition (R–N) from the Agno Batholith, Luzon. *Journal of Geophysical Research*, **87**: 9408–9418.

Appendix B



ELSEVIER

Tectonophysics 344 (2002) 137–156

TECTONOPHYSICS

www.elsevier.com/locate/tecto

The elastic properties of the lithosphere beneath Scotian basin

Ying Zheng*, Jafar Arkani-Hamed

Department of Earth and Planetary Sciences, McGill University, 3450 University Street, Montreal, Quebec, Canada PQ H3A 2A7

Received 7 November 2000; accepted 3 December 2001

Abstract

To assess the possibility that the North Atlantic Ocean may subduct at Scotian basin east of Canada, we investigate the present compensation state of this deep basin. A Fourier domain analysis of the bathymetry, depth to basement and observed gravity anomalies over the oceanic area east of Nova Scotia indicates that the basin is not isostatically compensated. Moreover, the analysis emphasizes that in addition to the sediments, density perturbations exist beneath the basin. The load produced by the sediments and these density perturbations must have been supported by the lithosphere. We simulate the flexure of the lithosphere under this load by that of a thin elastic plate overlying an inviscid interior. It is shown that a plate with a uniform rigidity does not adequately represent the lithosphere beneath the basin as well as the oceanic lithosphere far from the basin, rather the rigidity of the lithosphere directly beneath the basin is about one to two orders of magnitude smaller than elsewhere. We relate this weakening to the thermal blanketing effects of the thick sediments and the fact that the lithosphere has a temperature-dependent rheology. We suggest that this weak zone would have a controlling effect on the reactivation of normal faults at the hinge zone of the basin, that were formed during the break-up of Africa and North America and were locked in the early stages after the break-up. The weak zone would facilitate reactivation of the faults if tensional stresses were produced by possible reorientation of the spreading direction of the North Atlantic Ocean in the future. The reactivation of the faults would create a free boundary condition at the hinge zone, allowing further bending of the lithosphere beneath the basin and juxtaposition of this lithosphere to the mantle beneath the continent. This may provide a favorable situation for initiation of slow subduction due to subsequent compressional forces. © 2002 Elsevier Science B.V. All rights reserved.

Keywords: Scotian basin; initiation of subduction; rigidity of lithosphere; gravity anomaly modeling; thermal weakening of lithosphere

1. Introduction

Sedimentary basins of passive continental margins have been investigated for both tectonic importance and petroleum potential. The origin of the basins is tied to the rifting of the continents and spreading of

the oceanic floor. Investigation of the role of the lithosphere, at the earlier stages of extension that resulted in marginal-basin sites and at the later stages when the basins are thickly sedimented, is part of an attempt to understand the initiation of subduction. Gravity and bathymetry relationships have been used to study the compensation state of sedimentary basins (e.g., McNutt, 1980; Zuber et al., 1989; Pilkington, 1990). It is concluded that sedimentary loads are usually compensated on a regional scale, i.e., they

* Corresponding author.

E-mail address: zheng@eps.mcgill.ca (Y. Zheng).

are largely supported by the elasticity of the lithosphere. Thin elastic plate models have been employed to investigate the compensation state through the flexure of the lithosphere (Cloetingh, 1982; Cloetingh et al., 1982; Beaumont et al., 1982; Erickson, 1993). Sediments are treated as loads on an elastic plate that overlies a high-density fluid mantle. The extent to which the lithosphere can support the loads is determined by its flexural rigidity, or equivalently its elastic thickness. Most authors have considered constant rigidity plates (Brotchie and Silvester, 1969; Caldwell et al., 1976; Menke, 1981; Cloetingh, 1982; Erickson, 1993). However, weakening of the lithosphere beneath the basins due to thermal blanketing effect of thick sediments must be taken into account for a more realistic modeling of the lithospheric response to sedimentary loads.

The Scotian basin off Eastern Canada is a mature marginal basin with the thickest sediment on the eastern margin of North America. The thermal evolution and subsidence history of the basin have been studied intensively (Beaumont et al., 1982; Keen and Beaumont, 1990; Ghods and Arkani-Hamed, 1998). Beaumont et al. (1982) and Keen and Beaumont (1990) employed thermo-mechanical models, taking into account time-dependent temperature and rigidity. We first investigate the compensation state of the lithosphere in the Scotian basin using more recent gravity, bathymetry and depth to basement data. We then model the lithosphere by a thin elastic plate with laterally varying rigidity that is subjected to sedimentary load and the load associated with density perturbations in the lithosphere. The plate overlies a fluid mantle of higher density. We show that the lithosphere must be weaker beneath the basin to explain the observed basement topography. This weakening is related to the blanketing effect of the sediments on the thermal state and, thus, the rigidity of the lithosphere.

2. Geological setting

The study area includes the rifted margin off Nova Scotia, the transform margin of Grand Banks, the Scotian basin and surroundings (Fig. 1). The Scotian basin, located southeast of Nova Scotia, extends from the east of Georges Bank to the central Grand Banks,

a distance of about 1200 km, and has an area of about 300,000 km². It is a part of a system of basins extending from the southeastern United States to northern Baffin Bay, developed in Mesozoic and Cenozoic time during the initial rifting of Pangaea and seafloor spreading of the Atlantic Ocean (Keen and Piper, 1990; Keen et al., 1990). The continental rifting that created the passive continental margin off Nova Scotia started about 200 Ma ago (Beaumont et al., 1982; Keen and Piper, 1990; Keen et al., 1990) and final separation between Africa and Nova Scotia occurred in the early Middle Jurassic. During the rifting period of about 20 Ma and, more importantly, after the break up of the continent and initiation of sea floor spreading, the basin subsided, allowing both syn-rift and post-rift sediments to accumulate (Keen and Beaumont, 1990; Wade and MacLean, 1990). The sediment thickness increases rapidly across the hinge zone (which is the zone of normal faulting that separates the basin from the “coastal plain”), delineating the strong thinning of the continental crust beneath the thickest sediments oceanward of the zone.

3. Modeling the observed gravity anomalies

Offshore exploration in the study area has been conducted intensively over the last three decades. Geophysical and geological data such as gravity, magnetic, and sediment lithology provide good constraints on the lithospheric models (Keen and Piper, 1990). In this section, we model the observed gravity anomalies using bathymetry and depth to basement data. The bathymetry data are extracted from ETOPO5 (NGDC) and the depth to basement data are obtained from Atlantic Geoscience Center (Oakey and Stark, 1995). The observed gravity data consist of Bouguer gravity anomalies determined on the basis of surface gravity measurements on land and the offshore free-air gravity anomalies extracted from Geosat data (National Gravity Data Base, Geomatics, Canada, and Sandwell and Smith, 1997). The original data were in terms of latitude, longitude and the value, and were not uniformly distributed. We therefore gridded the data over 256 × 256 grid points of 6-km intervals to carry out data analysis in the Fourier domain. We also fill the gaps between the two sets of gravity data by 2-D interpolation. A gravity value in a gap is

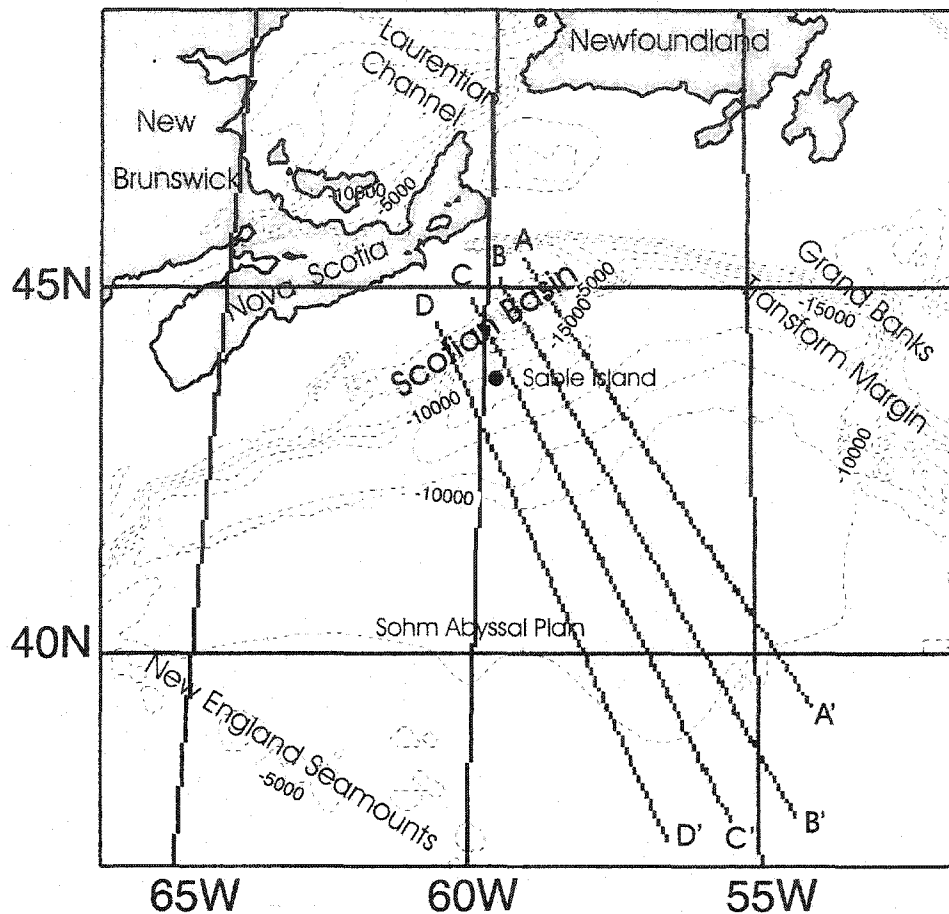


Fig. 1. Location of Scotian Basin and contiguous places based on Fig. 1.1 from Keen and Piper (1990). The lines across the Scotian Basin are the locations of the profiles used for gravity analysis and stacking the equivalent rock bathymetry (ERB), depth to basement and density perturbations. The black dot represents Sable Island. An equal area projection is used in this figure and other similar figures. The dashed contour lines are contours of the depth to basement with an interval of 2.5 km.

determined by weighted averaging of the surrounding values using the circular Hanning function for weighting,

$$W(r) = 0.5 \left[1 + \cos\left(\frac{\pi r}{R}\right) \right], \quad (1)$$

where r is the distance from the grid point and R ($= 18$ km) is the radius of the filter. Although the maps present the most dense gridded data over the entire area, the irregular spacing and many small gaps of the original gravity measurements on land do not allow resolution of wavelengths shorter than 30 km (Zheng and Arkani-Hamed, 1998). These wavelength components are dominated by noise and thus regarded as

useless. We filtered out these short wavelength components by Fourier transforming the data and applying a low-pass filter. The mean value of the gravity anomaly map is also removed, since we are concerned with the gravity anomalies. Fig. 2 shows the resulting gravity anomaly, bathymetry, and depth to basement maps, referred to as observed maps hereafter. The depth to basement map delineates the depth to the top of the oceanic basaltic crust. The depth is set to zero on land. Along the rifted Scotian margin and the transform margin of the Grand Banks, positive gravity anomalies exist along the shelf edge. The anomalies vary in amplitude from about 20 mGal southeast of the southern tip of Nova Scotia to over 100 mGal southeast of Sable Island (see Fig. 1 for the locations

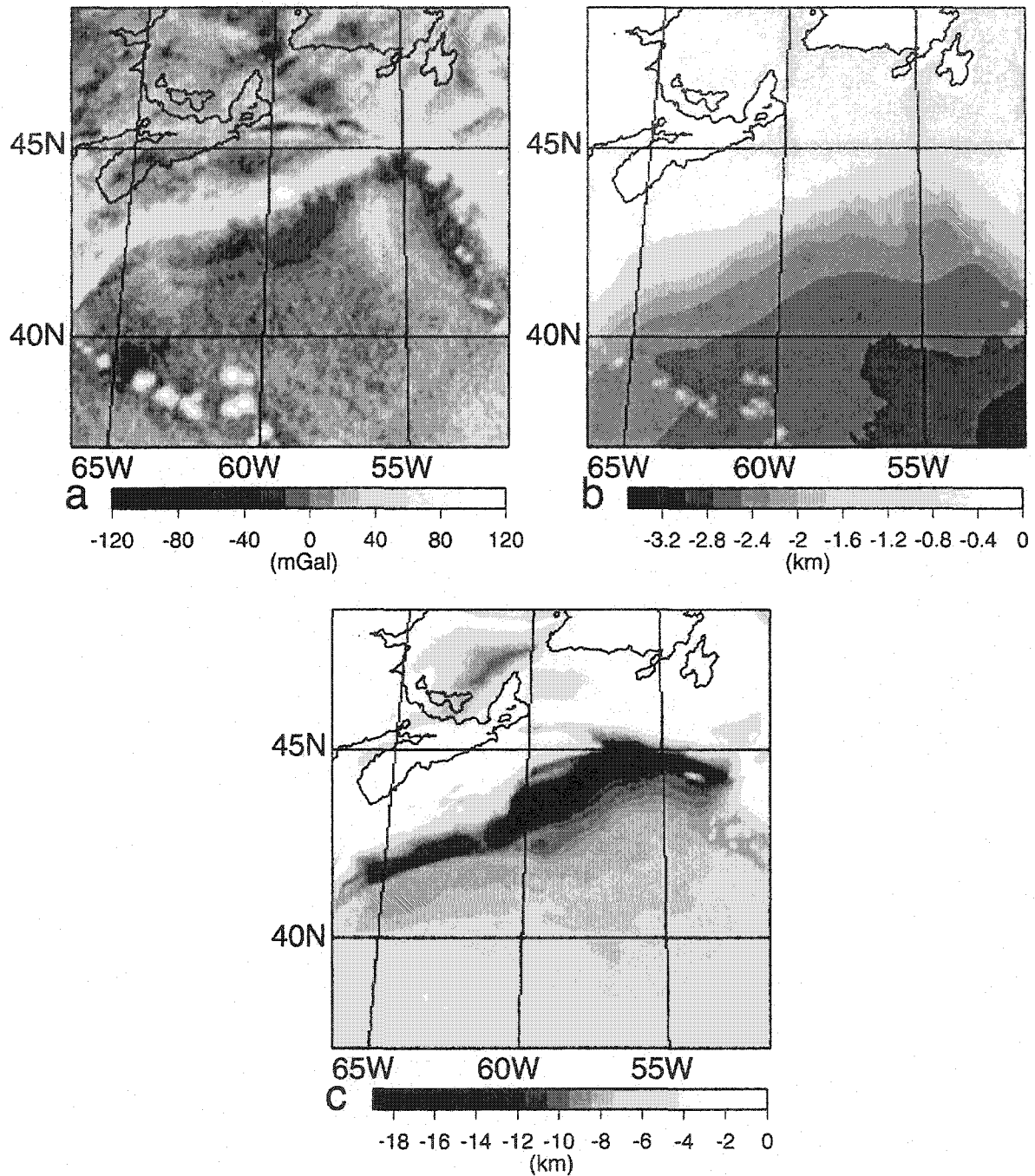


Fig. 2. (a) Observed gravity anomalies, free-air on the ocean and Bouguer on lands. (b) The equivalent rock bathymetry (ERB). The ERB of the continental areas is set to zero. (c) The depth to basement (after Oakey and Stark, 1995). The tapered zones near the boundaries, where data were tapered to suppress Gibb's ringing in the Fourier transformation are not shown in these maps, and in other similar maps including Fig. 1.

referred to in this paper). Flanking this positive anomaly are gravity lows near the foot of the continental slope and on the inner and middle shelf. The

New England seamounts in the southwest part of the study area have strong positive gravity anomalies up to about 150 mGal.

To interpret the observed gravity anomalies, it is required to take into account the contributions from water, sediments, crust, mantle, and possible density perturbations within sediments, crust and mantle. Following the first-order linear perturbation theory, we first construct a simplistic 3-D density model on the basis of the depth to basement and bathymetry (hereafter called the layered model) and regard this as a first-order approximation to a viable density model. We then determine perturbations to this first-order model such that the combination of this model and the perturbations produces a viable model that gives rise to the observed gravity anomalies. This is permissible because of the linear relationship between the density distribution and the gravity anomalies that allow superposition of the density of the simplistic model and the density perturbations. This layered model consists of four different layers of varying thickness: a water layer of density 1000 kg/m^3 , a sediment layer with a depth-dependent density, a crustal layer, and a mantle layer of density 3300 kg/m^3 . The crustal layer consists of a continental crust with a mean density of 2800 kg/m^3 and an oceanic crust with an average density of 2900 kg/m^3 . The mean density of the thinned continental crust beneath the continental shelf is probably somewhat higher than the mean density of the continental crust, since it largely consists of the lower crustal material. This is because, prior to rifting, the continent was most likely uplifted and the low-density upper continental materials were mainly removed by surface erosion. We use the average of the continental and oceanic crust density for the density of the thinned continent crust. The upper parts of the sediment layer have a lower density due to its appreciable porosity. The sediment density is determined using the porosity data at Scotian basin. The porosity ϕ decreases exponentially with depth,

$$\phi = \phi_0 \cdot e^{-cz} \quad (2)$$

where ϕ_0 ($=60\%$) is the porosity at the top of the sediments, z is the depth from the top, and c ($=0.55/\text{km}$) is the inverse of the characteristic length of the porosity decay with depth (Dehler and Keen, 1993). The sediment density ρ_s is calculated by

$$\rho_s = \phi\rho_w + (1 - \phi)\rho_g \quad (3)$$

where ρ_w and ρ_g are the densities of water and the sediment grain, respectively (Sclater and Christie,

1980). We adopt two different procedures to estimate ρ_g : (1) bearing in mind that sediments are the result of the erosion of the upper continental crust and that their grain density must be similar to that of the upper crustal rocks, we assume a ρ_g value of 2700 kg/m^3 which is the mean density of granitic rocks to represent the density of sediment grains, and (2) we test this value based on matching the gravity anomalies of our simplistic model to the observed anomalies (see below). The depth to the Moho for the continent is set to 35 km, which is the average Moho depth obtained from seismic measurements (Keen and Potter, 1995). The depth to the Moho for the ocean is determined by adding 7 km, the average thickness of the oceanic crust, to the depth to basement. The depth-to-basement map is smoothed before calculating the depth to the Moho, so that small-scale features such as the New England seamounts are not reflected in the depth to the Moho. These features are most likely supported by the rigid crust with minor flexure and introduce only minor undulation at the Moho. The ocean–continent transition zone of the Moho is not well defined from seismic velocities and other geophysical data. We calculate the Moho depth beneath the transition zone by a 2-D interpolation between the continental and oceanic Moho depth. The total thickness of the layered model is 35 km and the major characteristics of the model are similar to those of Beaumont et al. (1982).

The gravity anomaly of the layered model is calculated by dividing the model into 1-km-thick horizontal sublayers with laterally varying density. The sublayers are thin enough so that density can be assumed vertically constant within a given sublayer, but it varies laterally to take into account segments of different material (mantle, crust, sediments, and water) within a given sublayer. The boundary between two different materials in a given sublayer usually does not coincide with our grid points. We use linear interpolation of the densities of adjacent materials to determine the density of the grid point. The gravity anomaly of the model is determined by adding the gravity anomaly of each sublayer,

$$g_{u,v}(z) = 2\pi G \frac{e^{-kz}}{k} \sum_{n=1}^N (e^{-kd_n} - e^{-kd_{n-1}})^n \rho_{u,v}; \quad (4)$$

$$k = (u^2 + v^2)^{1/2}$$

where z is the observation altitude, which is set to zero at the sea level, N ($=35$) is the total number of sublayers, d_n is the depth to the top of the n th sublayer, and ${}^n\rho_{u,v}$ is the Fourier transform of the density of that sublayer. u and v are wavenumbers in the x and y directions and k is the 2-D wavenumber. Before applying the Fourier transform, the mean density of each sublayer is removed and the density near the boundaries of each sublayer is gradually tapered to zero at the boundaries using the 1-D version of the above Hanning function, to avoid Gibbs ringing. We note that the gravity anomalies of the layered model are consistently lower than the observed ones in the oceanic region, despite the fact that we remove the mean density of each sublayer before calculating its gravity field and also remove the mean of the observed gravity anomaly map. This systematic difference is most likely due to the fact that we have to use two different gravity data sets. On the continent, we use the Bouguer gravity data derived from gravity measurements on land, and on the ocean we use the Geosat data. These two data sets do not have a common zero level. A gravity anomaly map reflects the lateral variations of the gravity field. It does not provide information about the average gravity field, since the observed anomalies do not include the regional mean value. A constant level shift is usually made to the model anomalies in comparing them with the observed ones. The dimension of Scotian basin is small and its gravity field must have little effect on the observed anomalies in the far southeast region as clearly seen in Fig. 2a, where the anomalies have a negligible mean value. Therefore, we adjust the gravity anomalies of the layered model to have a near zero mean value over the far southeast region in order to compare them with the observed anomalies over the oceanic area, the area of primary concern in this paper.

We calculate gravity anomaly maps of the layered model for eight different density models in order to determine a density model that minimizes the misfit between the observed and model gravity anomalies. Fig. 3 shows the resulting gravity anomalies along profile CC' (see Fig. 1 for the location of the profile), as a representative profile. The gravity anomalies are level shifted to near zero values at the right-hand side far from the basin. Although no one particular density model explains the observed gravity over the entire length of the profile, many of the model gravity profiles are very close to the observed one over the

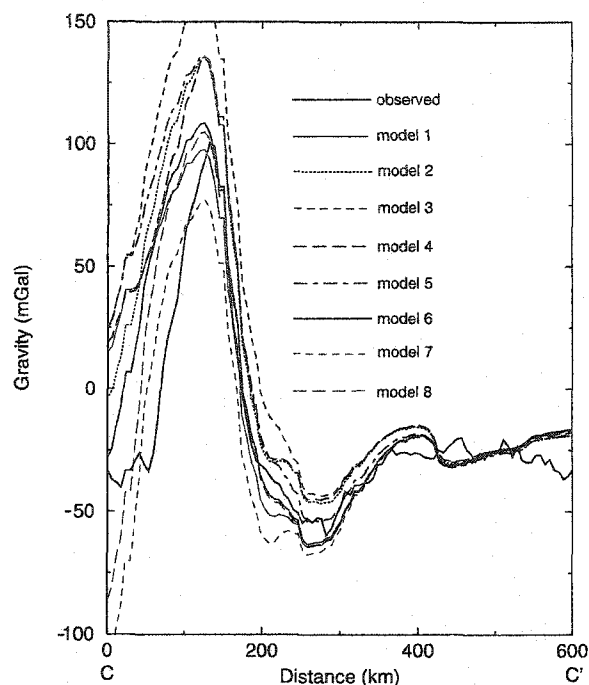


Fig. 3. Gravity anomaly of different layered models along profile CC' (see Fig. 1). Model 1, the nominal model with continental crust density $\rho_c=2800\text{ kg/m}^3$, oceanic crust density $\rho_o=2900\text{ kg/m}^3$, thinned continental crust density $\rho_t=2850\text{ kg/m}^3$ and sediment grain density $\rho_s=2700\text{ kg/m}^3$; Model 2, $\rho_c=2800\text{ kg/m}^3$, $\rho_o=2900\text{ kg/m}^3$, $\rho_t=2900\text{ kg/m}^3$ and $\rho_s=2800\text{ kg/m}^3$; Model 3, $\rho_c=2800\text{ kg/m}^3$, $\rho_o=2900\text{ kg/m}^3$, $\rho_t=2800\text{ kg/m}^3$ and $\rho_s=2800\text{ kg/m}^3$; Model 4, $\rho_c=2800\text{ kg/m}^3$, $\rho_o=2800\text{ kg/m}^3$, $\rho_t=2800\text{ kg/m}^3$ and $\rho_s=2800\text{ kg/m}^3$; Model 5, $\rho_c=2800\text{ kg/m}^3$, $\rho_o=2900\text{ kg/m}^3$, $\rho_t=2800\text{ kg/m}^3$ and $\rho_s=2750\text{ kg/m}^3$; Model 6, $\rho_c=2750\text{ kg/m}^3$, $\rho_o=2900\text{ kg/m}^3$, $\rho_t=2800\text{ kg/m}^3$ and $\rho_s=2700\text{ kg/m}^3$; Model 7, $\rho_c=2700\text{ kg/m}^3$, $\rho_o=2900\text{ kg/m}^3$, $\rho_t=2900\text{ kg/m}^3$ and $\rho_s=2700\text{ kg/m}^3$; Model 8, $\rho_c=2700\text{ kg/m}^3$, $\rho_o=2900\text{ kg/m}^3$, $\rho_t=2800\text{ kg/m}^3$ and $\rho_s=2700\text{ kg/m}^3$. The densities of seawater and mantle are 1000 and 3300 kg/m^3 , respectively, for all models.

major part of the basin. The main disagreement between the observed and modeled anomalies occurs over continent and continental shelf. The observed Bouguer anomalies over the continent reflect the lateral density variations in the continental crust. Such variations are not included in our layered model. We select model 1 with sediment grain density of 2700 kg/m^3 and the thinned continental crust density of 2850 kg/m^3 for the density structure of our nominal 3-D layered model, since it seems to explain the observed gravity profile somewhat better than the others.

Fig. 4 shows the observed and the nominal layered model gravity anomalies along four profiles seen in Fig. 1. The model profiles are vertically shifted to near zero values at the right-hand side far from the basin. Also included in the figure are the bathymetry, basement and Moho profiles to illustrate the crustal structure beneath. The profiles span almost the entire extent of the basin and provide a good estimate of the general properties of the basin. The major disagreement between the observed and modeled anomalies

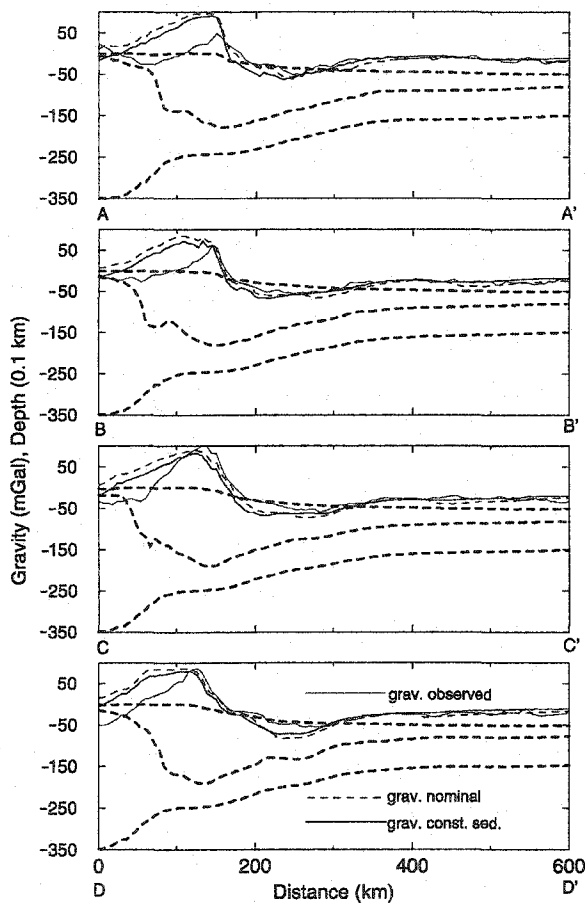


Fig. 4. Observed gravity anomalies, gravity anomalies of the nominal layered model and the constant sediment density model along four profiles (see Fig. 1). The thick solid curves show the observed gravity anomalies. The thin dashed curves show the gravity anomalies of the nominal layered model. The thin solid curves show the gravity anomalies of the constant sediment density model. The thick dashed curves show the bathymetry, depth to basement and depth to Moho along the profiles in 0.1 km for better illustration.

occurs over continent and continental shelf, as mentioned above. Over the oceanic area, the observed and model profiles have similar features. They decrease rapidly oceanward from the shelf edge and attain minima in the eastern part of Scotian basin, and gradually increase eastward of the basin. However, the misfit of the model anomalies to the observed ones differ among the profiles, emphasizing that the nominal layered model explains major characteristics of the crust but fails to represent local variations, as expected. Fig. 5a shows the gravity anomaly map of the nominal model, and Fig. 5b displays the differences between the observed and model gravity anomalies (observed-model). The model anomalies are lower than the observed ones over Scotian basin. However, they are in good agreement over the featureless regions in the southeast.

We also calculated the gravity anomalies of a model identical to the nominal model except that the sediment is taken to be non-porous having a constant density of 2700 kg/m^3 . Fig. 4 includes the gravity profiles of this model for comparison. Using the constant sediment density has minor effects on the resulting gravity anomalies. This is expected, because the porosity of the upper parts of sediments produces a surface layer parallel to bathymetry where density varies across the depth of the layer but not along the layer. It changes the mean density of the upper sublayers much more than introducing lateral density variations in those sublayers, except near the shelf edge where bathymetry has an appreciable slope. However, the total thickness of the sediments exceeds 10 km in this region and the porosity has minor effects on the total mass of a given sedimentary column there.

We now seek local density perturbations required to add to the nominal model in order to explain the observed gravity anomalies. The difference between the observed and the nominal model gravity anomalies must arise from some density perturbations that were not included in the model. For example, no salt layers, diapiric intrusives that likely occurred during continental rifting, and small-scale tectonic features associated with the initial rifting are taken into account in the nominal model. Another plausible source of misfit between the observed and modeled gravity anomalies is the variations of the crustal thickness. We use a mean crustal thickness of 35 km for the continent, by assuming a flat Moho beneath.

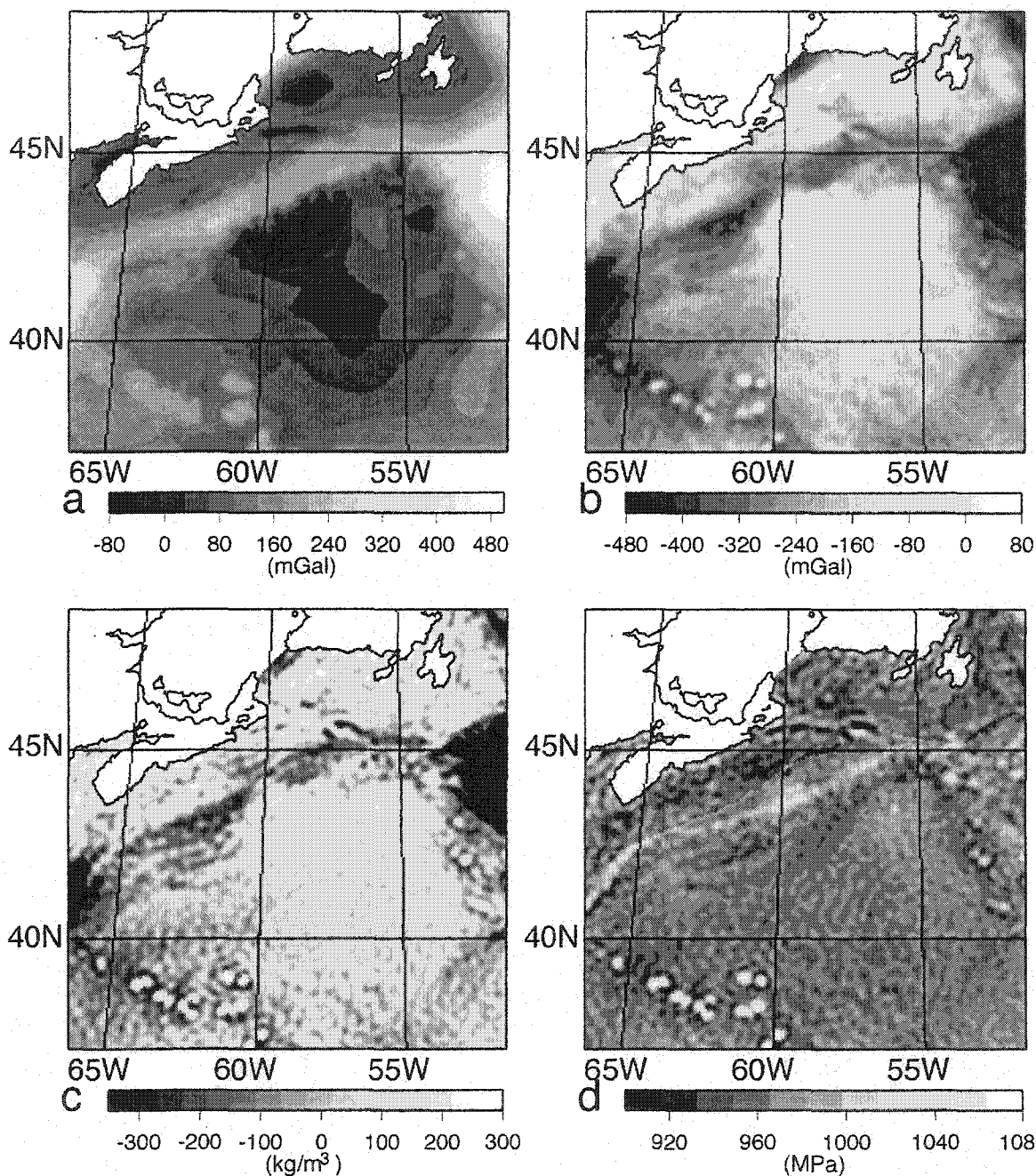


Fig. 5. (a) Gravity anomalies of the nominal layered model. (b) Differences between observed gravity anomalies and the gravity anomalies of the nominal layered model (observed minus model). (c) Density perturbations required to be added onto the nominal layered model in order to produce the observed gravity anomalies. (d) Lithostatic pressure at 35 km depth. The features on the continental part are not shown in this figure since we are only concerned with the oceanic part.

The depth to the actual Moho more likely varies from place to place by a few kilometers. The thickness of the oceanic crust is taken to be 7 km in the nominal

model for the entire oceanic area. Although the oceanic crust does not vary in thickness as much as the continental crust, variations of about 1 km are

quite common and are sufficient to explain the misfit over the oceanic area. Here, we adopt the simplest model to estimate these density perturbations. Bearing in mind that the gravity anomalies provide information about the lateral variations of the vertically integrated density perturbations, we seek vertically averaged density perturbations within our layered model of thickness H_c ($=35$ km). The density perturbations $\delta\rho$ are determined using (e.g., Zheng and Arkani-Hamed, 1998),

$$\delta\rho_{u,v} = \frac{ke^{kz}}{2\pi G(1 - e^{-kH_c})} \Delta g_{u,v} \quad (5)$$

where $\Delta g_{u,v}$ and $\delta\rho_{u,v}$ are the Fourier transforms of the gravity anomaly difference (observed minus the level shifted model) and the density perturbations, respectively. Again z is set to zero at the sea level. The density perturbations thus determined (Fig. 5c), together with our simplistic nominal model, give rise to the observed gravity anomalies. Over the oceanic area, small-scale features of the density perturbations mimic those of the observed gravity anomalies, especially where the layered model's gravity is smooth. At about 100 km towards the ocean, there are positive density perturbations required to add to the nominal model in order to produce the observed gravity anomalies. The density perturbations are in the order of 100 kg/m^3 . The total mass perturbations associated with these density perturbations, i.e., the density perturbations times the thickness of the layered model, are equivalent to an excess oceanic crustal thickness of about 1.2 km.

It is required to assess whether the improved 3-D layered model, the nominal model plus the density perturbations thus obtained, is in local equilibrium or it requires regional support. For this purpose, we calculate the pressure $P(x,y)$ at the base of the nominal model by

$$P(x,y) = \int_0^{H_c} g\rho(z)dz \quad (6)$$

where $\rho(z)$ is the density at a depth z (density of the nominal model plus the density perturbation) and g is the gravitational acceleration. The results (Fig. 5d) show appreciable lateral variations of the pressure, emphasizing that the entire structure is not in equi-

librium. The pressure in the central part of the basin is $\sim 50\text{--}60$ MPa more than its surroundings. This is equivalent to the pressure of a sedimentary column of thickness 1.8–2.2 km, about two times the pressure created by the density perturbations alone. This emphasizes that not only the density perturbations, but also a part of the sediments must have been supported by a rigid lithosphere beneath.

4. Support mechanism

Elastic plate models have been used to model the flexure of the lithosphere due to loads associated with surface topography, trenches, seamounts, and passive continental margins (e.g. Caldwell et al., 1976; Lambek and Nakiboglu, 1980; Lago and Cazenave, 1981; Cloetingh, 1982; Forsyth, 1985; McNutt et al., 1988; Zuber et al., 1989; Erickson, 1993). These studies suggest that the oceanic lithosphere respond to sedimentary loads as a thin elastic plate overlying a fluid-like asthenosphere of higher density. It was demonstrated above that Scotian basin must be supported by a rigid lithosphere. Here, we adopt a 2-D thin elastic plate model to estimate the rigidity required for the lithosphere. The undeformed plate is taken on the horizontal x,y plane with an infinite y dimension. It flexes in the z direction under the load consisting of the sediments, the lateral variations of mass associated with the density perturbations, and the overlying water. The water column is added to the bathymetry by calculating the equivalent rock bathymetry. The equivalent rock bathymetry in the ocean is determined by replacing a water column of density 1000 kg/m^3 by an equivalent rock column of density ρ_g while conserving the total mass of the column, and adding this equivalent rock thickness to the bathymetry. It is set to zero on land to be compatible with the Bouguer gravity anomalies there.

Fig. 6 shows the equivalent rock bathymetry, basement topography and density perturbations along the four profiles seen in Fig. 4. The profiles are stacked to the reference point at which the depth to basement of each profile is a maximum. The differences among the profiles indicate the effects of local variations. The profiles present major characteristics of the basin that we are interested in. From west to east, the thickness of the equivalent-sediments, i.e., the column between

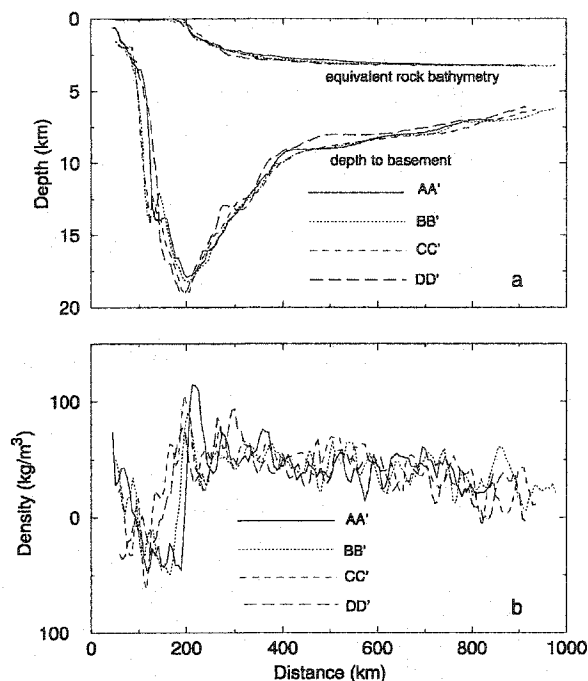


Fig. 6. (a) Selected profiles of the ERB, the depth to basement and density perturbations (see Fig. 1 for the locations of the profiles). The profiles are stacked to the reference point where the deflection is a maximum.

the equivalent rock bathymetry and the basement, increases very rapidly as we enter the thinned continental shelf, achieving a maximum of about 16 km. The thickness then gradually decreases toward the younger parts of the ocean, remaining almost constant at about 3 km at distances farther than about 800 km from the basin. Except very close to the continent, the density perturbations are positive and add to the sediment load. However, the overall amplitude of the perturbations is $\sim 50 \text{ kg/m}^3$, i.e., the mass perturbations $\sim 1.75 \times 10^6 \text{ kg}$ for the entire thickness of 35 km. This is equivalent to an extra $\sim 0.6 \text{ km}$ sediment, which is very small compared to the thickness of the equivalent sediment. We average these profiles to obtain representative profiles of the equivalent rock bathymetry, basement topography and density perturbations, which have been further smoothed to suppress the effects of detailed local features. These averaged profiles will be used in the following calculations.

We assume that the basement profile relative to the reference depth of the oceanic crust far from the basin

is the resulting flexure of the plate. This is a first-order approximation that does not account for the initial topographic features that were most likely created during the initial rifting, such as rift valleys. These topographic features are usually small-scale features compared with the broad depression of the basin that has been resulted from the deflection of the lithosphere under the sedimentary load. The governing equation of the deflection w of a thin elastic plate model under a surface load is (Turcotte and Schubert, 1982)

$$\frac{d^2}{dx^2} \left(D \frac{d^2 w}{dx^2} \right) + P \frac{d^2 w}{dx^2} + \rho_m g w = q(x). \quad (7)$$

P is the horizontal force and D is the flexural rigidity of the plate defined by

$$D = \frac{Eh^3}{12(1-\nu^2)} \quad (8)$$

where E ($=8 \times 10^{10} \text{ Pa}$) is the Young's modulus, ν ($=0.25$) is the Poisson's ratio, and h is the thickness of the plate. $q(x)$ denotes the surface load. We treat the equivalent-sediments and the excess mass associated with the density perturbations as surface loads on the elastic plate model,

$$q(x) = \left[\int_0^{H_s(x)} \rho_s dz + \delta\rho(x)H_c \right] g, \quad (9)$$

where ρ_s is the depth-dependent density of the equivalent sediment, $\delta\rho(x)$ denotes the vertically averaged density perturbations and $H_s(x)$ is the thickness of the equivalent-sediment at x .

It is desirable to pose Eq. (7) as an inverse problem and determine the lateral variations of the rigidity of the plate using the known load function $q(x)$ and the basement topography as the deflection w . However, this is not possible because of the singularities arising at the inflection points where the deflection curve changes from concave to convex, allowing its curvature to become zero. At these points d^2w/dx^2 vanishes and the rigidity term in Eq. (7) disappears. Therefore, we solve Eq. (7) by the forward method, using several rigidity values and comparing the resulting deflection with the basement profile in the ocean to determine the best rigidity estimate. A reasonable value for P that represents the ridge push has minor effects on the deflection, as also concluded by Caldwell et al.

(1976). Therefore, P is set to zero. Also, we impose pinned boundary conditions at both ends, i.e., $w=0$ and $dw/dx=0$. The normal faults, likely produced at the hinge zone during continental rifting, may lock by 10–20 Ma (Karner and Watts, 1982). In reality, the normal continental lithosphere west of the hinge zone is also deflected by the sedimentary load of the basin because of its coupling to the thinned continental lithosphere directly beneath the basin. However, the depth-to-basement profiles show that the possible deflection is very small (see Fig. 6). Erickson (1993) used two different models to investigate the deflection of the lithosphere beneath the Scotian basin: an infinite plate of constant rigidity 1.92×10^{23} Nm; and two semi-infinite layers: one for the continent with a rigidity of 1.56×10^{25} Nm, and the other for the ocean with a rigidity of 9.8×10^{22} Nm. The first model showed an unrealistically large deflection of the normal continental lithosphere. The second, his most favored model, showed a maximum deflection of about 3.5 km, which is still about a factor of 3 more than the observed one (see Fig. 2 of Erickson, 1993). This indicates that the normal continental lithosphere has even higher rigidity, and the pinned boundary is appropriate. Moreover, the very small deflection of the continental lithosphere west of the hinge zone only uniformly suppresses the entire lithosphere east of the hinge zone and has little effect on the deflection of the lithosphere directly beneath the basin relative to that of the oceanic lithosphere far from the basin that we are concerned with. Therefore, for the deflection calculations we use pinned boundary condition at the hinge zone and neglect the continental part west of the zone. We also use pinned boundary conditions at the ocean side because of the fact that the depth to the basement does not change appreciably at distances farther than about 800 km from the basin (see Fig. 6). Also, the oceanic plate is extended oceanward to have a length of 1500 km, using constant bathymetry and basement topography, to make sure that the boundary conditions at the ocean end have little effect on the relative deformation of the lithosphere beneath the basin and its immediate surroundings. We also calculate a model using free boundary conditions at the oceanic end. The resulting deflection within ~ 1000 km from the continent is almost identical to that with pinned boundary conditions (see below), ensuring that the boundary conditions have lit-

tle effect within this distance. The effect of the pinned boundary conditions is appreciable within about 300 km from the boundary, where the deflection gradually goes to zero at the boundary. For the free boundary, the deflection remains almost constant at distances farther than 1000 km from the continent. Therefore, we will show the deflection results up to a 1000-km distance from the hinge zone in the following figures.

The vertical load on the plate arises from the sediments depicted in our layered model and the density perturbations determined above. We note that it is possible for the lower parts of the sediments inside the basin to become rigid and thus support part of the load of the overlying sediments. However, the lower parts are confined to the basin and do not produce an extended plate. Therefore, the weight of the lower parts as well as that of the overlying sediments must eventually be supported by the oceanic plate, regardless of the rigidity of the lower parts. We also note that we adopted the simplest model for the density perturbations, by assuming that the perturbations are confined within a flat layer of 35-km thickness and have a vertically uniform distribution. The exact location of the perturbations cannot be constrained on the basis of the gravity anomaly analysis alone. They may be due to density variations in the sediments, in the crust, and/or in the upper parts of the mantle. Therefore, we consider two possibilities by either including or excluding them as a part of the load exerted on the plate. Including them implies that they are located somewhere inside the sediments, the crust, or the upper mantle where they are strongly coupled to the lithosphere. Excluding them implies that they are in the asthenosphere and are not coupled to the lithosphere.

We first examined a suite of elastic plate models with constant rigidity, ranging from 10^{20} to 10^{23} Nm and the above-mentioned boundary conditions (Fig. 7a). We note that the x axis of Fig. 7 is shifted eastward by 100 km relative to that of Fig. 6 to allow the hinge zone, the pinned boundary, to coincide with $x=0$. We also note that the continent–ocean topographic dichotomy of the earth, that continents are on the average 5 km above the ocean floors, arises because the thick and low-density normal continental crust is essentially in isostatic compensation on a global scale with the thin and denser oceanic crust. This essentially explains the difference between the depth to basement profiles

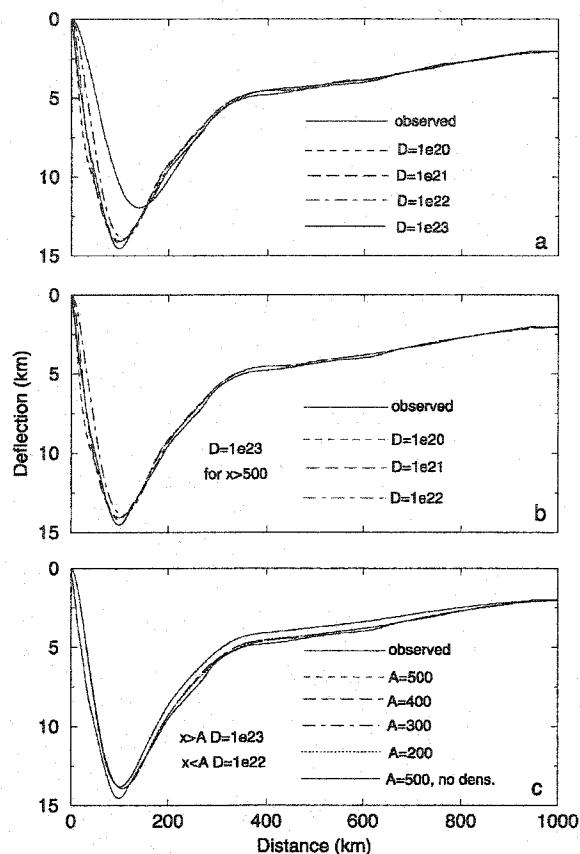


Fig. 7. Averaged profile of the depth to basement, and the deflections of various rigidity models. Density perturbations are included in the load. The thick solid curve shows the averaged depth to basement profile. (a) Deflections of the elastic plates with uniform rigidities, (b) deflections of the two-segmented model with weak zone up to 500 km. Rigidity is kept at 10^{23} Nm when x is beyond 500 km and (c) deflections of two-segmented models with different weak zone width from 200 to 500 km. The rigidity of the weak zone is 10^{22} Nm, beyond the weak zone it is 10^{23} Nm. Also included in (c) is the deflection of a two-segmented model with a weak zone up to 500 km, but with no contribution of the density perturbations to the surface load. Note that the x axis of this figure is shifted by 100 km eastward compared to that of Fig. 6 to put the hinge zone at $x=0$. We also show only the first 1000 km from the hinge zone.

shown in Fig. 6 and that shown in Fig. 7a. Fig. 6 is relative to the surface of the normal continent west of the hinge zone that is set at sea level in the process of calculating the Bouguer anomalies on land, as mentioned before. By matching the observed depth-to-basement profile to the deflection profiles of the models far from the basin in Fig. 7a, we have essentially

removed this dichotomy and focused on the deflection of the lithosphere beneath the basin relative to that far from the basin. For high rigidity values, the resulting basin is shallower and has a much smaller slope near the hinge zone compared to the observed one. However, as the rigidity decreases, the model basin approaches the observed one. Note that the deflection of the plate at regions far from the basin remains almost unchanged while the plate rigidity is reduced from 10^{23} to 10^{20} Nm, corresponding to elastic thicknesses of 24.1 to 2.4 km. This is because the load function over this region is dominated by very long wavelength components compared to these elastic thicknesses, and the plate behaves as a non-rigid plate, allowing the load to become isostatically compensated. Therefore, the rigidity of this region cannot be constrained. This point was demonstrated by Turcotte and Schubert (1982) who calculated the deflection of an elastic plate under a sinusoidal surface load. This is also the main reason that the boundary conditions at the oceanic end do not affect the deflection of the lithosphere farther than about 300 km from the boundary. The deflection of the plate with a constant rigidity of lower than about $\sim 10^{22}$ Nm (elastic thickness less than 11.2 km) explains the observed depth to basement over the entire profile. However, due to the unconstrained nature of the rigidity of the region far from the basin, such a constant rigidity plate model may not be adequate for this region. In fact, the normal oceanic plate older than about 50 Ma is much stronger (see Fig. 9). The oceanic lithosphere requires a rigidity of about 2.4×10^{23} Nm to support the Hawaiian islands, and the oceanic lithosphere near the Mariana trench is estimated to have a rigidity of 1.4×10^{23} Nm (Turcotte and Schubert, 1982). On the other hand, a constant rigidity plate model representative of the oceanic lithosphere far from the basin, with a rigidity of $\sim 10^{23}$ Nm or more, does not represent the lithosphere beneath the basin. Both models of Erickson (1993) resulted in much wider basins than the observed one. The thinned part of the continental lithosphere and the older part of the oceanic lithosphere beneath Scotian basin are overlain by thick sediments. These regions are most likely weakened by the thermal blanketing effects of the sediments (see below), and are most likely weaker than the normal oceanic lithosphere.

To incorporate the thermal blanketing effect, we consider two-segmented plate models with a weaker

zone beneath the basin. By varying two parameters, the width of the weak zone and the rigidity of the lithosphere beneath this zone, we investigate the major characteristics of the plate deflection and determine a range of acceptable models. Fig. 7b shows the deflection of a plate with a fixed width of 500 km but several rigidity values for the weak zone, and a fixed rigidity of $\sim 10^{23}$ Nm for the oceanic lithosphere farther than 500 km. The weak zone rigidity values of less than 10^{22} Nm are good representatives of the lithospheric rigidity beneath the Scotian basin, implying that thermal blanketing might have reduced the rigidity of the lithosphere by at least one order of magnitude. To illustrate the effect of the weak zone size on the plate deflection, we note that the equivalent sediment thickness decreases very rapidly from ~ 16 km beneath the shelf edge to ~ 5 km at about 400 km from the continent, and then decreases slowly from thereon (see Fig. 6). This suggests that the thermal blanketing effect is more important within 400 km from the continent. Fig. 7c shows the deflection of a plate with the weak zone widths of 500, 400, 300 and 200 km. The plate rigidity is 10^{22} Nm beneath the weak zone and 10^{23} Nm outside the zone. The plate deflection slightly decreases with the decrease of the weak zone width, but the difference is very minor for the weak zone widths of 400 to 500 km. It becomes noticeable for the width of 200 to 300 km. Fig. 7b and c shows that models with a weak zone width of 300–500 km and the lithospheric rigidity of 10^{21} – 10^{22} Nm (elastic thickness of 5–11 km) explain the observed basement profile almost equally. We will use the lithospheric model with a 500-km-wide weak zone of 10^{22} Nm rigidity, and 10^{23} Nm rigidity outside the zone in the remaining part of the paper.

We also consider the possibility that the density perturbations reside in the mantle and do not couple to the overlying elastic lithosphere, by removing the contribution of the density perturbations from the surface load function. Included in Fig. 7c is the resulting deflection of the plate model with a weak zone of 500-km width and 10^{22} and 10^{23} Nm rigidity beneath the weak zone and elsewhere, respectively. The deflection is slightly less than that of the corresponding model with density perturbations included. This is expected because of small mass associated with the density perturbations compared to the entire mass of an equivalent sediment column, as mentioned earlier.

5. Strength of the lithosphere

During continental rifting, the surface topography was most likely supported dynamically. Immediately after the continental break-up and the initiation of seafloor spreading, the surface subsided mainly because of thermal contraction as the hot thinned part of the continental lithosphere and the newly formed hot oceanic lithosphere cooled very rapidly. Subsidence was further enhanced by sedimentation which occurred largely on the thinned continental shelf east of Nova Scotia, resulting in a deep basin with a present sedimentary thickness of about 16 km, whereas the thickest sediments on the oceanic crust are only about 7 km (Ghods and Arkani-Hamed, 1998). The thermal evolution of the Scotian basin has been studied intensively by Royden and Keen (1980), Beaumont et al. (1982), Keen and Beaumont (1990), and Ghods and Arkani-Hamed (1998). In particular, Keen and Beaumont (1990) examined both the thermal and mechanical subsidence of elastic plate models with time-varying rigidity and sedimentary load. In the absence of sediments, the thermal subsidence of the oceanic lithosphere must be more than that of the thinned continental shelf, partly because of higher initial temperature of the oceanic lithosphere, and partly because the oceanic crust and the mantle beneath are denser than the adjacent continental crust.

Here, we first assess the early stages of subsidence of the basin due to sedimentary load. Adding subsidence due to thermal contraction will have minor effect on the deflection of the thinned continental shelf relative to that of the oceanic lithosphere. It will only deepen the oceanic part to some extent because of the larger thermal subsidence of the oceanic lithosphere compared with that of the continental lithosphere. In the early stages of cooling, both the thinned continental lithosphere and the newly formed oceanic lithosphere are hot and may not be very different mechanically. Therefore, we model both by a single plate with a constant density of 2900 kg/m^3 but with varying rigidity. The plate is overlain by sediments with a constant density of 2700 kg/m^3 and varying thickness, and is underlain by an inviscid mantle of density 3300 kg/m^3 . The model plate extends from the undeformed part of the continent, approximated by the hinge zone, to the oceanic ridge axis that recedes from the continent with time. We assume that the plate has a length

that increases by 10 km/Ma, corresponding to a sea floor spreading of 1 cm/year. Also, we adopt a sedimentation rate of 1 km/10 Ma in the early stages, as observed over this region (Gradstein et al., 1990). The model plate is pinned to the continent but it is free at the oceanic ridge axis. The sedimentary load is assumed to linearly decrease from a maximum at the continent side to zero at the ridge axis. The rigidity of the plate is mainly controlled by the thickness of its elastic core, which itself depends on the thermal state of the plate and the stress differences applied. We study these interconnected relationships through forward modeling. First, we calculate the thermal evolution of the plate using the conventional half-space cooling model of the oceanic lithosphere (Turcotte and Schubert, 1982),

$$\frac{T - T_s}{T_m - T_s} = \operatorname{erf}\left(\frac{z}{2\sqrt{\kappa x/u}}\right) \quad (10)$$

where T_s ($=0^\circ\text{C}$) is the surface temperature, T_m ($=1350^\circ\text{C}$) is the temperature at the ridge axis and beneath the plate. u ($=10$ km/Ma) is the spreading rate, and x and z denote the horizontal and vertical coordinates, respectively. x is measured from the ridge axis. κ ($=K/\rho c$) is the thermal diffusivity, where K ($=3.1$ W/m/K) is the thermal conductivity and c ($=1250$ J/kg/K) is the specific heat.

We then determine the strength envelope of the model plate. The near surface brittle portion of the plate is governed by Byerlee's law (Byerlee, 1978; Brace and Kohlstedt, 1980), and the deeper ductile portion obeys the creep law. The creep law for differential stresses less than 200 MPa is

$$\dot{\epsilon} = A\sigma^n \exp(-Q/RT), \quad (11)$$

where Q is the activation energy, R is the universal gas constant, σ is the differential stress, $\dot{\epsilon}$ is the strain rate, T is the temperature, and A is the pre-exponential constant. For the crust, we use Maryland diabase rheology after Caristan (1982), with $A=6.12 \times 10^{-2}$ MPa $^{-n}$ s $^{-1}$, $n=3.05$, and $Q=276$ kJ/mol. For the mantle, the dry olivine rheology of Goetze (1978) is adopted, with $A=7 \times 10^4$ MPa $^{-n}$ s $^{-1}$, $n=3$, $Q=510$ kJ/mol. For differential stresses greater than 200 MPa, the creep law is

$$\dot{\epsilon} = A \exp\left[-\frac{Q}{RT} \left(1 - \frac{\sigma}{8500}\right)^2\right]. \quad (12)$$

Again we adopt the dry olivine rheology for the mantle after Goetze (1978), with $A=5.7 \times 10^{11}$ MPa $^{-n}$ s $^{-1}$ and $Q=535$ kJ/mol. The strain rate adopted is 10^{-18} s $^{-1}$ (Cloetingh, 1982). A higher strain rate of 10^{-16} s $^{-1}$ has been used by Watts et al. (1980) and McAdoo and Sandwell (1985). Adopting this higher strain rate will increase the strength by a factor of 4.6. Fig. 8 shows the compressional and tensional strength envelopes of the plate under a given point at several times after the breakup. The elastic core is sandwiched between the upper brittle and the lower ductile parts with a thickness determined by the stress differences applied. The elastic thickness is determined from the compressional strength by setting the stress differences equal to the sedimentary load at that point. It rapidly increases in the first 10 Ma and then increases monotonically but with a decreasing rate (Fig. 9). Similar results were obtained by Cloetingh (1982). The elastic rigidity is determined through Eq. (8) with the elastic thickness h thus obtained. The rigidity of a given plate substantially decreases towards the ridge axis. For example, it decreases by a factor of about 50,000 from the hinge zone to the ridge axis in a 50-Ma-old plate.

In the final step, we determine the deflection of the plate with varying rigidity under the linearly decreasing surface load by solving Eq. (7) subject to the above-mentioned boundary conditions, i.e., the plate is pinned to the continent but is free at the ridge axis. Fig. 10 shows the resulting deflection for several plates

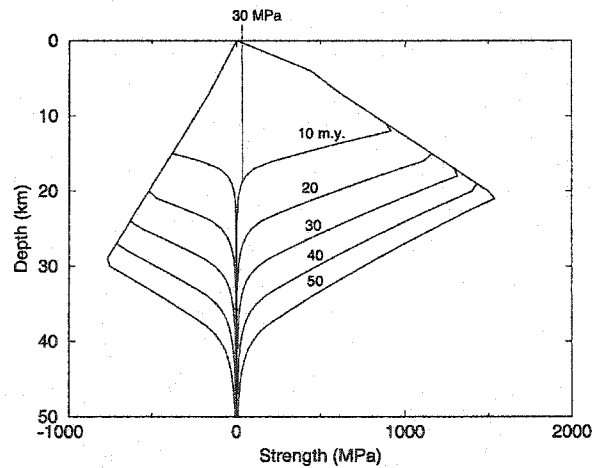


Fig. 8. The strength envelopes calculated from the half-space cooling model at 10, 20, 30, 40 and 50 Ma. The vertical thick line shows the elastic thickness of the 10 Ma old plate, as an example.

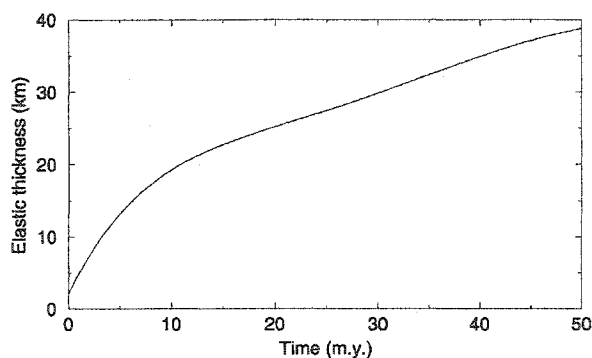


Fig. 9. The elastic thickness of the simple plate model versus time.

of different lengths corresponding to their ages. The similarity of the deflection profiles of these simplistic models to the basement profile of Scotian basin near the hinge zone emphasizes that the oceanic and continental lithospheres beneath the basin have been welded since very early in the history of the basin as also suggested by Karner and Watts (1982), and that major deflection in the basin is more likely associated with the response of the lithosphere to sedimentary loading. The distance between the pinned boundary and the maximum deflection zone of the models increases with the age of the plate. It reaches ~ 170 km by 50 Ma, which is $\sim 70\%$ farther than the distance observed in the basin (see Fig. 7). The major part of the deflection in the Scotian basin has occurred within the first 70 Ma, with a much higher rate in the early stages (Gradstein et al., 1990; Keen and Beaumont, 1990) and the lithosphere has become strong by this time (Cloetingh, 1982). The deflection amplitude of the model plates and the slope of the deflection near the hinge zone increase with the increase of the sediment thickness and length of the plates. However, the maximum deflection for the plate at 50 Ma age is less than 20% of the maximum observed deflection of Scotian basin. The model plate creates a basin that is much wider and much shallower than Scotian basin. Comparison of Figs. 7 and 10 emphasizes that the lithosphere beneath the basin has been weaker than the model plates that cooled monotonically obeying the half-space cooling criterion. The lithosphere beneath the Scotian basin has been further weakened due to the thermal blanketing effects of the sedimentary cover there.

After the break-up of the continent and the initiation of sea floor spreading, the continental lithosphere

beneath the shelf cools, as does the adjacent oceanic lithosphere. As time passes, the lithosphere becomes stronger and responds less to newly added sedimentary load. Modeling details of the time-varying strengthening process and dynamics of lithosphere requires extensive high-resolution stratigraphic information. Here, we estimate the blanketing effects of the sediments on the strength of the lithosphere beneath the Scotian basin using the steady state temperature condition. The temperature distribution inside an oceanic lithosphere becomes almost steady within the first 70 Ma during which major sedimentation in the basin has occurred, as mentioned above. The steady-state calculation provides a rough estimate of the thermal blanketing effects of the sedimentary cover since 70 Ma.

The steady-state temperature distribution T in the model lithosphere is calculated by

$$K \frac{d^2 T}{dz^2} = -A \quad (13)$$

where K is the thermal conductivity (1.88 W/m/K for sediments and 3.1 W/mK for the crust and mantle), z is the depth measured from the top of the sediments, and A is the rate of radiogenic heat generation per unit volume, assumed to be constant in time for each layer since the age of the oceanic lithosphere in the study area is much less than the half-lives of the radiogenic elements. Three layers are considered: sediments with a thickness determined from the averaged bathymetry and depth-to-basement profiles (note: we use bathymetry in this calculation and not the equivalent rock bathymetry), the crust with a thickness of 7 km in the ocean and a varying thickness in the continental shelf,

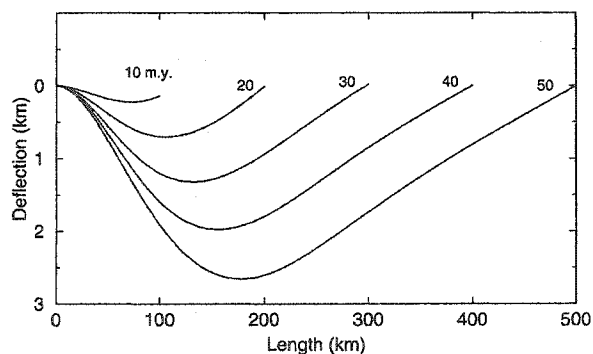


Fig. 10. The deflections of the simple plate model at different ages. Numbers on the curves show the ages.

and the mantle down to 100 km depth assumed to be the base of the thermal boundary layer of the mantle convection beneath. We used heat generation rates of $8 \times 10^{-8} \text{ W/m}^3$ for the oceanic crust, 10^{-6} W/m^3 for continental crust and sediments, and $2 \times 10^{-8} \text{ W/m}^3$ for the mantle. The temperature at the base of the lithosphere is kept at 1350°C . It is set to zero at the top of the sediments. The model is one-dimensional and no heat flow is allowed across the vertical boundaries,

because the steady-state horizontal temperature gradient is much smaller than the vertical temperature gradient. Detailed study of the time varying thermal evolution of the Scotian basin by Ghods and Arkani-Hamed (1998) showed that horizontal heat conduction is only significant in the very early stages during continental rifting, and in the later stages only near the oceanic ridge axis. We also note that the thick continental crust with high radiogenic heat sources west of

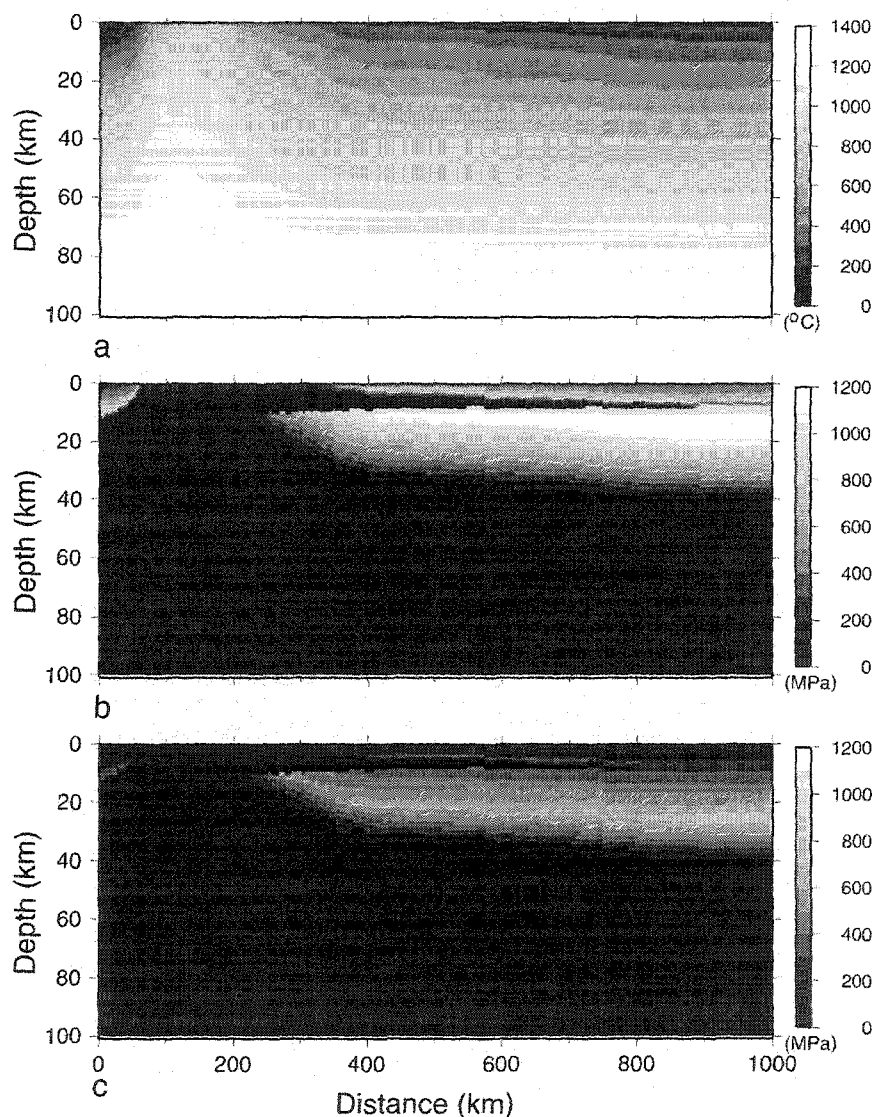


Fig. 11. (a) The steady-state temperature distribution of the lithosphere using the averaged sedimentary thickness profile. (b) Compressional and (c) tensional strength envelopes of the lithosphere. The depth is measured from the top of the basaltic crust, i.e., the base of the sediments. (b) and (c) are in absolute values.

the hinge zone does not directly attach to the oceanic crust with lower radiogenic sources. Rather, the continental crust gradually thins within about 180-km-wide transition zone before it is juxtaposed to the oceanic crust. The lateral heat flow from the normal continent to the ocean is substantially suppressed because of this large distance.

Fig. 11 shows the temperature distribution in the model lithosphere, where depth is relative to the top of the crust, i.e., the base of the sediment column. The temperature of the lithosphere beneath the basin increases with the increasing thickness of sediments, because of the thermal blanketing due to the sediments. This temperature enhancement has strong effects on the rheology of the crust and mantle beneath. To illustrate this point, we calculate the strength envelope of the lithosphere using the equivalent-sedimentary load as pressure at the surface, the temperature distribution shown in Fig. 11, and the rheology models of Caristan (1982) and Goetze (1978) described before.

Included in Fig. 11 are the compressional and tensional strength envelopes thus obtained. We show the absolute values for better comparison, although the stresses are positive for compression and negative for tension. For a given stress difference, the thickness inside the strength envelope is the elastic core of the lithosphere (see Fig. 8). The brittle failure is independent of temperature and rock type, but depends on pressure (Byerlee, 1968). The ductile property, on the other hand, strongly depends on the temperature and rock type (Brace and Kohlstedt, 1980). Diabase ductile rheology assumed for the crust is much weaker than dry olivine rheology used for the mantle. The vertical profiles of the strength envelopes (positive compression and negative tension) one at the maximum deflection point (~ 140 km from the continent) and another at 900 km from the continent are displayed in Fig. 12 for better illustration. The profiles at the maximum deflection are multiplied by 100 in order to display them with those at 900 km. The thinned continental crust is weak compared with the upper part of the underlying mantle. The oceanic crust is much thinner, 7 km, and its strength depends on the thickness of the covering sediments. It tends to couple to the mantle and produces a competent layer where sedimentary layer is thin. However, beneath the thick sedimentary cover of Scotian basin, the crust becomes

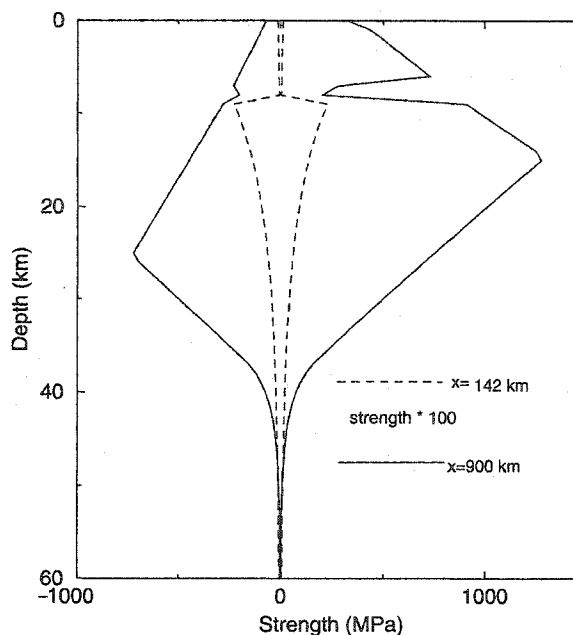


Fig. 12. Profiles of the strength envelopes at the maximum deflection point and a point far from the basin (142 and 900 km in Fig. 11, respectively). Compression is positive and tension is negative. The profiles at 142 km are multiplied by 100 for better illustration.

much weaker and decouples from the relatively strong upper part of the mantle. The effective rigidity of the lithosphere is more than two orders of magnitude smaller beneath the Scotian basin compared with that far from the basin, partly because of greater stress differences related to the sedimentary load and partly because of the weakening due to the thermal blanketing by the sediments. This supports our thin plate model with laterally varying rigidity. The weakening of the lithosphere beneath the sedimentary basins should be regarded as a significant factor when considering the potential site for the initiation of subduction at passive continental margins.

6. Initiation of subduction at Scotian basin

Despite extensive studies on plate tectonics in the last four decades, the initiation of subduction of an oceanic plate is poorly understood (e.g., Uyeda and Ben Avraham, 1972; McKenzie, 1977; Casey and Dewey, 1984; Okal et al., 1986; Cloetingh et al.,

1989; Muller and Phillips, 1991). The major driving forces, the ridge push and the negative buoyancy of the oceanic lithosphere, are not sufficient to overcome the resisting forces associated with the bending of the lithosphere prior to subduction and the frictional force along the thrust fault at the subduction zone. Muller and Phillips (1991) argued against subduction initiation at passive margins and related the initiation of subduction to congestion at pre-existing subduction zones as was suggested earlier by Okal et al. (1986). Erickson and Arkani-Hamed (1993) selected Scotian basin as the most favorable place for the initiation of subduction in the North Atlantic and suggested the thermal weakening of the continental lithosphere beneath the basin and the possible reduction of shear stresses along the subduction zone.

Faulting associated with continental rifting may lock within 10–20 Ma after rifting (Karner and Watts, 1982). However, reactivation of normal faults in the hinge zone is more likely in an extensional setting. This reactivation almost entirely eliminates the shear forces along the thrust faults and changes the hinge zone from a locked to a decoupled, free boundary. Erickson (1993) considered the possibility that the reorientation of the sea floor spreading may produce tensional forces and break apart the basin at the hinge zone, allowing the plate to further subside at its newly formed free boundary. Kemp and Stevenson (1996) investigated the possibility that the decoupling of the oceanic and continental lithosphere produces a rift through which molten basalt from beneath intrudes and erupts, covering the oceanic plate and creating a heavy load required for the initiation of subduction.

The initiation of subduction at passive margins has also been investigated through laboratory experiments. Shemenda (1992) concluded that a pre-existing favorably oriented weak zone is required for subduction at passive margins. Faccenna et al.'s (1999) experiment showed that a passive margin may transform to an active one when the oceanic plate attains considerable negative buoyancy while it is subjected to low compressional stress over geological times.

The weak part of the lithosphere directly beneath the Scotian basin in our model may facilitate the reactivation of the old normal faults and, thus, the break-up of the lithosphere if re-orientation of the spreading direction of the North Atlantic Ocean exerts sufficient tensional forces. To investigate this scenario, we let our

two-segmented plate model with a 500-km-wide weak zone of 10^{22} Nm rigidity break at the hinge zone by imposing a free boundary condition there. The equivalent rock bathymetry is kept unchanged, assuming that breaking of the plate and extra sedimentation occurs synchronously, i.e., sedimentation keeps pace with the fast subsidence. This assumption seems reasonable since the continental wall adjacent to the fast subsiding oceanic lithosphere may readily collapse. It is also possible that, due to the break up, extensive basaltic lava intrudes the crust and floods the sea floor as suggested by Kemp and Stevenson (1996), creating an appreciable load on the plate. The post-break subsidence is so fast that it does not allow enough time for thermal diffusion to change the thermal state of the plate during the subsidence. We therefore assume that the plate retains its rigidity during this rapid subsidence. The resulting deflection (Fig. 13) is much more than that of the plate with pinned boundary at the continent side which is also included in the figure for comparison. Also displayed in Fig. 13 are the deflection profiles of a plate with a uniform rigidity of 10^{23} Nm but one pinned and the other free at the continent side. The weakening of the lithosphere by thermal blanketing effect of sediments has a much stronger effect on the deflection of the lithosphere when it is pinned to the continent than when it is not.

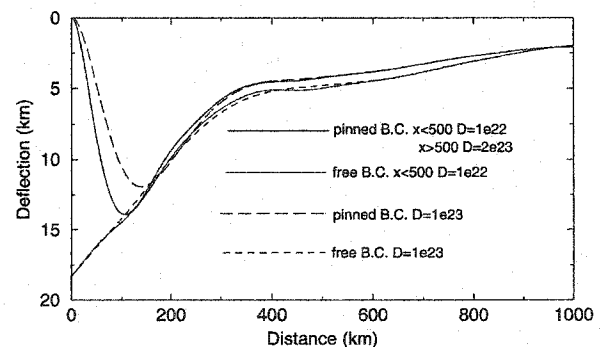


Fig. 13. The deflections of the elastic plate models with pinned boundary conditions, and the deflections of these models if they are decoupled from the continent. The thin solid curve denotes the two-segmented model with a weak zone rigidity of 10^{22} Nm and a 500-km width under pinned boundary conditions. The thick solid curve denotes the deflection of this model when decoupled from the continent. The long dashed curve denotes the deflection of the elastic plate with a uniform rigidity of 10^{23} Nm. The dashed curve denotes the deflection of the same model when it is decoupled from the continent.

The broken lithosphere bends and becomes juxtaposed to the mantle beneath the continent. As time passes, the lithosphere becomes weaker, because of slow heating due to thermal blanketing of the extra sediments and the lateral heat flow from the hotter and deeper parts of the adjacent continental mantle to the upper parts of the plate. This scenario leads us to conclude that the possible reactivation of the normal faults that causes rapid deflection of the oceanic plate and subsequent sedimentation may provide a favorable situation for the initiation of subduction as suggested by laboratory experiments. Low amplitude compression, such as ridge push or stresses produced due to possible reorientation of spreading of the North Atlantic Ocean, may then initiate subduction at the Scotian basin.

7. Conclusions

Our analysis of the observed bathymetry, depth-to-basement and gravity anomalies over the Scotian basin suggests that the basin has been supported by the elastic rigidity of the oceanic and continental lithosphere that became locked shortly after the break-up of Africa and North America and the start of sea floor spreading. Modeling the lithosphere by a thin elastic plate of laterally varying rigidity under the sedimentary load and the load produced by the lateral variations of density shows that the lithosphere is substantially weaker under the basin, by one to two orders of magnitude. We show that this reduction in rigidity may arise from thermal blanketing of the lithosphere by the thick sediments in the basin and the temperature-dependent rheology of the lithosphere. This weaker lithosphere has a tectonic importance. It can facilitate the reactivation of normal faults in the hinge zone, leading to the break-up of the lithosphere and the initiation of subduction of the Atlantic ocean in the Scotian basin.

Acknowledgements

This research was supported by the Natural Sciences and Engineering Research Council of Canada (NSERC) grant # OGP0041245 to JAH. We would like to thank Walter Roest at Geological Survey of

Canada for providing the geophysical data used in this paper, and Andrew Hynes at McGill University for discussions in the early stages of our research. We also like to thank Sonya Dehler, Jean-Claude Mareschal and an anonymous reviewer for their constructive comments.

References

- Beaumont, C., Keen, C., Boutilier, R., 1982. On the evolution of rifted continental margins comparison of models and observations for the Nova Scotian margin. *Geophysical Journal of Royal Astronomical Society* 70, 667–715.
- Brace, W.F., Kohlstedt, D.L., 1980. Limits on lithospheric stress imposed by laboratory experiments. *Journal of Geophysical Research* 85, 6248–6252.
- Brotchie, J.F., Silvester, R., 1969. On crustal flexure. *Journal of Geophysical Research* 74, 5240–5252.
- Byerlee, J., 1968. Brittle–ductile transition in rocks. *Journal of Geophysical Research* 73, 4741–4750.
- Byerlee, J., 1978. Friction of rocks. *Pageoph* 116, 615–626.
- Caldwell, J.G., Haxby, W.F., Karig, D.E., Turcotte, D.L., 1976. On the applicability of a universal elastic trench profile. *Earth and Planetary Science Letters* 31, 239–246.
- Caristan, Y., 1982. The transition from high temperature creep to fracture in Maryland diabase. *Journal of Geophysical Research* 87, 6781–6790.
- Casey, J.F., Dewey, J.F., 1984. Initiation of subduction zones along transforms and accreting plate boundaries, triple junction evolution, and forearc spreading centers: implications for ophiolitic geology and obduction. In: Grass, I.G., et al. (Eds.), *Ophiolites and Oceanic Lithosphere*. Geological Society of London Special Publication, vol. 13, pp. 269–290.
- Cloetingh, S., 1982. Evolution of passive continental margins and initiation of subduction zones. Ph.D. Thesis. Instituut voor aardwetenschappen der Rijksuniversiteit te Utrecht, No.29.
- Cloetingh, S.A.P.L., Wortel, M.J.R., Vlaar, N.J., 1982. Evolution of passive continental margins and initiation of subduction zones. *Nature* 297, 139–141.
- Cloetingh, S.A.P.L., Wortel, M.J.R., Vlaar, N.J., 1989. On the initiation of subduction zones. *Pure and Applied Geophysics* 129, 7–25.
- Dehler, S.A., Keen, C.E., 1993. Effects of rifting and subsidence on thermal evolution of sediments in Canada's east coast basins. *Canadian Journal of Earth Sciences* 30, 1782–1798.
- Erickson, G., 1993. Sedimentary loading, lithospheric flexure, and subduction initiation at passive margins. *Geology* 21, 125–128.
- Erickson, S.G., Arkani-Hamed, J., 1993. Subduction initiation at passive margins: the Scotia basin, eastern Canada as a potential example. *Tectonics* 12, 678–687.
- Faccenna, C., Giardini, D., Davy, P. et al., 1999. Initiation of subduction at Atlantic-type margins: insights from laboratory experiments. *Journal of Geophysical Research* 104, 2749–2766.
- Forsyth, D., 1985. Subsurface loading and estimates of the flexural

- rigidity of continental lithosphere. *Journal of Geophysical Research* 90, 12623–12632.
- Goetze, C., 1978. The mechanisms of creep in olivine. *Philosophical Transactions of the Royal Society of London, Series A* 288, 99–119.
- Ghods, A., Arkani-Hamed, J., 1998. Interpretation of the satellite magnetic anomaly of the Nova Scotia marginal basin. *Canadian Journal of Earth Sciences* 35, 162–174.
- Gradstein, F.M., Jansa, L.F., Srivastava, S.P. et al., 1990. Aspects of North Atlantic paleo-oceanography. In: Keen, M.J., Williams, G.L. (Eds.), *Geology of the Continental Margin of Eastern Canada*, Chapter 8. Geological Survey of Canada, Geology of Canada, vol. 2, pp. 351–389.
- Karner, G.D., Watts, A.B., 1982. On isostasy at Atlantic-type margins. *Journal of Geophysical Research* 87, 2923–2984.
- Keen, C.E., Beaumont, C., 1990. Geodynamics of rifted continental margins. In: Keen, M.J., Williams, G.L. (Eds.), *Geology of the Continental Margin of Eastern Canada*, Chapter 9. Geological Survey of Canada, Geology of Canada, vol. 2, pp. 391–472.
- Keen, M.J., Piper, D.J.W., 1990. Geophysical and historical perspective. In: Keen, M.J., Williams, G.L. (Eds.), *Geology of the Continental Margin of Eastern Canada*, Chapter 1. Geological Survey of Canada, Geology of Canada, vol. 2, pp. 5–30.
- Keen, C.E., Potter, D.P., 1995. Formation and evolution of the Nova Scotian rifted margin: evidence from deep seismic reflection data. *Tectonics* 14, 918–932.
- Keen, C.E., Loncarevic, B.D., Reid, I. et al., 1990. Tectonic and geophysical overview. In: Keen, M.J., Williams, G.L. (Eds.), *Geology of the Continental Margin of Eastern Canada*, Chapter 2. Geological Survey of Canada, Geology of Canada, vol. 2, pp. 31–85.
- Kemp, D.V., Stevenson, D.J., 1996. A tensile, flexural model for the initiation of subduction. *Geophysical Journal International* 125, 73–94.
- Lago, B., Cazenave, A., 1981. State of stress in the oceanic lithosphere in response to loading. *Geophysical Journal of Royal Astronomical Society* 64, 785–799.
- Lambeck, K., Nakiboglu, S.M., 1980. Seamount loading and stress in the ocean lithosphere. *Journal of Geophysical Research* 85, 6403–6418.
- McAdoo, D.C., Sandwell, D.T., 1985. Folding of oceanic lithosphere. *Journal of Geophysical Research* 90, 8563–8569.
- McKenzie, D.P., 1977. Initiation of trenches: a finite amplitude instability. In: Talwani, M., Pitman, W. (Eds.), *Island Arcs, Deep Sea Trenches and Back-Arc basins*. American Geophysical Union, Maurice Ewing Series, vol. 1, pp. 57–62.
- McNutt, M., 1980. Implications of regional gravity for state of stress in the Earth's crust and upper mantle. *Journal of Geophysical Research* 85, 6377–6396.
- McNutt, M.K., Diament, M., Kogan, M.G., 1988. Variations of elastic plate thickness at continental thrust belts. *Journal of Geophysical Research* 93, 8825–8838.
- Menke, W., 1981. The effect of load shape on the deflection of thin elastic plates. *Geophysical Journal of the Royal Astronomical Society* 65, 571–577.
- Muller, S., Phillips, R.J., 1991. On the initiation of subduction. *Journal of Geophysical Research* 96, 651–665.
- Oakey, G.N., Stark, A., 1995. A digital compilation of depth to basement and sediment thickness for the North Atlantic and adjacent coastal land mass. Geological Survey of Canada, open file # 3039, 1995.
- Okal, E.A., Woods, D.F., Lay, T., 1986. Intraplate deformation in the O-Gilbert-Ralik area: a prelude to a change of plate boundaries in the southwest Pacific? *Tectonophysics* 132, 69–77.
- Pilkington, M., 1990. Lithospheric flexure and gravity anomalies at Proterozoic plate boundaries in Canadian shield. *Tectonophysics* 176, 277–290.
- Royden, L., Keen, C.E., 1980. Rifting process and thermal evolution of the continental margin of eastern Canada determined from subsidence curves. *Earth and Planetary Science Letters* 51, 343–361.
- Sandwell, D.T., Smith, W.H.F., 1997. Marine gravity anomaly from Geosat and ERS 1 satellite altimetry. *Journal of Geophysical Research* 102, 10039–10054.
- Shemenda, A.I., 1992. Horizontal lithosphere compression and subduction: constraints provided by physical modeling. *Journal of Geophysical Research* 97, 11097–11116.
- Sclater, J.G., Christie, P.A.F., 1980. Continental stretching: an explanation of the post-mid-Cretaceous subsidence of the central North Sea basin. *Journal of Geophysical Research* 85, 3711–3793.
- Turcotte, D.L., Schubert, G., 1982. *Geodynamics—Applications of Continuum Physics to Geological Problems*, Chapter 3. Wiley, New York, pp. 104–133.
- Uyeda, S., Ben Avraham, Z., 1972. Origin and development of the Philippine Sea. *Nature* 240, 176–178.
- Wade, J.A., MacLean, B.C., 1990. The geology of the southeastern margin of Canada. In: Keen, M.J., Williams, G.L. (Eds.), *Geology of the Continental Margin of Eastern Canada*, Chapter 5. Geological Survey of Canada, Geology of Canada, vol. 2, pp. 167–238.
- Watts, A.B., Bodine, J.H., Steckler, M.S., 1980. Observation of flexure and the state of stress in the oceanic lithosphere. *Journal of Geophysical Research* 85, 6369–6376.
- Zheng, Y., Arkani-Hamed, J., 1998. Joint inversion of gravity and magnetic anomalies of eastern Canada. *Canadian Journal of Earth Sciences* 35, 832–853.
- Zuber, M., Bechtel, T., Forsyth, D., 1989. Effective elastic thickness of the lithosphere and mechanisms of isostatic compensation in Australia. *Journal of Geophysical Research* 94, 9353–9367.